Earth Science Department
University College London

Stall and Collapse in Mantle Plumes: An experimental and numerical fluid dynamics perspective

Marie Pears

Abstract

Collapsing thermal plumes were investigated through experimental and numerical simulations. Collapsing plumes are an uncommon fluid dynamical phenomenon, usually observed when the heat source is removed.

A series of fluid dynamical experiments were conducted on thermal plumes at a variety of temperature and viscosity contrasts, in a cubic plexiglas tank of inner side dimension 26.5cm and no-slip sides. The fluid was heated by a small 2cm diameter heater. Experimental fluids included Lyle's Golden syrup and ADM's Liquidose 436 syrup, which have strongly temperature-dependent viscosities and high Prandtl numbers (10^3-10^5 at experimental conditions). Visualisation techniques included white light shadowgraphs and Stereoscopic Particle Image Velocimetry (SPIV) of the tank's central plane. Temperature contrasts ranged from 3-60°C, and two differing forms of collapse were identified. At very low temperature differences "stalled" collapse was observed, where the plumes stall in the lower third of the tank before collapsing. At temperature differences between 7-23°C normal plume evolution occurred, until "lenticular" collapse developed between midway and two-thirds of the distance from the base of the tank. The "lens shape" originated in the top of the head and was present throughout collapse. At temperatures above ΔT=23°C, the plumes followed the expected growth and shape and the head flattened out at the top of the tank.

Thermal collapse remains difficult to explain given experimental conditions (continuous heating). Instead, it is possible that small density differences arising from crystallisation at ambient temperatures changes plume buoyancy and therefore induces "lenticular" collapse. The evolution of the refractive index of the syrup through time to ascertain this possibility was measured. Additionally, SPIV revealed the presence of a large, downwelling, low velocity mass in the tank that inhibited the growth of low temperature difference "stalled" collapse plumes.

In the mantle it is likely that the "stalled" collapse plumes would be unable to be detected by tomography because they would be unable to traverse far from the thermal boundary layer and would collapse back to the base. This would mean that they would have little impact on redistributing material in the mantle. The plumes in this "stalled" collapse regime had rise times comparable to diffusion times, which is an additional reason for the collapse. The "lenticular" collapse in the mantle could cause depletion of a deep-source and redistribute the material in the region where the plume began to collapse with some material flowing back to the base of the mantle.

Numerical simulations using Fluidity[1] were undertaken to explore the parameter range where the two collapse phenomena were observed experimentally. These simulated plumes did not show signs of collapse in the purely thermal simulation but at temperature differences up to 14°C the plumes stalled and were unable to ascend to the top of the tank. The aspect ratio of the tank was changed to explore the effect this had on plume stalling. At increased tank height the plume ascended further in the tank whilst the conduit radius remained constant. However, the very low temperature difference plumes remained unable to reach the upper surface of the tank. In contrast, when the tank width was increased the plumes ascended a little further in the tank but stalled at an earlier time and the plume conduit width generally increased. This implied that the tank width was inhibiting the growth of the plume marginally. Therefore, changing the aspect ratio of the tank does not inhibit the stalling of the simulated plumes and is unlikely to be influencing the experimental plumes growth, stalling and collapse.

---

[1]Fluidity, is an adaptive mesh finite element package

I, Marie Pears, confirm that the work presented in this thesis is my own. Where information has been derived from other sources, I confirm that this has been indicated in the thesis.

Signed _____   Date _____

Acknowledgements

Contents

List of Figures

14

List of Tables

Nomenclature

Symbol	Description	Units
α	Thermal expansion coefficient	$^\circ\text{C}^{-1}$
κ	Thermal diffusivity	m^2/s
η	Dynamic viscosity	Pa s
ν	Kinematic viscosity	m^2/s
C_p	Specific Heat Capacity	$\text{J/kg}^\circ\text{C}$
ρ	Density	kg/m^3
T	Temperature	$^\circ\text{C}$
k	Thermal conductivity	$\text{W/m}^\circ\text{C}$
v	Plate Velocity	m/yr
$\Delta\text{T}=\text{T}_h\text{-T}_\infty$	Temperature Difference	$^\circ\text{C}$
$\eta^*=\eta_\infty/\eta_h$	Viscosity Contrast	-
U	Velocity	m/s
δ	Thermal boundary layer thickness	m
l_c	Height of tank	m
τ_c	Diffusion time	s
τ_b	Onset time	s
g	Gravitational acceleration	m/s^2
D	Plume conduit Diameter	m
P	Pressure	Pa
B	Buoyancy	kg/s
R	Plume radius	m
H	Head width	m
m	Mass	kg
V	Volume	m^3
n	Refrative index	-
t	Time	s
$\Delta\text{t}=\text{t}_1\text{-t}_0$	Inter-frame time	s
$\Delta\text{x} = \text{x}_1\text{-x}_0$	Distance moved by particles between frames	mm
$\omega = \text{curl U}$	Vorticity	s^{-1}
subscript		
h	Heater	
∞	Ambient	
b	onset	
o	non-dimensionalised value	
p	plume in shadowgraph image	
1	frame 1	
0	frame 0	

Chapter 1

Introduction

Space exploration missions have enabled extensive information to be discovered about the other planets in the solar system and planetary satellites (Schubert et al., 2001). This led to the discovery that plate tectonics is unique to Earth. However, gaining knowledge of Earth's inner workings remains elusive, due to the extremes of pressures and temperatures which exist in the planet's interior. Lava expelled from Earth via volcanoes reveals information about the workings, chemical composition and structure of the mantle. Nonetheless, the fluid dynamics of Earth are challenging to understand and numerous unknowns remain that are critical to our understanding of Earth's mantle, including its evolution and circulation (Bercovici, 2007).

Surface plate motions reflect the solid-state thermal convection in Earth's mantle, which provides a framework for interpreting volcanism at plate boundaries, namely along spreading ridges (divergent boundaries) and subduction zones (convergent boundaries). There are also prominent features which cannot be explained by plate tectonics such as linear chains of oceanic islands and sea-mount chains (Wilson, 1963a, 1965; Morgan, 1971), where anomalous volcanism is present. The locations of anomalous volcanism are termed hotspots (Wilson, 1963b), which occur intra-plate away from plate boundaries (Burke and Wilson, 1976; Hamblin and Christiansen, 2003; Turcotte and Schubert, 2002) and the volcanism is unlike that associated with island arcs and spreading ridges.

Hotspots are traditionally characterised by some or all of the following features:

1. An age progressive volcanic chain (Figure 1.1 and 1.2)

2. Large Igneous Provinces, a term including continental flood basalts and oceanic plateaus.

3. Topographic swells.

4. Hotspot basalts or Ocean Island Basalts (OIBs), which are geochemically distinct and more diverse than mid-ocean ridge basalts (MORBs) (Morgan, 1972; Ribe et al., 2007; Farnetani and Hofmann, 2011).

5. Gravity anomalies and geoid highs (as discovered at Hawaii and Iceland) (Schubert et al., 2001).

6. The material expelled from hotspots is 200-300°C hotter than "normal" mantle (Ribe et al., 2007; Herzberg et al., 2007) and the volume produced is estimated to be $<1km^3$ year^{-1} which is $\lesssim 5\%$ of the volume of volcanic material produced at mid-ocean ridges (Suetsugu et al., 2004).

Image removed due to copyright, it can be located on page 589 Fig. 2 of Relative motions of hotspots in the Pacific, Atlantic and Indian Oceans since late Cretaceous time. Nature (327) 587-591 Molnar and Stock (1987).

Figure 1.1: Age progression of the Hawaiian-Emperor sea-mount and island chain (Molnar and Stock, 1987) The bold printed text are the dates inferred from magnetic anomalies and the dated seamounts are in normal print.
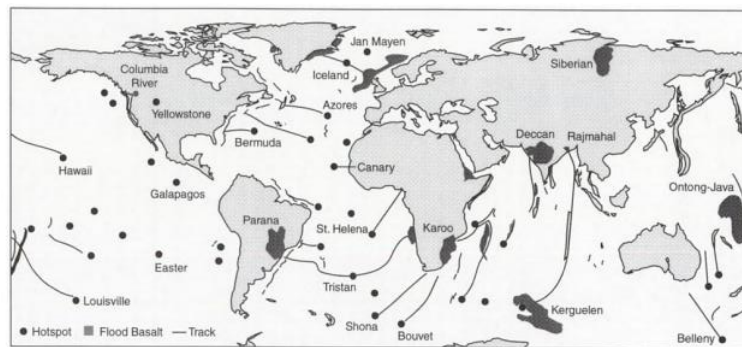
Figure 1.2: Map of major hotspots, hotspot tracks and flood basalts (Schubert et al., 2001).

Hawaii is viewed as the archetypal hotspot, with 107 volcanoes in the sea-mounts, ridges and islands which stretch 6,000km into the northern Pacific (Bargar and Jackson, 1974). Wilson (1963a) postulated that the Hawaiian islands were one of seven, parallel linear chains of islands and sea-mounts in the Pacific Ocean which had properties different from all other mid-ocean ridges. The source of the volcanism on Hawaii was likely to have occurred within the relatively stagnant centre of a jet-stream type of cell and as the convection current moved north-westerly

over the source, a succession of older volcanoes occurred to the north-west (Wilson, 1963a). The volcanoes in the chain were discovered to have experienced the same life cycles and have monotonic age progression (Morgan, 1972, 1981). Burke and Wilson (1976) furthered this idea suggesting one magma source generated all the islands in the chain.

The idea of Morgan's (1971) that the surface signatures of hotspots are due to the rise and melting of hot plumes in the mantle has had a lasting impact on geoscience, though much remains to be explained. For example, one of the most enduring problems is the persistence of hotspot volcanoes over geological time (Jellinek and Manga, 2004). Each hotspot may have a lifetime of more than 100Myr but remain transient features on Earth's surface (Schubert et al., 2001). The time spans of hotspots can be classified into categories where hotspots of 100Myr and younger are deemed active, those born between 100-140Myr are either "wandering" or "failing" and hotspots of 150Myr or older generally have no active trace (Farnetani and Hofmann, 2011; Courtillot et al., 2003). Over the years, the estimated number of hotspots has varied from 20 (Morgan, 1971), to a maximum of 117 in the 1980s (Farnetani and Hofmann, 2011). The total number of hotspots is still debated, but has been modified to around 40-50 (Richards et al., 1988; Sleep, 1990), of which 8 or 9 are associated with flood basalts (Richards et al., 1989; Courtillot et al., 2003). As increasingly more data has been gathered, it has been determined that there is likely to be more than one type of hotspot on Earth (Morgan, 1978; Davaille, 1999a; Courtillot et al., 2003) as shown in Figure 1.3.
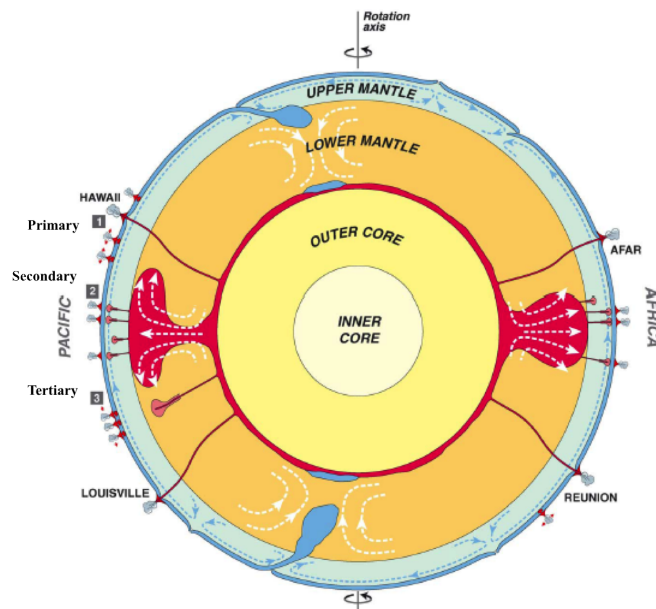
Figure 1.3: A cross-section of the dynamic Earth displaying the three types of plumes/hotspots: 'primary' hotspots (7 found from the 49 investigated) which originate in the lower mantle also known as 'Morganian' hotspots, 'secondary' hotspots originating at the bottom of the transition zone and the 'tertiary' hotspots which are upper mantle features associated with tensile stresses, also known as 'Andersonian' hotspots. From Courtillot et al. (2003).

Other viewpoints have been put forward as a reason for the formation of hotspots. Intra-

plate volcanism which is typically basaltic, effusive and low in volume, could occur because of various localised processes such as; cracking of the lithosphere (Forsyth et al., 2006; Turcotte and Oxburgh, 1978; McKenzie and Bickle, 1988), small-scale convection in the mantle beneath the lithosphere (King and Ritsema, 2000; Elkins-Tanton, 2007; Ballmer et al., 2009) or shear-induced melting of low-viscosity pockets of asthenospheric mantle which have become embedded along the base of the lithosphere (Conrad et al., 2011). In the case of the latter, Conrad et al. (2011) observed correlation between recent continental and oceanic intra-plate volcanism and areas of the asthenosphere which are undergoing rapid shear due to mantle convection. The authors suggested that low-volume intra-plate volcanism is caused by melting induced by asthenospheric shear flow and other less important localised processes.

1.0.1 Geochemical considerations

Image removed due to copyright, it can be located on page 222 Fig. 3 of Mantle geochemistry: the message from oceanic volcanism. Nature (385) 219-229 Hofmann (1997).

Figure 1.4: Nd and Sr isotropic compositions of MORB and OIB, with extreme HIMU (high time-integrated U/Pb mantle), EM1 and EM2 (enriched mantles 1 and 2) samples. FOZO stands for "focal zone"(Hofmann, 1997).

OIBs formed from the modern mantle often display a characteristic enrichment of light rare earth elements relative to MORBs which have been detailed since the mid 1960s (Gast et al., 1964; Engel et al., 1965; Tatsumoto, 1966) and show a large variation in composition (Hofmann, 1997). The variations in isotopic chemistry between MORBs and OIBs informs the standard geochemical model of separate chemical reservoirs, which remain chemically isolated. MORBs are derived from a well mixed convecting part of the mantle (Allègre, 1987; Kellogg and Wasserburg, 1990; Hofmann, 1997). The OIBs are derived from a separate and perhaps deeper reservoir, which is further subdivided into three separate reservoirs, HIMU (high time-integrated U/Pb mantle), EM1 and EM2 (enriched mantles 1 and 2). Figure 1.4 shows that the ^{143}Nd/^{144}Nd correlates negatively with ^{87}Sr/^{86}Sr (Zindler and Hart, 1986). The MORB data forms a relatively

tight cluster of ^{143}Nd/^{144}Nd between 0.5130-0.5134 and ^{87}Sr/^{86}Sr between 0.702-0.703. A number of the OIBs, EM1 and EM2 basalts plot near the PRIMA point (primitive mantle) on Figure 1.4 with $\sim$0.5126^{143}Nd/^{144}Nd and $\sim$0.705^{87}Sr/^{86}Sr, whilst the HIMU data points are positioned below the FOZO point and near to the Indian and Atlantic MORBs data points. All the OIBs are between the continental crust and MORBs data, suggesting OIBs could result from back-mixing of various types of continental material.

Most uniform mid-ocean ridges have lower ^{3}He/^{4}He ratios than many hotspots (Zindler and Hart, 1986). As He is so volatile, un-reactive and too light to be captured in the atmosphere, the isotopic He ratios reflect those of the solid Earth. In the mantle ^{3}He is not created by radioactive decay, whereas ^{4}He is dominated by the decay of U and Th (Hofmann, 1997). Therefore, the presence of any ^{3}He can be interpreted as preservation of volatile components in the mantle since its formation. The emission of ^{3}He at hotspots also leads to the isolation of the source of OIBs from that of MORBs (Figure 1.5a). Additionally, the uniform values of MORB ratios indicate that mantle mixing cannot be considered as a source of the surface variations. Therefore, the high ^{3}He/^{4}He ratios of OIBs support the theory of separate reservoirs located in the mantle at the core-mantle boundary (CMB) to minimise the possibility of degassing (Allègre et al., 1995; Hanan and Graham, 1996).
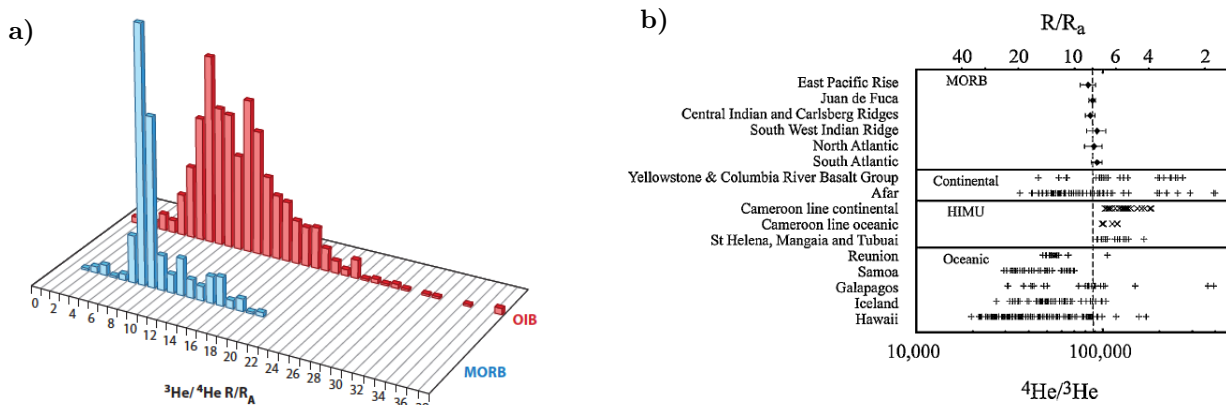
Figure 1.5: Plots showing the helium ratio for a selection of MORBs and continental and oceanic hotspots worldwide. The tight clustering of the MORBs has been explained by a homogeneous well mixed reservoir in stark contrast with the widespread range of other volcanism. The MORBs have a R/Ra=8 and OIBs have a greater range of values a) from White (2010) and b) from Barfod et al. (1999).

Hofmann (1997) postulated that plumes may come from both the 660-km discontinuity and the CMB. Small short-lived plumes and those carrying no enrichment in primordial ^{3}He, are most likely of shallow origin, whereas large, long-lived ^{3}He-rich plumes, especially those that have generated enormous volumes of oceanic or continental flood basalts, are more likely to have originated from the base of the lower mantle. The distinctly different geochemistry is also observed in the ^{3}He/^{4}He isotope ratio compilation of Figure 1.5b which significantly added to

the strength of the argument that mantle plumes cause hotspots.
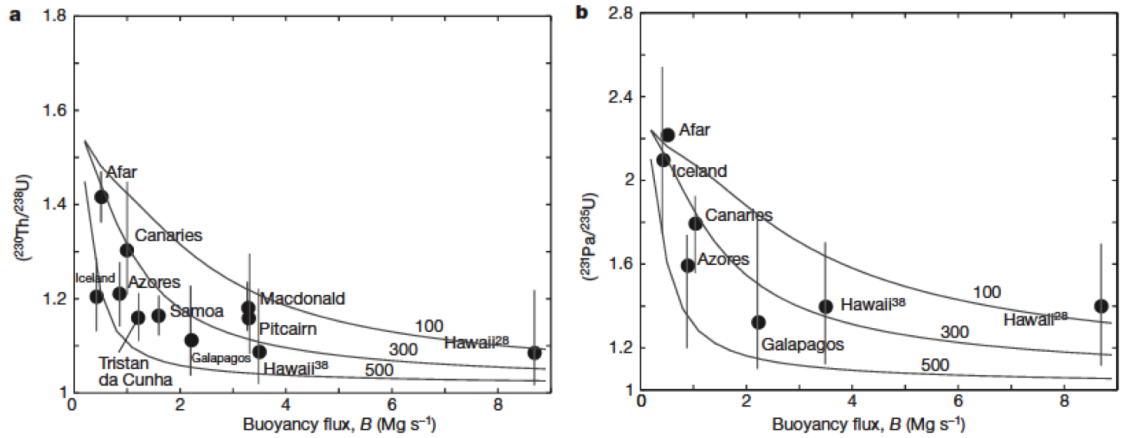
Figure 1.6: The Uranium-series activity ratios versus buoyancy fluxes for recent hotspot lavas. The mean for each hotspot is represented by a black spot and the range by the vertical line (Bourdon et al., 2006). a) is the $(^{230}\text{Th}/^{238}\text{U})$ b) $(^{231}/^{235}\text{U})$. The model curves are labelled with excess temperature in the boundary layer generating the plume (100, 300 and 500°C).

An additional measurement from hotspots lavas is the Uranium-series disequilibria of Bourdon et al. (2006) as shown in Figure 1.6. This model provides evidence that hotspots are associated with increased buoyancy and temperature upwellings in the mantle, whilst the position of low buoyancy flux plumes is not fixed as they are likely to be affected by upper mantle convection. Additionally, it provides constraints on the velocity of the mantle upwellings, the mantle temperature (controlling the degree of melting) and the horizontal length scale of the upwelling. Therefore, a unique link has been established between the geochemical and geophysical constraints of mantle dynamics (Bourdon et al., 2006). There is a weak dependence of $(^{231}\text{Pa}/^{235}\text{U})$ and $(^{230}\text{Th}/^{238}\text{U})$ on the ΔT_{bottom} where mantle plumes originate and has little influence on the curve of Figure 1.6. These curves show that the initial excess temperatures, ΔT_{bottom}, in the range of 100-300°C are consistent with geophysical inferences and geochemistry because plumes with low buoyancy fluxes cool more during upwelling (Bourdon et al., 2006). Many previous models such as Chabaux and Allègre (1994) have neglected the thermal aspects of the problem of mantle plume upwellings which have been included in the model of Bourdon et al. (2006).

1.1   Mantle Plumes

Currently accepted theory, since Morgan (1971) first proposed the concept of hotspots, considers mantle plumes as the most likely cause of hotspot tracks and hotspot volcanism and that they play a key role in models of Earth dynamics (Hill et al., 1992; Coulliette and Loper, 1995). Mantle plumes (especially thermal plumes) are hypothesised to originate from the CMB (Morgan, 1971; Sleep, 1990; Griffiths and Campbell, 1990; Griffiths, 1991; Davies and Richards, 1992; Schubert

et al., 2001; King and Redmond, 2007). The flow pattern of mantle plumes is distinct from the mantle convective pattern (Loper, 1984; Davies, 1988) and plumes survive due to their rapid ascent through the mantle (10^6-10^7yr). Plumes are hotter than the surrounding mantle, with the standard model of a plume having a large, bulbous head and a trailing narrow conduit (Campbell and Griffiths, 1990), which develop as instabilities from thermal boundary layers (Loper and Stacey, 1983). The conduit is likely to remain in existence for at least 100Myr as long as there is hot material supplied from the base. However, mantle plumes remain difficult to observe and this is the primary cause for our rudimentary understanding of plumes in the Earth (Ribe et al., 2007).

1.1.1   Geophysical evidence

The existence and presence of mantle plumes can be investigated by seismic tomography. The variable resolution of seismic studies is due to a number of factors including the size of the array, the depth of imaging and the method of interpreting the raw data.

Nataf and VanDecar (1993) were the first to detect mantle plumes using tomography and indicated there were good prospects for detecting plumes in the lower mantle through seismology. Ritsema and Allen (2003) suggest mantle plumes can remain elusive in tomographic images due to the poor resolution of the technique, leading to continued debate on the existence of plumes. Davaille and Vatteville (2005) point out that tomography provides present-day snapshots, adding to the difficulty of detectability. To assess seismic visibility of thermal mantle plumes, consideration of the temperature sensitivity of seismic velocity is needed as it varies considerably with temperature, depth, phase transitions and anelasticity (Goes et al., 2004). It is likely that a viscosity reduction by a factor of 30-100 would be needed (as a jump of strong gradient) for narrow upper-mantle plumes to be located from surface observation and tomography. Implying that for whole-mantle thermal plumes to be detected by seismic tomography they need to have buoyancy fluxes of $\geq$ 4Mg/s (Goes et al., 2004).

Recently, Ribe et al. (2007) has indicated that surface-wave tomography has identified broad ponds ($\sim$1000km) of slow material to a depth of 200km beneath numerous hotspots, but not individual plumes. Despite the improving resolution of tomographic models, hot plume conduits deep in the mantle under hotspots could remain undetectable, if between 50 to 100km wide (according to the classic plume model) (Campbell and Griffiths, 1990; Kumagai et al., 2008). However, the existence of plumes has been recently discovered beneath at least ten hotspots to the CMB from cylindrical slow seismic P-wave velocity anomalies (300-500km in diameter)
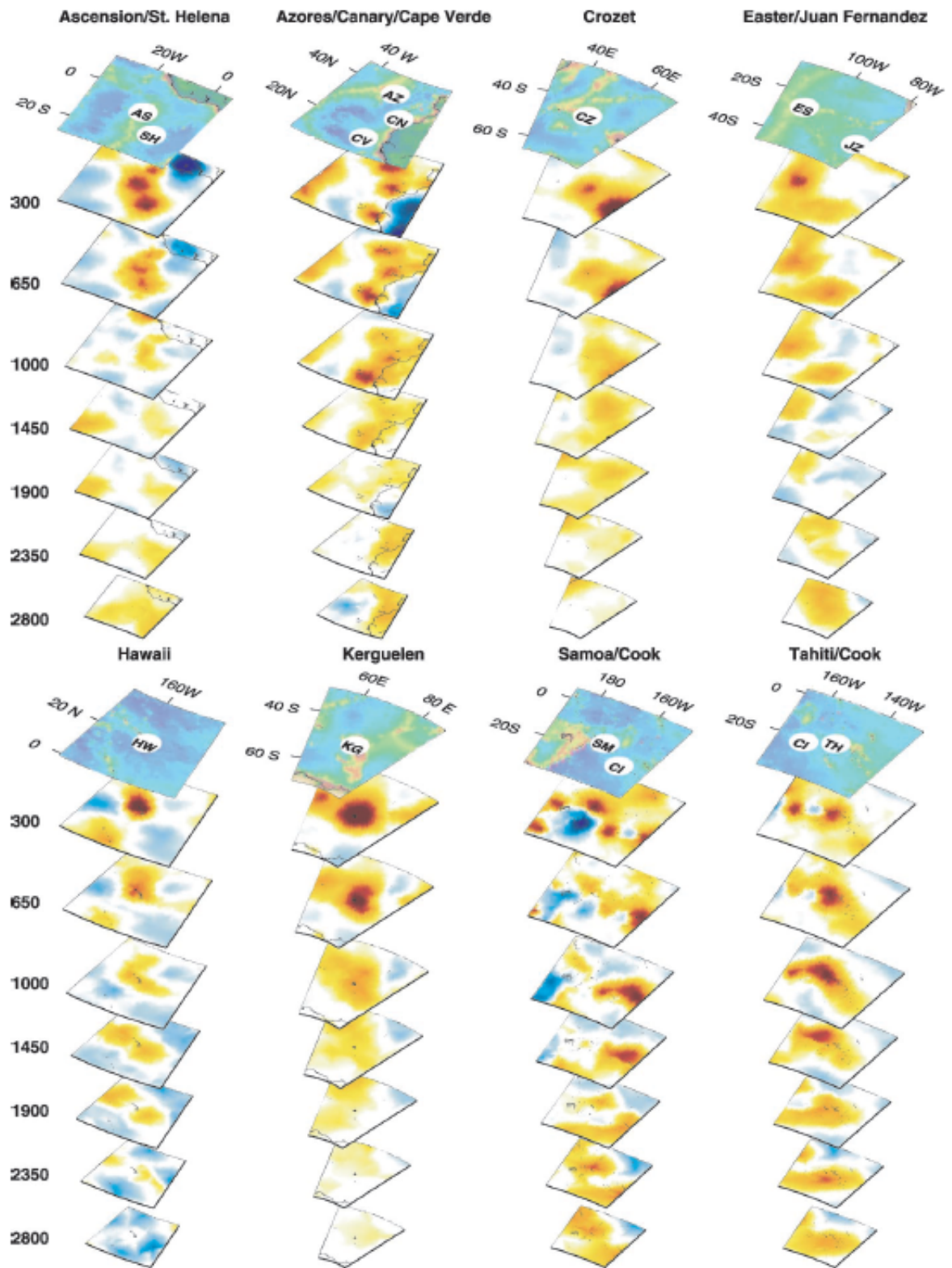
Figure 1.7: The three-dimensional view tomographic model of deep plumes. The maps are 40° by 40° and are scaled appropriately with depth, however after 1000km the depth spacing has been changed. The Ascension, Azores, Canary, Easter, Samoa and Tahiti hotspots all have well-resolved deep-rooted origins near the bottom of the mantle.From Montelli et al. (2004).

(Zhao, 2001; Montelli et al., 2004; Ribe et al., 2007) as shown in Figure 1.7. Although this is a highly contested view because there is difficulty detecting a continuous conduit to the D″ layer. Hwang et al. (2011) believe that narrow lower mantle plume tails are not detectable and suggest it would be difficult to design experiments by which lower mantle plumes could be detected by

seismological methods.

One of the most thoroughly investigated hotspots is Iceland, yet it has remained difficult to constrain the width and temperature of the plume from seismological and geodynamic studies in the past (Wolfe et al., 1997). The results examined by Wolfe et al. (1997) from P- and S-waves from regional seismic arrays have observed a cylindrical region of low velocity extending from 100km to at least 400km beneath central Iceland. This was concluded to be a hot, narrow plume of upwelling mantle material with a 150-200km radius at 300km depth. Bijwaard and Spakman (1999) imaged a "bent" mantle plume under Iceland, extending from the surface to the CMB (Figure 1.8). The imaged deflection of the slow velocity anomaly fits the views of Steinberger (2000) and Steinberger and O'Connell (1998, 2000) that plume conduits deflected by mantle convection currents will not be imaged directly under the current location of hotspot volcanism.
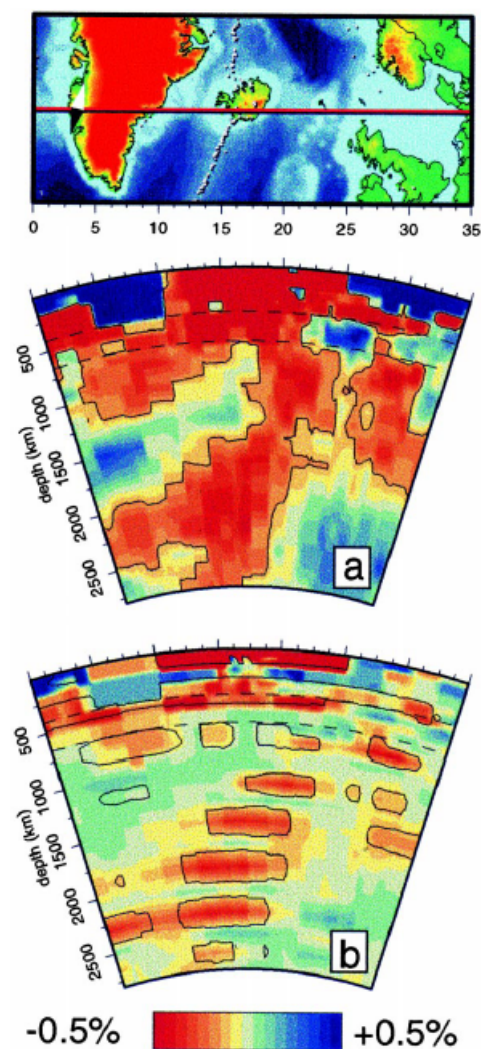
Figure 1.8: The cross-section through the model of Bijwaard and Spakman (1999) showing a large plume-shaped anomaly in the mantle below Iceland. The dashed lines display the 410km and 660km discontinuities (Bijwaard and Spakman, 1999).

Nonetheless, narrow column-like anomalies of low seismic velocity that can be associated with high temperatures as expected under hotspots remain uncommon (Suetsugu et al., 2004). However,

where present, it has been determined that low seismic velocities extend to depths of 200km below hotspots, whereas beneath ridges they are confined to the upper 100km (Suetsugu et al., 2004). This suggests that hotspots are caused by active upwellings, namely mantle plumes with deeper sources, compared to ridges, which are produced by passive upwellings. Recent research by French et al. (2013) using full-waveform seismic tomography has imaged a pattern of horizontally elongated bands of low shear velocity between 200-350km depth, which is well below the well developed low-velocity zone. The structures imaged are quasi-periodic and finger-like, with a wavelength of $\sim$2000km, which align parallel to the direction of absolute plate motion for at least 1000km, many of which underlie regions associated with hotspot tracks or sea-mount chains. Below 400km depth, the velocity structure is organised into fewer, vertically coherent, undulating low-velocity plumelike features which appear rooted in the lower mantle (French et al., 2013). The PLUME experiment that took place on Hawaii discovered zones of fast velocities surrounding the islands, which were particularly strong in shear velocity, to the south-west near to 300km depth (Wolfe et al., 2011; Laske et al., 2011). This corresponds with the model of French et al. (2013) where there is a domain of higher velocities between the low-velocity fingers. These two studies link together isolated observations and suggest that there is a single consistent pattern of low-velocity fingers in the mantle. Globally these fingers have been observed by French et al. (2013) to be associated with many hotspot tracks or sea-mount chains.

1.1.2   Dissenting Voices

Although mantle plume theory is widely accepted, some scientists continue to argue vehemently against it and their research is active in attempting to disprove the theory (White, 2010). Since the 1970s much of the evidence presented for mantle plumes has been debated and alternative mechanisms and explanations have been postulated based on physics and observations.

Observations do not agree with the predictions of the classical plume model. Many volcanic tracks are not time-progressive, such as the Ontong Java Plateau which lacks the volcanic track associated with a plume tail. Hotspots are expected to be underlain by quasi-cylindrical hot bodies of rock which extend to the CMB. However, seismology has failed to observe these structures despite vast advances in the technology used for imaging the deep mantle. Additionally, Forsyth and Uyeda (1975) proposed that plumes were not required because gravitational and pressure forces such as slab pull, ridge push and slab suction could alone drive tectonic plates.

The changing estimate of the number of mantle plumes over time, leads to the theory continually

evolving. Over the years, the estimated number of hotspots has varied from 20 (Morgan, 1971), to a maximum of 117 in the 1980s (Farnetani and Hofmann, 2011). The present estimate of the number of moderate size mantle plumes is approximately 5200 (Malamud and Turcotte, 1999) and 8 or 9 primary plumes, a drastic increase from the original number. This evolution and change in the definition and number of plumes should actually be regarded as valuable to the geodynamic community as research refines and expands the understanding and interpretation of mantle plumes within Earth.

Much of the geochemical evidence for different reservoirs for MORBs and OIBs, such as the radiogenic isotopes of Sr, Nd and Pb and most incompatible trace elements have now been discredited as evidence for mantle plume. The presence of high maximum $^3He/^4He$ ratios have been suggested to explain that the lower mantle is high in primordial ^3He. However, some hotspot basalts fail to show high $^3He/^4He$ ratios. Instead, it is suggested that the geochemical arguments can be accounted for by involvement of components derived from Earth's crust such as varieties of sediment and altered ocean crust (Zindler and Hart, 1986; Hofmann, 1997).

Although Hawaii fits the plume theory well, as it was designed around the location, the increased magmatism over the past 6Myr is an anomaly which cannot be explained by the theory. One possible suggestion is that the Hawaiian swell could be attributed to both recent and ancient buoyant residues (Phipps Morgan, 1997). Additionally, linear time progressive volcanism and high magmatic productivity can be explained by other mechanism such as propagating cracks, shear heating and high mantle fertility.

The effect of high pressure on convection in the deep mantle is critical in the argument against mantle plumes because, given the physics of the interior of Earth, it is unlikely that convective upwellings from the deep mantle rise to the surface and produce hotspots (Foulger, 2010). Pressure has a strong non-linear effect on thermal expansion, conductivity and viscosity. At the base of the mantle pressure is 1.4 million atmospheres, approximately 200 times the pressure at the base of continental crust (Anderson and Natland, 2005). At high-pressure, temperature has little effect on density and very little buoyancy is imparted to material warmed by the CMB. Thermal conductivity increases with pressure and viscosity, increasing by 1-2 orders of magnitude from the surface to the core; this will hinder convection and the ability for plumes to form and take heat away by advection (Foulger, 2010). Additionally, the effects of pressure may lead to the lower mantle being chemically stratified and thus the temperature variations in the deep mantle could cause density variations that are smaller than in the chemical interfaces. This would inhibit plume formation and ascent from the deep mantle. Experiments cannot simulate such deep mantle pressures and many numerical simulations neglect these pressures. Therefore,

the research is not truly representative of Earth. If hot plumes need to form at thermal boundary layers but cannot form in the deep mantle, and no other thermal boundary layers are observed, as the other major seismic discontinuities are known to result from mineralogical changes and not temperature changes, the question is asked: How then can thermal plumes form in the mantle?

1.2 Unanswered questions

In spite of a considerable volume of research our understanding of plumes in Earth's mantle is still rudimentary. Indeed, recent advances demonstrate there is still no general consensus on the important questions concerning plumes in the mantle: their depth of origin, morphology, longevity and indeed their very existence (Ribe et al., 2007). The key controversies result in two main questions, which are often investigated in separate studies:

a) How do plumes behave in a fluid dynamical sense? Can plumes originate and survive in an internally heated, vigorously convecting mantle, likely dominated by the large-scale flow associated with plate motions?

b) If mantle plumes are able to reach the surface (Jellinek and Manga, 2004), can they explain the surface volcanism and geochemistry as revealed by the isotopic signatures of ocean island basalts? (Zindler and Hart, 1986; Hart et al., 1992; Hofmann, 1997)

For this thesis the focus is on a more limited fluid dynamical question that contributes to a),

"What are the conditions of buoyancy that lead to plume failure or survival?"

Investigating plumes via experimentation, such as in the work of Newsome (2011) and Moses et al. (1993), is desirable because they are small features compared to the length scale of the mantle, which requires very high-resolution numerical models (tens of million finite elements); often hard to achieve despite present codes running on as many as 256 processors. Mantle plumes are particularly amenable to experimental approaches, because it is possible to replicate the fluid dynamical conditions leading to their formation and make a number of testable predictions. Additionally, laboratory experiments on mantle plumes have been crucial for exploring new physics and testing theories (Davaille and Limare, 2007), with many studies undertaken since the mid-1980s. However, early studies focused on the simpler case of an isolated, laminar "starting plume" rising from a point source of buoyancy, usually injected into the fluid, rather than generated thermally (Ribe, 2007). More recent studies on thermal plumes have focused on

global features, where the entire bottom boundary layer becomes unstable through basal heating (Lithgow-Bertelloni et al., 2001; Gonnermann et al., 2002; Le Bars and Davaille, 2004a; Jellinek and Manga, 2004). The analysis to-date has centred around the volume and ascent rate of the plume head (Davaille and Limare, 2007), the fixity of plumes (Jellinek and Manga, 2004), their behaviour in the presence of plates (Gonnermann et al., 2002) or the diameter of the head and conduit (Lithgow-Bertelloni et al., 2001). No previous research has studied the fluid dynamical conditions that might lead to their failure (collapse).

1.3 Research Motivation
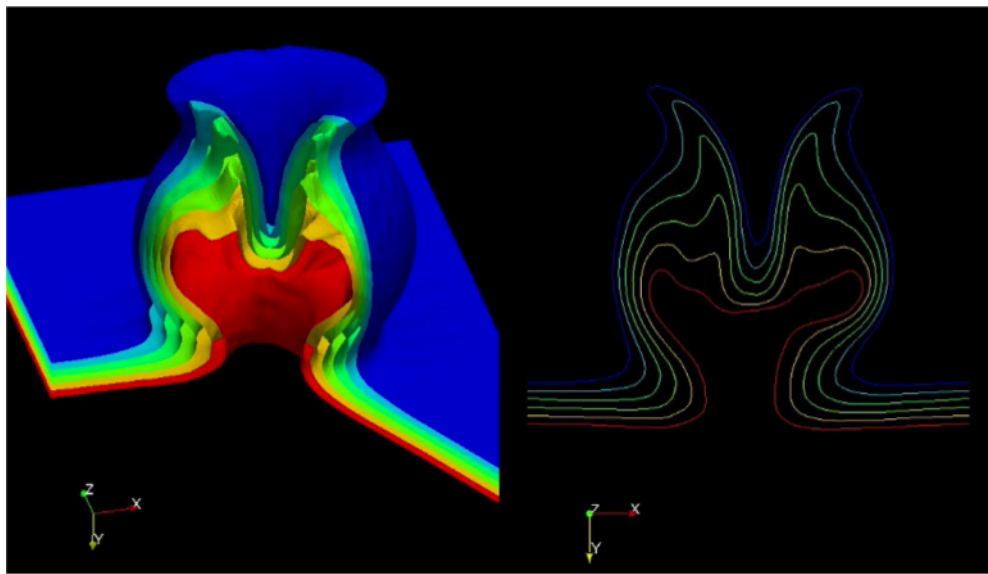
Figure 1.9: Laboratory data on plume collapse. The image is a 3D rendering of material surfaces defined by digital dye advected with the flow measured in the laboratory. A single thermal plume was generated at 38°C, rising in ambient fluid at 25.2°C. The plume reached halfway up the tank before collapsing. (Newsome, 2011)

Collapsing plumes are not common fluid dynamical features and, at first glance, the fluid dynamics of the mantle are such that thermal plumes should always survive due to their high Rayleigh number (definition in Appendix C). However, previous unpublished data from Newsome (2011) suggested that collapse could happen in thermal plumes. Newsome (2011) generated a thermal plume (ΔT=12.8°C, where ΔT is the difference between the temperature of the heater and the ambient temperature of the fluid) by a circular heater at the base of a cubic (26.5cm each side) tank filled with Liquidose 436 syrup, immersed in a larger tank with water controlled at 25.2°C to maintain isothermal condition of the Liquidose 436 syrup. In Figure 1.9, the centre of the plume head collapsed on itself when the plume traversed half-way through the tank. This suggested there could be conditions in which plumes failed to reach the surface. This was further corroborated by Pears (2010) using Lyle's Golden syrup (Figure 1.10) at ΔT=7°C.
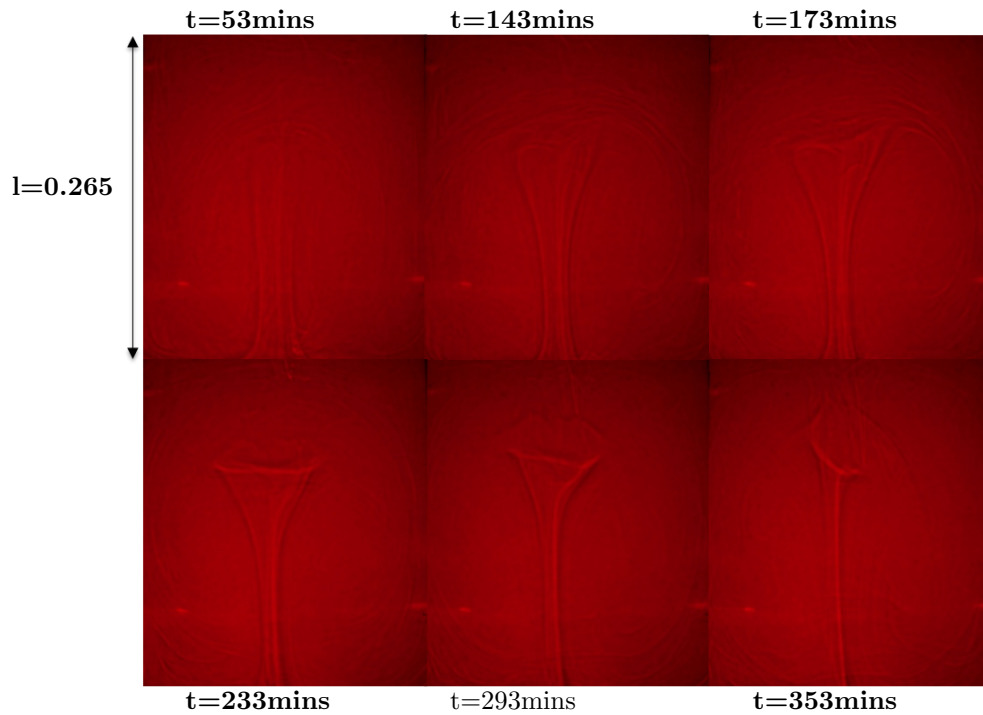
Figure 1.10: Laboratory data of collapse with Lyle's Golden syrup from past research (Pears, 2010). The shadowgraph images display the evolution of a single $\Delta T=7°C$ plume, which ascended approximately $\frac{2}{3}$ of the tank before collapsing down the centre of the plume.

Additionally, Pears (2010) observed another type of collapse at $\Delta T=3°C$ in the Golden syrup. The plume failed to ascend more than a third of the way up the tank and stalled for a period before collapsing back to the base of the tank (Figure 1.11). This further suggested that thermal plumes can collapse.
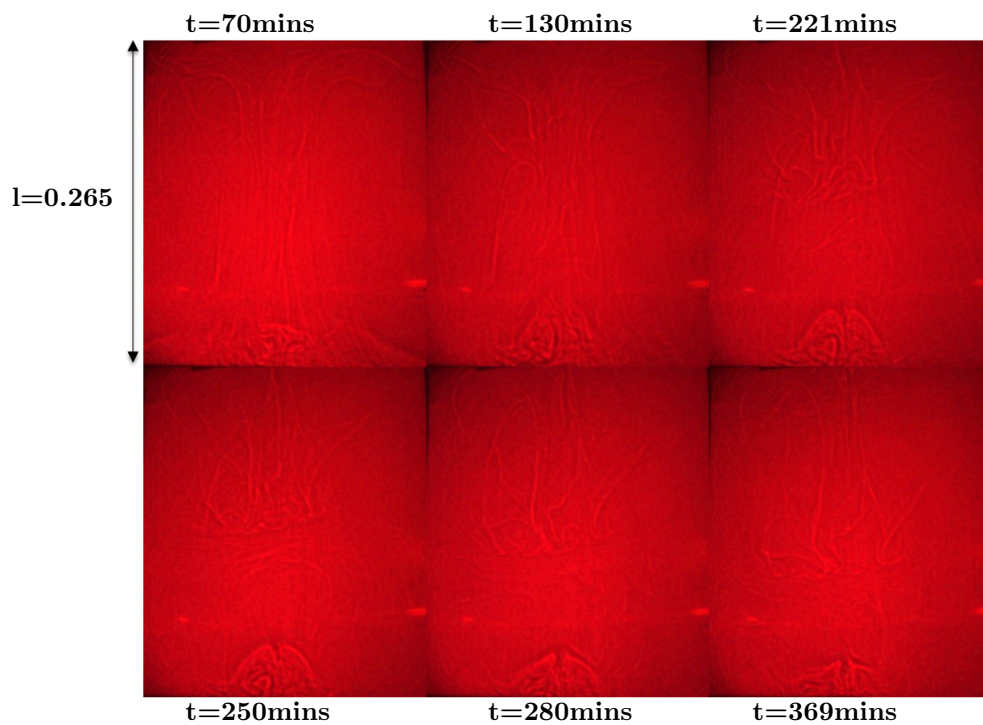
Figure 1.11: Laboratory data of a different type of collapse with Lyle's Golden syrup from past research (Pears, 2010). The shadowgraph images display the evolution of a single $\Delta T=3°C$ plume, which ascended a third of the way in the tank before collapsing back to the base.

1.4 Aims and Thesis outline

The research aim of this thesis is to ascertain whether collapse is possible in thermal plumes. To achieve this goal I explored a wide parameter range for plume generation both experimentally and numerically. The experiments in this thesis were conducted in the Fluid Dynamics Laboratory at UCL at a range of temperature differences, using shadowgraph and Particle Image Velocimetry (PIV) methods for visualisation of the plumes. The innovative PIV system designed by Newsome (2011) was implemented, configured and used to gain further understanding of plume generation and evolution through the central plane. Numerical research was conducted using the finite element package, Fluidity (AMCG, 2014).

Subsequent chapters are organised as follows:

Chapter 2 discusses previous experimental and numerical work on mantle plumes.

Chapter 3 discusses shadowgraph and Particle Image Velocimetry (PIV), the two visualisation techniques employed.

Chapter 4 introduces the governing equations and non-dimensional numbers important to this research, which are used in Chapter 8 to analyse the results.

Chapter 5 describes the characterisation of fluid properties relevant to the experiments: viscosity, density and refractive index. The experimental configuration and the experiments undertaken are also discussed.

In Chapter 6, the findings from the shadowgraph and PIV experiments from the fluid dynamics laboratory are presented. The results are compared to a previous study (Pears, 2010) using a different sugar syrup.

In Chapter 7, the results of the numerical simulations reproducing and extending the laboratory results are presented and compared to the experimental results.

In Chapter 8, the results are analysed and conclusions drawn as to the causes of collapse. Implications of the research in relation to previous work are discussed and an attempt made to scale the plumes to Earth and Mars.

Finally, in Chapter 9 the main conclusions of this research are drawn together and recommendations of further work are given.

Chapter 2

Overview of Previous Mantle Plume Investigations

The investigation of thermal plume collapse has not been previously researched using experimental or numerical methods. Therefore there is little literature which relates directly to this study. However, the large volume of previous work on mantle plumes, both experimental and numerical has been important in the implementation and understanding of plumes, such as the methods for generating plumes and scrolling in the plume head. Additionally previous work has laid the foundation for understanding the possible causes of thermal plume collapse in this thesis. Therefore, the laminar plume experimental and numerical work reviewed in the chapter focuses on two different types of mantle plumes: thermal and thermochemical. Thermal plumes form in a tank of one fluid. Conversely, thermochemical plumes involve two differing density fluids, both of which are entrained into the plume as it rises through the tank. In experimental investigations viscous fluids (silicone oil, sugar syrup or oil) are used as analogues to the mantle. The investigations presented are those visualised through shadowgraph and Particle Image Velocimetry (PIV) techniques. Other visualisation techniques can be used, such as dyes and differential interferometry (Kaminski and Jaupart, 2003), but will not be focused on in this overview. The shadowgraph method is an integrated optical system, using a whole-field two-dimensional method, where white light projects line of sight information onto a viewing screen as one plane (Davaille and Limare, 2007). PIV is implemented to provide, non-invasive capabilities for measuring velocity. The numerically simulated plumes are investigated through finite element and finite difference codes in square and cylindrical tanks. Some previous work has also investigated the similarity of results from numerically simulated and experimental methods.

2.1 Experimental work on mantle plumes
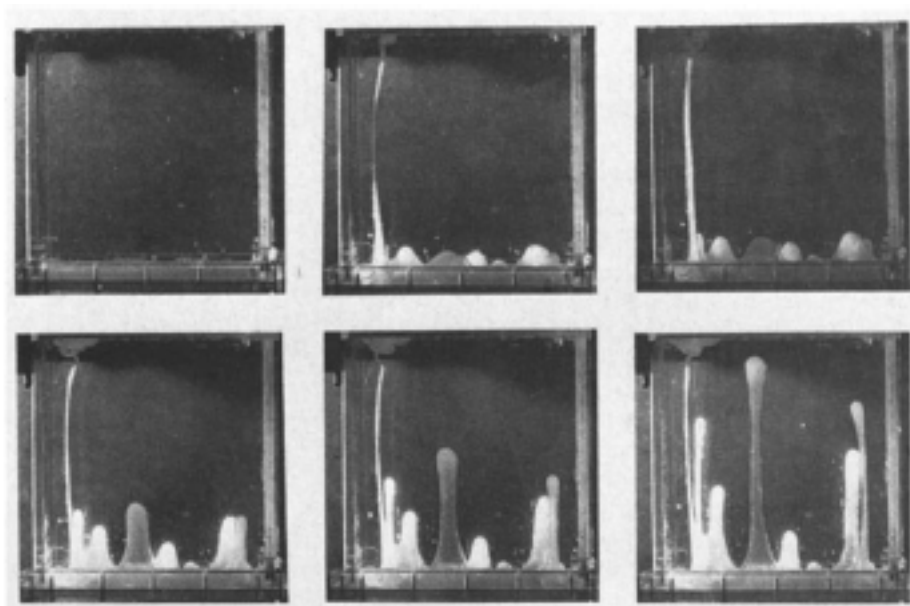
Figure 2.1: A thin layer of viscous fluid trying to penetrate into a fluid with a viscosity 1/44th of the original fluid (Whitehead and Luther, 1975)

The first laboratory experiments which developed the understanding of mantle plumes were those of Whitehead and Luther (1975). They observed that the viscosity of the fluid had a strong effect on the form of a starting plume (Figure 2.1), with a plume of higher viscosity than the ambient material rising in the form of a finger. This study and early studies of Olson and Singer (1985), Griffiths (1986a), Griffiths (1986b), Campbell and Griffiths (1990) and Griffiths and Campbell (1990) produced the "standard model" of mantle plumes, where a plume of lower viscosity than the surrounding fluid appeared to ascend with a large head and thin conduit connected to the source. This can be accurately described as a "mushroom" shape. This has informed current theories on the flow structures of plumes, including head:tail ratios and the amount of (and distribution of) entrained material, which permeate the interpretation of geophysical models (Lithgow-Bertelloni et al., 2001). The plume growth and evolution are governed by thermal diffusion, continuous feeding from source and laminar entrainment of surrounding material into the plume head (Griffiths and Campbell, 1990; Kumagai, 2002; Davaille et al., 2011).

2.1.1 Thermal Plume experiments

A thermal starting plume is essentially an ascending thermal connected by a stem to a source of buoyancy (Ribe et al., 2007). Since the mid-1980s, numerous experimental investigations of thermal plumes in viscous fluid have been conducted (Davaille and Limare, 2007). The shadowgraph visualisation technique has been implemented for both heating and injection plume
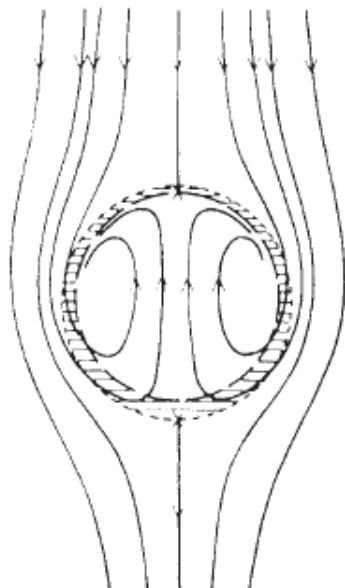
Figure 2.2: The path of the fluid particles outside a hot rising diapir with the superposition of the fluid flow through the conduit.   The particles that approach close to the diapir are heated by diffusion in the thin thermal boundary layer (hatched area), become buoyant and are incorporated into the enlarging spherical vortex by entrainment displaying a bifurcated flow pattern (Richards and Griffiths, 1989).

experiments. In vigorously convecting fluids the instabilities which develop are transient and chaotic features and their local characteristics are difficult to quantify. Therefore many of the early studies of mantle plumes have focused on isolated laminar "starting plumes" arising from a point source of buoyancy (Ribe et al., 2007). This point source buoyancy can be easily studied in the laboratory.

The thermal plume injection experiments of Griffiths (1986a,b), Richards and Griffiths (1989), and Griffiths and Campbell (1990) involved a lighter, hotter fluid injected through the base of a tank filled with the same fluid. In the gravitationally elevated reservoir plume experiments (Richards and Griffiths, 1989; Griffiths and Campbell, 1990) where injection was continuous, the buoyant fluid constantly rose up the plume. However, there was limited buoyant fluid in the finite injection experiment of Griffiths (1986b), where injection lasted 5-10 seconds. Despite differing methods of injection and diverse shaped experimental tanks, the results of the experiments led to a similar observations - that the material injected formed a rising spherical vortex in the head which entrained heat and adjacent fluid into the head as it ascended (Griffiths, 1986b; Griffiths and Campbell, 1990). This phenomenon was also observed by Griffiths (1986a) and Richards and Griffiths (1989) as shown in Figure 2.2 and Figure 2.3. Campbell (2005) postulated that new plumes have a large head of approximately 1000km in diameter followed by a narrower tail as they ascend through the mantle. The plume head would flatten to a diameter between 2000km and 2400km at the base of the lithosphere, such as observed in the Figure 2.3d. The plumes ascent through the mantle was postulated to take over 100Myr.
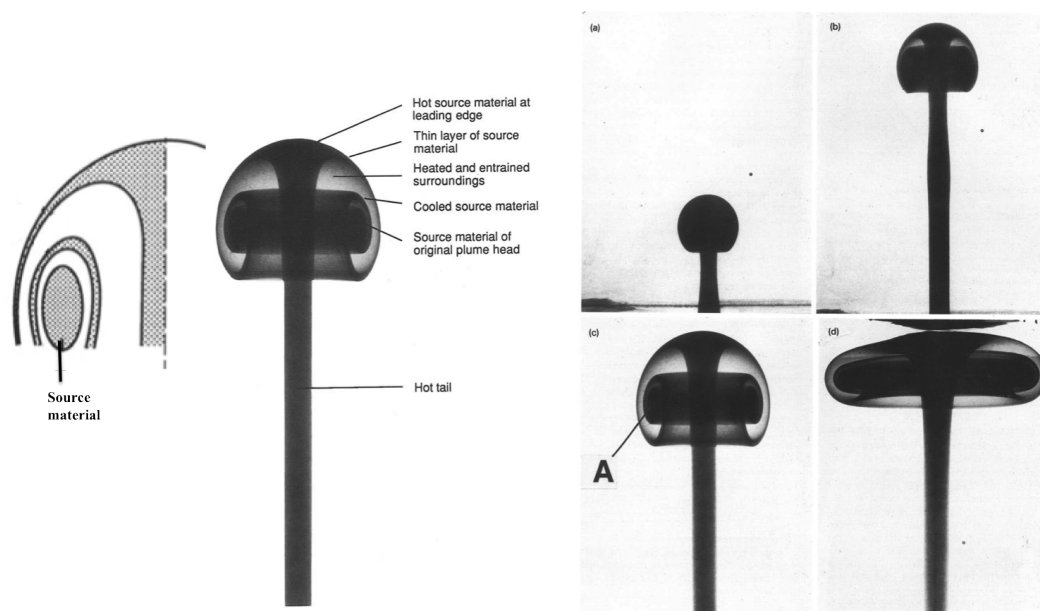
Figure 2.3: Left: A sketch of the internal structure of the plume head from the experimental shadow-graphs (shown in next two images) (Griffiths and Campbell, 1990). Middle: A laboratory starting plume. The structure is caused by conduction of heat and entrainment of surrounding fluid. The dark areas have been dyed from the source and wrapped between layers of entrained mantle in the head (Campbell and Griffiths, 1990). Right: The sequences of the starting plume in glucose syrup during the ascent. Time lapsed photographs a) 60s, b) 130s, c) 397s with head 6.9cm and d) 540s (Griffiths and Campbell, 1990)

The thermal plume experiments described thus far have involved injecting a hotter fluid into a tank of the same fluid. Significantly, these artificial injection experiments do not address all the boundary layer instabilities that give rise to plumes (Lithgow-Bertelloni et al., 2001). It is hypothesised that in the mantle, plumes develop as instabilities of thermal boundary layers (e.g. Parmentier et al., 1975; Loper and Stacey, 1983). Therefore other laboratory investigations have concentrated on the more classical Rayleigh-Bénard investigations, where plumes are generated by a heat source in viscous fluids rather than by injection (Davaille and Limare, 2007). The use of injection to generate plumes adds an additional controlling variable to the experiments; the volume flow rate and the plumes produced are visibly different from the experiments of point source heating. Injection plumes have larger heads, bigger scrolls and often-thinner conduits than point source generated plumes. The plume conduits in the latter plumes are often dynamic features that change over the length of the experiment.

The first point source heat experiments were conducted by Shlien and Thompson (1975) and Shlien (1976) using water and a narrow electrode as the heater. Although their investigations were not motivated by geophysical applications (Davaille and Limare, 2007), their scalings and findings about the cap of the plume are relevant for many investigations today where more viscous fluids are utilised as analogues to Earth's mantle. Analogue mantle plumes have been generated experimentally from point source heaters in the work of Moses et al. (1991), Moses et al. (1993) and Kaminski and Jaupart (2003). Moses et al. (1991) and Moses et al. (1993)

expanded the simple experiments of Shlien and Thompson (1975) and Shlien (1976), finding scaling laws for the head of the plume. Moses et al. (1993) showed that the head velocity of a plume increases rapidly for a short time before attaining a nearly constant value.
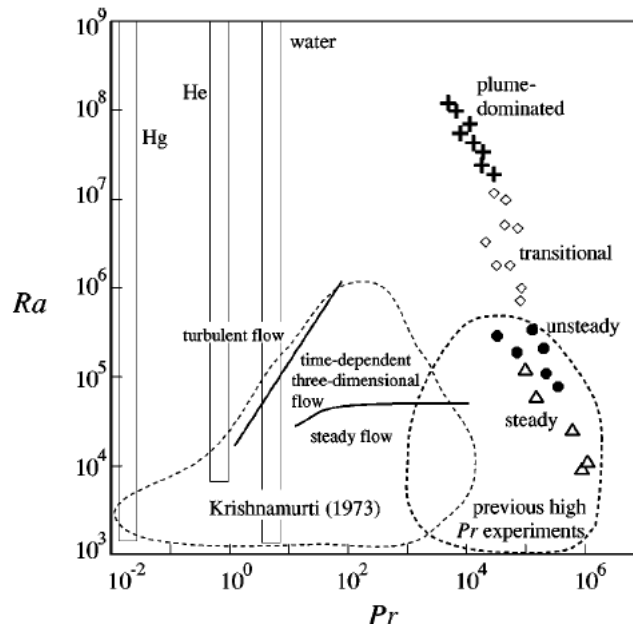
Figure 2.4: A regime diagram showing the experiments of Manga and Weeraratne (1999) and Krishnamurti (1973) and other previous high Prandtl number (definition in Appendix C) studies. Rayleigh number (Ra) is shown as a function of Prandtl number (Pr), with the four styles of convection observed: steady, unsteady, transitional and plume-dominated. From Manga and Weeraratne (1999).

The point source heating experiment of Kaminski and Jaupart (2003) investigated the dependence of the Prandtl number ($7\text{-}10^4$) on laminar axisymmetric starting plumes using viscous oil. Unlike many experimental fluids utilised, the viscosity variations due to temperature were negligible, yet two different regimes were discovered. The plumes generated were similar in shape and conduit thickness to the plumes of Moses et al. (1991, 1993). In contrast to a point source generated single plume, Manga and Weeraratne (1999), Schaeffer and Manga (2001) and Lithgow-Bertelloni et al. (2001) conducted thermal convection shadowgraph experiments where basal heating generated multiple thermal plumes. The investigation of Lithgow-Bertelloni et al. (2001) observed new regimes were possible in Earth's mantle where bursting behaviour and apparent mode transitions in plume frequency and size, were likely to mean that the plume hypothesis is not as simple as first proposed. The Rayleigh number played a key role in the resultant plume dimensions, with head and tail dimensions decreasing as the Rayleigh number increased, representing an important observation for experimental work. The work of Manga and Weeraratne (1999) illustrated some of the physical processes that occur during high Rayleigh number and high Prandtl number convection. They compared their corn syrup investigations with the experiments of Krishnamurti (1973), and other previous high Prandtl number experiments, and observed that the styles of convection changed. The flows were characterised into steady, unsteady, transitional and plume-dominated as shown in Figure 2.4. When the Rayleigh number of an experiment was

low, the flow was unsteady in nature in terms of the large-scale convective patterns.

Schubert et al. (2001) focused on the temporal interaction of plumes formed from boundary layers in Earth showing that plumes can form with more than one frequency and size. This implies that the hot plumes form by different processes - either by thermal boundary layer instability or from cold plumes sinking from the surface. There is observational evidence for mantle plumes of different sizes and properties co-existing in the same system (Herrick, 1999).

Despite all the experimental work visualised through shadowgraphs, the understanding of the appearance of mantle upwellings is still largely dominated by plumes generated from steady point sources of buoyancy (Davaille and Vatteville, 2005). This is because to investigate new phenomena, it is easiest to first understand how the plume behaves from point source heating before furthering the understanding through multiple plume generation through basal heating. Single plumes are hard to distinguish in basal heating, even though it is a more accurate portrayal of the thermal boundary layer at the core-mantle boundary from where plume originate. Further basal heating investigations led to the understanding of how multiple plumes in the mantle interact and how plumes formed by large mantle down-wellings e.g. Gonnermann et al. (2004). Gonnermann et al. (2004) postulated that plates thin the thermal boundary layer and that multiple regimes are possible in a complex mantle system. In a different basal heating experiment Jellinek et al. (2002) determined that plumes may play a role in plate tectonics.

Compared to shadowgraph experiments, PIV experiments produce both qualitative and quantitative results and have been implemented to fully characterise experimental plumes (Davaille and Vatteville, 2005; Davaille et al., 2011). In these experiments the plume was generated through either point source (Davaille et al., 2011) or basal heating (Davaille and Vatteville, 2005). Davaille and Vatteville (2005) investigated the birth, life and death of plumes, whereas, the later experiment (Davaille et al., 2011) studied the anatomy of a single plume and different stages of plume development. Davaille and Vatteville (2005) used thermochromic liquid crystals (TLCs) and glass particles to visualise simultaneously the temperature and velocity fields of the plume. The visualisation of the plumes was further expanded in the experiments of Davaille et al. (2011) with a second method to visualise the temperature - Differential Interferometry (DI). This involved a more complex apparatus configuration (Figure 2.5), with divergent and convergent lenses and a white light source. When the two methods (PIV and DI) for ascertaining the temperature were compared, they produced quantitatively similar results.

The TLCs generated isotherms of plume temperature, which remained a horizontal front as the plume migrated from the boundary by conduction. As the plume cooled by heat diffusion
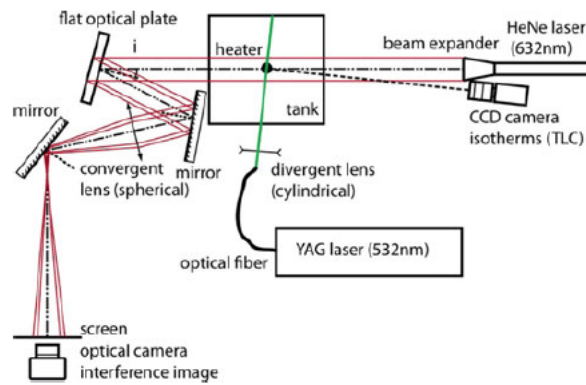
Figure 2.5: Top view of the PIV experimental configuration from Davaille et al. (2011). Showing the mirrors and optical plate used with the laser to image a plane of the tank.

during its ascent the hottest isotherm, 40.5°C disappeared, displaying the transient behaviour of plumes. It is possible that the plume stem would fade away once the thermal boundary layer (TBL) became exhausted. This was occasionally observed prior to the plume reaching the upper surface. The three fluids investigated by Davaille et al. (2011) produced the same time sequence and morphology. TLCs present a challenge in PIV experiments because only a few isotherms are measured, and need to be used with a laser scanning PIV system to enable full imaging of 3D anomalies, although no axisymmetric hypothesis is needed (Limare et al., 2008). The PIV technique only gives a spatial average of the velocity field and can lead to missed details where the velocity gradients are larger around the plume axis (Davaille et al., 2011). Limare et al. (2008) and Davaille et al. (2011) importantly state that sugar syrups gave the most accurate results when using DI and TLCs because the effectiveness of the results achieved depended on the response time of the fluid, in comparison to the transit time of the TLCs.

2.1.2   Thermochemical plumes

The compositional heterogeneity thought to exist in the lower mantle is one factor that can create the conditions to explain the observed characteristics of hotspots (Ribe et al., 2007). Thermochemical convection can be investigated via plumes whose density depends on temperature and composition. Thermochemical experiments involve a tank initially stratified with two viscous fluids with different densities and viscosities (Kumagai et al., 2008). Once heated, the low-density material moves upwards through the experimental tank. There have been a number of investigations of convection in two stratified fluid layers via numerical simulations and experimental techniques (e.g. Kumagai et al., 2007; Farnetani and Samuel, 2005). The two-layer system is controlled by the compositional and thermal buoyancy interactions, which can be measured by the buoyancy number (B) shown in Equation 2.1 from Le Bars and Davaille (2004a).

$$B = \frac{\Delta\rho_x}{\rho_0 \alpha \Delta T} \tag{2.1}$$

where $\Delta\rho_x = \rho_1\text{-}\rho_2$ is the chemical stratification and $\rho_0 = (\rho_1 + \rho_2)/2$. Subscript $_1$ and $_2$ are the labels of the layers. This buoyancy number is the ratio of the stabilising chemical density anomaly to the destabilising thermal density anomaly. Equation 2.1 will therefore, determine the stability of the whole system and the ability of the interface to deform (Le Bars and Davaille, 2004a; Oldham and Davies, 2004).

Often, thermochemical injection experiments are referred to as compositional injection experiments. The "classical" early experiments of Whitehead and Luther (1975) and Olson and Singer (1985) involved the injection of compositionally buoyant fluid at a constant rate through a pipe at the base of the tank (Davaille and Limare, 2007). A great advantage of the experiments was the lack of temperature control required, enabling investigations to be conducted with ease. Whitehead and Luther (1975) concentrated on the starting plume for the period of time after injection until the sphere produced migrated away from the injector at the base. The sphere was discovered to lift-off when the rate of increase of the radius was exceeded by the buoyant ascent speed (Whitehead and Luther, 1975). Whitehead and Luther (1975) and Olson and Singer (1985) believed that after lift-off, the morphology and dynamics of the plume were greatly affected by the viscosity contrast of the fluid.

More recently, Kumagai (2002) conducted compositional plume experiments where fluid was injected by gravity into the base of the tank. This injection method was similar to the thermal injection experiments of Griffiths (1986b), Richards and Griffiths (1989), and Griffiths and Campbell (1990); similar entrainment was discernible. This entrainment in the starting plumes of Kumagai (2002) was categorised into two depending on the viscosity contrast. In the vortex ring plumes of Kumagai (2002) (viscosity contrast <11), the plume heads entrained ambient material and were similar to vortices in the plume head seen in Figure 2.3 (Griffiths and Campbell, 1990; Campbell and Griffiths, 1990). In contrast, a different type of entrainment, termed "chaotic stirring", was observed for plumes (104<viscosity contrast<856) with a double layered structure in the plume head. The buoyant fluid was in the upper layer of the head and the entrained material in the lower (Figure 2.6).

Thermochemical basal heating shadowgraph experiments have been conducted by Le Bars and Davaille (2002), Le Bars and Davaille (2004a) and Le Bars and Davaille (2004b) to investigate the stability of two-layer thermal convection using miscible fluids. There was no surface tension and negligible chemical diffusion between the layers in the fluids investigated. The behaviour of
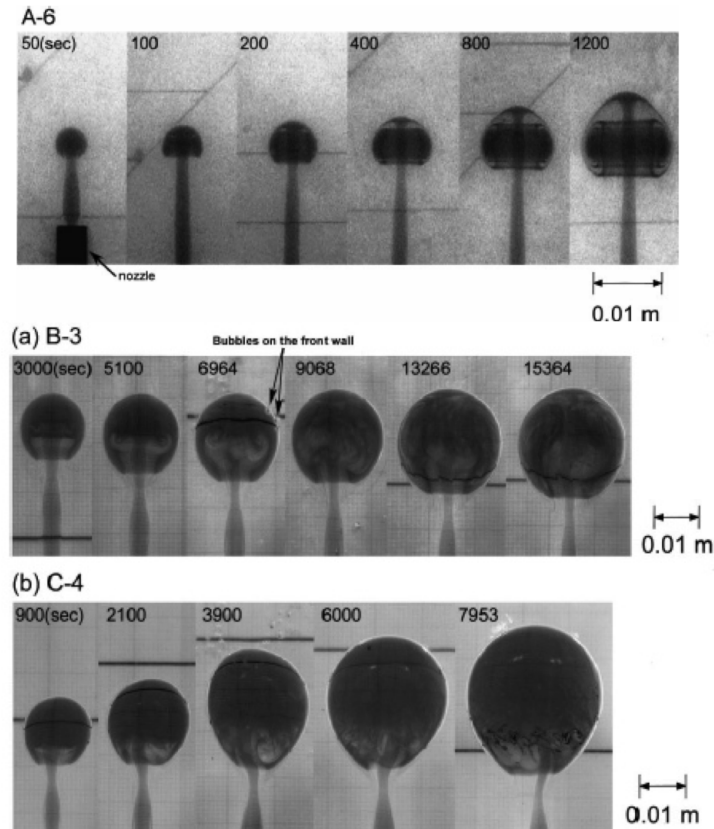
Figure 2.6: The experimental images of the "vortex ring" plume (A-6), with the viscosity contrast=11, where the ambient fluid is entrained (transparent in photograph) into the plume head, forming the scrolling structure. B-3 (viscosity contrast=110) and C-4 (viscosity contrast=760) are plumes with "chaotic stirring" type entrainments. From Kumagai (2002).

convection from the two fluids was classified into regimes by calculating the buoyancy number, B, from Equation 2.1. The regimes observed in Le Bars and Davaille (2002) were stationary or oscillatory. The oscillatory regimes developed when B was lower than the critical buoyancy value. The interface between the two fluids would become deformed and whole layer convection was observed because the whole system destabilised (Le Bars and Davaille, 2004a). If B was larger than the critical buoyancy value a stratified regime developed between the layers and purely thermal convection occurred within the layers (Le Bars and Davaille, 2004a). Le Bars and Davaille (2004b) furthered this research into three regimes and discussed its application to Earth. When B<0.3-0.5, the oscillatory regime occurred and the system over time evolved to Rayleigh-Bénard convection. If B>1, convection developed above and below the interface and fixed or long-lived thermochemical plumes were generated. When 0.3-0.5<B<1 the interface of the fluid layers remained stable, but was deformed significantly by thermal features coming from the layers causing dynamic topography.

An important observation by Le Bars and Davaille (2002) was that at density contrasts smaller than 1%, the dynamics of convection could change radically if coupled with viscosity contrast. However, a nearly flat interface required a chemical density contrast of typically greater than 5% for strongly stratified convection (Le Bars and Davaille, 2004b). This is unlikely in the

present mantle because density stratification of chemical origin cannot exceed a few percent (Bina, 1998). However, whole layer convection could take place in the mantle for a density anomaly of less than 2%. Le Bars and Davaille (2004b) made a clear distinction that the whole layer regime cannot be assimilated with a one-layer regime and that even very small density contrasts can perturb convection for a long time and give rise to many transient behaviours. These small density contrast findings of Le Bars and Davaille (2002) and Le Bars and Davaille (2004b) will be returned to further in the thesis in light of the collapse results achieved in this thesis.

The buoyancy number of plumes was further investigated through point source heating using PIV to visualise the plumes in the work of Kumagai et al. (2007) and Kumagai et al. (2008) in order to understand different aspects of thermochemical plumes in terms of failure and death. TLCs and fluorescent dye (Rhodamine B) were used to aid visualisation in PIV. Kumagai et al. (2007) investigated the buoyancy number in terms of the fate of thermally buoyant mantle plumes at density interfaces, whereas Kumagai et al. (2008) investigated how plumes of different buoyancy number changed if the heater was extinguished during the experiment, compared to investigations with constantly present heat sources. The heater was extinguished to simulate the death or failure of thermochemical plumes.

Both Kumagai et al. (2007) and Kumagai et al. (2008) observed different plume regimes dependent on the buoyancy number. These regimes led to different plume morphologies and did not show the typical expected plume shapes, which has implications for the idea of all plumes forming the typical mushroom shape head and thin conduit. In Kumagai et al. (2007), when B<0.6 the "pass through mode" was observed, where material from the lower boundary was able to penetrate the upper layer, due to the large thermal buoyancy, and rise to the surface of the tank. When B>0.6 the "rebirth mode" was observed and the thermal spreads under the chemical boundary layer and secondary thermal plumes are generated in the upper boundary. Only when the buoyancy ratio was ∼1 was the term "thermochemical" plume used by Kumagai et al. (2007). Thermal plumes were generated in the individual fluid layers and often the heat from one could generate a second plume in the layer above.

Different plume morphologies were observed when varying the buoyancy number as shown in Figure 2.7 (Kumagai et al., 2008). Kumagai et al. (2008) observed that when the B was tending to 0, a mushroom shaped purely thermal plume was reproduced similar to the result of Griffiths and Campbell (1990). Conversely, when B>1, the thermal effects did not counterbalance the chemically denser anomaly. The upper part of the thermal boundary layer became unstable and deformed the compositionally denser material layer into a cusp (Davaille, 1999a; Jellinek et al.,
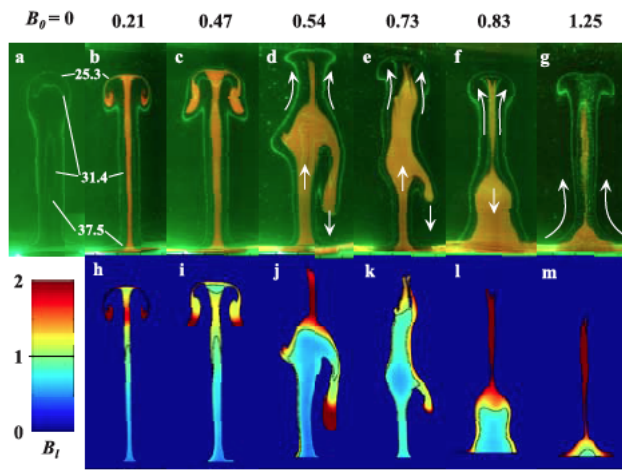
Figure 2.7: The morphology of thermochemical plumes as a function of increasing initial Buoyancy number. The 532nm laser illuminates the plumes with isotherms (25.3, 31.4, 37.5°C). The orange is the Rhodamine B dye (Kumagai et al., 2008).
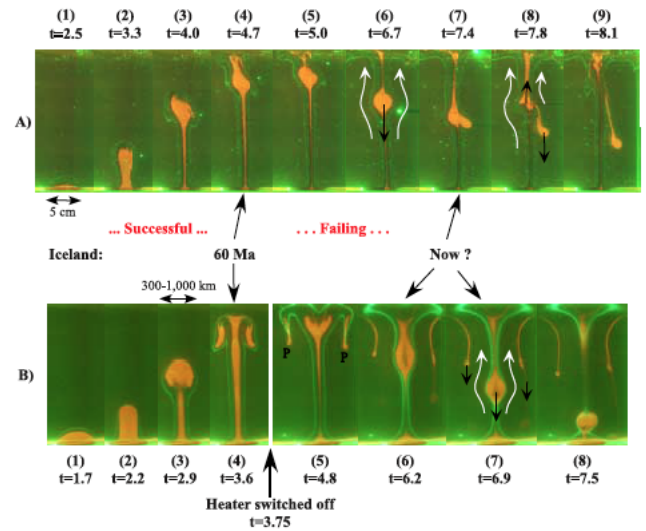
Figure 2.8: Successful and failing plumes, which are time dependent (Kumagai et al., 2008). A) B=0.67 and the power is constant during the experiment. In B) B=0.47 and the the heater is turned off at t=3.75.

2002; Kumagai et al., 2007). Complex shapes are observed in Figure 2.7 for the intermediate buoyancy numbers - where (d-f) displays sinking and (c-f) rising. The plume characteristics were time dependent because of the varying nature of heating in the experiments (Kumagai et al., 2008). In Figure 2.8, the evolution of the thermochemical plume was investigated at a constant buoyancy. In A8, the chemical plume began to disintegrate, whilst some material continued ascending to the surface. This was also a sign of the plume failing. Material separated within the plume, whereby the chemically denser material began to sink back to the base while the heated surrounding mantle kept ascending. Thermal diffusion causes all plumes to cool as they rise and the thermochemical plume in Figure 2.8, most especially A8, shows the plume eventually attained a level of neutral buoyancy, then began to 'fail'. This concept of failing, whereby material falls to the base of the tank is termed 'collapse' in the results presented in this thesis. Kumagai et al. (2008) concluded that the morphology of composite plumes depended on both B and time and that separation between the active rising and sinking regions occurred for B=1.0. Once the power was turned off in Figure 2.8B the core of the plume head, which was initially hotter than the ambient material but chemically denser, descended through the conduit as it cooled, despite maintaining a higher temperature than the ambient fluid. This observation will be returned to in light of collapse results in this thesis.

2.2 Numerical Simulations

Since the development of the computer, numerical simulations have become an integral part of many scientific and technical enterprises (Farrell et al., 2011). Numerical analysis, simulation or computer experimentation has played a major role in understanding convection in Earth's mantle (Blankenbach et al., 1989). As computational hardware becomes ever cheaper, numerical simulations become more attractive relative to experimentation (Farrell et al., 2011). Therefore many scientists investigate mantle plumes through numerical simulations because they can provide detailed observations of key properties in parameter ranges that are impossible to achieve in the laboratory (Coulliette and Loper, 1995). However, despite the large number of numerical codes in existence it is not apparent which is the most favourable due to advantages and disadvantages between methods (Blankenbach et al., 1989).

Two benchmark studies (Blankenbach et al., 1989; Busse et al., 1994) have been used to validate numerical codes and models since the 1990s. These benchmarks compare studies on problems related to convection in Earth at high Rayleigh numbers (Blankenbach et al., 1989) and high Prandtl numbers (Busse et al., 1994). Most recently these two benchmarks have been used to ascertain the reliability and accuracy of the finite element code, Fluidity by Davies et al. (2011). The two-dimensional benchmark of Blankenbach et al. (1989) focuses on steady state convection, with Fluidity utilised to examine three isoviscous cases at $Ra = 10^4$, 10^5 and 10^6, and a variable viscosity case (varying with temperature), using both structured and adaptive unstructured meshes (Davies et al., 2011). The results from Fluidity were in excellent agreement with the benchmark predictions of Blankenbach et al. (1989) as shown in Figure 2.9.

Furthermore, Fluidity was tested against the three-dimensional benchmark of Busse et al. (1994) using the same boundary conditions, for steady state cases with constant and temperature-dependent viscosity. There was excellent agreement with the benchmark values (Davies et al., 2011). Fluidity was therefore, determined to be suitable for both two and three-dimensional, steady state, isoviscous and variable viscosity simulations.

2.2.1 Thermal Plumes

Many numerical simulation codes have been used to investigate thermal plumes for many decades. Steady-state thermal convection was investigated by Parmentier et al. (1975). This investigation found that for plumes to be prominent features in the mantle there must be continuous basal heating to generate steady-state thermal convection. Steady-state plumes were
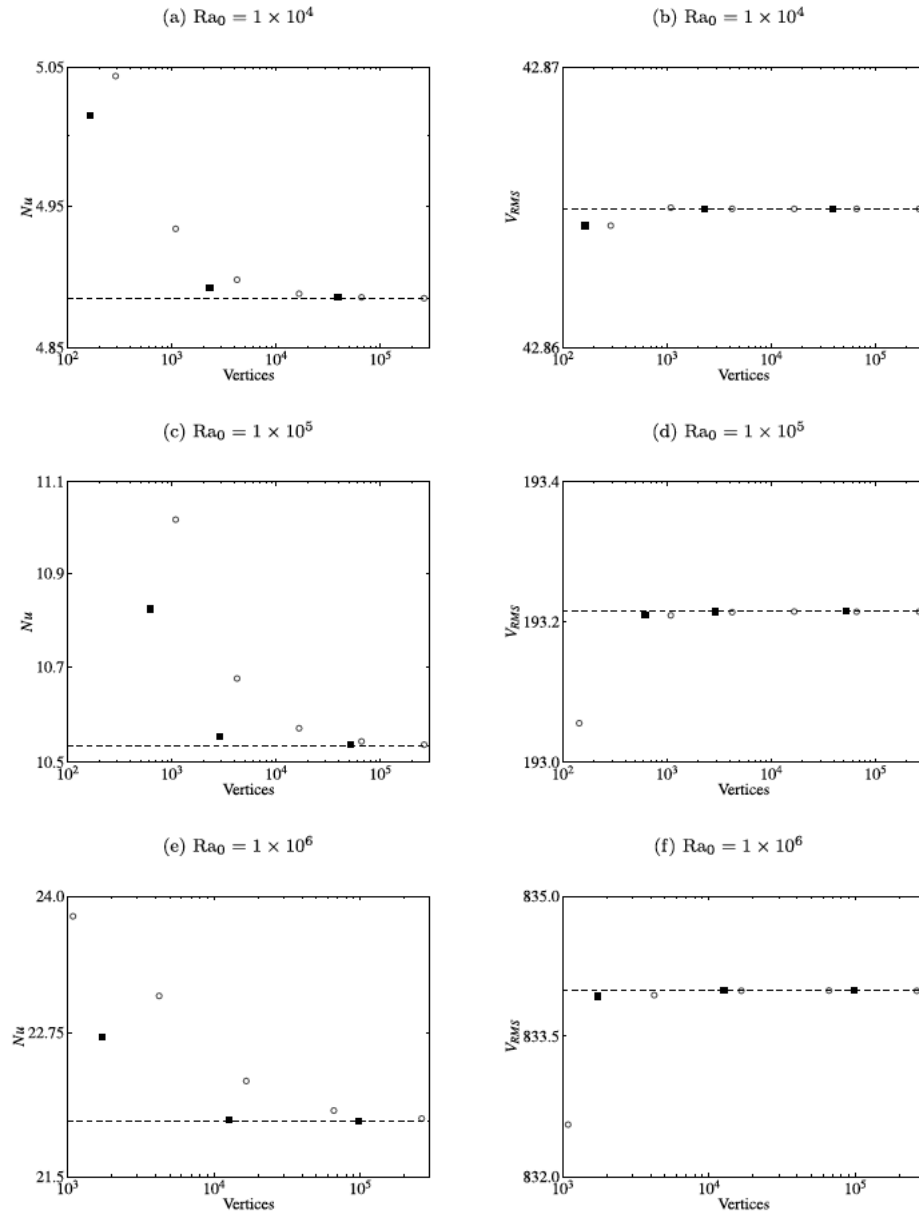
Figure 2.9: Results from 2-D isoviscous square convection benchmark cases. The horizontal dashed lines denote the benchmark values (Davies et al., 2011). (a, c, e) represent Nusselt number (definition in Appendix C) vs number of triangle vertices and (b, d, f) represent RMS velocity versus number of triangle vertices. a) Relates to case 1a, c) and d) relate to case 1b, e) and f) relates to case 1c from Blankenbach et al. (1989). Open circles are uniform, structured meshes and filled squares are adaptive unstructured meshes.

additionally investigated by Davies (2005) using whole mantle convection. These plumes were steady and virtually fixed, which was controlled by the smaller but numerous cold downwellings, implying that the upper surface of Earth is important in plume production.

In later research, Ribe and Christensen (1994) investigated thermal plumes with a moving lithosphere in three-dimensions using a hybrid spectral/ finite difference technique to understand the dynamics of hotspots such as the Hawaiian-Emperor chain. Their model neglected the dynamic effects associated with pressure-release melting in the plume, due to the cancelling of the positive chemical and thermal buoyancy, which is less dense than the starting material. Nonetheless, the simulations predicted loosely the shape of the Hawaiian swell, which included

the initial rapid stage of uplift, a feature that many thermal numerical models fail to predict. However, it failed to accurately predict the geoid/topography ratio, obtaining a number twice the observed value of 0.004-0.006 (Crough, 1978; Monnereau and Cazenave, 1990). These results have implications for determining the buoyancy fluxes of plumes. The buoyancy of a swell could be up to 80% of the buoyancy transported in the plume, implying that the findings of B=B$_{swell}$ of Davies (1988) andSleep (1990) were too large. Reducing the value of Davies (1988) and Sleep (1990) by 1.80 gave buoyancy values (B=3500kg/s and 4800kg/s), which fitted more closely with the preferred value of 4100kg/s from Ribe and Christensen (1994). This preferred value implied a 90km plume radius under Hawaii and an assumed plume/mantle temperature contrast of 300°C. Ribe and Christensen (1994) additionally extended the refracted plume model of Olson (1990) through the relationship of the streamline stagnation of the plume.

The numerical model of Farnetani and Richards (1995) examined thermal entrainment of mantle plumes from a thermal boundary layer in the deep mantle. Their model accounted for temperature-dependent viscosity and phase transitions. Using a tracer field it was observed that primary plume magmas represent >90% of the original plume source material. The plume tail had more than 80% of the total buoyancy flux due to a high concentration of source material. Their results corroborate findings from Griffiths (1986b) of confinement of source material to the plume axis and in the torus. Conversely, the results conflict with the idea that magmas from plume heads should reflect a large degree of entrainment of surrounding mantle (Griffiths and Campbell, 1990). This research helped to further shape the theoretical idea of mantle plumes.

2.2.2   Thermochemical Plumes

Farnetani (1997) furthered the research of Farnetani and Richards (1995) by adding a thin chemical layer across the D″ to investigate the dynamics of plume formation and ascent. The model that gave the most accurate temperature results for the plume head, was the one that had the chemical layer 5% denser than the surrounding mantle. The chemical layer has the role of preventing the lower part of the thermal boundary layer becoming entrained into the plume. There may be a trade off between the need for excess density and the thickness of the thermal boundary layer, which could only be clarified by further knowledge about the nature of the D″. Later research by Lin and van Keken (2006b) indicated that the compositionally distinct region in D″ could persist throughout Earth's history, provided that the density contrast with respect to the overlying mantle was >2%. Lin and van Keken (2006a) stated that the concept of plumes sampling the ambient mantle material whilst traversing the mantle to reach the base of the lithosphere cannot be ruled out. A different type of investigation was undertaken by Lassak et al.

(2007) who investigated thermochemical piles as a location for the formation of thermal plumes and a mechanism for the different observed geochemistry in OIBs and MORBs (e.g. Davaille, 1999a; Tackley, 2000; Davaille et al., 2003; Jellinek and Manga, 2004). Additionally, numerous seismic studies have revealed the presence of two large, low velocity anomalies beneath Africa and the central Pacific, which are hypothesised to be long-lived thermochemical piles (Lassak et al., 2007). The model of Lassak et al. (2007) and many others have proposed that the thermochemical pile model would involve an intrinsically more dense (2-5%) mantle component which is swept along the base of the mantle away from regions of ancient subduction and accumulates into large piles in upwelling regions (e.g. Davaille, 1999a; Jellinek and Manga, 2004).
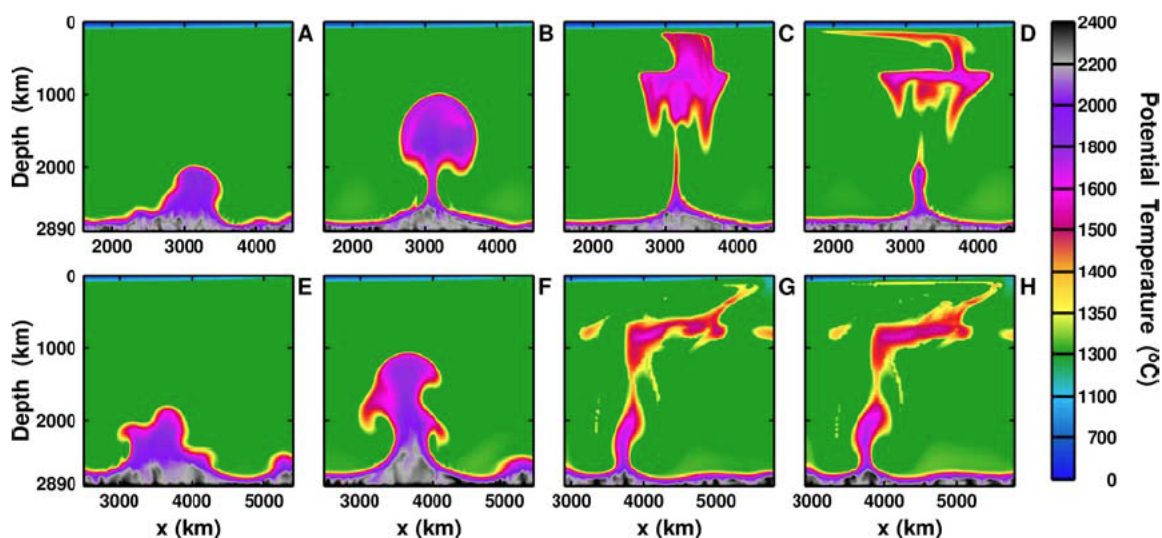
Figure 2.10: Complex morphologies of thermochemical plumes during their interaction with a phase transition at 660km depth. From Farnetani and Samuel (2005)

.

The numerical work of Farnetani and Samuel (2005) in Figure 2.10 showed that mantle plumes differ from the classical plume model and have a variety of shapes and sizes. The results they observed were visually similar in the failing plumes to the later work of Kumagai et al. (2008). Farnetani and Samuel (2005) postulated that the plumes would impinge on the base of the lithosphere with a head-tail or tail without a head formation.

2.3   Comparison between numerical and laboratory models

It is possible to compare laboratory and numerical mantle plume models as they complement each other in the understanding of high viscosity fluids, which are relevant as an analogue for mantle flow, to investigate mantle convection (Busse et al., 1994). The comparison of the two methods is undertaken infrequently because scientists tend to focus on one aspect; generating

plumes either experimentally or numerically. Very few undertake both methods of investigation for a hypothesis. The results from laboratory experiments and numerical models at present necessitates simplifications regarding physics, geometry, rheological and thermodynamic properties. However, experimental investigations provide insight into the key factors in the construction of analytical and numerical models and can provide means of verifying these models (Coulliette and Loper, 1995). Conversely, numerical models may use either incorrect or inconsistent mathematical physical descriptions or could be contaminated by numerical errors (van Keken, 1997). Additionally, they are less likely to determine new physical phenomena such as failure and collapse. Busse et al. (1994) believed that comparison studies of numerical and laboratory experiments can complement each other in many applications, and that semi-quantitative (or better) agreement can be achieved.

Coulliette and Loper (1995), van Keken (1997), Vatteville et al. (2009) and van Keken et al. (2013) conducted detailed comparisons between laboratory investigations and numerical simulations using finite element methods. The experiments of Coulliette and Loper (1995) were designed to incorporate the buoyancy vs. viscosity effects studied by Whitehead and Luther (1975) and Olson and Singer (1985) and the entrainment dynamics observed by Griffiths (1986b) and Griffiths and Campbell (1990). The experimental work of Coulliette and Loper (1995) was similar to that of Griffiths and Campbell (1990), except they used higher viscosity contrasts of 400, 30,000 and 10^8 and plumes were generated from thermal input. The viscosity contrast was implemented by varying the temperature of the tank from sub-zero, to -0.1°C to -26.3°C. They observed that the highest viscosity ratio plumes had novel morphologies implying that plumes do not have to have the traditional mushroom shaped head and thin tail. However, the small viscosity ratios followed the traditional plume shape. The numerical and experimental plume heads rose at constant speed; a contrast to most previous studies where the plume head accelerated at the beginning of the investigation. Their investigation showed that numerical and experimental velocity results were in good agreement.

Van Keken (1997) investigated the initiation and development of plumes. The numerical simulations were designed around the experimental work of Griffiths and Campbell (1990). Prior to this numerical investigation, bulbous head plumes, growing by entrainment of surrounding material followed by a feeder conduit were generally not seen numerically. Unlike the injection experiments, van Keken (1997) simulated plumes arising from a thermal boundary layer using cylindrical axisymmetric geometry. These simulations differed to the model of Coulliette and Loper (1995), which used rectangular geometry. The plumes simulated by van Keken (1997) showed that the time evolution, size and shape of the plumes were almost identical to the in-
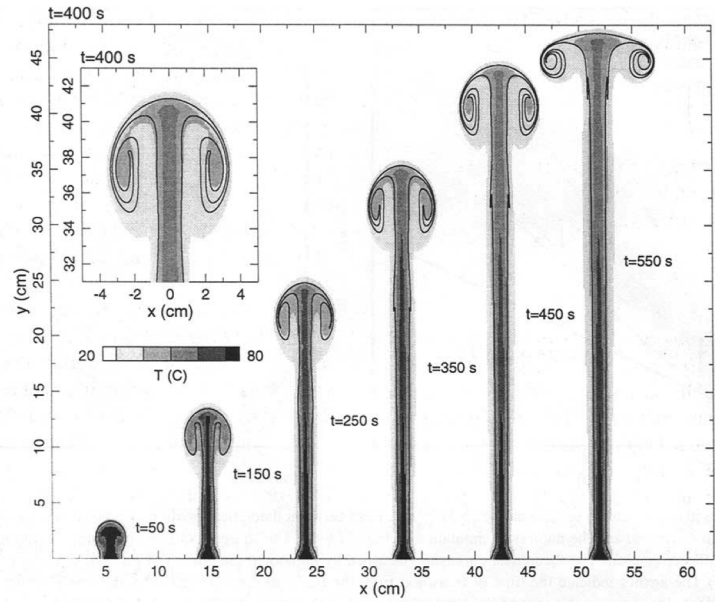
Figure 2.11: The evolution of the simulated Griffiths and Campbell (1990) thermal plume. The scale is temperature in degrees. The plume is similar to Figure 2.3, showing good agreement between the numerical and experimental method. From van Keken (1997).

jection experiments of Griffiths and Campbell (1990), as shown in Figure 2.11. Therefore, the numerical investigation successfully reproduced the laboratory experiments.

The aim of the work of Vatteville et al. (2009) was to investigate starting plumes both experimentally and numerically. Van Keken et al. (2013) used the experimental work of Vatteville et al. (2009) to compare with their numerical work investigating the steady state structure of thermal plumes, arising from a point source heater, at high Prandtl numbers. The experimental work of Vatteville et al. (2009) produced plumes from circular point source heating, a method also used in the experiments of Coulliette and Loper (1995). However, the mode of visualisation differed from Coulliette and Loper (1995), who used shadowgraphs. Vatteville et al. (2009) used PIV visualisation for the velocity and differential interferometry and TLCs for the temperature imaging component of the study. The experimental tank had a free-slip top surface and no-slip sides and bottom. This was modelled in numerical simulations using cylindrical geometry in the work of Vatteville et al. (2009) and van Keken et al. (2013). The results of the Vatteville et al. (2009) simulation revealed that PIV methods always under-estimate conduit velocity, due to the averaging window used to compile velocities, corroborated by Limare et al. (2008) and Davaille et al. (2011). However, there was good agreement between the numerical and experimental investigations of Vatteville et al. (2009) in the fine details of stem velocity close to the heater. Nonetheless, a systematic shift remained between laboratory measurements and numerical predictions at the top half of the plume conduit (Figure 2.12).

Van Keken et al. (2013) observed good agreement between numerical and experimental techniques, which was also observed in the other numerical and experimental comparison work
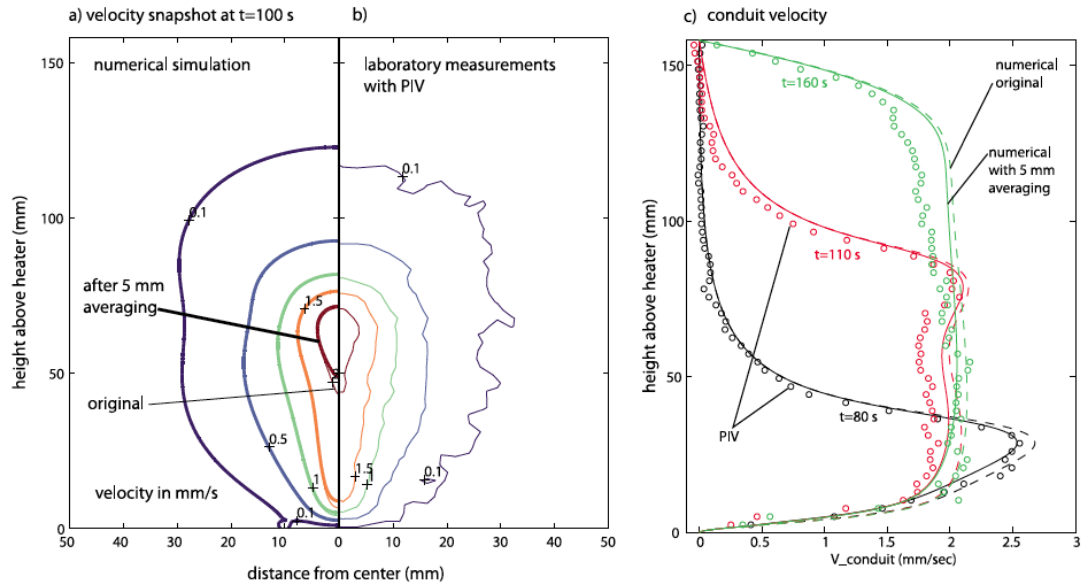
Figure 2.12: a) and b) displays the comparison of velocity fields from numerical simulations and laboratory experiments respectively for the same silicone fluid and heater power of 1.0W. c) plots the velocity along the conduit for three times t=80, 100 and 160s. PIV is represented by open circles, solid lines represent PIV averaged data and dashed lines the numerical predictions (Vatteville et al., 2009)

presented. The evolution of velocity agreed within 5%. It was observed that velocity data from PIV experiments was generally noisier than velocity data from simulations. The velocity structure was found to change strongly as the aspect ratio of the simulated tank increased. The free-slip surface at the top remained a strong influence on the velocity structure under all conditions simulated, whereas the side effects became less important for large aspect ratios. The steady-state velocity and thermal structure of the plume was also observed to not depend upon the initial heating history of the simulated plume. A major difference in the simulated heater to the experiments of Newsome (2011) and Pears (2010) is that the point source heater was set a few millimetres above the bottom of the box causing a lateral temperature gradient to develop at the edge of the heater. In the experiments of Newsome (2011) and Pears (2010), the heater was flush with the base of the tank, allowing plumes to form from a flat surface.

Fluidity has been validated by Davies et al. (2011) by simulating the combined experimental and numerical mantle plume experiments of Vatteville et al. (2009) using fixed and adaptive meshes in three-dimensions (Figure 2.13). Fluidity compared quantitatively well with the velocity field from the PIV experiments and corroborated the consistently predicted higher conduit-velocity of Vatteville et al. (2009). This adaptive meshing, and validation against previous experimental work within a similar system (Newsome, 2011), made it ideal for the numerical simulations in this thesis.
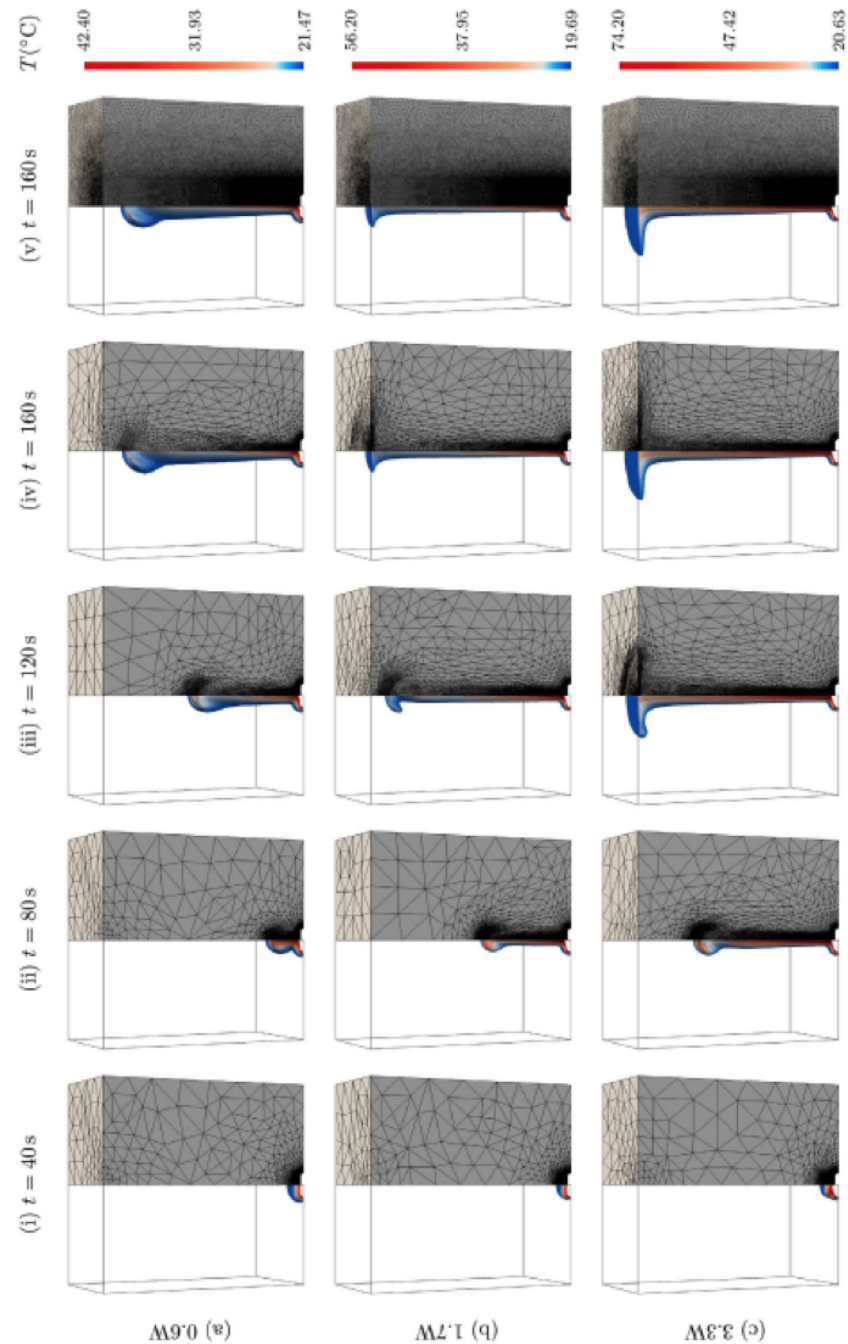
Figure 2.13: Comparison of several time frames showing isosurfaces of the temperature field, T, and underlying computational adaptive mesh from the simulation of a thermal plume using Fluidity. A quarter of the tank (0.075m x 0.075m x 0.161m with a 0.009m radius and a 0.003m high heater) was simulated at three heater power levels. For comparison, a time frame from a fixed mesh simulation using the same minimum element edge length and equivalent resolution from Vatteville et al. (2009) is shown in v) Vatteville et al. (2009). From Davies et al. (2011).

Chapter 3

Visualisation Methods

3.1 Visualisation

The following two methods are established techniques for mantle plume research in an experimental environment.

3.1.1 Shadowgraph

Image removed due to copyright, it can be located on page 30 Fig. 2.1 of Schlieren and Shadowgraph Techniques.
Author: Settles (2001).

Figure 3.1: The direct shadowgraph method in its simplest form (Settles, 2001)

The use of shadowgraphs to visualise plumes in a transparent tank is quick and simple to implement. There are different ways to execute the shadowgraph technique, but the "simple" or "direct" shadowgraph method as named by Schardin (1932, 1934 and 1970) after the invention of Hooke (1665), Marat (1780) and Dvorák (1880) remains the most straight-forward. Figure 3.1 shows that this method requires a light source, an object S (in these experiments, the tank) and a reflective flat surface onto which the shadow produced from the light source and object can be displayed (Settles, 2001). The principle of shadowgraphs in plume experiments is that the

bright halos (coldest material) surround the darkest shadows (hottest material) (Figure 3.2). A bright "point" light source casts a sharp shadow on the screen (Settles, 2001). Without an object S, in the field-of-view, the light is undisturbed and illuminates the viewing screen uniformly. Conversely, with an object present, some rays are refracted, bent and deflected from their original paths and produce a shadow (Burton et al., 1953; Settles, 2001; Davaille and Limare, 2007). Shadowgraphs can image strong temperature gradients and thus are implemented as a visualisation technique for mantle plume experiments. The negative linear temperature-dependence of the refractive index of the experimental fluid means that the hot material acts as a diverging lens and appears dark, while the cold material acts as a focusing lens and appears light (Laudenbach and Christensen, 2001; Davaille and Limare, 2007).
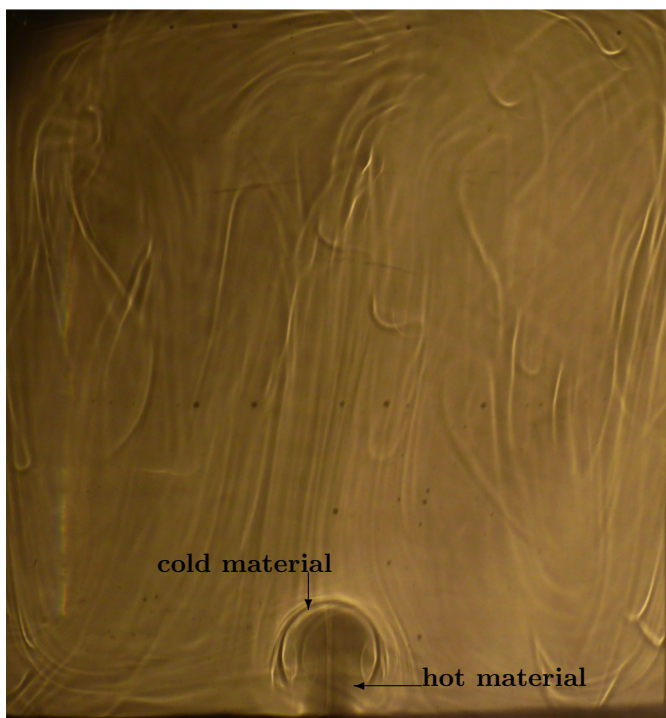
Figure 3.2: Shadowgraph image of a $\Delta T=59°C$ plume. The plume head has limbs rolling up on themselves. Background convection and flow in the tank is observed.

A great advantage of the technique is its simplicity and adaptability to large fields of view (Settles, 2001). Additionally, shadowgraphs can be produced on any reasonably flat, diffusely-reflecting surface. A major limitation of the shadowgraph technique is the imaging of a 3D image onto one plane; therefore it is difficult to know where on the z-axis the flow occurred. A second limitation is that there is no 1:1 correspondence between the object and the resultant shadow; therefore measuring may not be a true representation of the plume geometry. Thirdly, shadowgraphs are generally not to scale. Finally, parallax needs to be taken into consideration when configuring shadowgraphy, because the difference in the apparent position of an object, viewed along two different lines of sight, leads to nearby objects having a larger angle of inclination between the two lines than distant objects. The magnification, m, involved with the

Image removed due to copyright, it can be located on page 148 Fig. 6.3 of Schlieren and Shadowgraph Techniques. Author: Settles (2001).

Figure 3.3: Diagram of the direct shadowgraph technique with diverging light (Settles, 2001).

divergent light source must be taken into consideration and calculated (Figure 3.3).

3.1.2   PIV and Stereoscopic PIV (SPIV)

The use of PIV as a method has facilitated renewed advancement in fluid dynamics research, particularly examining flows that were previously difficult to map instantly (Raffel et al., 1998, 2007; Stamhuis, 2006). PIV provides a powerful, non-invasive and quantitative optical flow visualisation method. It can be characterised as an ideal tool for imaging slow flows and is capable of providing velocity measurements within two or three dimensions (Dabiri, 2009). The PIV method was first implemented by Ludwig Prandtl in 1904, who designed and used the technique in a water tunnel to investigate aspects of unsteady separated flows behind wings and other objects (Raffel et al., 2007). The flow data at the time of Ludwig Prandtl's experiment could only be analysed qualitatively. However, in the last century, with the advances in digital imaging and computer technology it is now possible to extract instantaneous flow field data from images. From the early 1980s onwards PIV has been developed for use in fluid dynamic research.
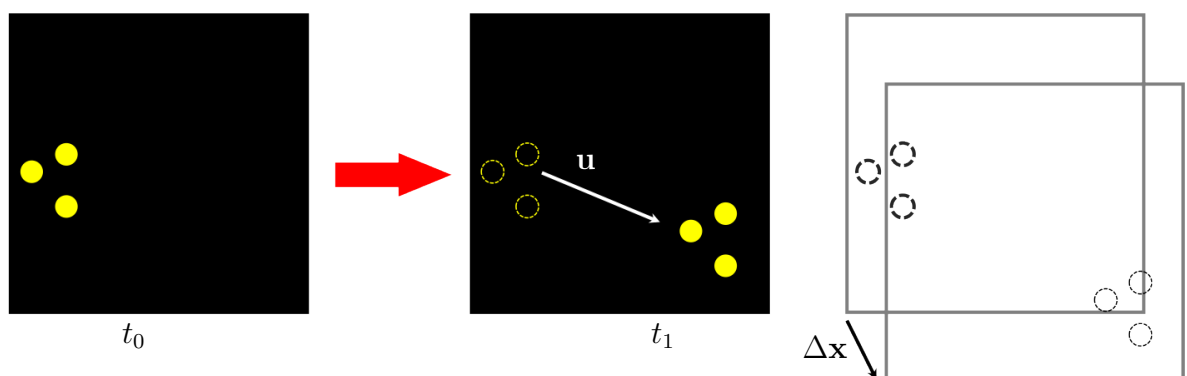
Figure 3.4: The basis of PIV

PIV relies on a simple principle. The technique allows for in-depth knowledge to be gained of the velocity of the plume in experiments, through the use of neutrally buoyant tracers seeded in the experimental fluid. It works on the premise of capturing two successive image frames of the same plane over a short time interval ($\Delta t = t_1 - t_0$) (Figure 3.4). With a known time interval, it is possible to track the particles' distance (Δx) and movement and, therefore, compute the velocity, U, (Equation 3.1).

$$U = \frac{\Delta x}{\Delta t} \tag{3.1}$$

The accuracy of determining the velocity field is limited by the ability of the tracer particles, which scatter light, to follow the instantaneous motion of the continuous phase (Melling, 1997). Care should be taken in the practical implementation of PIV in order to enable reliable measurements and reduce uncertainty (Brossard et al., 2009).
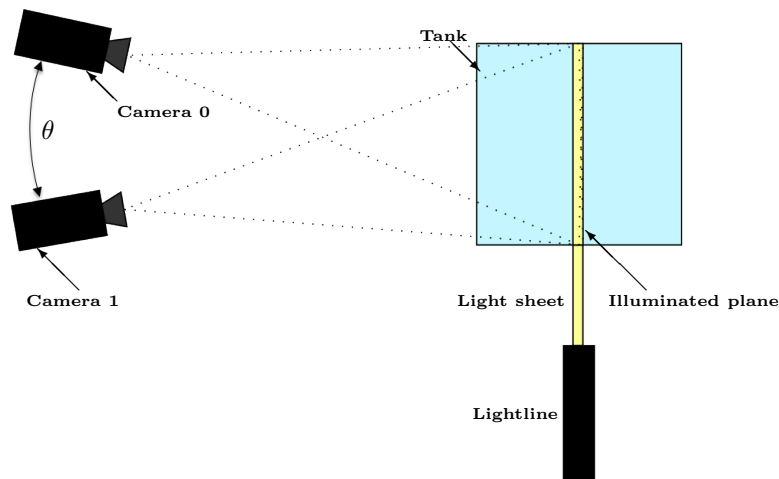
Figure 3.5: The Stereoscopic set up of the cameras, including the camera angle (θ), drawn in Google Layout

The main advantage of the PIV technique is that it is a whole field non-invasive measurement technique. This enables the capture of the instantaneous flow fields through tracking clusters of particles, assuming no deformation (relative motion) within the cluster. However, in the event that deformation occurs, this could lead to spurious vectors. In order to mitigate this, particle tracking velocimetry could be used, which tracks individual particles. However, this method is computationally expensive and was therefore not employed.

The "classical" PIV method uses one camera. Adding another camera from a different viewing direction is generally referred to as Stereoscopic PIV (SPIV, Figure 3.5). In SPIV, the two cameras simultaneously record a plane, but with distinct off-axis views of the same object, to give an illusion of depth (Prasad, 2000; Brossard et al., 2009). The two offset images are combined to extract the z-axis (the 3D perception of depth) and allow the determination of any out-of-plane flow, further reducing uncertainty (Prasad, 2000).

The seeded particles for experiments need to be non-toxic, non-corrosive, non-abrasive, non-volatile, chemically inert (Melling, 1997) and neutrally buoyant (Stamhuis, 2006) to ensure no interaction with/or chemical change of the properties of the fluid. Uniform seed size is necessary to avoid the excessive light intensity from larger particles and background noise, decreasing the accuracy of the vectors extracted from small particles (Melling, 1997). The distribution of the tracer particles is important for SPIV images. If the seeding is too dense then no flow field would be detected. Therefore, a homogeneous distribution of medium concentration is desired for high quality recordings, to obtain optimal evaluation (Raffel et al., 2007). The tracer particles are required to be highly reflective to yield good images and to move with the local flow velocity between the two frame illuminations (Raffel et al., 2007; Stamhuis, 2006). In choosing tracer particles there is therefore a need for a balance between the illumination and the velocity lag. A typical particle size for fluid flow applications ranges from 5-200μm depending on the flow speed and camera magnification (Stamhuis, 2006). Small particles are most ideal because they follow the flow better (Raffel et al., 2007). Conversely, larger particles have better efficiency when scattering light. In most applications, a compromise between reducing the particle size to improve flow tracking and increasing the particle size to improve light scattering is necessary (Melling and Whitelaw, 1973; Melling, 1997). In liquid flows, larger particles are often chosen because light with lower peak power can be used.

Chapter 4

Governing equations and non-dimensional parameters

4.0.3 Parameters for Experimental Analysis

While the mantle behaves as a solid on the short-time scales of passing seismic waves, it behaves as a fluid on geological time scales, such as those associated with post-glacial rebound and plate tectonics. The energy source for mantle convection comes from the release of energy, due to the radioactive decay of Potassium (K), Thorium (Th) and Uranium (U), and Earth's secular cooling. From the fluid dynamical point of view the dynamics of Earth's mantle appear relatively simple; because there is no turbulence and inertial forces are not important. It is possible to demonstrate this by the conservation of momentum for an incompressible Newtonian fluid in non-dimensional form (Equation 4.1):

$$\frac{1}{Pr}\left(\frac{D'v'}{Dt'}\right) = -\nabla'P' + {\nabla'}^2 v' + Ra \cdot T\widehat{k} \tag{4.1}$$

where the prime denotes non-dimensional variables, v is the velocity, P the pressure, Ra and Pr are the Rayleigh and Prandtl numbers respectively, and k the unit upward vector.

The Prandtl number (Pr) is the ratio of momentum to thermal diffusivity (Equation 4.2, Tritton (1988)):

$$Pr = \frac{\eta}{\rho\kappa} \tag{4.2}$$

where η is the viscosity, ρ the density and κ the thermal diffusivity. For typical mantle values of viscosity (η=10^{21}Pas), density (ρ=4500kg/m^3) and thermal diffusivity (κ=10^{-6}m^2/s) this

number is in excess of 10^{23}. It is virtually infinite for mantle convection, so that $(\frac{dv}{dt})$ is very small, because the average viscosity of the mantle is of the order of 10^{21}Pas (Haskell, 1935). When Pr $\gg 1$, the fluid motion ceases immediately when the heat source disappears and inertial effects are negligible compared to viscous effects (Davaille and Limare, 2007).

In other words, these are flows within the laminar domain where the ratio of inertial to viscous forces, the Reynolds number (Re, Tritton (1988)), Equation 4.3 is $\ll 1$:

$$Re = \frac{vl_c\rho}{\eta} \tag{4.3}$$

For typical values of plate velocity (v=5.1cm/yr) (Antonelis et al., 1999) and length scales (l_c) comparable to the depth of the mantle (2891km), the mantle's Reynolds number is 10^{-20}.

The Rayleigh number (Ra) is the ratio of two time-scales that are necessary for a buoyant mass to create a displacement and that of the resisting effects of thermal diffusion (Davaille and Vatteville, 2005) and can be defined following White (1988), Davaille and Jaupart (1993) and Lithgow-Bertelloni et al. (2001) as Equation 4.4. In the Rayleigh-Bénard experiments, where there is secular heating and where the fluid has a strongly temperature dependent viscosity, the Rayleigh number does not have a unique definition.

$$Ra = \frac{\rho\alpha g\Delta Tl_c^3}{\eta\kappa} \tag{4.4}$$

where ΔT is the temperature difference applied across the depth of the convecting domain, g the gravitational acceleration and α the thermal expansivity, l_c is the characteristic length scale (height of the tank). Conduction is the primary heat transfer when the Rayleigh number is below the critical value for a fluid to convect. The Rayleigh number for the mantle is $\sim 10^6$-10^8, which far exceeds the 2,772 (Schubert et al., 2001; Turcotte and Schubert, 2002) critical value for convection with no-slip velocity boundary conditions.

In fluid dynamics the Grashof number (Gr, Equation C.5) approximates the ratio of buoyancy to viscous stress force acting on the fluid (Tritton, 1988) and is defined as:

$$Gr = \frac{g\alpha(T_h - T_\infty)l_c^3}{\nu^2} \tag{4.5}$$

The T_h and T_∞ relate to the heater surface temperature and the bulk temperature respectively. Since Re represents the ratio of momentum to viscous forces the relative magnitudes of Gr and

Re are an indication of the relative importance of natural and forced convection in determining the heat transfer. When the ratio is of the order of 1, the combined effects of natural and forced convection are taken into account, which is expected for the plume experiments. The Gr number differs to the Ra number by not taking into account the thermal diffusion of the fluid.

Mantle plumes represent a different scale and kind of flow from plate motions and are well described by Equation 4.1. For this study the Rayleigh number, Prandtl number and Grashof number are used to aid understanding of the plumes growth and evolution in the experimental tank. The use of the Rayleigh number and Grashof number will help us understand the relative importance of viscosity to thermal diffusion in the experimental plumes.

Chapter 5

Experimental Procedure and Experiments

5.1 Experimental Configuration

The experimental configuration was designed to study laminar plumes generated with a localised point heat source. The main apparatus for the shadowgraph and PIV visualisation experiments consisted of an experimental tank with a copper heater, assembled on an optical table. The optical table (250cm long by 125cm wide) had passive isolator legs, designed to remove floor vibration in the critical 10Hz to 50Hz frequency range. This ensured vibrations from foot and vehicle traffic would not cause small movements of the PIV cameras.
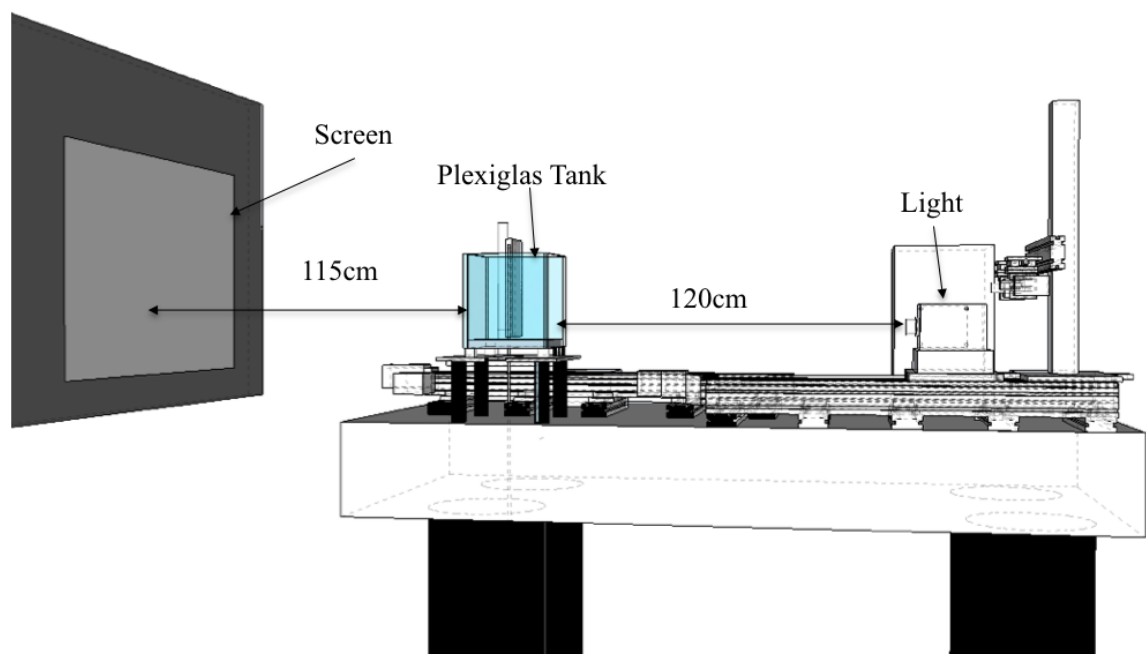
Figure 5.1: A schematic of the layout of the shadowgraph apparatus, drawn in Google SketchUp

The cubic experimental tank in the laboratory had inner dimensions of 26.5cm per side (Figure 5.1). The tank was constructed out of Plexiglas (GS233), chosen as an alternative to glass because of its superior strength and non-reflective qualities, with the transmissibility of light at ~92%. The Plexiglas had a relatively small thermal conductivity (k=0.19W/m°C) compared to the experimental fluid chosen (Davaille and Limare, 2007). Additionally, the refractive index of Plexiglas is the same as the experimental fluid (n=1.4991). These reasons make it the ideal material for an experimental tank containing a high viscosity fluid. The thickness of the Plexiglas used in the tank for the walls and top was 1cm thick. The tank was configured with no-slip sides, which ensured the viscous fluid at the solid boundary had zero velocity. The small 2cm copper heater was centrally mounted at the base of the experimental tank and attached to a programmable closed-loop controller.
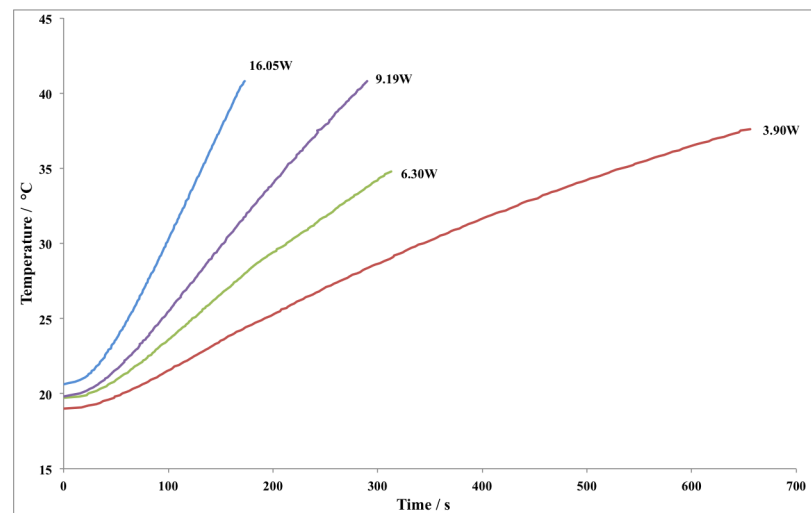
Figure 5.2: The heater function derived from measuring the heater temperature rise time at different powers up to the highest heater temperature value for an experiment at that power. The heater was turned off as soon as the temperature reached the required set point. The lowest power led to the heater coming up to temperature the slowest but had the smallest overshoot (±0.2°C). On average the median powers had an overshoot of ±0.4°C.

The heater came up to temperature faster at higher powers (Figure 5.2) and in the median powers varied in temperature by ±0.4°C. The power was altered between experiments (Table 5.6) to take into account this effect. The top surface of the heater was positioned flush with a black Plexiglas non-reflecting false bottom, in order to ensure a smooth surface with the heater for plume generation. This tank design was chosen in order to attempt to replicate and further understand the previously unpublished collapse data of Newsome (2011), whose inner tank had the same dimensions. The tank size was sufficient for high Rayleigh number experiments and the aspect ratio adequate to eliminate side wall effects. All stray light inside and outside the laboratory was eradicated with blackout blinds and black paper. This was necessary to enable clean shadowgraph and PIV images without other light contamination.

The temperature of the laboratory was controlled at 19°C ±0.5°C by an air conditioning unit to maintain a steady ambient temperature (T_∞) of the fluid. However, a small horizontal temperature gradient was observed at the base of the tank as shown in Figure 5.3, and a vertical temperature gradient of 0.5°C from base (coldest material) to the top of the tank (hottest material). It was difficult to achieve complete homogeneity of temperature in the syrup without insulation.
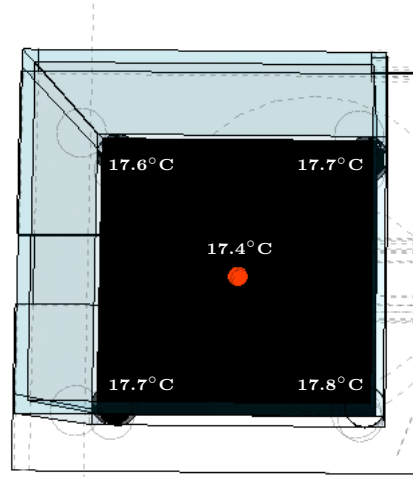
Figure 5.3: The temperature at different locations at the base of the tank before an experiment

Mantle material is assumed to flow like a Newtonian fluid with a linear relationship between stress and strain (Davaille and Limare, 2007). Therefore, the experimental fluid selected was Liquidose 436 Corn syrup (supplied by Archer Daniels Midland (ADM)); a pale yellow Newtonian fluid chosen not only because it was an analogous fluid for the mantle, but also because of its use in the previously unpublished collapse observed by Newsome (2011). In addition, the thermal conductivity of Liquidose 436 Corn syrup is 0.34W/m°C, similar to that of Plexiglas. The experimental fluid (volume 18.61 litres) was seeded after the photogrammetric calibration with tracer particles at 10ppm (0.1488grams). The particles, a high gloss white polymer powder from TopCoat, had an approximate diameter of 1-40μm. This powdered paint, used in the coating industry, could be easily obtained from various sources that market powder coating media.

5.1.1   Shadowgraph Visualisation Configuration

The experimental configuration used for shadowgraph visualisation is shown in Figure 5.1. A Volpi Intralux 250HL white light was used for the experiments and a piece of white cartridge paper as the screen. This paper was inexpensive and easily sourced and thus perfect for quick configuration of the shadowgraph experiments. The distance and configuration of the apparatus was as in Figure 5.1. The distance between the back of the tank and the screen was set at 115cm and between the tank and the light source 120cm. The magnification expected from the

divergent light source was 1.96. The shadowgraphs were recorded by photographing the screen using a Nikon D3000, 10.2MP camera (positioned on top of the tank).

5.1.2   SPIV Visualisation Configuration
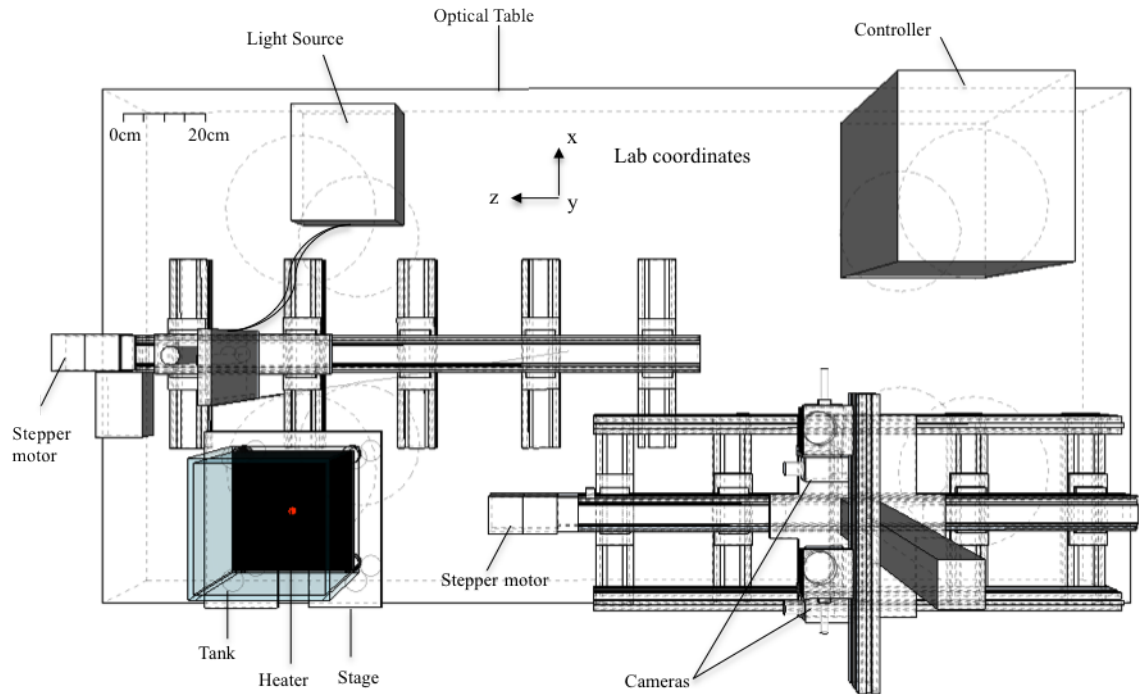
Figure 5.4: A schematic diagram of the motion-controlled system configuration from top-down view, drawn in Google SketchUp

The PIV visualisation system (Figure 5.4) designed by Dr. William H. Newsome was devised specifically for imaging slow flows. The arrangement allowed for non-invasive 3D optical rendering of velocity to characterise the whole plume and the aim of comparing datasets from different experimental runs (Newsome, 2011). This velocity was determined by seeding the experimental fluid with tracer particles. The motion-controlled system captured the motion of the particle clusters in a number of planes spanning the world z-axis (motion in planes away from the cameras for the length of the experimental tank).

The system for PIV experiments consisted of two linear slides connected to stepper motors, connected to Applied Motion Products Stac6-Si drives. The illumination or imaging elements of the system are placed on vertical arms on the traversing carriages. A lightline (a thin beam of vertical light) illuminated the tank. The imaging component consisted of two 3-Charge coupled device (CCD) cameras (JAI CV-M9CL). The double–shaft stepper motors had incremental encoders with a feedback connector for high-level position control. This motion-controlled system was programmable and automated from the main controller, with information supplied from the software. This in-house software was designed by Newsome for Stereoscopic Particle

Image Velocimetry and Thermometry (SPIVET) measurements and will herein be referred to as SPIVET-Control. Details about placement and configuration of the equipment (including the cameras and lightline) and measurements for automating the SPIVET-Control software are documented in Appendix A.

The two 3-CCD cameras, with a 15mm focal length lens and a resolution of 1024 x 768 pixels, were attached to the crossmember on the carriage and individually angled at -6° and 6.5° respectively, the resultant angle between them was of 12.5° to enable the largest field-of-view for stereoscopy (for more information about the cameras see Appendix A). The lenses of the cameras were therefore able to image the whole thickness of the light sheet.

Often PIV systems involve the use of laser light sheets. These lasers emit bright monochromatic light in a sheet with almost constant thickness without diffusion. Instead, for this laboratory configuration (Figure 5.4) white light was chosen because it was relatively inexpensive compared to high power lasers. Unfortunately, there were some disadvantages to this type of light source. The white light had to be collimated using optics to ensure that the light sheet was suitably thin (for details of configuring the lightline see Appendix A). Additionally, the intensity of white light sources can be an issue for PIV analysis. This was taken into account through long exposure times and wide camera lens apertures (Newsome, 2011).
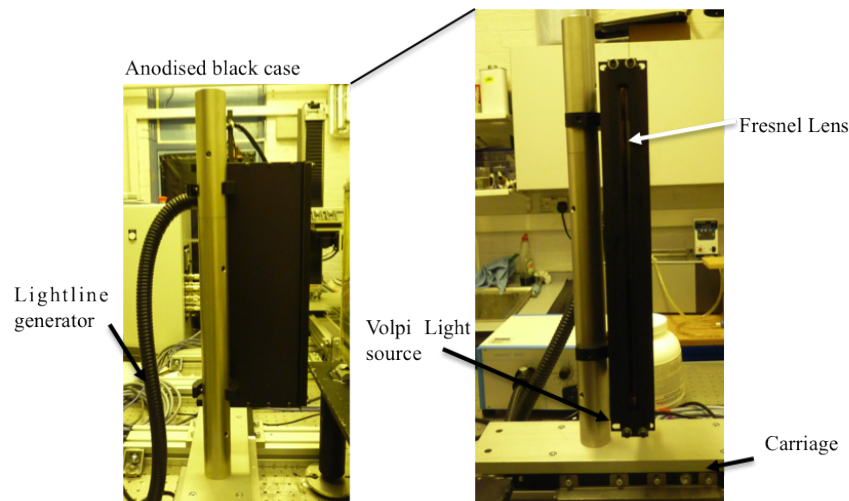
Figure 5.5: Lightline in the black anodised case

The light sheet was produced by a Volpi Intralux 9000 light source (Figure 5.5), generated from a 150W halogen light bulb attached to a fibre optic lightline generator shining through a Fresnel lens. This lens, with a 51mm focal length, collimated the light from the Volpi light generator into a thin beam of white light, fixed at 2.12mm thickness which shone through the tank. Without the lens, the light from the fibre optic lightline would converge and not produce a focused fine plane for SPIV experiments. This narrow sheet of light was necessary to define the plane of

investigation (Stamhuis, 2006). As a rule, the thickness of the lightline should be less than the smallest feature of the flow perpendicular to the light plane (Newsome, 2011).

The locations for the beginning of the experiments are as depicted in Figure 5.6. These locations were set on the computer system to enable repeatability of the carriages movement during the experiment and reduced error when extracting velocity field from the raw data (for more information see Appendix A).
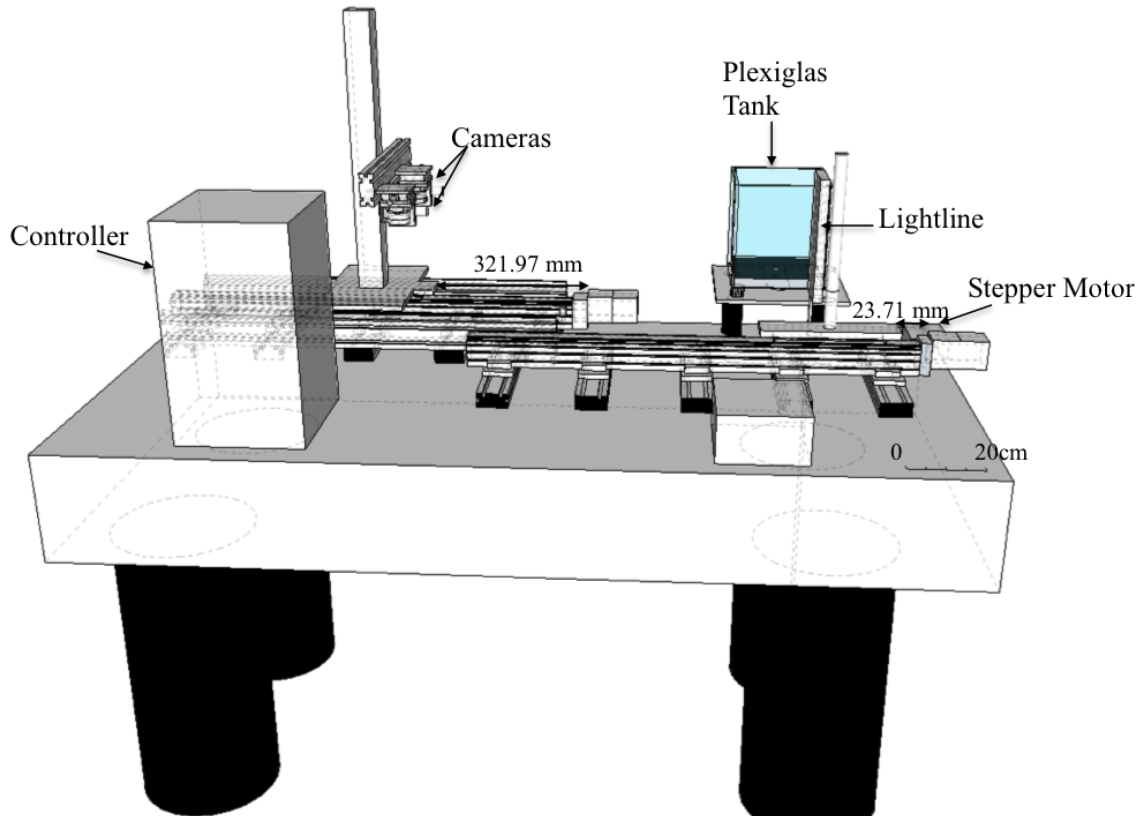
Figure 5.6: A schematic of the layout of the PIV apparatus

5.2 Experimental Procedure

5.2.1 Heater temperature characterisation
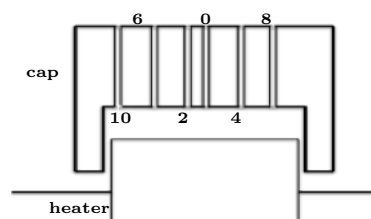
Figure 5.7: The cap holes with mm spacing for measurements

The spatial temperature distribution was important to understand if the heat was equally distributed across the copper heater and was characterised parallel and perpendicular to the white light source. Measurements were undertaken using a plastic with graphite cap and a K-type

thermocouple. The cap fitted on top of the heater with holes at spacings as in Figure 5.7 and was used to locate the thermocouple junction on the heater. The heater was left to equilibrate before measurements were taken parallel and perpendicular to the white light source. These measurements were taken at 30°C, 40°C and 50°C.

The heater had a small spatial temperature distribution parallel and perpendicular to the white light source, with the data measured remaining within error bounds in both directions for all heater temperatures set (Figure 5.8). The exception to this however, is position 10, when the heater was set at 50°C, where the temperature measured orientated towards the cameras was 2°C higher than the parallel to lightline direction measurement. This is 4% above the set temperature. However, this was deemed unimportant as the focus of the experiments were at temperatures below 50°C and thus it would not have an effect on the experiments.
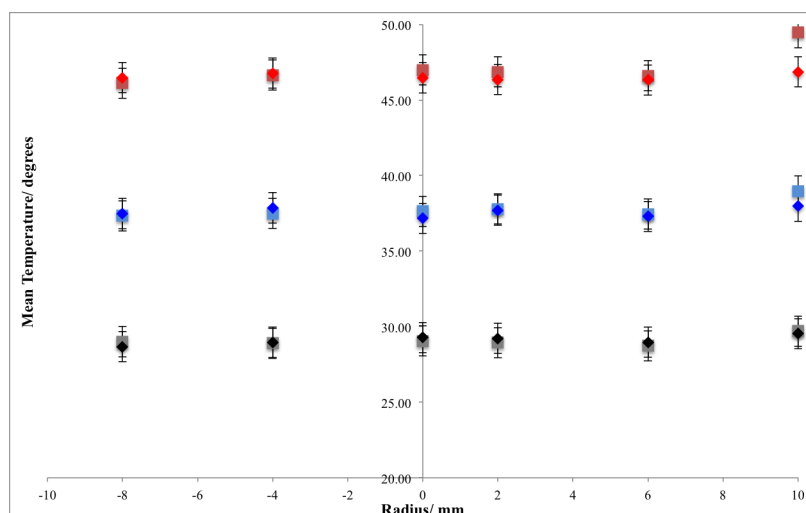
Figure 5.8: The spatial temperature distribution over the heater. squares - orientated towards to cameras, diamonds - parallel to lightline. Red - heater set at 50°C, Blue - heater set at 40°C and Black/grey - heater set at 30°C

5.2.2 Fluid preparation procedure

Before experiments were conducted, the experimental fluid was thoroughly mixed because the syrup was prone to crystallite formation, which can generate small chemical density contrasts. Stirring and mixing ensured the syrup was homogeneous prior to placement in the tank. Two large water containers, heated at 45°C, were used to heat and mix two separate 5 gallon vats of syrup. After two days of heating, each vat was stirred with a mechanical mixer (ColeParmer 50004-00) at 900rpms for a day of simultaneous heating and stirring. After combining the two vats, the syrup was simultaneously heated and stirred for yet another day. Heating and stirring of combined vats is important because syrup viscosity was likely to vary by as much as 10% between batches (Newsome, 2011). The fluid at 45°C, was decanted into the tank, firstly down

the sides of the tank, to avoid bubbles fixing to the sides, and then the remainder of the tank was filled and subsequently left for one week to allow any bubbles to disperse. If too many bubbles were present, the shadowgraph images would be rendered unclear for interpretation and reduce accuracy in the PIV vectors obtained.

5.2.3 Motion-Controlled System Movement Error
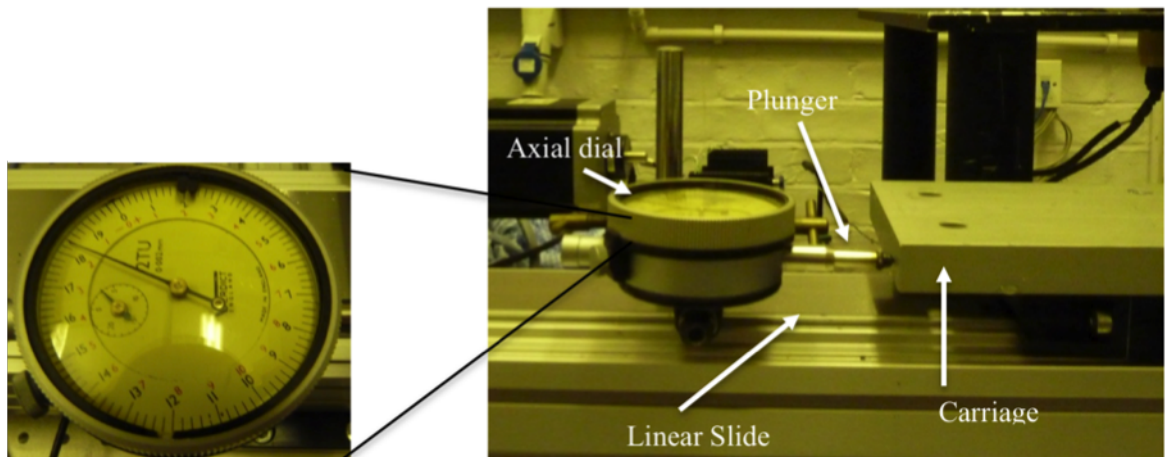
Figure 5.9: The configuration of the axial dial indicator

Confirming the reliability and potential error of the carriages returning to the same position on the linear slides was important for the accuracy of ascertaining the PIV vectors. Repeatability and error tests were conducted with a Verdict axial sprung plunger dial to determine the accuracy of the carriages' movement. This dial was attached to a magnet base, which allowed it to remain in a fixed position on the optical table during testing, with the depressed plunger touching the carriage ready for measurement (Figure 5.9). Preceding a test, the plunger was exercised and the dial rotated to eliminate hysteresis.

Before every test the following steps were followed: a) The axial dial was set to zero and installed at the back of the carriage. b) The dial was read. c) The step interval at 5mm and Post Home offset (PHO, the distance from the home switch to the beginning of capturing data) were configured on the SPIVET-Control software. Finally, d) After the test the dial was read and the error observed. For descriptions of the individual tests performed see Appendix A.

Each test was carried out three times and the average error calculated (Table 5.1). The overall error of the system was 0.5 microns and the accuracy in the movement of the carriages was also approximately 0.5-1 microns/mm travelled, constituting a negligible percentage error. The repeatability of the movement was more important than absolute accuracy and the data suggested that the slides returned to the same position with very high precision (to within half a micron).

Test	Error/ microns
Home test	0.25
Accuracy	0.5
Backlash	1.00
Long PHO	0.5
Step Repeatability	0.5

Table 5.1: The errors for the various repeatability tests undertaken

Therefore, in an experiment the same position in the tank would be analysed and produce high quality vectors.

5.2.4 SPIV Photogrammetric Calibration

The calibration was undertaken to map the image coordinates of the camera CCD sensor to the coordinates in the laboratory and characterised how the cameras projected the 3D light sheet into a single 2D image. Once calibrated, the tank was sealed to maintain structural integrity and inhibit air from drying the top surface of the syrup. A calibration target was imaged to provide correspondence between points in the image and points in physical space (Horn, 2000). After this, to achieve accurate estimates of the flow, the image coordinates were related back to a location in the tank space.

It was important that all items in the system used in the experiments were present during calibration, except for the tracer particles. These particles were added in trace amounts and therefore were not necessary during calibration (Newsome, 2011). The photogrammetric mapping produced during the calibration is specific to a given refractive environment (Newsome, 2011). The refractive index of air (n=1.000293) and water (n=1.3330) differed from that of the experimental fluid (Liquidose 436 syrup, n=1.4991). Since calibrating without the syrup would greatly affect the quality of the experimental data, the syrup was therefore present in the tank during the photogrammetric calibration to ascertain the real world positions of the target in the experimental refractive environment.

A common approach to calibrating a SPIV imaging system relies on images of a planar calibration target, placed coincident with the light sheet (Raffel et al., 2007). These calibration targets form a precise grid of markers (dots, crosses, lines grid, checker board) which can be easily detected with simple imaging processing techniques (Raffel et al., 2007). Therefore, for the experimental system a gridded target with squares of 6.2mm was used and printed on photographic paper. This paper was chosen because it withstood the effect of the viscous syrup during calibration. The grid was mounted on glass and attached to a rigid brace for the calibration (Figure 5.10).
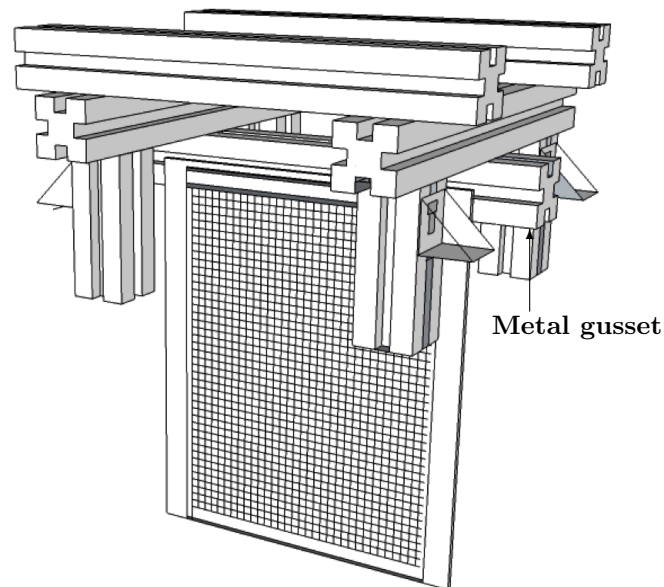
Figure 5.10: The rigid mount for the photogrammetric calibration, with the grid attached, drawn in Google SketchUp

For the most accurate real world positions of the particles in the tank, all components (glass and grid) were arranged parallel to the light sheet and perpendicular to the side walls.
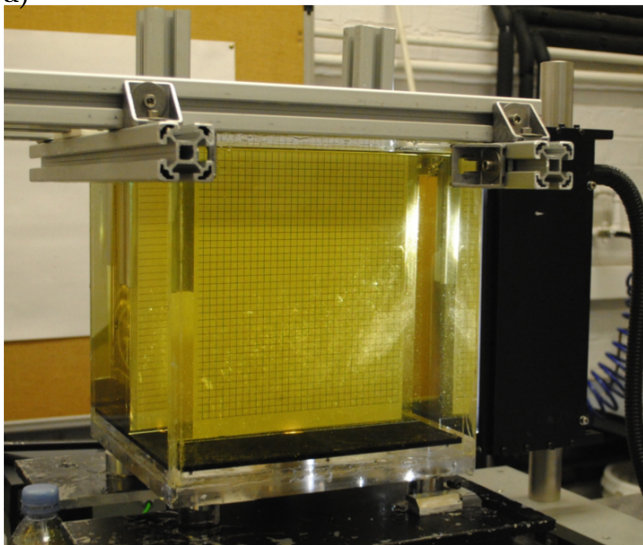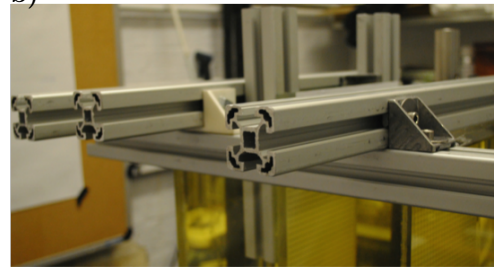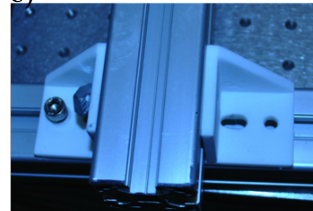
Figure 5.11: a) The rig on the tank b) A close up of how the bracket sits on the new rig c) A close up of the bracket

For the photogrammetric calibration, a rigid structure was designed and engaged with the top of the tank, with the grid central in the filled tank and levelled (Figure 5.11). The structure guaranteed stable and exact placement for this and future calibrations. In order to capture accurate images, the target was required to be perpendicular to the cameras and thus was mounted as shown in Figure 5.12. The viscous nature of the fluid caused difficulties ensuring the target was perpendicular to the cameras. The structure allowed controlled movement of the target in the negative z-axis (towards the cameras, where the positive x axis was towards the lightline and positive y axis towards the lid of the tank) using two brackets (Figure 5.11b). The
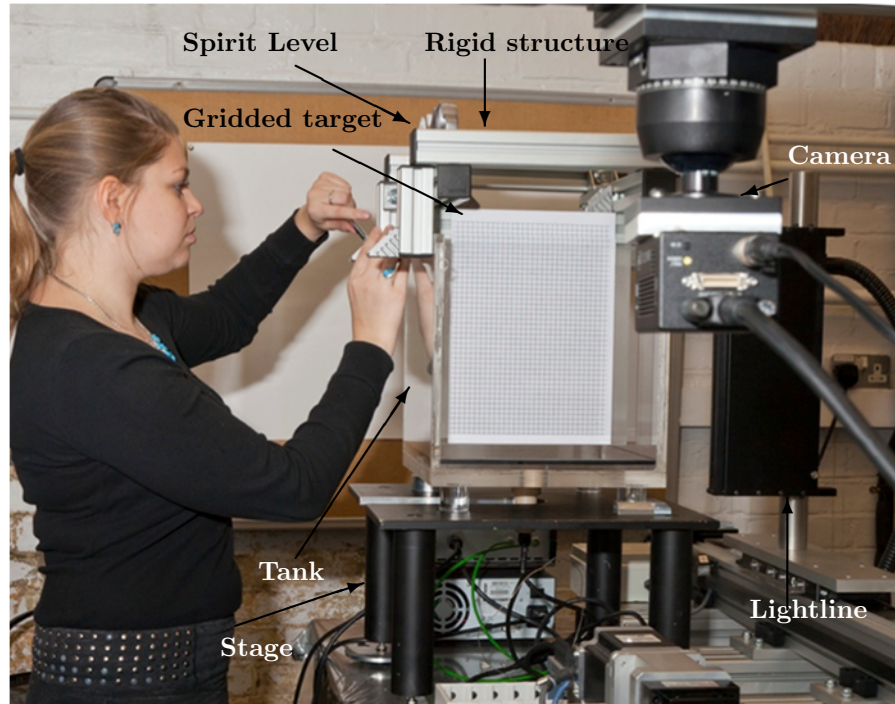
Figure 5.12: Displays the set up of the metal rig with the target placed into the tank. Ensuring the rig is level and tightly fitting the tank

brackets were bolted to the structure and the target moved to a new position by sliding the bolts a controlled distance in the bracket. This system enabled accurate displacement on both sides of the tank.

The cameras remained stationary during the calibration and were adjusted, focused and set to image a common region of the target, prior to capturing images of the target. The focal length was chosen to allow the largest field of view possible for both cameras. Any change in the camera focus would render the calibration invalid. For the calibration, the central plane of the tank was captured and the target moved in 2mm increments in the negative z-axis, to image a further five planes. At each position, photographs were acquired of the target and the displacement recorded (in mm to two decimal places). The accuracy of the target position was imperative for the later stage of the calibration, using the in-house python software called SPIVET, to ensure the vectors obtained from the raw experimental data were as precise as possible.

Great care was taken to avoid generating bubbles during the movement of the target to minimise imperfections in the calibration images. The calibration from cameras to laboratory coordinates is critical and relies on the refractive index of the fluid and the configuration of the system to remain the same, if any change occurred the process would need to be repeated.
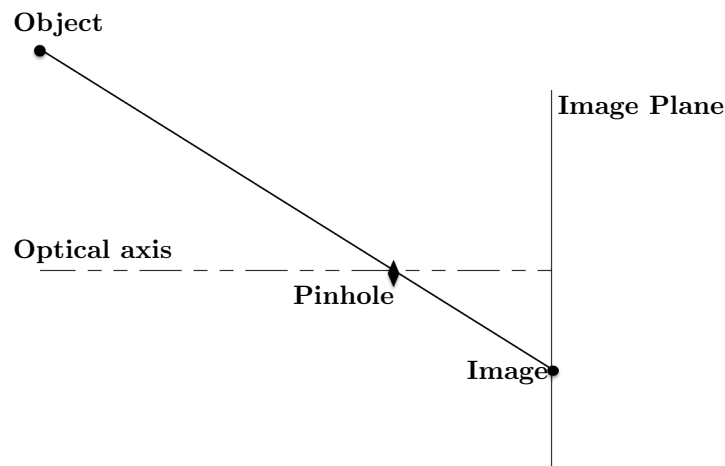
Figure 5.13: A schematic of the pinhole camera displaying all object points along the illustrated ray which mapped the same point on the image plane, adapted from Newsome (2011)

5.2.4.1   Photogrammetric image calibration technique

After the photogrammetric calibration in the tank, the photographs captured were edited (lightened, enhanced and obstructions to intersections removed) with the GNU Image Manipulation Program (GIMP, a multi-platform photograph manipulation tool). GIMP was additionally used to establish the starting point (top left hand corner) and ending point (bottom right hand corner) of the images to locate the intersections. This followed the usual convention in computer vision literature, where the origin of the image coordinate system was in the upper left corner of the image array (Heikkila and Silven, 1997).

The SPIVET software for calibration, analysed images and extracted the pixel coordinates of the intersections using two main methods. Firstly, the locations of the line intersections were computed using linear Hough Transforms[1]. Secondly, this was recomputed to a higher precision through cross-correlation (for high accuracy calibration) and a cross-shaped template.

In essence the Hough transform ordered the intersections, while the cross correlation extracted the intersection coordinates. This two-stage process allowed for any missing intersections from the first stage to be found during the second stage. If an obstruction existed, cross-correlation was unable to determine the intersection location. The Hough transform would then compute the intersection location from the already extracted lines. If the calibration target was not parallel with the tank the SPIVET software would struggle to calibrate the images. A further, alternative method for locating the intersections was implemented and this method is detailed in Appendix A. However, this image calibration led to less accurate vectors and therefore calibration with the parallel target was used in preference for the experiments.

After the line intersections had been determined, the pinhole camera model of Tsai (1987) was

---

[1]This is an extraction technique used in image analysis and digital image processing.

applied to fit the data for each camera to corresponding 3D point coordinates from the 2D pixels in the image. The cameras were modelled as distortion-bearing pinhole cameras. This calibration method offered the possibility to calibrate internal and external parameters separately. The pinhole camera model was based on the principle of collinearity, where each point in the object space was projected by a straight line through the projection centre (pinhole) onto a single point (such as a pixel) in the image plane (Heikkila and Silven, 1997) as shown in Figure 5.13. In practice, the location of the pinhole was located along the optical axis within the camera lens and could be easily approximated for larger observation distances. For more details on the Tsai (1987) method see Appendix A.
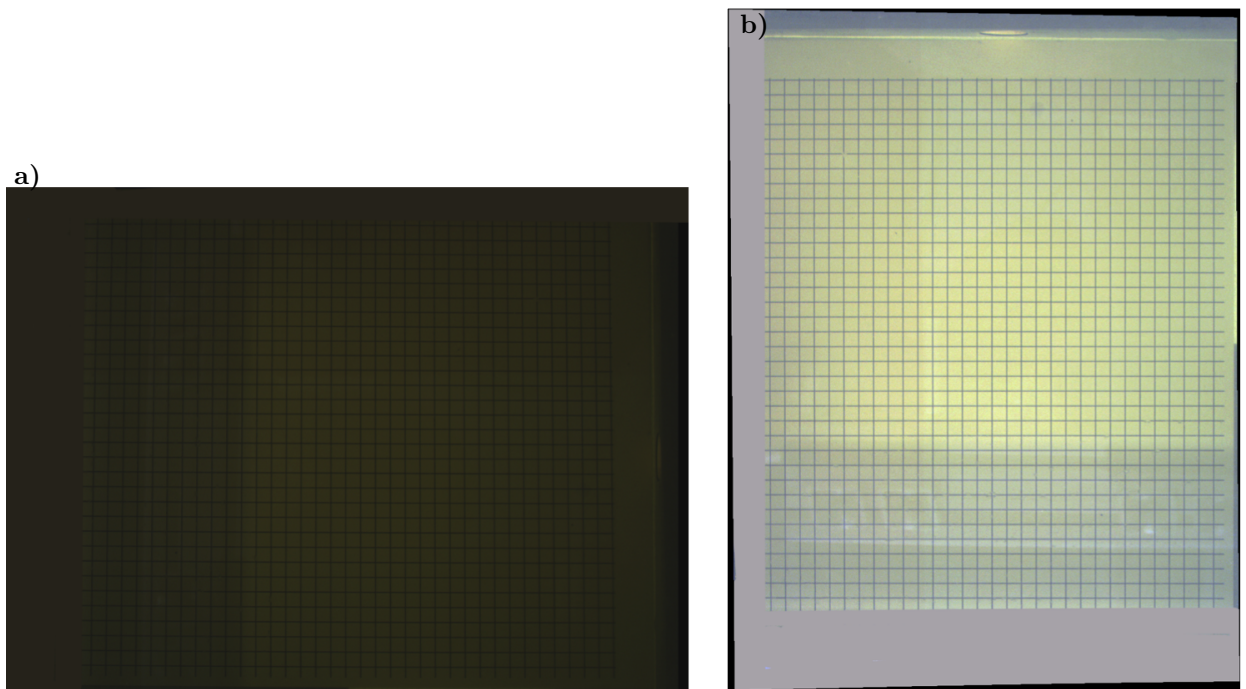
Figure 5.14: a) One of the calibration images before post-processing, b) the image after GIMP was used and the image dewarped - the image has been rotated and the intersections became orthogonal

As the basic pinhole model has no concept of refraction in lenses or other objects, these are modelled as distortions or accommodated by other parameters such as the focal length. The internal parameters described the pinhole camera (principal point or image centre, focal length and distortion coefficients) and could be fixed. The external parameters (position and orientation relatively to the world co-ordinate system) within 3D space were discovered with the pinhole camera method. This was a two stage process to compute: first the position and orientation and, secondly, the internal parameters of the camera. Unlike a pinhole camera, a real camera would only maintain sharp focus for objects that were within a certain range of distances from the lens (Newsome, 2011). Therefore, a fit was performed using an approach similar to that of Heikkila and Silven (1997). Furthermore, a direct linear transform was used to solve for an idealised imaging system and real world effects such as radial distortions (Raffel et al., 2007; Newsome, 2011). The calibration software additionally incorporated a distortion model using

the Levenberg-Marquardt method[2]. This method utilises an optimisation algorithm to solve the standard non-linear least-squares problem.

The final stage of the photogrammetric image calibration was dewarping. In the laboratory the tank was mapped by the calibration and the raw images obtained were projected onto the mid-plane of the light sheet (dewarped). The pixels were then directly related to lab units (e.g. mm) by a constant scale factor (Newsome, 2011). Figure 5.14 shows an example of a calibration frame pre- and post-dewarping.

5.2.4.2   Data processing and vector extraction
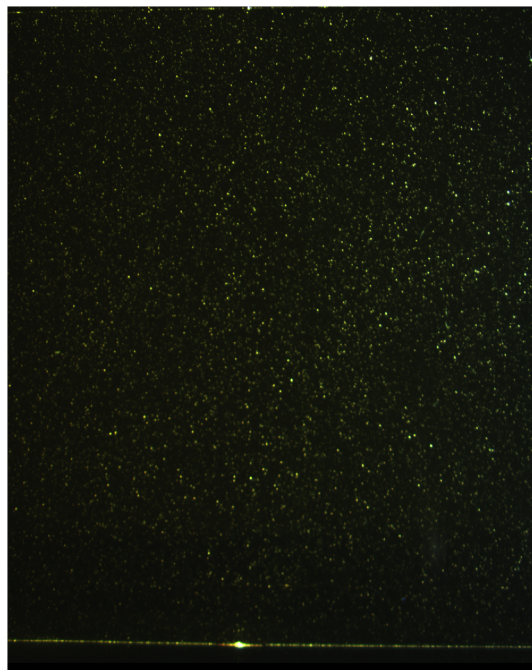
Figure 5.15: An unprocessed image captured during a SPIV experiment. The bright flecks are the tracer particles illuminated by the lightline.

Raw experimental data images, such as that shown in Figure 5.15 are first dewarped as shown in Figure 5.14 and then processed to obtain vectors using SPIVET. The computation of the two component displacement vectors for the two 3-CCD cameras (the in-plane components) is discovered by extracting the three components of the velocity vectors.

Small clusters of particles move together whilst preserving the relative orientation of the pattern. This aids the identification of unique particle clusters during image processing. Evaluating the SPIV images can be achieved by dividing one image from the pair of frames into small sub-sections called "interrogation areas", of M by N pixels (i.e. a template) in size (Raffel et al., 2007; Newsome, 2011). This method is called Correlation Image Velocimetry (CIV). The interrogation window is required to be sufficiently small for the velocity gradients to have

---

[2]The Levenberg-Marquardt algorithm is a curve fitting algorithm and is an iterative procedure.

significant influence on the results. A unique cluster of particles is chosen in the first image and then iteratively this cluster is searched for in the second image over a larger search region, via image registration[3] techniques (Brown, 1992; Newsome, 2011). All particles within one interrogation area were assumed to have moved homogeneously between the two frames (Raffel et al., 2007). At each location of the template, a similarity measure was computed based on how accurately the template matched the underlying search region. The translation, which maximises the similarity is taken as the two component (2C) displacement vector. The interrogation area allows for the maximum possible vectors to be produced and attain the single displacement vector from each window. The distance travelled by the cluster between frames is related from the photogrammetric calibration, to the velocity of the syrup.

In order to implement the CIV scheme two different similarity measures were employed to register the template window to extract the 2C vectors in the search region:

- Normalized cross-correlation (NCC)

- The similarity measure of Barnea and Silverman (1972) for Sequential Similarity Detection Algorithm (SSDA)(Newsome, 2011).

This enables the extraction of all three components (3C) of the velocity vector and begins with the computation of the 2C displacement vectors for each camera (the in-plane components). These two similarity measures are used to reduce the computational cost in processing the raw data. NCC is a complex, computationally expensive, image registration technique. The two frames of one camera are a dewarped pair of images. In the second image the average M by N region from the search window is evaluated for every location of the template. The SSDA algorithm is less complex and uses a similarity measure to sum the absolute difference between the template and the search block (Newsome, 2011). This was undertaken using a search area (32x32 pixels) over which the similarity was computed. The coarse 32x32 pixel template window allowed for the extraction of the 2C vectors and accommodated for a large degree of particle translation between frames (Fincham and Spedding, 1997; Newsome, 2011). The same template window size was used for the next stage in the processing, where the NCC measure was applied to a region of a few pixels in both dimensions and produced sub-pixel precision when fitting a Gaussian peak in each direction (Willert and Gharib, 1991; Newsome, 2011).

Once the similarity measures for registration of the template window have been undertaken, the extraction of the 2C vectors can occur (Figure 5.16). The camera calibration was used to project

---

[3]Registration is inherently basic to any image processing system and is used to detect changes or perform mapping for two similar images, it is necessary for meaningful results to have the images registered (Barnea and Silverman, 1972).
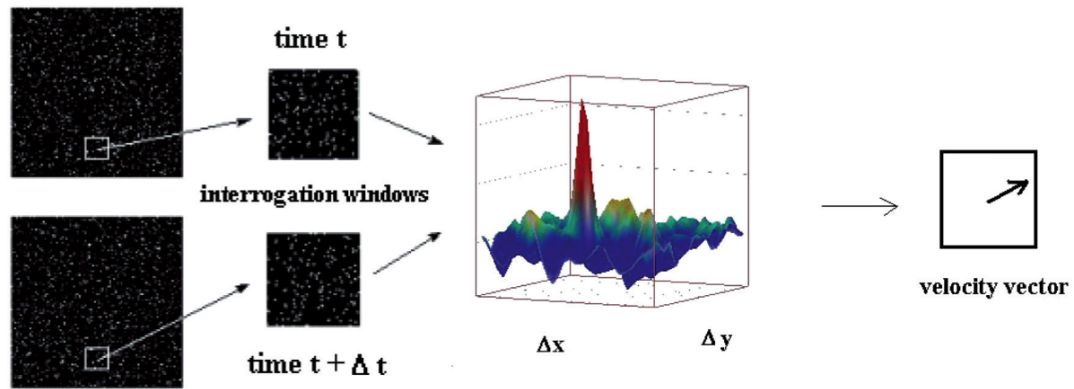
Figure 5.16: The local 2C-displacement vector of the particle images between the two illuminations is determined for each interrogation window by means of a spatially statistical cross-correlation function which determines the velocity vector (Brossard et al., 2009).

the camera images back into the laboratory coordinates. The optical flow was determined for the projected (dewarped) images by using a 3x3 median filter to effectively remove clusters of bad displacement vectors. Additionally, a second median time filter was applied to remove spurious vectors using a different sized window (5x5). Finally, the image was filtered with a standard weak Gaussian filter, which smoothed results. The smoothed results (2D displacement vectors) were then iteratively refined by warping the images until the tracers line up, producing two iteratively refined flow fields (one for each camera). These were then used to construct the 3D flow field, which is referred to at one instant in time. Therefore, the whole data set was splined and adjusted within each epoch (where an epoch is an instant in time for which the flow should be measured). Following this, the 3D displacements were converted into velocities using the inter-frame time (time between each frame, Δt) and Equation 3.1.

5.3 Fluid characterisation

The density and viscosity (Section 5.3.2 and 5.3.1) of the experimental fluid were characterised over a range of temperatures. Additionally, measurements were conducted each time the experimental fluid was changed in the tank. From these fluid properties the thermal diffusivity and thermal expansion were computed. The thermal diffusivity (κ) was calculated using Equation 5.1 and the coefficient of thermal expansion (α) was determined from the gradient of the line in Figure 5.20.

$$\kappa = \frac{k}{\rho C_p} \tag{5.1}$$

As thermal conductivity (k) and specific heat capacity (C_p) remained similar between batches, it was possible to use values given by the manufacturer (Davaille and Limare, 2007), ADM supplied

these values. The refractive index was also measured as a function of sugar concentration in the experimental fluid using different proportions of the experimental fluid and deionised water. Finally, a time series analysis of the refractive index of the experimental fluid was investigated over a period of one year to look for chemical unmixing.

5.3.1 Viscosity Measurements
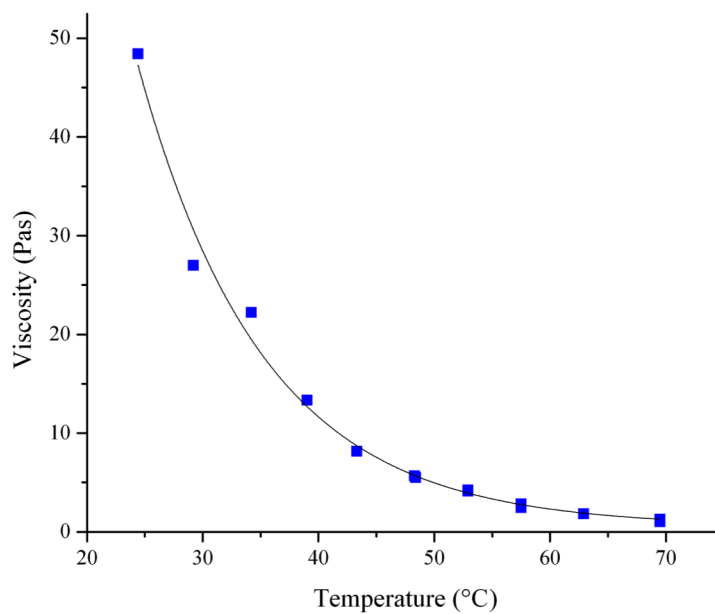
Figure 5.17: The measured viscosity changes with temperature of the Liquidose 436 syrup. The functional dependence is y=443.36751e$^{(-T/10.84392)}$+0.55944

Viscosity measurements of the experimental fluid were undertaken using a viscometer, a jacketed beaker, a thermocouple and a water bath. A rotating Haake viscometer VT 7L plus measured the torque needed to rotate a spindle in the fluid. The temperature of the fluid was equilibrated with a jacketed beaker. A K-type thermocouple was inserted into the syrup to measure the temperature independently from the water bath and was left to equilibrate prior to the recording of the first reading. This rotating Haake viscometer was chosen for its ability to test medium and low viscosity fluids in the range of 3-6,000 Pas. The accuracy of the measured values from the viscometer was $\pm 1\%$ of the full scale in use.

The viscosity of Liquidose 436 syrup varied strongly with temperature and was measured from 24°C to 70°C. The viscosity measurements decreased exponentially with increasing temperature (Figure 5.17) with a fit of R^2=0.98903. This exponential fit agreed with previous studies by Giannandrea and Christensen (1993), Lithgow-Bertelloni et al. (2001), Jellinek et al. (2003), Kincaid and Griffiths (2004) and Newsome (2011). Comparison of the data from Lithgow-Bertelloni et al. (2001), Newsome (2011) and ADM is shown in Figure 5.18 and Appendix B, Table B.5.
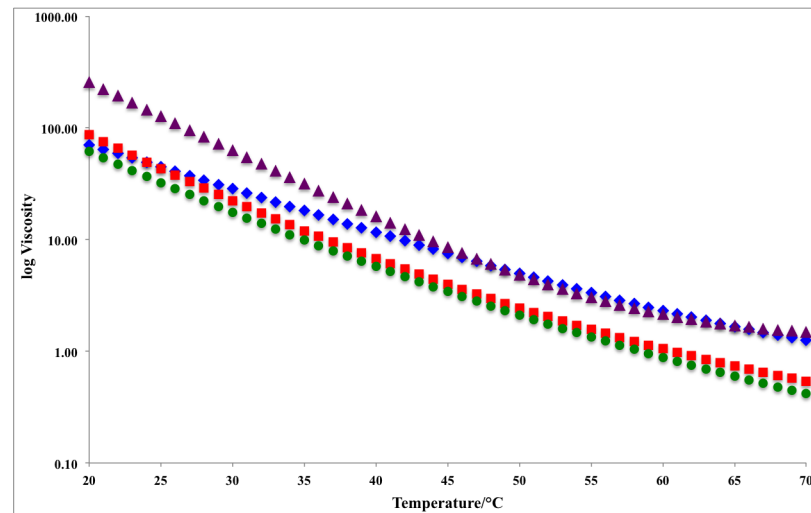
Figure 5.18: A comparison of different fits for the viscosity from different Liquidose 436 syrup data sets. Blue diamonds represent my data, red squares represent Lithgow-Bertelloni et al. (2001), green circles represent Newsome (2011) and purple triangles represent ADM data.

5.3.2   Density Measurements
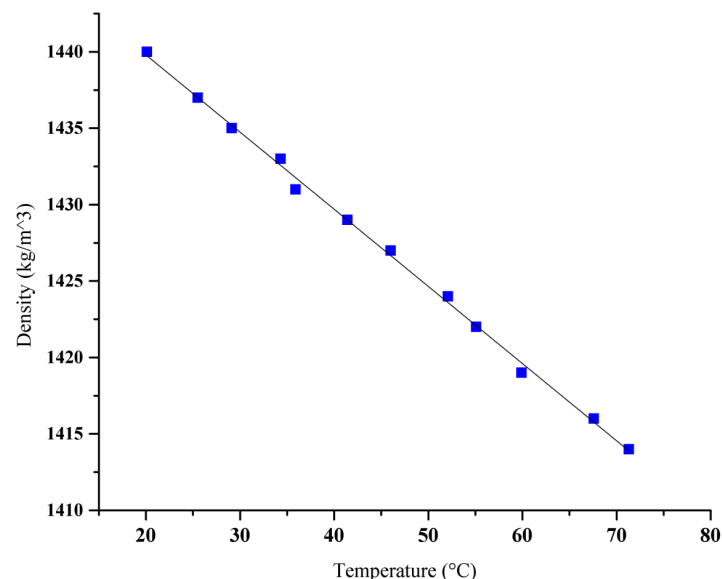
Figure 5.19: The measured density data against temperature. The line of fit is density=1449.89-0.5047T.

Density measurements were undertaken using a similar arrangement to the viscosity configuration, except a set of Cole Parmer glass hydrometers were used instead of the viscometer. These hydrometers consisted of a cylindrical stem and a bulb weighted with lead shots, which float in the fluid and measure the ratio of the density of the fluid to the density of water. The hydrometer often needed 10 minutes to equilibrate in the fluid prior to reading where the fluid touched the stem of the glass hydrometer. The error of the reading was $1kg/m^3$; half of the smallest division on the hydrometer. The density of the Liquidose 436 syrup was measured from 20°C to 72°C (Figure 5.19) and had a linear temperature-density relationship ($\rho = 1449.89\text{-}0.5047T$), similar to previously measured values by Jellinek et al. (2003) and Newsome (2011) for the
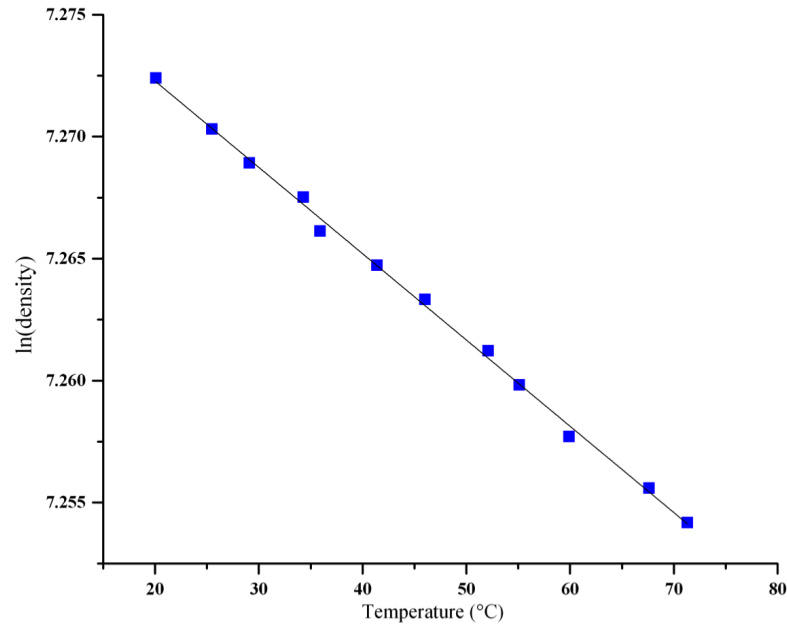
Figure 5.20: The natural logarithm of the density data changes linearly with temperature. The linear fit is ln(density)=-3.54x10^{-4}T+7.27936

same grade of Liquidose 436 syrup. The natural logarithm of the density data (Figure 5.20) was used to determine the thermal expansion of the syrup (the gradient of the line), where α=3.54x10$^{-4\circ}$C^{-1}.

5.3.3 Refractive index measurements

An Abbe refractometer was used for measuring the refractive index (n) of the experimental fluid. The refractometer was chosen for its ability to measure liquids with a refractive index between 1.3 to 1.7 and to investigate solids, turbid and highly coloured liquids - specifically measuring sugar syrups. Furthermore, only a small drop of liquid was required and the full range of syrup changes could be investigated with just one instrument. This differed from density measurements where a large volume of fluid was required when using glass hydrometers.
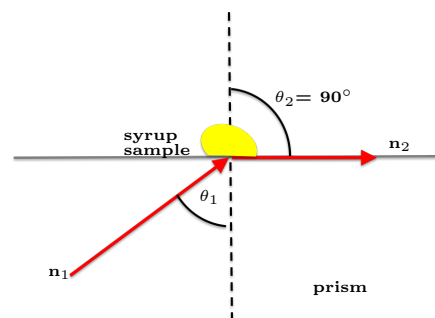
Figure 5.21: Total internal reflection

The refractometer worked on the principle of the critical angle for total reflection, in the substance to be examined, enclosed between two prisms. The refractive index is defined by Snell's

law (Equation 5.2 and Figure 5.21):

$$n_1 sin\theta_1 = n_2 sin\theta_2 \tag{5.2}$$

where for total reflection the angle of $sin\theta_2$ is 90°. Thus the angle at which the light emerged from the prisms is given by Equation 5.3:

$$\frac{n_1}{n_2} = \frac{1}{sin\theta_1} \tag{5.3}$$

A thermometer was attached to the refractometer and recorded the temperature of water leaving the upper prism jacket to an accuracy of 0.1°C.

The substance to be measured was placed on the prisms and the jacket closed. A mirror to reflect adequate light into the prisms was set to allow suitable illumination to the eye piece and maintained for all measurements. The eye piece was focused on the cross-line and the reader on the scale. With a substance present, a shadow was observed and the index arm adjusted for the shadow to be positioned on the horizontal cross-line. A measurement was obtained, with a precision to the fourth decimal place (although the fourth decimal place was estimated). After each solution was investigated the prism was cleaned twice. Firstly, with warm water to remove the experimental fluid. Secondly, with deionised water to ensure future measurements were not contaminated from the previous solution or from ions in the tap water. Tissues were used to dry the prism without scratching it.

The refractive index for five different proportions of Liquidose 436 syrup and deionised water and the temporal variation over a year, as a proxy for crystallite formation and density stratification, were determined.

The five different proportions were measured into small plastic bottles. A bottle was placed on an enclosed mass balance (accuracy to five decimal places) and the door closed to ensure accurate measurements in a stable environment. The weight was set to zero, syrup added and the bottle lid applied (to ensure no evaporation of water from the syrup or drying effect from the air). The amount of deionised water to be added was calculated by volume (in grams) from Equation 5.4:

$$\rho = \frac{m}{V} \tag{5.4}$$

where m is the mass of the fluid and V is the volume of the fluid, depending on the already

determined proportions (Table 5.2). The density of the syrup at room temperature (19.8°C) was 1445.63kg/m^3. In adding the water, the bottles were placed on the mass balance and drops added slowly to confirm the correct weight (syrup and water measurements displayed in the Table 5.2).

Label	Syrup/ g	Water / g	Volume syrup /m^3	Volume of Water/ m^3	n	T/ °C	Description
1	8.02146	1.86450	5.5488x10^{-6}	1.8600x10^{-6}	1.4608	19.5	The deionised water is $\frac{1}{3}$ the volume of syrup
2	4.98518	3.44792	3.4485x10^{-6}	3.4500x10^{-6}	1.4187	19.8	The same volume of deionised water and syrup
3	Pure Syrup	-	-	-	1.4991	19.5	Pure syrup
4	1.87060	3.94417	1.2940x10^{-6}	3.9400x10^{-6}	1.37509	19.8	The deionised water volume is 3x volume of syrup
5	-	Pure Water	-	-	1.3329	19.5	Pure deionised water

Table 5.2: The refractive index and temperatures of the different solutions

The five solutions were required to be well mixed to obtain accurate refractive index measurements. This was undertaken by placing the bottles in boiling water to lower the viscosity of the Liquidose 436 syrup in order to speed up mixing. Following this the bottles were shaken, re-heated and then left to cool to room temperature.

The refractive index and temperature for each of the solutions were recorded (Table 5.2) and the concentration by volume and refractive index plotted (Figure 5.22).
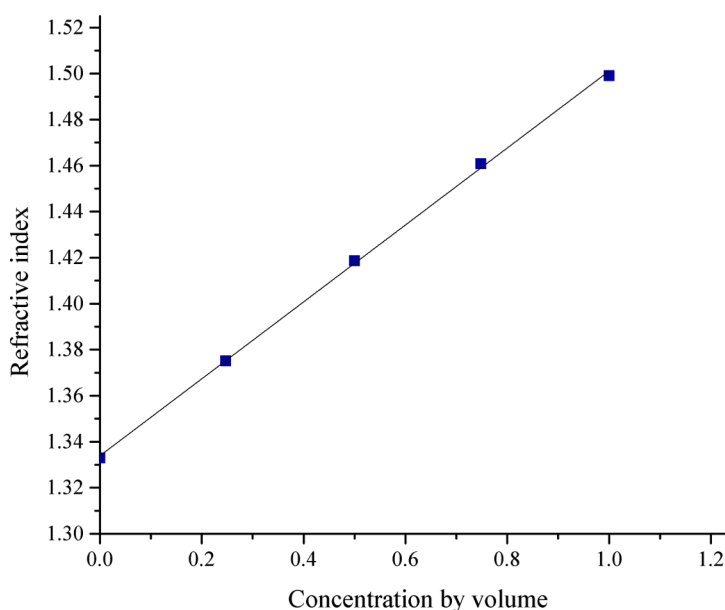
Figure 5.22: The fit of the line is y=0.16717x+1.3339 and it is fitted with R^2=0.99972

The time series was configured by placing mixed Liquidose 436 syrup into a bottle of similar

height to the experimental tank. The bottle was placed next to the tank in order to undergo the same conditions as the tank. Syrup was removed from the bottle with a metal rod and a glass tube (for extraction of syrup from the base). Measurements were taken at various time intervals (Figure 5.23). At the beginning of the study the time between refractive index measurements was doubled; a measurement was initially taken then taken one week later, then two weeks after that and then one month later. After this time measurements were taken monthly until 163 days into the investigation. At which point it was decided that measurements would be taken at shorter time scales of every 2 weeks to understand if there was an annual trend occurring. The same method was used for the Lyle's Golden syrup (See Appendix B for the graph).
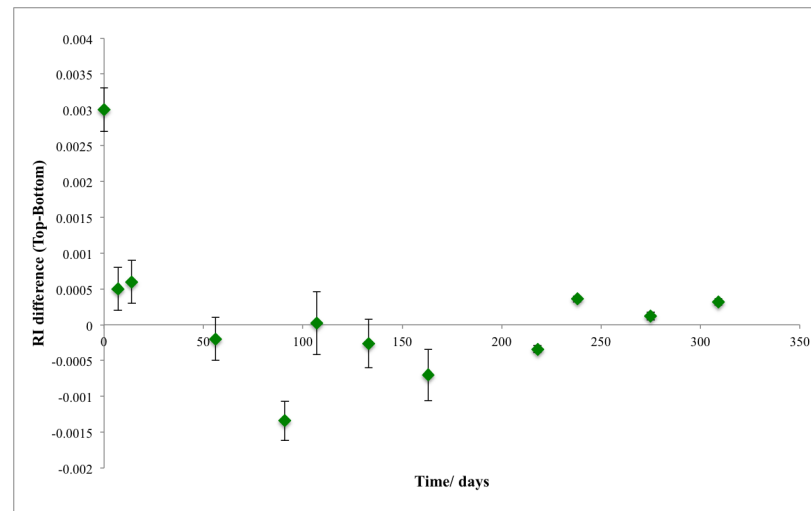
Figure 5.23: The time series analysis of the refractive index of the Liquidose 436 syrup. The error bars are twice the standard error.

5.3.4 Physical Properties

Parameter	Equation	Unit
Viscosity	$443.36751\mathrm{e}^{(-T/10.84392)}+0.55944$	Pa s
Density	1449.89-0.5047T	kg/m^3
Refractive index	1.5036-$2\mathrm{x}10^{-4}T$	-

Table 5.3: The formulations for different fluid properties

The formulations for the viscosity, density and refractive index are presented in Table 5.3 and the comparison of the physical properties of the experimental fluid and Earth's mantle are presented in Table 5.4. The important parameters for dynamical similarity between Earth and the experiments are the dimensionless numbers; namely the Rayleigh, Prandtl and Reynolds numbers. There is dynamical similarity between the two systems if the Rayleigh and Prandtl numbers are high and the Reynolds number is low. If so the systems can behave in a similar way. Table 5.4 shows the similarity of the Rayleigh numbers which is the most important parameter to match to Earth.

Parameters	Symbol	Liquidose 436 syrup	Earth's Mantle	Units
Viscosity at 20°C	η	58.86	10^{20}-10^{22} (Mitrovica, 1996)	Pa s
Density at 20°C	ρ	1435.45	3700-5500 (Dziewonski and Anderson, 1981)	kg/m^3
Thermal Expansion	α	3.54 x 10^{-4}	0.4-4.0x10^{-5} (Chopelas and Boehler, 1992; Chopelas, 2000)	°C^{-1}
Thermal Diffusivity	κ	1.04x10^{-7}	1x10^{-6} (Turcotte and Schubert, 2002)	m^2/s
Thermal Conductivity	k	0.340	8.4±1.2 (Manthilake et al., 2011)	W/m°C
Specific heat Capacity	C_p	2.28x10^3	914 (Turcotte and Schubert, 2002)	J/kg°C
Refractive index at 19.5°C	n	1.4991	-	-
Rayleigh number	Ra$_h$	10^4-10^7	10^6-10^8	-
Reynolds number	Re$_h$	10^{-4}-10^{-6}	10^{-20}	-
Prandtl number	Pr$_h$	10^4-10^5	10^{23}	-

Table 5.4: The comparison of the physical and calculated parameters for Liquidose 436 syrup and Earth's mantle. The Rayleigh number, Reynolds number and Prandtl number are calculated using the heater temperature.

5.4   Experiments undertaken

Numerous experiments were undertaken using shadowgraph visualisation. Two experiments were undertaken using unmixed Golden syrup. The remaining experiments were undertaken using either unmixed or well mixed Liquidose 436 syrup. The majority of experiments conducted at low and intermediate temperature differences (ΔTs). With seven undertaken at ΔT=4°C, two at ΔT=5°C at low ΔTs. A further ten were conducted between ΔT=6-8°C. In the intermediate ΔT region, eight experiment were undertaken between ΔT=10-17°C and three between ΔT=20-25°C. A further three experiments were undertaken at a high ΔTs greater than 40°C.

Nine SPIV experiments were undertaken during this research using Liquidose 436 syrup. Three experiments were undertaken at ΔT=5°C, four at ΔT=13.3°C and one at ΔT=21.0°C and ΔT=41.2°C.

5.4.1   Shadowgraph visualisation experiments

Each plume generation run began at t=0, when the fluid was at ambient temperature. Once the heater was activated, a thermal boundary layer grew and became unstable forming a thermal plume. A Nikon camera was connected to free automatic shooting software (DiyPhotoBits), enabling the shadowgraph photographs to be captured at 5-minute intervals for the experimental

run of 24 hours. The error in the automated shooting was ±1 minute, compared to the timescale of the experiments the error was considered unimportant.

Following previous work (Pears, 2010), Lyle's Golden syrup was originally utilised for the experimental programme. Unfortunately, due to an unforeseen change in light source, the dark orange colour of the syrup produced unclear shadowgraph images. Therefore, only Liquidose 436 syrup (pale yellow fluid) was used to complete the experiments with a temperature range between $\Delta T = 4°C$ and $51°C$.

All shadowgraph experiments conducted in the experimental programme for this thesis are listed in Table 5.5 and 5.6, including whether plume collapse was observed and whether the fluid was originally well mixed or unmixed. More details of the experiments can be found in Appendix B.

Experiment Number	Heater temperature (T_h)/ °C	Ambient Temperature (T_∞) /°C	ΔT/°C	Power/ W	Mixed/ Unmixed	Collapsed Yes/ No/ ?
1	27.6	19.6	8.0	16.05	Unmixed	No
2	77.0	19.7	57.3	16.05	Unmixed	No

Table 5.5: Shadowgraph Lyle's Golden syrup experiments

5.4.2 Shadowgraph image processing

The expected magnification from the tank to the shadowgraph image was calculated using the equation in Figure 3.3 to be 1.96. However, the processing of the images was undertaken with ImageJ (a java processing and analysis program Abramoff et al. (2004)) where the length and width of the tank in the image was set at 26.5cm. All the measurements of the dynamic thermal plume geometries were scaled accordingly to the size of the tank. The shadowgraph images were analysed quantitatively for the head and conduit widths and the plume ascent times. The measurements of the head and conduit diameters were used to characterise the sizes of the plumes.

The height of the plume was measured from the top of the plume head to the base of the tank in each photograph (l_p). The absolute velocity (U) was then calculated using Equation 5.5:

$$U = \frac{l_p}{t_p} \tag{5.5}$$

where t_p is the time difference from the first shadowgraph image to the image where measurement is occurring.

Experiment Number	T_h/ °C	T_∞ /°C	ΔT/°C	Power/ W	Mixed/ Unmixed	Collapsed Yes/ No/ ?
1	23.3	19.3	4.0	16.05	Unmixed	No
2	27.0	19.0	8.0	16.05	Unmixed	Yes
3	70.0	19.0	51.0	16.05	Unmixed	No
4	23.1	19.1	4.0	16.05	Unmixed	No
5	22.0	18.0	4.0	16.05	Unmixed	No
6	26.0	18.0	8.0	16.05	Unmixed	No
7	26.5	18.5	8.0	16.05	Unmixed	Yes
8	28.9	18.9	10.0	16.05	Unmixed	Yes
9	26.6	18.6	8.0	16.05	Unmixed	?
10	26.9	18.9	8.0	16.05	Unmixed	Yes
11	33.0	19.2	13.8	16.05	Unmixed	No
12	80.0	19.0	61.0	16.05	Unmixed	No
13	70.0	19.0	51.0	16.05	Unmixed	Yes
14	23.4	19.4	4.0	3.985	Unmixed	No
15	60.0	18.8	41.2	3.985	Unmixed	No
16	40.0	19.0	21.0	3.985	Unmixed	Yes
17	30.0	16.8	13.3	3.985	Unmixed	Yes
18	35.6	18.6	17.0	3.985	Unmixed	Yes
19	42.4	17.4	25.0	3.985	Unmixed	No
20	23.4	18.4	5.0	9.19	Unmixed	Yes
21	40.2	17.2	23.0	9.19	Unmixed	Yes
22	21.2	17.2	4.0	9.19	Unmixed	No
23	27.3	19.3	8.0	9.19	Unmixed	No
24	32.6	19.6	13.0	9.19	Unmixed	No
25	34.1	19.1	15.0	6.30	Mixed	No
26	32.6	19.6	13.0	6.30	Mixed	No
27	27.3	19.3	8.0	6.30	Mixed	No
28	21.7	17.7	4.0	6.30	Mixed	No
29	26.3	18.3	8.0	6.30	Mixed	No
30	25.6	18.6	7.0	6.30	Mixed	No
31	24.1	18.1	6.0	6.30	Mixed	No
32	25.0	20.0	5.0	6.30	Mixed	No
33	22.2	18.2	4.0	6.30	Mixed	No
34	28.5	18.4	10.1	9.19	Mixed	No

Table 5.6: Shadowgraph Liquidose 436 syrup experiments

5.5   SPIV visualisation experiments

For the experimental programme, only the central plane of the tank above the centre of the heater was imaged because the flow is largely axisymmetric and there is little out of plane flow. Additionally, 3D processing of data is computationally expensive and was deemed not necessary at this stage. The central plane allowed for an understanding of how the plume velocity vectors changed during the experiments. To configure an experiment, the ambient temperature of the syrup was measured using a K-type thermocouple and the heater set. During an experiment the heater was activated once the first epoch of data were recorded, capturing the tank prior to any

added heat in the system. Two experiments were conducted with a piece of cardboard shielding the side of the tank closest to the air-conditioning. This was undertaken to ascertain whether the laboratory air-conditioning had an effect on the plume forming asymmetrically. It was observed to have little effect and no further experiments were conducted with this configuration. The parameters used in each experiment are outlined in Table 5.7 and further descriptions are in Appendix B. The experiments were conducted using unmixed Liquidose 436 syrup as the dark colour of Golden syrup was not suitable for vector extraction in SPIVET.

Experiment Number	T_h /°C	T_∞/ °C	ΔT /°C	Power / W	Inter frame time (Δt)/ ms	Inter Epoch time /ms	Collapsed Yes/No/?
1	24.2	19.2	5.0	9.19	150,000	140,000	Yes
2	31.3	18.0	13.3	9.19	60,000	150,000	Yes
3	31.0	18.0	13.0	9.19	55,000	288,000	No
4	23.8	18.8	5.0	9.19	150,000	360,000	?
5	23.4	18.4	5.0	9.19	150,000	360,000	Yes
6	31.6	18.3	13.3	9.19	55,000	288,000	No
7	39.4	18.4	21.0	9.19	30,000	170,000	No
8	59.4	18.2	41.2	9.19	5,000	100,000	No
9	31.2	17.9	13.3	9.19	60,000	150,000	No

Table 5.7: SPIV experiments undertaken

A total of nine experiments were undertaken in unmixed Liquidose 436 syrup whilst varying the temperature difference, the inter-frame time and the run time of experiments. The time interval (inter-frame time, Δt) between the image frames in experiments was chosen to ensure the magnitude of the tracer particle motion is sufficient for reliable detection, but not so large that the particles begin to deform under the influence of the velocity gradient (Raffel et al., 2007). The Δt needed to be adequately long to determine displacement (Δx) between the images of the tracer particles with sufficient resolution. Alternatively, it was required to be sufficiently short to avoid any particles with an out-of-plane velocity component leaving the light sheet between subsequent illuminations (Raffel et al., 2007). The inter-frame time was the single most important adjustable variable in the SPIV system to enable the maximum and minimum velocities that are possible to be measured (Adrian, 1991).

The inter-frame time at two different temperature differences (5°C and 13°C) was investigated and the maximum velocity of the plume discovered. A linear relationship was expected for the Δt and found to be $\Delta t=1080(1/U)+15000$. This relationship was used for ascertaining the Δt of the remaining experiments using the highest velocity from the shadowgraph experiments. The linear relationship was expected because the ideal number of pixels that the cluster of particles should move between frames was chosen to be 5 so as to not leave the light sheet between subsequent

frames. Therefore, when the speed of the flow doubles the particles travel for half as long. Thus to obey the relationship of $\Delta t \propto \frac{1}{U}$ if the velocities doubled, Δt is halved. The original two experiments had Δt determined from taking multiple images of the tank with the heater on at different Δt's and observing when a chosen cluster had moved approximately five pixels between frames. It is important for this value to not be too small as this induces larger errors in the vectors extracted from the particle clusters. It was expected to be linear up to the experiment of $\Delta T = 21°C$ because of the intermediate temperature used. However, for the $\Delta T = 41.2°C$ plume the predicted Δt was deemed to be too large, based on the understanding of how quickly the plume reached the surface in the shadowgraph experiment. Therefore, judgement was used and the Δt value set very low at 5,000ms.

SPIVET-control was configured prior to an experiment with the amount of images to be collected (number of epochs), the inter-epoch time (time between epochs) and the inter-frame time (The SPIVET interface is shown in Appendix A Figure A.4). The camera and lightline stepped in sync for the duration of the investigation and captured the planes for all the epochs specified and terminated movement once the last epoch was captured. When the cameras and lightline completed a move, a photograph was captured of the illuminated plane and the process was repeated, Δt later. The exposure of the camera was configured depending on the length of time the shutter was required to be kept open. After testing different values, the exposure was set at 200,000 lux seconds.

Chapter 6

Experimental stall and collapse

6.1 Plume generation

Isolated plumes were generated from a point source heater, whose strength was constant with time. Once the heater was activated a thermal boundary layer developed surrounding the heater, which grew diffusively, eventually became unstable and produced a plume. At the ambient temperature of the fluid the Rayleigh number (Ra) was one order of magnitude higher than the critical Rayleigh number (Ra_c). Three different regimes were observed from the experiments. At low temperature differences (ΔT) the plumes stalled for a period before collapsing. Intermediate ΔT plumes collapsed after the formation of a "lens shape" was observed and high ΔT plumes ascended to the top of the tank.

6.2 Experimental Results

In all the experiments undertaken background convection was observed due to the low Ra_c, calculated to be 1700.33. This value was calculated based on the assumption that the properties of the tank were the same as the no-slip boundary critical Rayleigh number Equation 6.1 from Turcotte and Schubert (2002).

$$Ra_c = \frac{\pi^4(1 + l_c)^3}{l_c^2} \tag{6.1}$$

Therefore, 1°C above the ambient temperature of the fluid is an order of magnitude greater than the Ra_c.

6.2.1   Shadowgraph experimental results

The experiments conducted had Rayleigh numbers (calculated using heater temperature, Ra_h) between 10^4-10^7. From the numerous shadowgraph experiments undertaken three unmixed fluid experiments were chosen as the most representative of the three different phenomena observed: one experiment at low ΔT, one at medium ΔT and one at high ΔT (Table 6.1). The shadowgraph images selected from the experiments are at times when there was observed to be distinctive behaviour occurring in the plume.

$\mathbf{T}_h$ /°C	$\mathbf{T}_\infty$ /°C	$\mathbf{\Delta T}$ /°C	**Power /W**	$\mathbf{Ra}_h$	$\mathbf{Pr}_h$	η^*
23.4	18.4	5.0	9.19	8.64×10^4	3.47×10^5	1.58
30.1	18.6	13.3	3.98	4.17×10^5	1.91×10^5	3.36
42.4	17.4	25.0	3.98	2.34×10^6	6.33×10^4	9.49

Table 6.1: The selection of shadowgraph experiments conducted. The table shows show the different parameters and temperature of each investigation. Where $\eta^* = \frac{\eta_\infty}{\eta_h}$.

To compare experiments to each other, times, length scales and absolute velocity were rendered non-dimensional by choosing a time-scale, length and velocity appropriate for this dynamical regime. The diffusion time (Equation 6.2) was chosen for non-dimensionalising of the time of the plume experiments:

$$\tau_c \simeq \frac{l_c^2}{\kappa} \tag{6.2}$$

where τ_c is the characteristic diffusion time of the tank, calculated to be 6.75×10^5s and l_c is the characteristic length scale for the tank (0.265m), chosen because the whole study of collapse and survival of the plumes is inherently related to the height the plumes ascend to in the tank. The non-dimensional time was represented by τ_o.

All lengths measured in the tank, such as the plume height, conduit width and head width, were non-dimensionalised with the characteristic length l_c and represented as l_o, D_o and H_o respectively. The absolute velocity was rendered non-dimensional with Equation 5.5 using the the length scale of the tank and τ_c calculated as 3.92×10^{-7}m/s. The non-dimensional absolute velocity was represented by U_o.

The flow in the experiments was always time-dependent but the pattern of convection was dominated by long-lived asymmetric plumes in the low temperature difference experiments and axisymmetric plumes in the high temperature difference experiments. The upwelling, cylindrical plumes are the primary structure of the flow that was expected for a fluid with temperature-dependent viscosity, heated from below and convecting at high Ra numbers (White, 1988;

Davaille and Jaupart, 1993). The conduit tail remained attached to both the head and the base of the tank for the length of the experiment and was visible in all the experiments conducted.

6.2.1.1 ΔT=5°C plume experiment
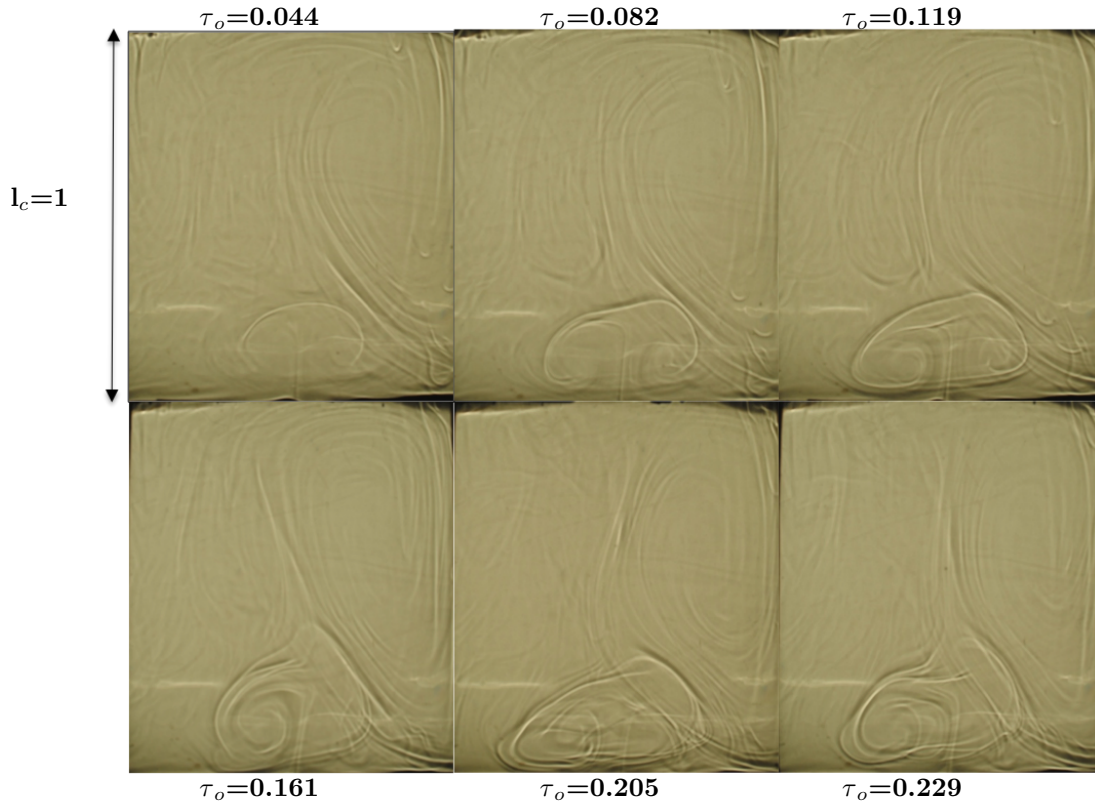
Figure 6.1: Six shadowgraph images at τ_o=0.044, 0.082, 0.119, 0.161, 0.205 and 0.229 after the beginning of the ΔT=5°C unmixed Liquidose 436 syrup experiment. The images were chosen based on distinctive changes in the plume. Note the inability of the plume to rise out of the lower quarter of the tank.

The ΔT=5°C experiment had a heater temperature of 23.4°C and ambient temperature of 18.4°C. The viscosities at these temperatures were 51.80Pas and 81.81Pas respectively, where the η^* was 1.58. Figure 6.1 shows that the plume evolved with the typical plume shape while strong background convection was occurring in the tank. The plume does not grow before τ_o=0.004 (Figure 6.2) because of thermal boundary layer (TBL) building, which occurred slowly because of the low ΔT. After this, the plume ascended steadily to l_o=0.245 height by τ_o=0.030. For a further τ_o=0.06, the plume remained stalled in the lower quarter of tank with the l_o increasing by 0.015. Between τ_o=0.044 and 0.082 the plume head width was growing in size but the height appeared constant. The plume height decreased between τ_o= 0.09-0.122 by 16.2% before increasing by l_o=0.13 at τ_o=0.161 because the plume was swept up in the background convection. After τ_o=0.164 the plume began to collapse back to the base of the tank despite the ever present heat source. However, the plume began to rise again at τ_o=0.229 as the plume head was observed to be a greater distance from the base of the tank. The head width was not observed before τ_o=0.008, because the head takes time to form. By τ_o=0.08 the head of the

plume had grown laterally to H_o=0.45 instead of ascending in the tank and increasing in length. After τ_o=0.08 the plume head width grew steadily to a peak of H_o=0.51, until τ_o=0.134 when it decreased by 13.5% for a period of τ_o=0.019. The head width increased to a maximum of H_o=0.556 while the plume collapsed towards the base of the tank. It was difficult to measure the conduit width because the plume did not "lift-off" from the base of the tank; the head of the plume remained in the lower quarter of the tank.
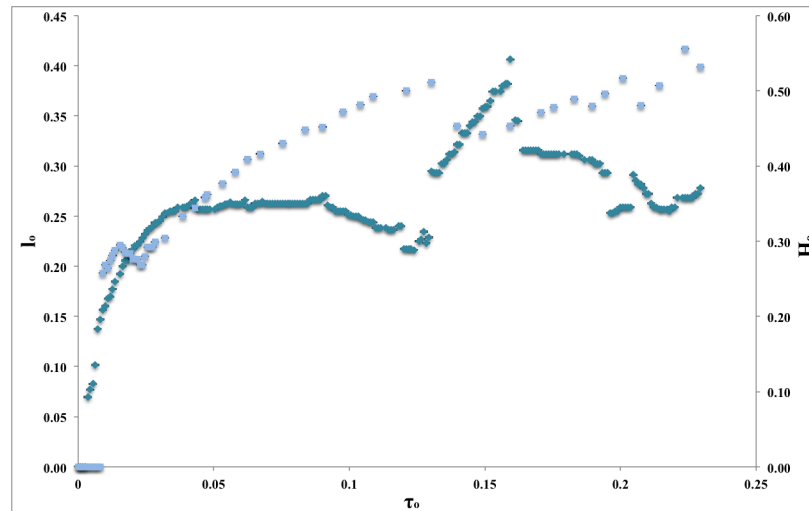
Figure 6.2: The non-dimensional height of the ΔT=5°C plume ($l_o=\frac{l_p}{l_c}$, turquoise diamonds) and the non-dimensional head width ($H_o=\frac{H_p}{l_c}$, pale blue squares) as a function of non-dimensional time ($\tau_o=\frac{t_p}{\tau_c}$), where the error bars are 5×10^{-4}m averaged from multiple measurements of the same dimension in ImageJ. The plume height was measured from the top of the plume head to the base of the tank and the head width from the outer most edges of the head.
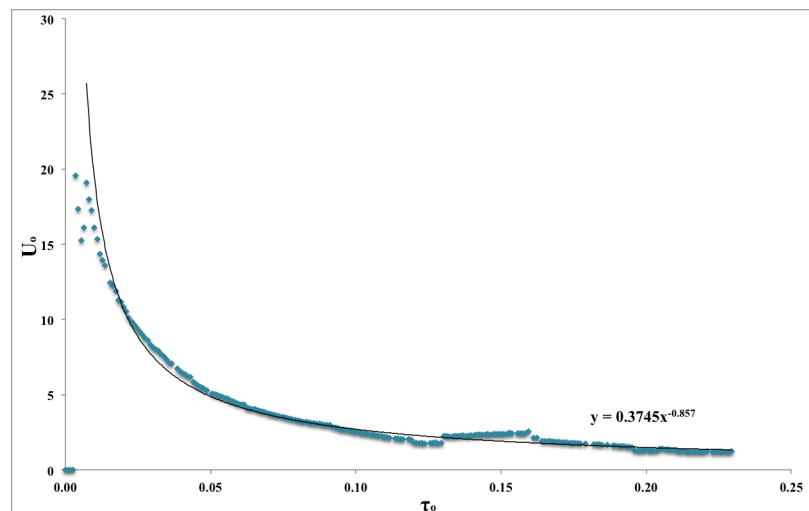
Figure 6.3: The non-dimensional absolute velocity ($U_o=\frac{U_p}{U_c}$) of the top of the head of the ΔT=5°C plume ascending in the tank as a function of non-dimensional time. The power-law fit of the line is $U_o=0.3745\tau_o^{-0.857}$.

Figure 6.3 presents the absolute velocity of the ΔT=5°C plume, which increased to a maximum U_o=19.54 at τ_o=0.003, before decreasing by the power-law $U_o=0.3745\tau_o^{-0.857}$ to U_o=1.19 at the termination of the experiment. The absolute velocity reaches a peak τ_o=0.026 earlier than the plume ceases growing in the tank. There is a small rise in absolute velocity at τ_o=0.134-0.164, when a portion of the plume head was swept upwards by the background convection.

6.2.1.2 $\Delta T = 13.3°C$ plume experiment
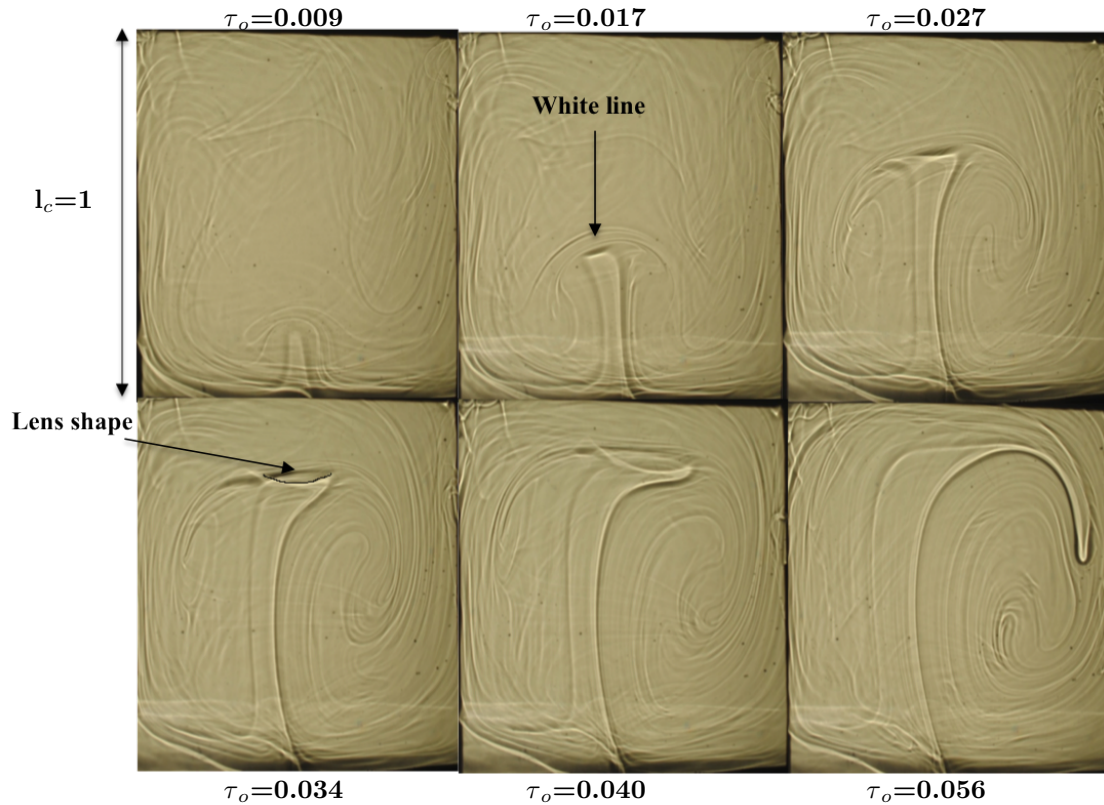
Figure 6.4: Six shadowgraph images at τ_o 0.009, 0.017, 0.027, 0.034, 0.040 and 0.056 after the beginning of the $\Delta T = 13.3°C$ experiment. The plume develops a white line at $\tau_o = 0.017$ which develops into a "lens shape" which grows as the plume ascends further in the tank. Shadowgraph images were chosen based on the distinctive changes in the behaviour of the plume during ascent.

The unmixed syrup $\Delta T = 13.3°C$ plume experiment was conducted at ambient temperature 18.6°C and background convection was very strong in the tank during the experiment (Figure 6.4). The heater temperature was 30.1°C with a viscosity of 28.18Pas at this temperature. The η^* of the experimental fluid was 3.36. At $\tau_o = 0.009$ the plume had a defined conduit and a less well defined head. The conduit remained well defined at $\tau_o = 0.017$ however, a bright white line began to form at the top of the conduit. This later formed a "lens shape" and material was observed flowing down the centre of the plume conduit and the plume was collapsing. The sides of the plume continue to ascend whilst the central part of the conduit remained stationary in height in the tank during the collapse, when material was flowing down the central conduit. The material that continued to ascend at the sides of the plume was purely due to the buoyancy from the heater. Figure 6.5 presents the plume height up to the point when the "lens shape" was observed. After this point the definition of rise was no longer relevant, because material began to descend to the base of the tank. The plume grew linearly after $\tau_o = 0.001$ after TBL building. The plume reached a maximum $l_o = 0.609$, when the measuring ceased due to the "lens shape" growth. Whilst the plume height grew linearly, the conduit width additionally increased until $\tau_o = 0.017$ when it reached a maximum of $D_o = 0.165$ and then decreased to $D_o = 0.113$ by the end of the measuring.
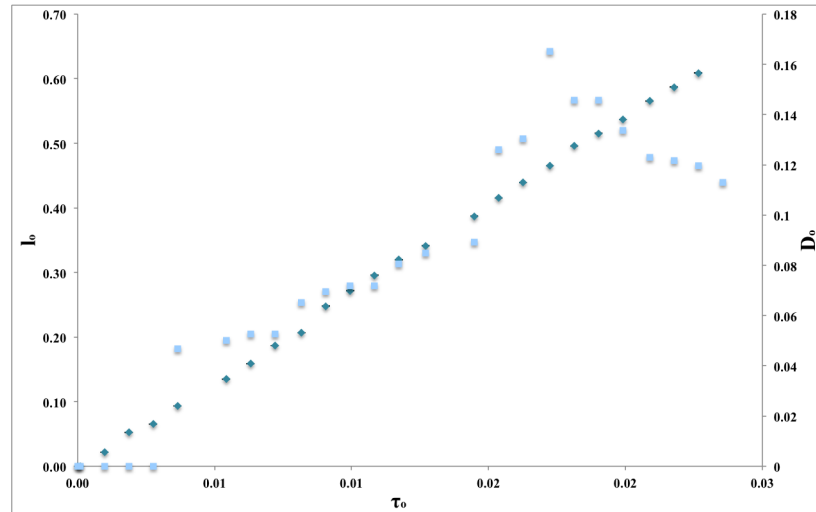
Figure 6.5: The non-dimensional height of the $\Delta T=13.3°C$ plume (l_o, turquoise diamonds) and the non-dimensional conduit width (D_o, pale blue squares) as a function of non-dimensional time, where the error bars are 5×10^{-4}m averaged from multiple measurements of the same dimension in ImageJ. The plume height was measured from the top of the plume head to the base of the tank and the conduit width from the outer most edges of the conduit. Note measuring ceased once the "lens shape" was observed (Discussed in the text) as the definitions of rise was no longer relevant.

The absolute velocity of the plume was fairly constant at $U_o=26.0$ up to the period when the "lens shape" was observed (Figure 6.6). There was no distinctive peak in the absolute velocity as observed in Figure 6.3 and U_o is 20.0 larger than the $\Delta T=5°C$ plume absolute velocity for the majority of the experiments.
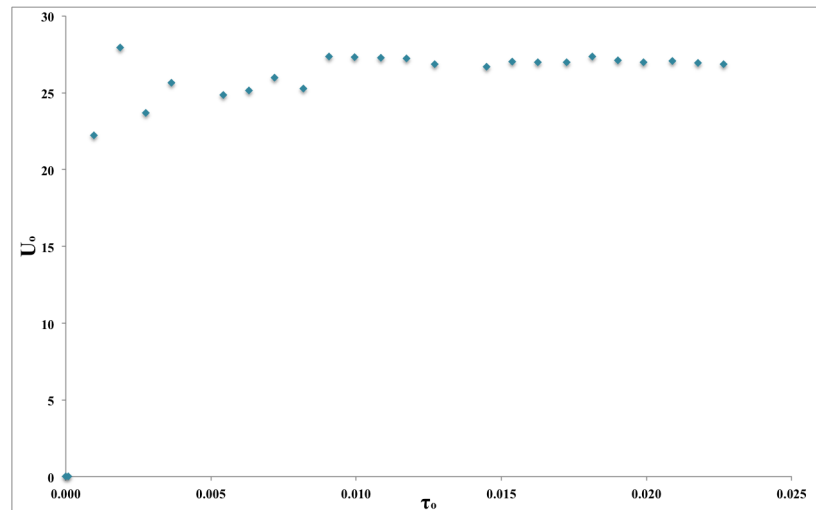
Figure 6.6: The non-dimensional absolute velocity of the top of the head of the plume for the $\Delta T=13.3°C$ experiment as a function of non-dimensional time.

6.2.1.3 ΔT=25°C plume experiment
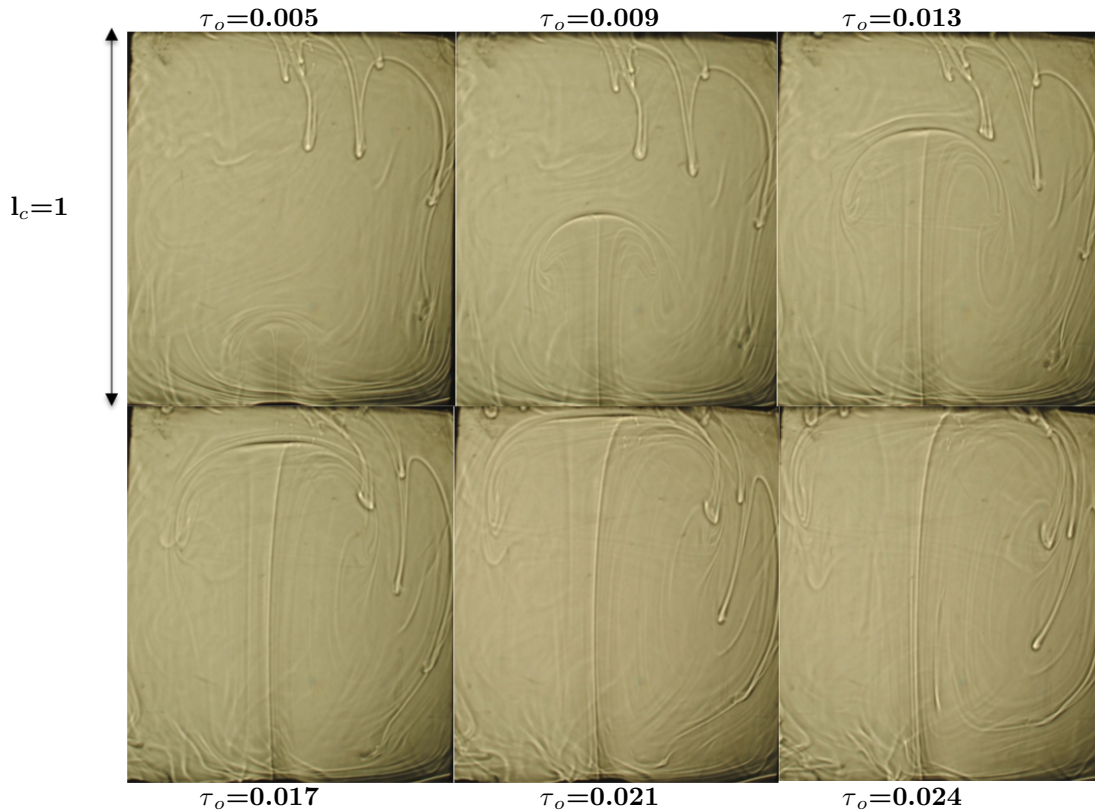
Figure 6.7: Six shadowgraph images at τ_o 0.005, 0.009, 0.013, 0.017, 0.021 and 0.024 after the beginning of the ΔT=25°C experiment. The plume ascended to the top of the tank. Shadowgraph images were chosen based on the distinctive changes in the behaviour of the plume during ascent.

The ΔT=25°C plume experiment had a heater temperature of 42.4°C and the ambient temperature of the syrup was recorded at 17.4°C. The respective viscosities of the fluid were 9.44Pas and 89.66Pas for those temperatures, with an η^* of 9.49. During the experiment, the plume ascended to the top of the tank as shown in Figure 6.7. Figure 6.8 shows the detailed growth of the plume in the tank. The plume began to grow after the first τ_o=3x10^{-4} and reached the top of the tank by τ_o=0.021. Once the plume was at the surface the plume head width continued to increase and filled the tank laterally by τ_o=0.034. The plume conduit width in this experiment is observed to be thinner than the conduit width in the ΔT=13.3°C plume.

The absolute velocity of the ΔT=25°C plume reached a peak at τ_o=0.012 (Figure 6.9). At the beginning of the experiment the absolute velocity decreased slightly, but began to rise at τ_o=0.006. The plume absolute velocity began to decrease again at τ_o=0.011, when the plume started to feel the top of the tank and continued to decrease when the plume was at the surface, with the power-law U$_o$= 1.2693$\tau_o$$^{-0.916}$ from U$_o$=58.71 to U$_o$=10.75 by the end of the experiment.

Figure 6.8: The non-dimensional height of the $\Delta T = 25°C$ plume (l_o, turquoise diamonds) and the non-dimensional conduit width (H_o, pale blue squares) as a function of non-dimensional time, where the error bars are 5×10^{-4}m. The plume height was measured from the top of the plume head to the base of the tank and the head width from the outer most edges of the head.

Figure 6.9: The non-dimensional absolute velocity of the top of the head of the plume for the $\Delta T = 25°C$ experiment as a function of non-dimensional time. The absolute velocity declines with the power-law $U_o = 1.2693\tau_o^{-0.916}$.

6.2.2   Classifying Collapse

Utilising the ability of ImageJ to convert photographs into videos it was possible to move slowly between images and understand the evolution of the plume. The behaviour from the experiments presented has been classified into three regimes based on detailed observations of the experiments after each run and the previous observations in Pears (2010). The three regimes are surviving, "lenticular" collapse and "stalled" collapse. Collapse was observed when the plume was decreasing in height in the tank or material was flowing down the conduit from the plume head.

The first type of collapse observed in the Liquidose 436 syrup occurred at very low temperature differences. The plume grew in the lower quarter or third of the tank but then stalled for a

period of time before collapsing back to the base of the tank. This collapse displayed some similar behaviour to the low temperature difference plume observed in Pears (2010) as shown in Figure 1.11 and was named "stalled" collapse.

The second type of collapse observed involved the plume ascending to between half to two thirds of the way up the tank before a full "lens shape" was observed in the plume. This "lens shape" slowly grew in width and material was observed to flow down the centre of the conduit and was named "lenticular" collapse. This collapse was unexpected as buoyant material was still rising up the conduit. This type of collapse was also observed in Pears (2010) as shown in Figure 1.10 and the material flowing down the centre was similar to observations in the work of Newsome (2011) shown in Figure 1.9.

6.2.3 Comparison of previous shadowgraph experiments

Parameter	Liquidose 436 syrup	Golden syrup	Units
η at 20°C	70.67	87.15	Pa s
ρ at 20°C	1439.80	1443.02	kg/m^3
α	3.54x10^{-4}	6.00x10^{-4}	°C^{-1}
κ	1.04x10^{-7}	1.23x10^{-7}	m^2/s
k	0.34	0.356	W/m°C
C_p	2280	2020	J/kg°C
Ra$_h$	10^4-10^6	10^4-10^6	-
Ra$_c$	1700.33	1700.33	-
Pr$_h$	10^3-10^5	10^4-10^5	-

Table 6.2: Material and calculated properties for Liquidose 436 syrup and Golden syrup. The functional forms of the viscosity, density and thermal expansion are discussed in the text.

(a) The viscosity of the syrups with error bars, 0.5% of the absolute value

(b) Density of the syrup where the error bars are ±1 kg/m^{-3}

Figure 6.10: The fits of the measured viscosity and density of the two syrups- Liquidose 436 syrup (turquoise) and Golden syrup (purple)

The previous experimental data from Pears (2010) using unmixed Lyle's Golden syrup were compared with the unmixed Liquidose 436 syrup experimental results. The Rayleigh and Prandtl

numbers presented are for the experimental range undertaken using the syrup type (Table 6.2). The comparison of the viscosity and density for the two syrups is presented in Figure 6.54. The Golden syrup experimental lengths, times and velocities were rendered non-dimensional in the same method as for the Liquidose 436 syrup, where the τ_c=5.76x10^{5}s and U$_c$=4.60x10^{-7}m/s.

6.2.3.1   "Stalled" collapse shadowgraph visualisation comparison

The "stalled" collapse phenomena was observed in both the Liquidose 436 syrup and Golden syrup fluid at small temperature differences. These plumes have different Ra$_h$ numbers, viscosities, densities and differing ambient temperature of the fluid (Table 6.3).

Parameter	Liquidose 436 syrup	Golden syrup	Units
T$_h$	23.4	25.0	°C
T$_\infty$	18.4	22.0	°C
ΔT	5.0	3.0	°C
η_h	51.80	41.71	Pa s
η^*	1.58	1.55	-
ρ_h	1438.08	1438.55	kg/m^3
Ra$_h$	8.64x10^4	9.25x10^4	-
Pr$_h$	3.47x10^5	2.37x10^5	-

Table 6.3: Comparison of parameters for "stalled" collapse experiments for the two differing syrups.

Figure 6.11: A comparison plot of the non-dimensional height as a function of non-dimensional time for the ΔT=5°C Liquidose 436 syrup (turquoise diamonds) and the ΔT=3°C Golden syrup (purple squares) plumes.

The Golden syrup and Liquidose 436 syrup plumes did not ascend to the top of the tank and, instead, stalling was observed in both plumes in the lower quarter to third of the tank (Figure 6.13). In both experiments there was strong background convection. Despite the similar collapse phenomenon the shape of the plumes differed. The Golden Syrup plume (Figure 6.13b) had a lower temperature difference and therefore, does not have the expected shape of a thin conduit with a mushroom shaped head. In fact, the ΔT=3°C plume had no distinctive conduit

and was observed to have the shape of a mountain with some discernible structure inside the plume. At τ_o=0.023 the top of the plume had a clear divide between the two sides of the plume and, over time, this plume collapsed back to the base of the tank. However, the ΔT=5°C (Figure 6.13a) Liquidose 436 syrup plume exhibited the expected shape and there was no observed splitting at the top of the plume. The ΔT=5°C plume did, however, collapse in a similar fashion to the base of the tank by the end of the experiment. The "stalled" collapse occurred τ_o=0.243 earlier in the Golden syrup than in the Liquidose 436 syrup (Figure 6.11). A final difference observed between the two experiments was that the Golden syrup plume was axisymmetric, while the Liquidose 436 syrup plume was asymmetric.

Figure 6.11 shows that the height reached by the two plumes was significantly different but that they both rose in the tank before collapsing back towards the base. The experiment for the Golden syrup plume was τ_o=0.208 shorter than the Liquidose 436 syrup experiment because the plume collapsed earlier. Therefore, the stagnation, growth and then collapse that occurs in the ΔT=5°C experiment was not observed in the ΔT=3°C experiment. Both plumes had the same growth in height until τ_o=0.016. However, after this time the Liquidose 436 syrup plume continued to grow and the Golden syrup plume collapsed τ_o=0.148 earlier than the Liquidose 436 syrup plume. In Figure 6.12 the absolute velocity in both plumes began to decrease at τ_o=0.0074. However, the absolute velocity of the Golden syrup plume decreased almost linearly with a steeper gradient than the power-law decrease of the Liquidose 436 syrup plume and therefore, reached the minimum absolute velocity of U_o=2.55 about τ_o=0.208 earlier than the Liquidose 436 syrup plume.

Figure 6.12: A comparison plot of the non-dimensional absolute velocity as a function of non-dimensional time for the ΔT=5°C Liquidose 436 syrup (turquoise) and the ΔT=3°C Golden syrup (purple) plumes.

(a) Liquidose 436 syrup $\Delta T = 5°C$ shadowgraph experiment with images chosen to display distinctive changes in behaviour. The non-dimensional times are $\tau_o = 0.044$, 0.082, 0.119, 0.161, 0.205 and 0.229 from the beginning of the experiment.

(b) Golden syrup $\Delta T = 3°C$ shadowgraph experiment with images chosen to displays changes in the plume behaviour to reflect the collapse phenomenon. The non-dimensional times of the images are $\tau_o = 0.007$, 0.014, 0.023, 0.026, 0.029 and 0.039 from when the heater was activated.

Figure 6.13: "Stalled" collapse comparison plumes. The unmixed Golden syrup plume collapses earlier than the unmixed Liquidose 436 syrup plume and does not display the typical plume shape.

6.2.3.2 "Lenticular" collapse shadowgraph plumes comparison

The plumes which showed the "lenticular" collapse phenomenon have similar heater temperature (T_h) but differing temperature differences (Table 6.4) because the ambient temperature of the Golden syrup was 6.2°C higher than the Liquidose 436 syrup. Despite this differing temperature difference and the viscosity contrast (η^*), the plumes have similar Ra_h numbers.

Parameter	Liquidose 436 syrup	Golden syrup	Units
T_h	30.1	30.0	°C
T_∞	16.8	23.0	°C
ΔT	13.3	7.0	°C
η_h	28.44	20.62	Pa s
η^*	3.39	2.71	-
ρ_h	1434.70	1434.07	kg/m^3
Ra_h	4.17×10^5	4.35×10^5	-
Pr_h	1.91×10^5	1.17×10^5	-

Table 6.4: Comparison of measured and calculated material parameters for the "lenticular" collapse experiments in the two different syrups

The main difference between the growth of the two plumes is that the $\Delta T=13.3$°C plume ascended with linear growth and reached a maximum height of $l_o=0.596$ (Figure 6.14), whereas the $\Delta T=7$°C plume rose with non-linear growth and reached a maximum height of $l_o=0.794$ and subsequently collapsed.

Figure 6.14: A comparison plot of the non-dimensional plume height measured from the top of the plume head for the $\Delta T=13.3$°C Liquidose 436 syrup (turquoise diamonds) and the $\Delta T=7$°C Golden syrup (purple squares) plumes as a function of non-dimensional time.

Figure 6.15 compares the $\Delta T=13.3$°C Liquidose 436 syrup and $\Delta T=7$°C Golden syrup experiments, which both display the same "lenticular" collapse phenomena. A similar white line was observed in both plumes at the top of the conduit prior to plume collapse. The head of the $\Delta T=7$°C plume was observed to have a heart shape during the collapse, similar to collapse observed by Newsome (2011).

(a) Liquidose 436 syrup $\Delta T=13.3°C$ shadowgraph images chosen at non-dimensional time τ_o=0.009, 0.017, 0.027, 0.034, 0.040 and 0.056 after heater activation. The images were chosen based on the changes in behaviour of the plume and the developing collapse phenomenon.

(b) Golden syrup $\Delta T=7°C$ shadowgraph experiment with images chosen at non-dimensional time τ_o=0.016, 0.026, 0.029, 0.035, 0.041 and 0.047. These images were chosen based on the development of the "lens shape" and the subsequent collapse.

Figure 6.15: "Lenticular" collapse comparison plumes. Both plumes developed the same lens shape, although the unmixed Golden syrup plume showed more distinctive signs of collapse. The "lens shape" began to develop earlier in the unmixed Liquidose 436 syrup plume with a white line, than the unmixed Golden syrup plume.

In Figure 6.15b ($\Delta T=7°C$) the conduit is distinctive in the tank and the plume head is less well defined. This is similar to the Liquidose 436 syrup plume (Figure 6.15a). The Golden syrup plume rose quicker in the tank and collapsed earlier. This follows the findings of the Golden syrup "stalled" collapse experiment.

Figure 6.16: A comparison plot of the non-dimensional absolute height for the $\Delta T=13.3°C$ Liquidose 436 syrup (turquoise diamonds) and the $\Delta T=7°C$ Golden syrup (purple squares) plumes as a function of non-dimensional time.

The absolute velocities of the two plumes differed significantly (Figure 6.16). The $\Delta T=7°C$ Golden syrup plume shows the beginning of exponential decay (when the measuring ceased) like the other plume experiments conducted. However, the $\Delta T=13.3°C$ plume maintained an almost constant $U_o=26.0$ up to when the "lens shape" appeared. The absolute velocities of both plumes were within the same order of magnitude. The $\Delta T=7°C$ plume had a maximum absolute velocity $U_o=51.64$ at $\tau_o=0.013$ and at this time the $\Delta T=13.3°C$ plume had a maximum absolute velocity of $U_o=26.86$. However, by the time the measuring of the plumes ceased they had similar absolute velocities.

6.2.3.3 Surviving shadowgraph plume comparison

Parameter	Liquidose 436 syrup	Golden syrup	Units
T_h	42.4	40.0	°C
T_∞	17.4	22.0	°C
ΔT	25.0	18.0	°C
η_h	9.44	6.28	Pa s
η^*	9.49	10.30	-
ρ_h	1428.49	1425.13	kg/m^3
Ra_h	2.34×10^6	3.65×10^5	-
Pr_h	6.33×10^4	3.57×10^4	-

Table 6.5: Comparison of measured and calculated properties of the Liquidose 436 syrup and Golden syrup surviving plumes. The Rayleigh numbers are one order of magnitude different due to the difference in ΔT.

Surviving plumes (those that ascended to the surface) were observed at high ΔTs in both the Golden syrup and Liquidose 436 syrup. Despite the $\Delta T=7$°C difference, different magnitude of Ra_h numbers and ambient temperatures of the fluid (Table 6.5), the plumes showed similar evolution in the tank, were axisymmetric and ascended to the surface as expected (Figure 6.17).

Figure 6.17: A plot comparing the non-dimensional height of the Liquidose 436 syrup $\Delta T=25$°C plume (turquoise diamonds) and the Golden syrup $\Delta T=18$°C plume (purple squares) as a function of non-dimensional time.

Figure 6.18 displays that the the Golden syrup plume rose dramatically in the first $\tau_o=0.016$ before reaching the surface of the tank, whereas the Liquidose 436 syrup plume required an additional $\tau_o=0.007$. The plumes were both axisymmetric. Figure 6.19 demonstrates that the absolute velocity of the Golden syrup plume during the rising stage was $U_o\approx45.04$ higher than the Liquidose 436 syrup plume. The peak of the velocities occurred $\tau_o=5\times10^{-3}$ earlier in the $\Delta T=18$°C, which related to the differing times the plumes ascended to the surface. The velocities decreased once at the surface with the $\Delta T=18$°C plume absolute velocity decreasing exponentially ($U_o=136.03e^{-47.85\tau_o}$), whereas the $\Delta T=25$°C plume absolute velocity decreased with a power-law ($U_o=1.2693\tau_o^{-0.916}$).

(a) Liquidose 436 syrup ΔT=25°C shadowgraph experiment with images chosen at non-dimensional time τ_o=0.005, 0.009, 0.013, 0.017, 0.021 and 0.024 after the heater activation experiment.

(b) Golden syrup ΔT=18°C shadowgraph experiment with images chosen at non-dimensional time τ_o=0.002, 0.005, 0.006, 0.008. 0.026 and 0.033 after the heater activation.

Figure 6.18: Comparison of Surviving plumes. Both plumes ascended to the surface of the tank. The Golden syrup plume rose to the top of the tank earlier than the Liquidose 436 syrup plume.

Figure 6.19: A plot comparing non-dimensional absolute velocity (U_o) of the Liquidose 436 syrup $\Delta T=25°C$ plume (turquoise diamonds) and the Golden syrup $\Delta T=18°C$ plume (purple squares) as a function of non-dimensional time. The lines of fit of the decreasing absolute velocities are shown on the graph.

6.2.4   Comparison between well mixed and unmixed syrup plumes

When the Liquidose 436 syrup was well mixed the experiments conducted behaved differently to the unmixed experiments. The well mixed syrup experiments were undertaken at the same temperature differences as for the unmixed experiments, enabling a comparison of the behaviour of the plumes. In well mixed syrup it was observed that the plumes were much fainter, and that collapse was absent. One temperature difference was chosen to represent how the plumes differed in the mixed and unmixed syrup.

6.2.4.1 $\Delta T=5°C$ plumes mixed and unmixed syrup results

Parameter	Unmixed syrup experiments	Well mixed syrup experiment	Units
T_h	23.4	25.0	°C
T_∞	18.4	20.0	°C
ΔT	5.0	5.0	°C
η_h	51.80	44.77	Pas
η_∞	81.81	70.67	Pas
η^*	1.58	1.58	-
ρ_h	1438.08	1437.27	kg/m^3
Ra_h	8.64×10^4	9.99×10^4	-
Pr_h	3.47×10^5	3.00×10^5	-

Table 6.6: Measured material and calculated properties of the unmixed and well mixed experiments at $\Delta T=5°C$.

Table 6.6 shows the plumes had the same η^* but different viscosities related to the heater temperature and the ambient temperature of the fluid.

(a) Unmixed syrup shadowgraph images chosen at non-dimensional times τ_o 0.044, 0.082, 0.119, 0.161, 0.205 and 0.229 from the beginning of the experiment.

(b) Well mixed syrup shadowgraph images chosen at non-dimensional times τ_o 0.023, 0.030, 0.037, 0.045, 0.056 and 0.068 from the beginning of the experiment.

Figure 6.20: A visual comparison of the shadowgraph images for the ΔT=5°C Liquidose 436 syrup plumes. The well mixed syrup plume is very faint throughout the experiment but ascended to the surface, whereas the unmixed syrup plume is distinctive; stalling and then collapsing in the tank.

Figure 6.21: Comparison of the unmixed (turquoise diamonds) and well mixed syrup (dark blue triangles) plumes at $\Delta T=5°C$ l_o as a function of τ_o. The well mixed syrup plume ascended to the surface, whereas the unmixed syrup plume stalled and then collapsed.

In the unmixed syrup (Figure 6.20a) the plume was distinctive and background convection was readily observed. However, in the well mixed fluid experiment (Figure 6.20b) the plume was so faint that the appearance was not detected until $\tau_o=0.022$, when the plume was $l_o=0.615$ high. The background flow was also generally fainter, except for one line of distinctive background circulation in the centre of the tank, which migrated upwards for a period before the plume was detectable. In contrast in the unmixed fluid, the plume was measurable once it formed from the TBL, growing, stalling and then collapsing. The height that the plumes ascended to in the tank differed by $l_o=0.594$ as shown in Figure 6.21, as the well mixed fluid plume ascended to the surface and the experiment terminated shortly after.

Figure 6.22: Comparison of the H_o with for the unmixed (turquoise diamonds) and well mixed (dark blue triangles) syrup plumes $\Delta T=5°C$ as a function of τ_o. Error bars are 5×10^{-4}m. The well mixed syrup plume head spread to fill the tank laterally once the plume reached the surface.

Figure 6.22 shows that once the well mixed plume reached the surface the plume head spread laterally, filling the tank. In contrast, the unmixed syrup plume head width exhibited irregular behaviour, as width increased to $H_o=0.511$ at $\tau_o=0.13$, then decreased to $H_o=0.442$ at $\tau=0.019$,

before the width expanded again to a maximum H_o=0.556. The non-dimensional absolute velocities of the two plumes differed by U_o=20.0 at τ_o=0.022 (Figure 6.23) and decreased after this time. The absolute velocity of the well mixed syrup plume decreased more steeply and was U_o=7.0 higher than the unmixed plume absolute velocity at the end of the experiment.

Figure 6.23: Comparison of the U_o as a function of τ_o for the ΔT=5°C unmixed (turquoise diamonds) and well mixed (dark blue triangles) syrup plumes.

6.3 SPIV Experimental results

T_h /°C	T_∞ /°C	ΔT /°C	Power /W	Ra	Pr	η^*
24.2	19.2	5.0	9.19	9.29×10^4	3.23×10^5	1.58
31.3	18.0	13.3	9.19	4.68×10^5	1.70×10^5	3.36
39.4	18.4	21.0	9.19	1.51×10^6	8.23×10^4	6.66
59.4	18.2	41.2	9.19	1.49×10^7	1.62×10^4	34.54

Table 6.7: The measured and calculated properties of the selection of SPIV experiments.

The SPIV plume experiments were conducted in unmixed Liquidose 436 syrup with temperatures selected based on the three regimes observed in the shadowgraph results. Experiments were conducted at ΔT=5°C for the "stalled" collapse regime, ΔT=13.3°C and ΔT=21°C for the "lenticular" collapse regime and ΔT=41.2°C for the surviving plume regime. From the SPIV experiments conducted a selection of four were chosen (one at each temperature) and the experimental parameters listed in Table 6.7. The vorticity of the fluid motion in the plumes was determined from the PIV velocity vectors using Equation 6.3:

$$\omega = curl\mathbf{U} \tag{6.3}$$
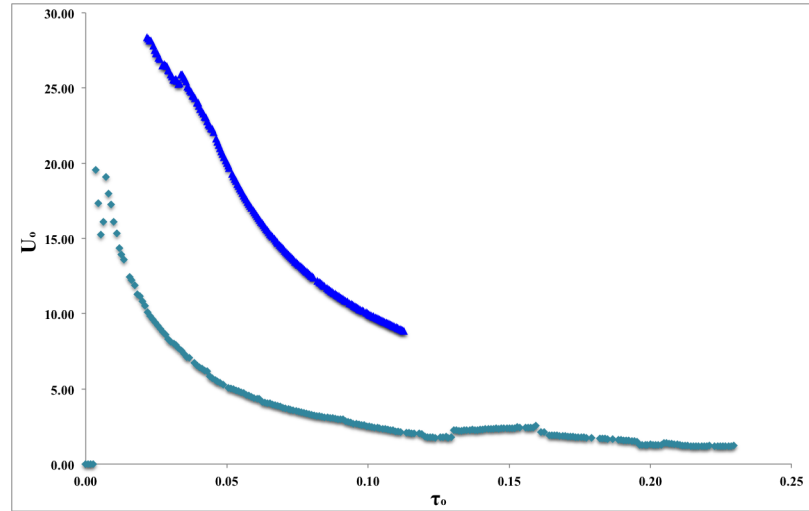
where ω is the vorticity of the fluid and U is the velocity determined through the processing from the tracer particles. After processing, the results were visualised in Paraview (an open source

application for interactive, scientific visualisation (Henderson et al., 2004)), with the velocities chosen at $\pm$ the same value for ease of understanding.

6.3.1   SPIV ΔT=5°C plume
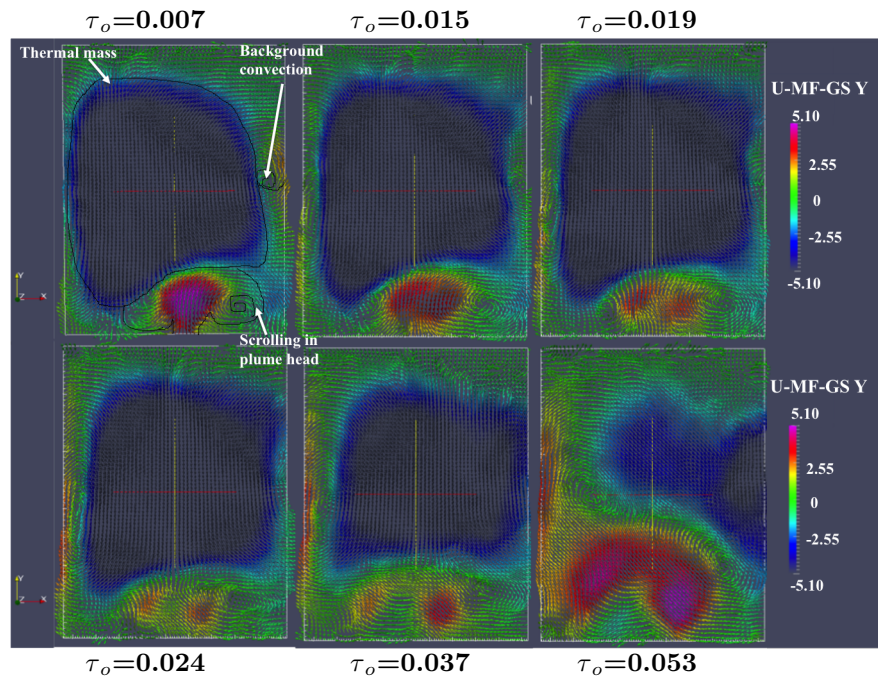
Figure 6.24:   The non-dimensional velocity vectors (U_o) for the ΔT=5°C SPIV plume with non-dimensional time. The images were chosen based on distinctive changes in the plume at τ_o= 0.007, 0.015, 0.019, 0.024, 0.037 and 0.053 from the beginning of the experiment. Labels are added to the images to highlight important features in the flow. The velocity vectors point in the direction of flow, with a large downward flowing low velocity mass in the centre of the image.

The ΔT=5°C plume was unable to ascend to the top of the tank (Figure 6.24). A large thermal mass with downward low velocity (U_o=-5.10), which hindered the plumes growth, was observed in the centre of the tank. This mass remained present throughout the experiment. The plume was asymmetric because of the background flow and the low velocity thermal mass, which differed from other plume experiments where the plumes are axisymmetric in isothermal environments (Kaminski and Jaupart, 2003). From Figure 6.24 it is possible to observe the central plume velocity changing strength during the experiment. Therefore, the evolution of the plume was divided up into three different regions.

In Figure 6.25 the maximum U_o varies during the experiment with three distinctive regions (time periods) determined. In region 1, the plume velocity increased by $U_{o\ max}$=2.55 from the beginning of the experiment, which relates to the plume ascending in the tank as shown in the first image in Figure 6.24. Region 2, began when the maximum velocity of the plume was decreasing from $U_{o\ max}$=6.26 to $U_{o\ max}$=3.10 by τ_o=0.024, as reflected in the images of τ_o=0.015 to τ_o=0.024. In Figure 6.26 the minimum velocity has been changed to positive. In region 1 the minimum velocity was increasing as the plume was ascending in the tank from $U_{o\ min}$=11.33 to $U_{o\ min}$=13.60. When the plume reached maximum velocity at τ_o=0.007 in
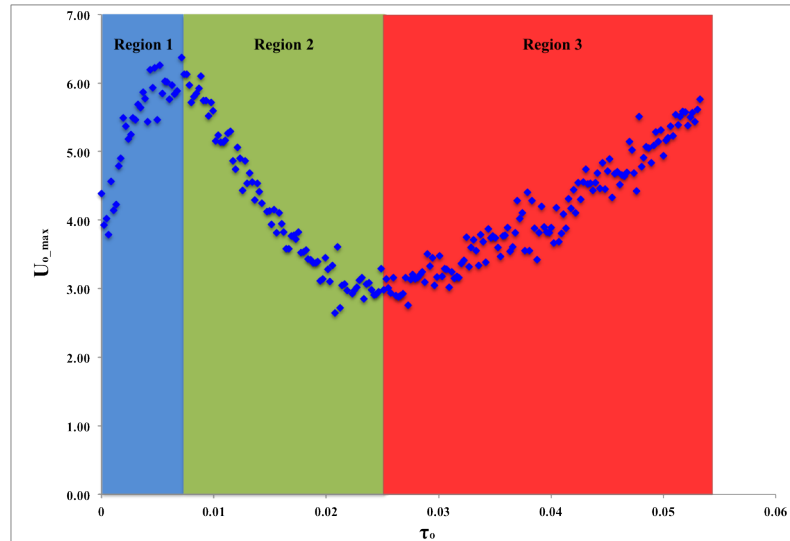
Figure 6.25: The maximum non-dimensional velocity of the $\Delta T=5°C$ plume as a function of non-dimensional time. The non-dimensional velocity is divided up into three distinctive regions which will be focused on further in the text.

Figure 6.25, the minimum velocity began to become more constant at $U_o=13.60$. However, at $\tau_o=0.016$ the minimum velocity of the plume began to decrease, which fits with the maximum velocity reaching $U_{o\ max}=3.10$ at $\tau_o=0.024$. Region 3 began when the minimum velocity was the same value as at the beginning of the experiment. It then decreased to $U_{o\ min}=6.22$ and then remained constant towards the end of the experiment. The maximum velocity began to increase again as shown in the last two images of Figure 6.24; the plume was once more ascending in the tank as shown by the low-velocity thermal mass decreasing in size and moving to the right hand side of the tank. The three regions displayed in Figure 6.25 and Figure 6.26 will be discussed in further detail below.
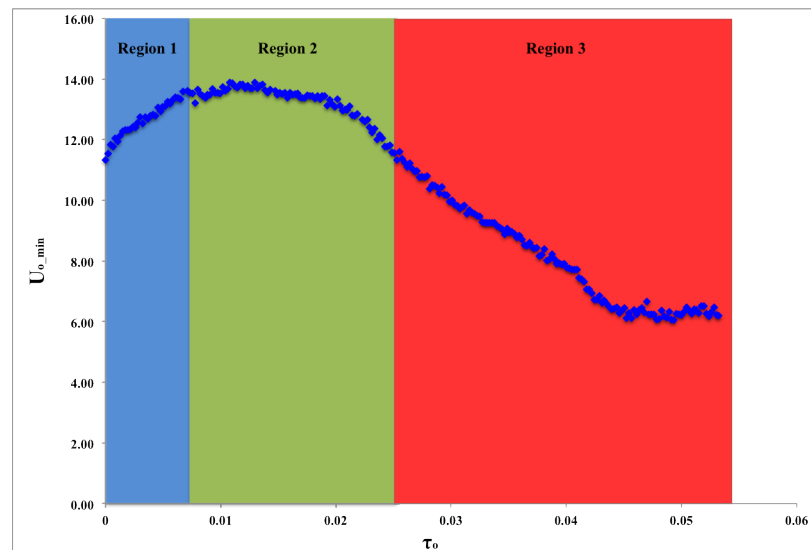
Figure 6.26: The minimum non-dimensional velocity of the $\Delta T=5°C$ plume as a function of non-dimensional time. The three regions are placed at the same non-dimensional times for comparison with Figure 6.25.

6.3.1.1   Region 1
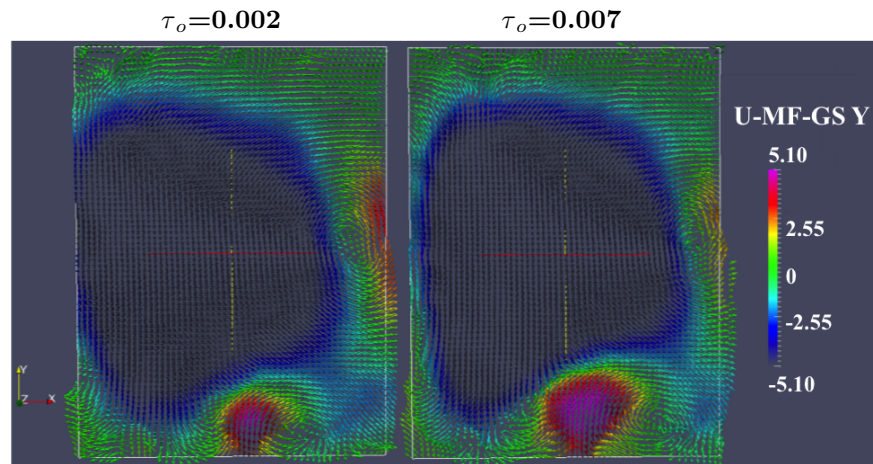
Figure 6.27: Region 1, non-dimensional velocity vectors (U_o) for the ΔT=5°C plume. The images shown are at τ_o=0.002 and 0.007 after the beginning of the experiment when the thermal mass in the tank was large and inhibiting the plume's ability to rise in the tank.

In region 1 (Figure 6.27) the plume was beginning to form from the TBL layer. The plume began to grow and ascend in the tank. At τ_o=0.002, a large off-centre thermal mass was flowing downwards in the centre of the tank with U_o=-5.10. The head of the plume was forming and attempting to ascend in the tank. The centre of the plume (U_o=5.10) had the largest velocity of all the fluid moving in the tank and the down-welling thermal mass flowing was around the plume head inhibiting its ascent. A scroll was present at the centre of the right hand side (RHS) of the tank, displaying the background convection present prior to the experiment. At τ=0.007 the plume head was beginning to scroll on the RHS with U_o=±1.0 and the plume was asymmetric because of the down-welling low velocity mass which moved towards the centre of the tank. Material continued to flow around the head of the plume, and the scroll in the head increased in size, as the background convection scroll on the RHS decreased in size. This led to the plume ascending further in the tank.
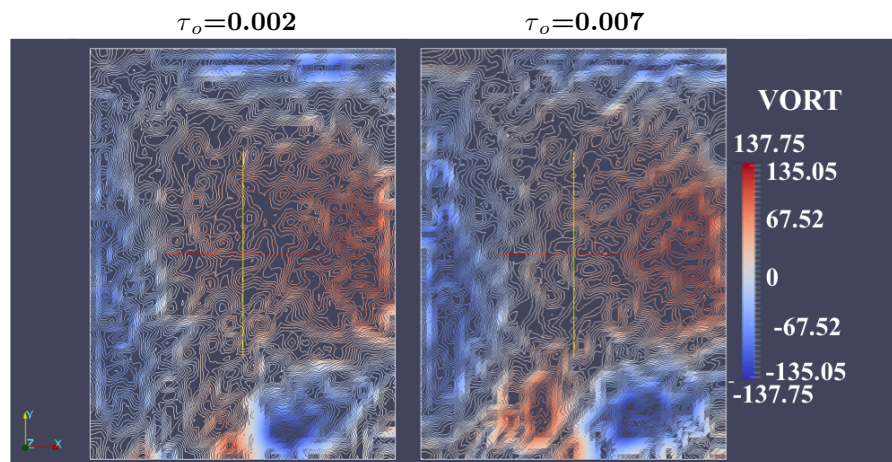
Figure 6.28: The non-dimensional vorticity (ω_o) contours for the ΔT=5°C plume in region 1. The images are at τ_o=0.002 and 0.007 after the beginning of the experiment, where red is anticlockwise spin and blue is clockwise spin of the fluid particles at each position in the tank. The large thermal mass in the centre of the tank has anticlockwise rotation and the plume appears asymmetric, as seen in Figure 6.27.

The vorticity contours in Figure 6.28 portray the local spinning motion of the fluid at each point. The study of the vorticity enabled observations to be made about the two sides of the plume not discerned solely from velocity vectors and the data was rendered non-dimensional so that all images are comparable between experiments. The large down-welling mass in the tank had anticlockwise movement, and the largest vorticity at the right hand side of ω_o=137.75 was occurring near to where the background convection scroll is present in Figure 6.27. The central plane of the plume had neutral vorticity as it was the axis of the plume. Around this neutral vorticity were two asymmetrical extrema. The right hand side of the plume exhibited strongly clockwise rotation (ω_o=-137.75) in the position of the scroll in the plume head. The left hand scroll in the plume head became larger at τ_o=0.007 as the anticlockwise fluid lobe increased in size and almost became equal in magnitude to the RHS vorticity of the plume head.

6.3.1.2   Region 2
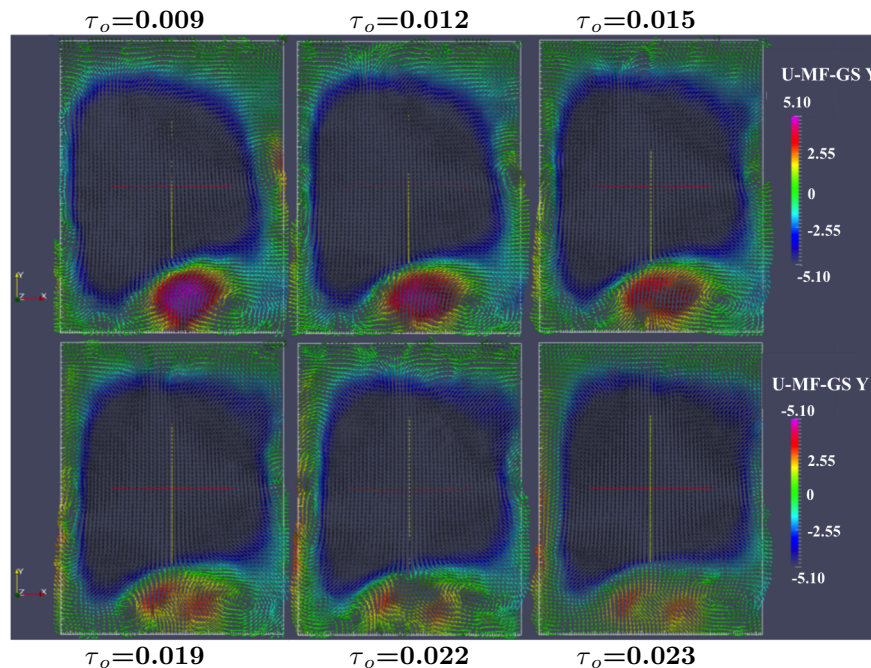
Figure 6.29: The non-dimensional velocity vectors (U_o) for region 2 of the ΔT=5°C plume. Images were selected at τ_o=0.009, 0.012, 0.015, 0.019, 0.022, 0.023 after the beginning of the experiment. The thermal mass remains present in the centre of the tank inhibiting plume ascent in the tank. The plume velocity has weakened by τ_o=0.023 with the velocity similar to the background flow.

After τ_o=0.007 there were two scrolls observed in the plume head and the down-welling low velocity thermal mass in the centre of the tank continued to inhibit the plume ascent (Figure 6.29). Between τ_o=0.009-0.015 the plume appeared to have stalled and the plume head instead spread laterally under the low velocity thermal mass, with the left hand side (LHS) scroll in the head becoming more pronounced. During this stalling the velocity in the centre of the plume decreased. As a consequence, by τ_o=0.015 the velocity had fallen by U_o=3.37 and decreased further by τ_o=0.019. The central plume velocity decreased further between τ_o=0.022-0.023, with the velocity in the majority of the plume matching the velocity of the ambient material. By τ_o=0.023

the scrolling in the head of the plume began to weaken and the background convection scroll at the RHS edge had disappeared due to the down-welling thermal mass migration to the RHS of the tank.
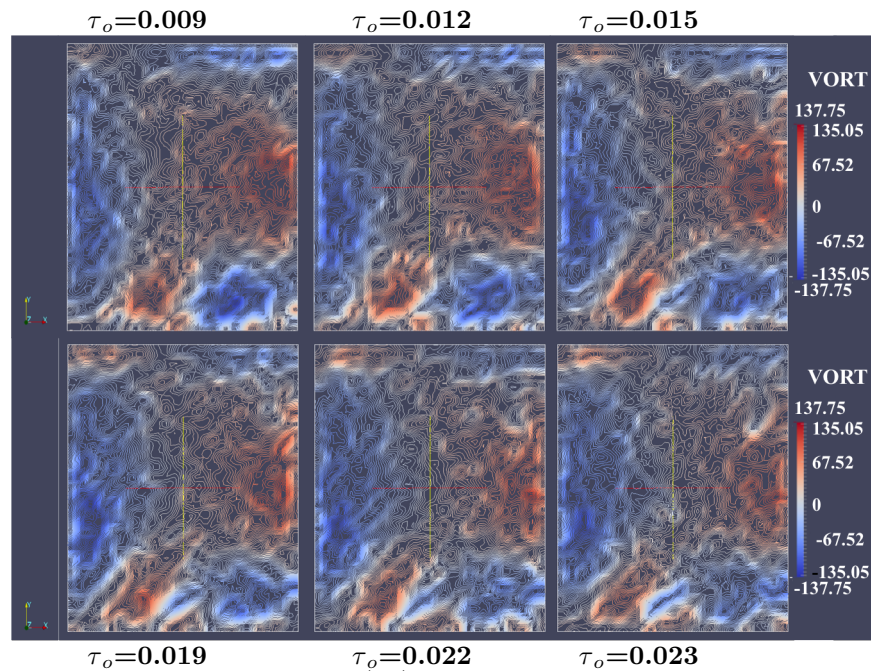
Figure 6.30: The non-dimensional vorticity (ω_o)contour map for region 2 of the $\Delta T = 5°C$ plume. Images were selected at τ_o=0.009, 0.012, 0.015, 0.019, 0.022 and 0.023 after the beginning of the experiment.

At the beginning of region 2, the vorticity of the ambient temperature material in the tank increased in strength, where the clockwise material on the LHS was between ω_o=-67.52 and -135.05 as shown in Figure 6.30. This increase in strength corroborated the scrolling observed in the background convection. The two extrema of the plume head showed a marked decrease in vorticity in both directions during region 2, implying that the spin of the fluid was diminishing. This fits with the observation that the velocity of the plume was also decreasing. Additionally, as the scrolls in the head of the plume spread laterally, the central maximum and minimum in the plume head also increased in size. However, as the vorticity in the plume reduced, the background vorticity increased. At τ_o=0.023 the vorticity in the plume head was observed to be weaker than the vorticity in the ambient flow.

6.3.1.3 Region 3

In region 3 the plume velocity varied in relation to the movement of the down-welling thermal mass, from the beginning of the region to the termination of the experiment (Figure 6.31). At τ_o=0.024 the down-welling low velocity thermal mass was central in the tank and scrolling material on both sides of the plume head were observed once again. The vortex on the RHS had increased in width, whereas the LHS vortex was at the base of the tank, creating the appearance of a tilted plume. By τ_o=0.031 the thermal mass migrated further towards the RHS and the

τ_o=0.024 τ_o=0.031 τ_o=0.037

τ_o=0.041 τ_o=0.048 τ_o=0.053
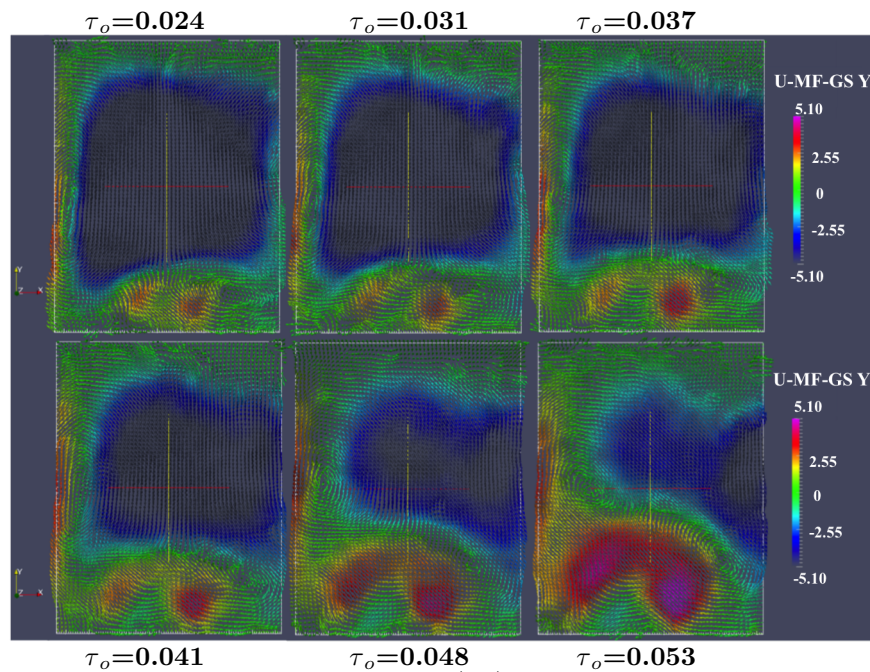
Figure 6.31: The non-dimensional velocity vectors (U_o) for region 3 of the ΔT=5°C plume with images chosen at τ_o=0.0024, 0.031, 0.037, 0.041, 0.048 and 0.053 after the beginning of the experiment. The downward flowing thermal mass is decreasing in size and moving to the left hand side of the tank. The plume then is able to ascend further in the tank and the non-dimensional velocity in the plume increases.

plume became less distinctive; the majority of the plume showed velocity between U_o=±2.55, with a higher velocity region near the base of the tank. At τ_o=0.037 the larger velocity region near the base had grown in size, and it appeared that the plume was gaining in strength, because the velocity increased ($U_o \approx 3.5$). At this time the down-welling thermal mass remained in the centre but had decreased in size. Scrolling material was observed in the LHS of the tank, showing convection had overturned due to a change in location and scrolling in the opposite direction. The ambient fluid and background convection had a velocity of U_o=±1.78. By τ_o=0.048, the downward thermal mass had a significantly reduced size and had migrated further to the RHS of the tank, whilst the scrolling convection increased in size in the LHS of the tank. The plume continued to rise at τ_o=0.053 with the central velocity area becoming larger, as the down-welling thermal mass migrated further to the RHS of the tank. As shown in Figure 6.32, as the velocity of the plume increased, the vorticity in the plume head decreased and thus the fluid rotated faster in a clockwise direction. As the plume began to rise again at τ_o=0.048 the vorticity extrema in the plume head became stronger, implying that the spin in the fluid was increasing again. However, the plume head was not so easily discernible from the vorticity because the anticlockwise spinning fluid was situated above the heater, where it was expected that two oppositely spinning extrema would be observed. This does however, fit with similar small scrolling seen in Figure 6.31 near the base of the tank in this area.
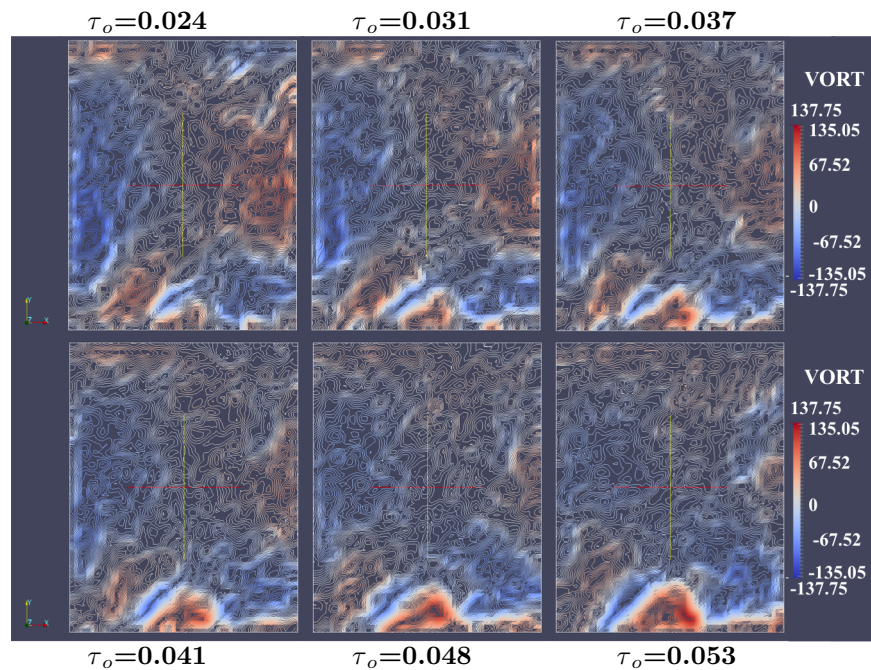
Figure 6.32: The non-dimensional vorticity (ω_o) contours for region 3 of the ΔT=5°C plume. Images were selected at τ_o=0.024, 0.031, 0.037, 0.041, 0.048 and 0.053 after the beginning of the experiment. As the down-welling thermal mass moves to the left hand side of the tank the vorticity of the plume increases. The plume head is not easily discernible towards the end of the region.

6.3.2 ΔT=13.3°C SPIV plume
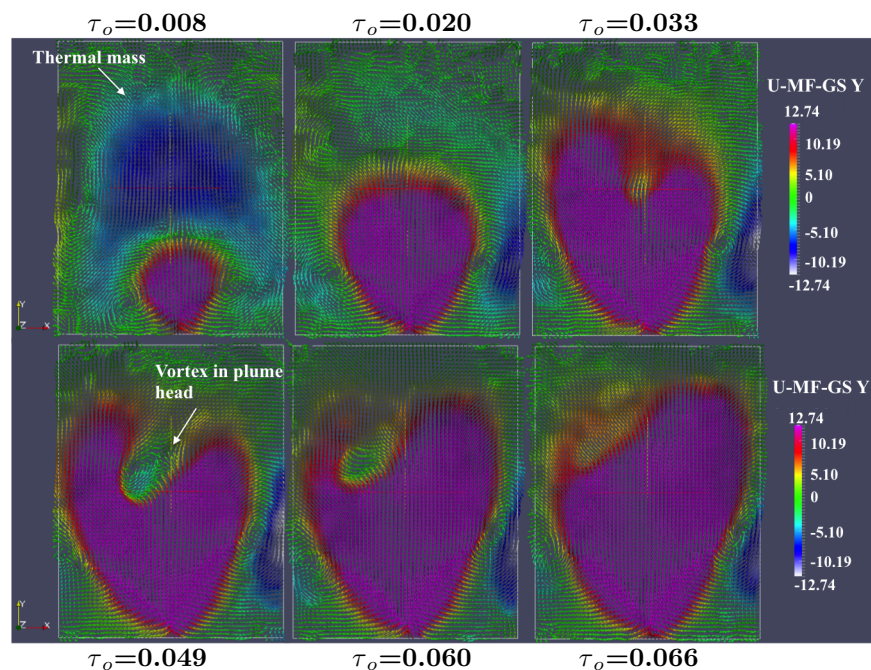
Figure 6.33: The non-dimensional velocity vectors (U_o) of the ΔT=13.3°C experimental plume, with images chosen at τ_o=0.008, 0.020, 0.033, 0.049, 0.060 and 0.066 after the beginning of the experiment. The dark blue region in the first image is the thermal mass present in the tank and by τ_o=0.049 a vortex has formed in the centre of the plume head.

Figure 6.33 presents the evolution of the ΔT=13.3°C plume with time and displays that the plume did not ascend to the top of the tank. At the beginning of the experiment (τ_o=0.008) a large low velocity down-welling of U_o=-12.74 was present in the centre of the tank, flowing around the head of the plume as it was ascending. The plume at this stage of development was asymmetric, with scrolling in the head and the RHS scroll higher in the tank. At this time the centre of the plume had velocity of U_o=12.74. By τ_o=0.020 the low velocity mass (U_o=-10.19)

had moved to the RHS of the tank as the plume ascended. At τ_o=0.033 the centre of the plume had split and the beginning of a lower velocity zone in the middle of the plume (U_o=5.10) was observed. The velocity of the centre of the plume remained high (U_o=12.74) but a heart shape was appearing, which was unexpected and this migrated towards the LHS by τ_o=0.060 with a lower velocity (U_o=-2.55 to U_o=5.10) than the plume. At this time (τ_o=0.060) the material in the plume had begun ascending again around the central vortex. During the experiment the ambient temperature material in the tank remained at $U_o \approx \pm 1.0$ with a low velocity zone on the RHS (U_o=-12.74), where material was descending. Towards the end of the experiment (τ_o=0.066) the vortex at the centre of the plume had decreased in size and the RHS of the plume had the highest velocity (U_o=12.74).
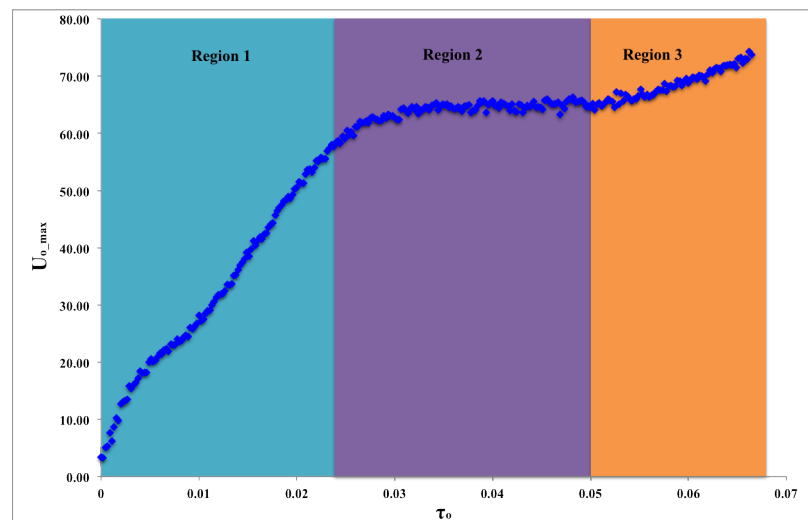
Figure 6.34: The maximum non-dimensional velocity of the ΔT=13.3°C plume as a function of non-dimensional time. The non-dimensional velocity is split into three distinctive regions discussed in the text below.

In Figure 6.34 the maximum velocity extracted from the SPIV images was divided into three distinctive regions. Region 1, where the plume was rising in the tank, region 2, where the plume was in steady state and the velocity of the plume was almost constant and region 3, where the plume was rising again. In region 1, the maximum velocity of the plume increased as the plume ascended in the tank. At approximately τ_o=0.025 the velocity (U_o=59.71) became steady and remained constant for region 2. By region 3, the maximum velocity began increasing once again, which fits with the observations from Figure 6.33.
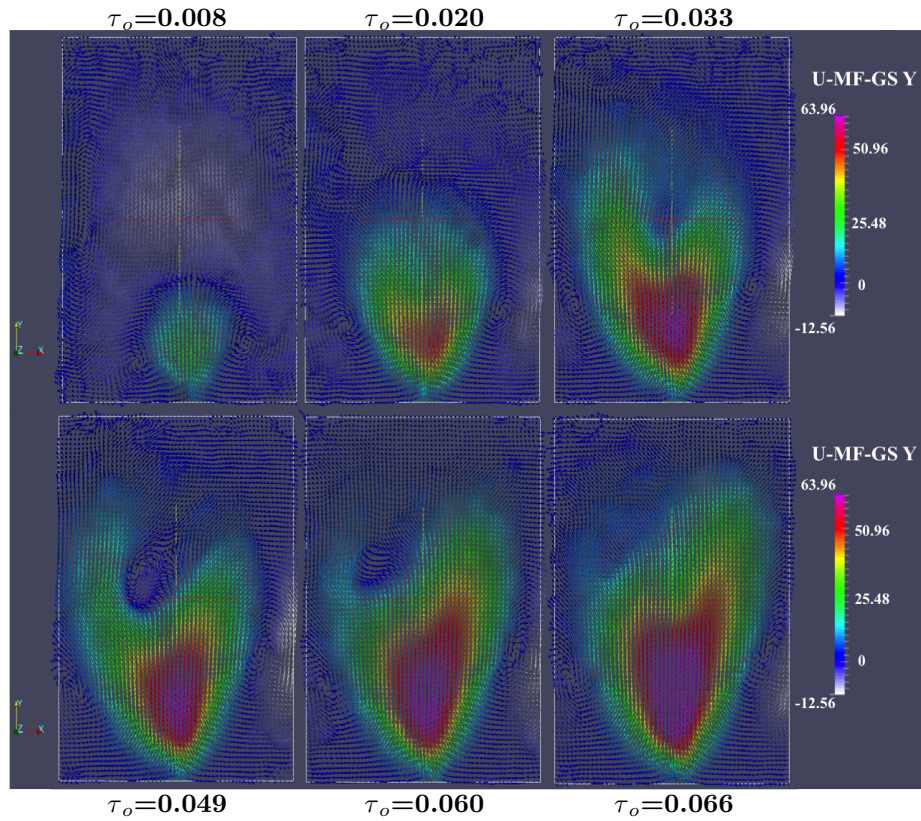
(a) Unsaturated non-dimensional velocity vectors (U_o) for the ΔT=13.3°C plume with images chosen at non-dimensional times τ_o 0.008, 0.020, 0.033, 0.049, 0.060 and 0.066 from the beginning of the experiment.
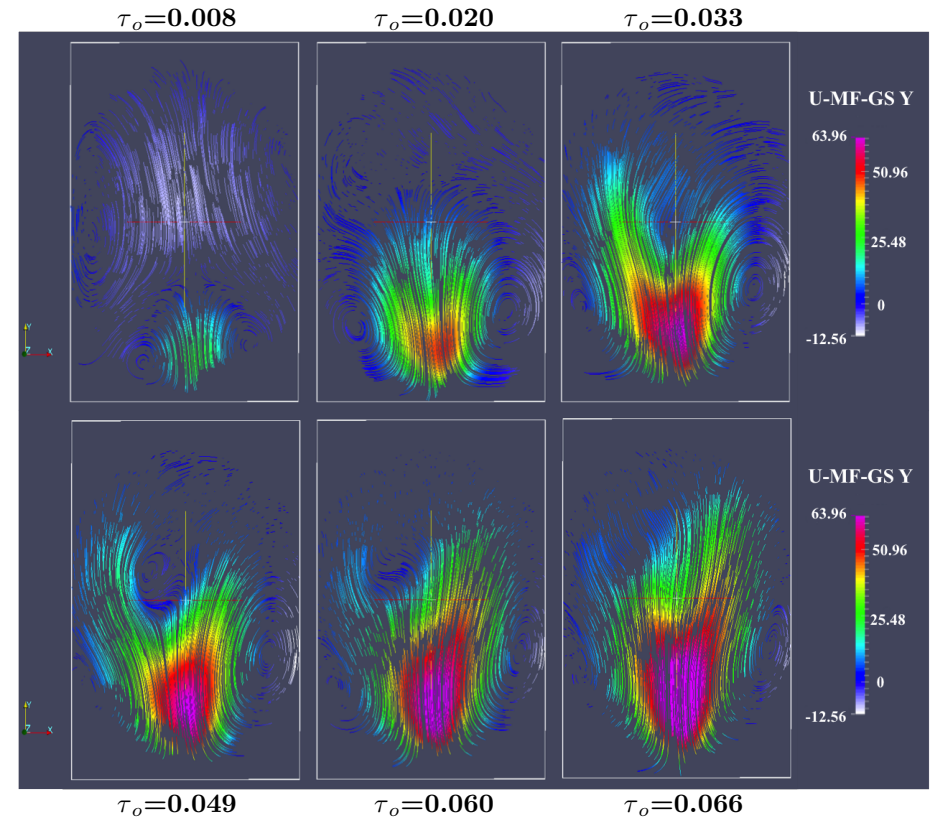
(b) Stream lines for the ΔT=13.3°C SPIV experiment with images chosen at non-dimensional times τ_o 0.008, 0.020, 0.033, 0.049, 0.060 and 0.066 from the beginning of the experiment.

Figure 6.35: A visual comparison of the unsaturated non-dimensional velocity vectors and the stream lines defining the vector field of the velocity for the ΔT=13.3°C Liquidose 436 syrup plume. The stream lines provide a snapshot of the flow at a given instant in time and depict the path a particle takes flowing though a velocity field.

Figure 6.35a shows the unsaturated velocity vectors for the $\Delta T = 13.3°C$ plume. This shows that the background flow in the tank had a velocity on average of $U_o=0$. At $\tau_o=0.008$ the low velocity down-welling thermal mass had a velocity of $U_o=-12.56$, whilst the centre of the plume had a velocity of between $U_o=20.38$ and $U_o=30.58$. By $\tau_o=0.020$ the plume was well developed and had ascended half way up the tank. The plume appears to be beginning to change in the middle of the head of the plume. The down-welling thermal mass had dissipated at this stage. However, there was the beginning of a low velocity zone on the RHS of the tank near the plume head scroll. At $\tau_o=0.033$ the plume head was beginning to separate and the low velocity zone on the RHS was larger. The heart shape in the centre of the plume had increased and the velocity in this region was $U_o=63.96$. This central high velocity region in the plume continued to grow in size during the rest of the experiment. This growth was in spite of the plume head having split and the presence of the central vortex which was observed at $\tau_o=0.049$. This vortex had dissipated by $\tau_o=0.066$.

The stream lines in Figure 6.35b show in more detail the background flow of the plume. At $\tau_o=0.008$ there was large background circulation on the LHS of the tank above the plume. This was not observed in the saturated or unsaturated images of the experiment. The stream lines at this time also show that the plume scroll was higher on the RHS compared to the LHS. By $\tau_o=0.020$ the stream lines do not show clearly the top of the head of the plume. However, they display that the large LHS circulation in the background flow of the tank had decreased in size as the plume had ascended. The plume remained asymmetric and there was a heart shape forming in the middle of the plume at a velocity of $U_o=50.96$. At $\tau_o=0.033$, it was observed that the central vortex was beginning to form in the plume as the stream lines were separating. The background flow was no longer evident but the fluid at the top of the plume is flowing to the RHS. At $\tau_o=0.049$ the central vortex which formed where the top of the plume head split was large and well defined, but started to dissipate in $\tau_o=0.060$ and had disappeared by $\tau_o=0.066$. At $\tau_o=0.066$ the plume was beginning to ascend again in the tank, observed by the increase length of the heart shape in the centre of the plume, but the scrolling in the head of the plume was smaller on both sides.

6.3.2.1 Region 1

In Figure 6.36 at $\tau_o=0.002$ the down-welling low velocity thermal mass ($U_o=-9.0$) in the centre of the tank had a velocity of $U_o=-12.74$ and the plume appeared axisymmetric. The plume had two scrolls in the head with the same velocity as the ambient fluid and the down-welling mass was flowing around the head of the plume. The centre of the plume had a velocity between
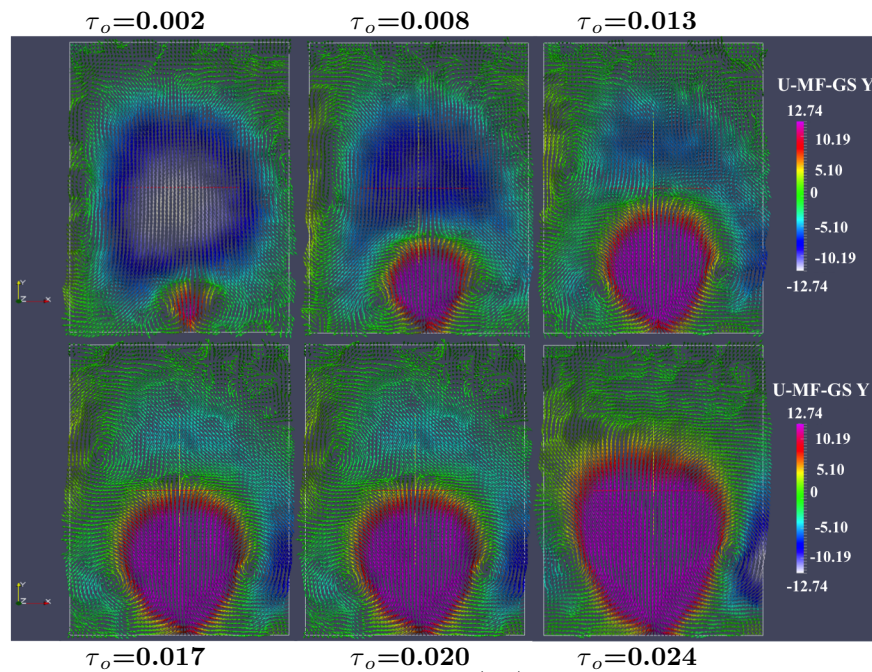
Figure 6.36: The non-dimensional velocity vectors (U_o) for region 1 of the ΔT=13.3°C plume with images chosen at τ_o=0.002, 0.008, 0.013, 0.017, 0.020 and 0.024 after the beginning of the experiment. The down-welling thermal mass at the beginning of the experiment dissipates by τ_o=0.024 and the plume is able to ascend in the tank.

U_o=10.19-12.74. The down-welling thermal mass decreased in size by τ_o=0.008 because the asymmetric plume was ascending, with the scrolls in the head not aligned. At τ_o=0.017 the plume appeared to have stalled, with the velocity changing to U_o=-6.00, despite the dispersal of the down-welling low velocity thermal mass to a ring shape surrounding the top of the plume. The plume remained asymmetric with the RHS vortex higher and increasing in size. At this time, through visual inspection of the magnitude of velocity of the plumes in Paraview, there were signs of collapse which is not evident when the velocity is set to be U_o=±12.74 in the y-direction. The magnitude of the velocity vectors was set like this to give definition to the results; raising it too high would lead to all background material having the same velocity and therefore the low velocity down-welling mass would not be clearly discernible. After τ_o=0.024 the plume was ascending in height again as the surrounding low velocity thermal mass had disappeared, although a new low velocity region appeared on the lower RHS of the tank.

In Figure 6.37 the background vorticity was between ω_o=±100.00. As the plume began to grow (τ_o=0.002) the plume displayed two extrema close to the heater, showing material spinning in opposite directions but of the same magnitude (ω_o=±270.10). By τ_o=0.013 these two lobes were separating in the centre, implying that this was when the vortex was beginning to form. Two secondary lobes were beginning to form by τ_o=0.017 counter-rotating against the plume material on each side. These secondary lobes fit with the observed heart shape in the plume head. Additionally, two small thin regions, counter-rotating to the plume material were observed at the base of the tank, which give the appearance of shear. This is, however, due to the inability of this material to move at the bottom boundary.
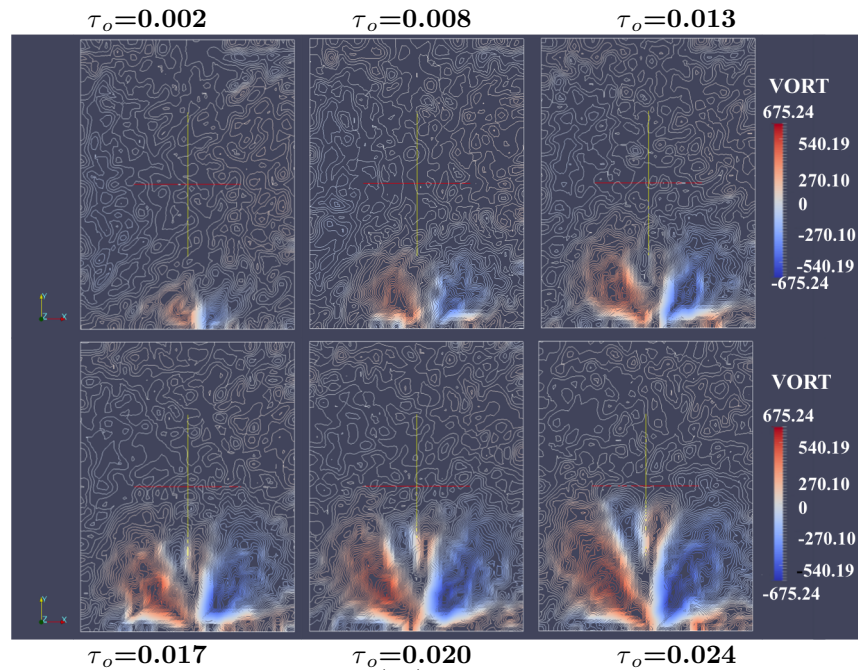
Figure 6.37: The non-dimensional vorticity (ω_o) contours for region 1 of the ΔT=13.3°C plume. The images were at τ_o=0.002, 0.008, 0.013, 0.017, 0.020 and 0.024 after the beginning of the experiment. The central vortex observed in Figure 6.33 is evident at τ_o=0.017 with the head of the plume splitting and the beginning of two new lobes counter-rotating to the original plume lobes.

6.3.2.2   Region 2
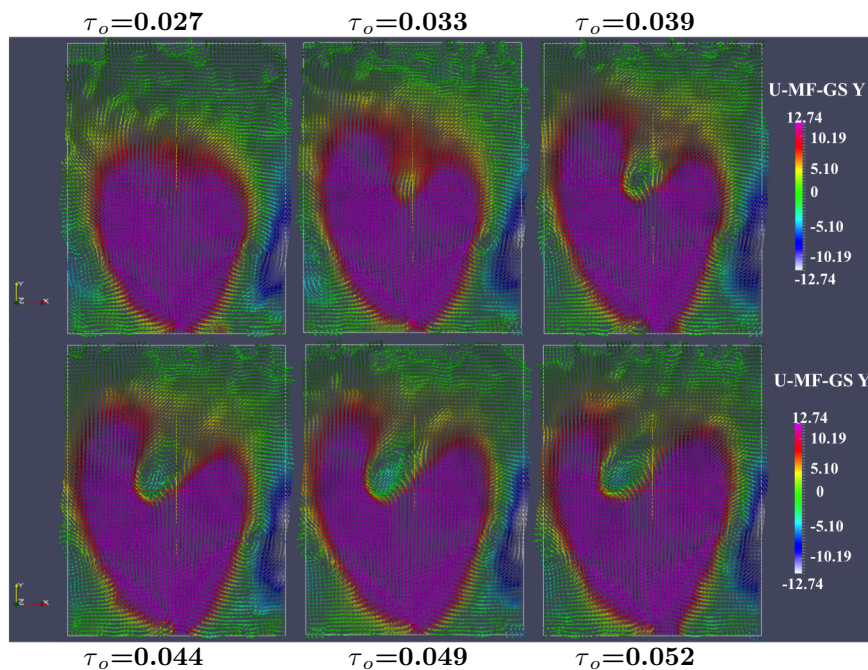
Figure 6.38: The non-dimensional velocity vectors (U_o) for region 2 for the ΔT=13.3°C plume. The images were at τ_o=0.027, 0.033, 0.039, 0.044, 0.049 and 0.052 after the beginning of the experiment. A central vortex begins forming in the plume at τ_o=0.033 and splits the head of the plume. This vortex is observed as the "lens shape" in the ΔT=13.3°C shadowgraph experiment.

In region 2 the plume was at steady-state in terms of the maximum velocity (U_o=12.74). In Figure 6.38, at τ_o=0.033, the plume split in the centre and a lower velocity region (U_o=5.10) formed. As the experiment continued (τ_o=0.039) a vortex was observed at the top of the plume centre, with a velocity between U_o=±2.55, which continued expanding in size. Between τ_o=0.044-0.049, the plume stalled, the central vortex decreased in velocity and moved towards the LHS of the top of the plume. Figure 6.39 shows that the two additional lobes in the centre of the plume

had increased in size and strength as the central vortex in the plume head began rotating. The two lobes were of equal magnitude and size and the plume appeared more axisymmetric from Figure 6.39. As the central vortex in the plume head increased in size and moved further to the LHS, the lobes in the vortex became more elongate and increased in strength $\omega_o=\pm400.00$. The plume vorticity was strongest close to the heater, this was the material had strongest spin in the tank ($\omega_o=\pm675.24$).
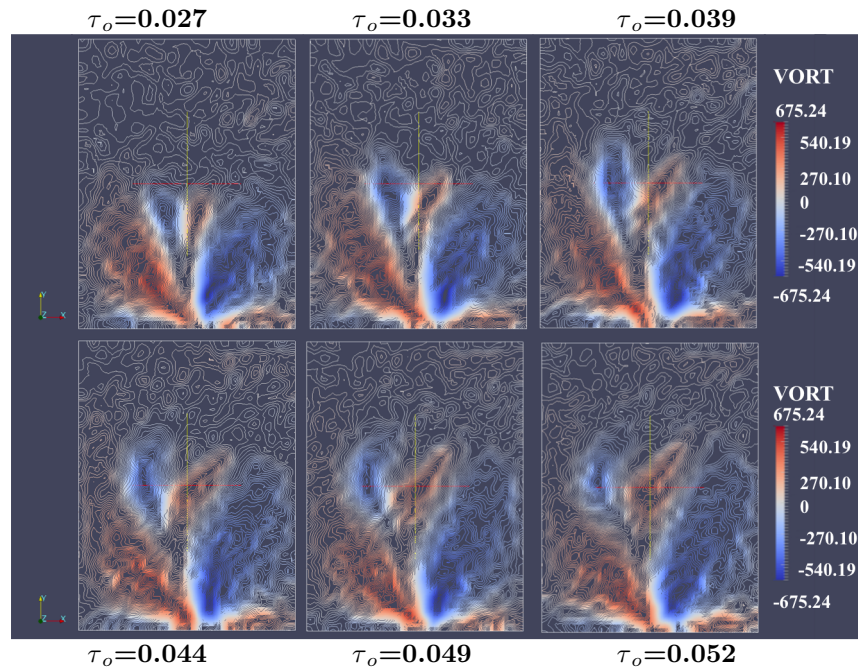
Figure 6.39: The non-dimensional vorticity (ω_o) contours for region 2 of the ΔT=13.3°C plume. The images were selected at τ_o=0.027, 0.033, 0.039, 0.044, 0.049 and 0.052 after the beginning of the experiment. The vorticity displays the counter-rotating fluid vortex and the plume split at the centre of the head.

6.3.2.3   Region 3

Between τ_o=0.053-0.058 the central plume vortex became wider and velocity increased to $U_o=\pm2.00$, as the plume remained stagnant in height (Figure 6.40). However, by τ_o=0.060 the plume began ascending once again and the central vortex decreased in size, with velocity increasing. By the end of the experiment (τ_o=0.066) the vortex in the centre had disappeared. The vorticity in the tank remained the same between τ_o=0.053-0.056 (Figure 6.41), with the plume and central vortex lobes continuing to counter-rotate against one another. During this period the plume was stagnant in height. The velocity vectors of the right lobe of the central vortex appeared to be in the centre of the plume head, implying the material was rotating in an anticlockwise direction. The central vortex in the plume head appeared to be mostly anticlockwise spinning fluid with the clockwise lobe almost disappearing by τ_o=0.060. At the end of the experiment there was an increased amount of anticlockwise spinning material flowing around a small clockwise flowing region of material in the centre of the plume. This was observed alongside increased velocity
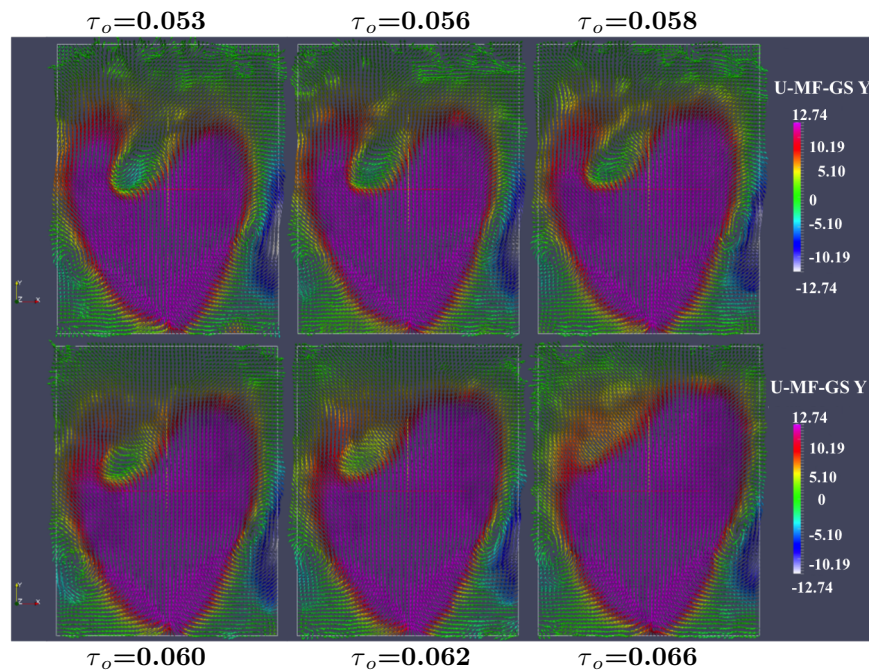
Figure 6.40: The non-dimensional velocity vectors for region 3 of the $\Delta T=13.3°C$ plume with images at $\tau_o=0.053$, 0.056, 0.058, 0.060, 0.062 and 0.066 after the beginning of the experiment. The plume continued to ascend around the edges of the vortex, which disappeared by $\tau_o=0.066$.

in the z-direction during this period, as shown in Figure 6.42, where the anticlockwise material was a small region where material was rotating in the opposite direction to the background fluid.
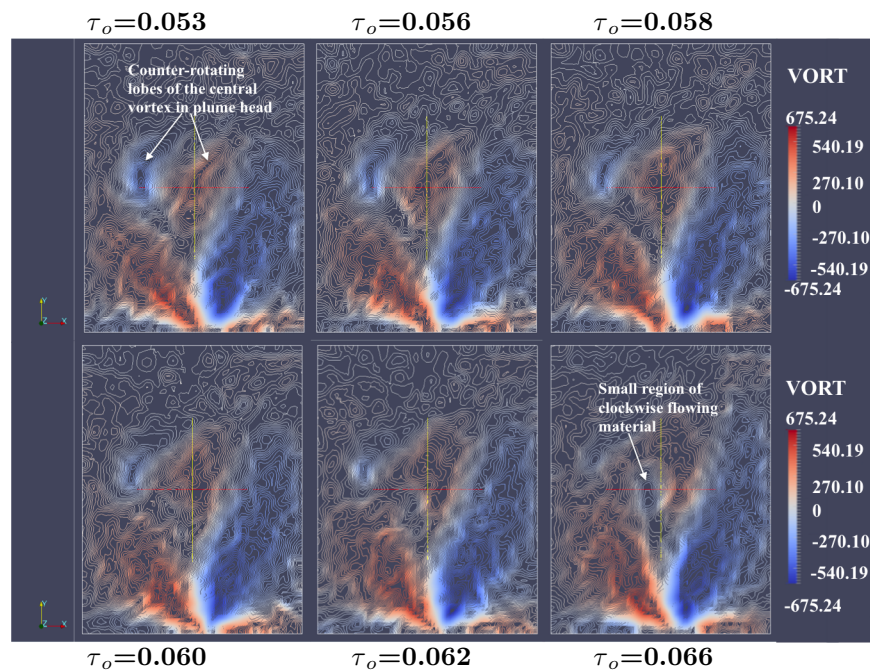
Figure 6.41: The non-dimensional vorticity contours for region 3 of the $\Delta T=13.3°C$ plume. Images are at $\tau_o=0.053$, 0.056, 0.058, 0.060, 0.062 and 0.066 after the beginning of the experiment.

Before region 3 the velocity in the z-direction of the tank did not display distinctive results and thus was not presented. In Figure 6.42 convective overturning was observed where the red colour represents fluid moving away from view and blue towards. The central vortex in the plume head was observed as a low velocity region ($U_o=-20.38$) in the z-direction flowing towards the reader. This central vortex was moving in the opposite direction to the high velocity fluid flowing away from view. Between $\tau_o=0.053$-0.066 the low velocity central vortex region increased in size while
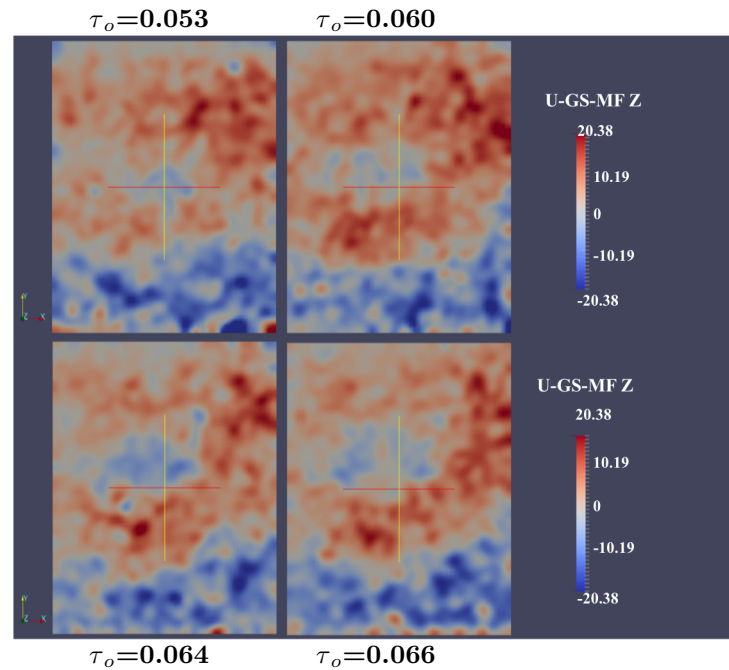
Figure 6.42: The non-dimensional velocity in the z-direction of the $\Delta T=13.3°C$ plume. The vortex in the centre (blue coloured) is moving towards the reader and in the opposite direction to the red material in the upper half of the tank which is flowing inwards to the page.

the red region was descending in the tank. The low velocity material flowing inwards surrounded by high velocity material fits with the shape of the vortex observed in the centre of the plume head (Figure 6.40). It appeared that the central vortex had an axis and was spinning inwards and anticlockwise whilst it existed in the experiment.

6.3.2.4 $\Delta T=21°C$ SPIV plume
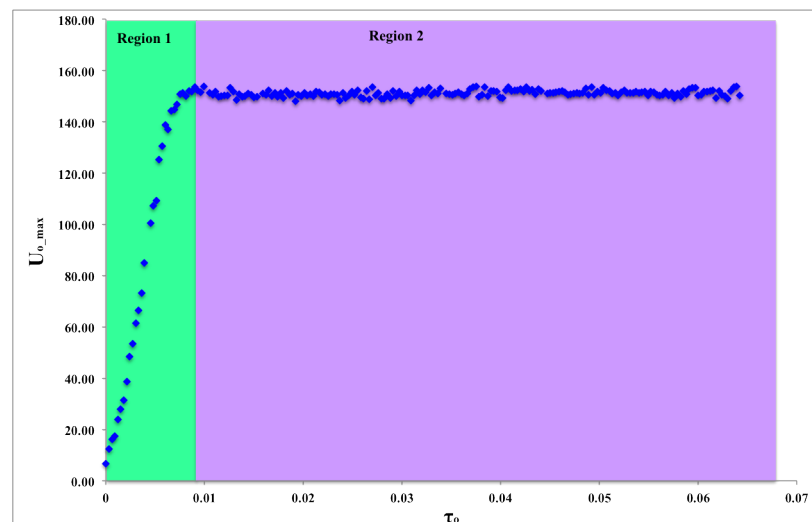
Figure 6.43: The maximum non-dimensional velocity of the $\Delta T=21°C$ plume as a function of non-dimensional time. The non-dimensional velocity is divided into two regions, discussed in the text.

The maximum velocity of the plume was divided into two main regions as shown in Figure 6.43. Region 1 when the plume is ascending and region 2 when the plume is feeling and reaching the top of the tank. These regimes are expected for high temperature difference plumes which rose to the surface. The plume velocity increased rapidly at $\tau_o=0.009$ to $U_o=152.88$. Region 2 began

when the plume velocity remained constant and the plume was in steady-state - near the top or at the surface of the tank.
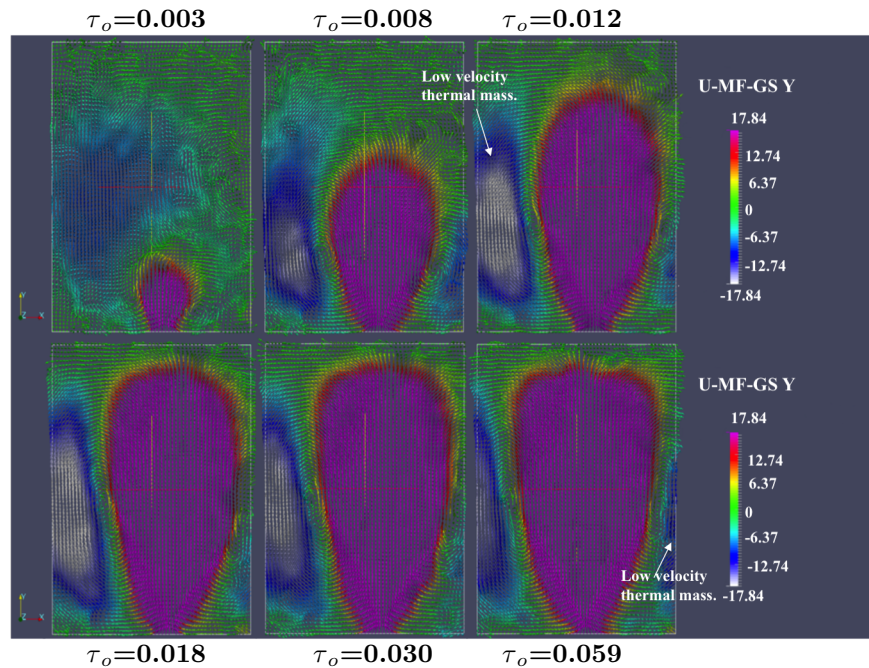
Figure 6.44: The non-dimensional velocity vectors (U_o) for $\Delta T = 21°C$ plume. Images were selected at $\tau_o = 0.003$, 0.008, 0.012, 0.018, 0.030 and 0.059 after the beginning of the experiment. The plume appears axisymmetric and ascends to the top of the tank.

In Figure 6.44 the plume velocity was higher by $U_o = 5.10$ than for the $\Delta T = 13.3°C$ plume. There was evidence of a small down-welling low velocity thermal mass ($U_o = -6.37$) towards the LHS of the centre of the tank. The plume was axisymmetric with the highest velocity at the centre and scrolling in the head less distinctive on the LHS. By $\tau_o = 0.008$ (region 1) the low-velocity thermal mass had migrated to the LHS, elongating and thinning with decreasing velocity. The centre of the low velocity thermal mass was $U_o = -17.84$ as the plume was ascending and the scroll in the RHS of the head was slightly lower than the LHS. By region 2, the thermal mass began to increase in size by $\tau_o = 0.012$ and appeared to be pushing the axisymmetric plume to the RHS as it ascended further in the tank. Later ($\tau_o = 0.030$), the thermal mass was thinner but longer as the plume was at the surface and became more central in the tank. At the termination of the experiment an additional down-welling low velocity region ($U_o = -12.74$) was present on the RHS. No sign of "lenticular" collapse was observed in this experiment despite the shadowgraph experiment at this temperature difference displaying such phenomena.

The vorticity shown in Figure 6.45 was as expected, with two extrema for the plume, with anticlockwise spin fluid on the LHS and clockwise fluid on the RHS. The highest vorticity ($\omega_o = 1613.82$ and $\omega_o = -1613.82$) is in the centre of the plume near the heater. The background vorticity in the tank was not distinctive compared to the plume. The down-welling mass observed from the velocity vectors was not discernible in the vorticity of the ambient material.
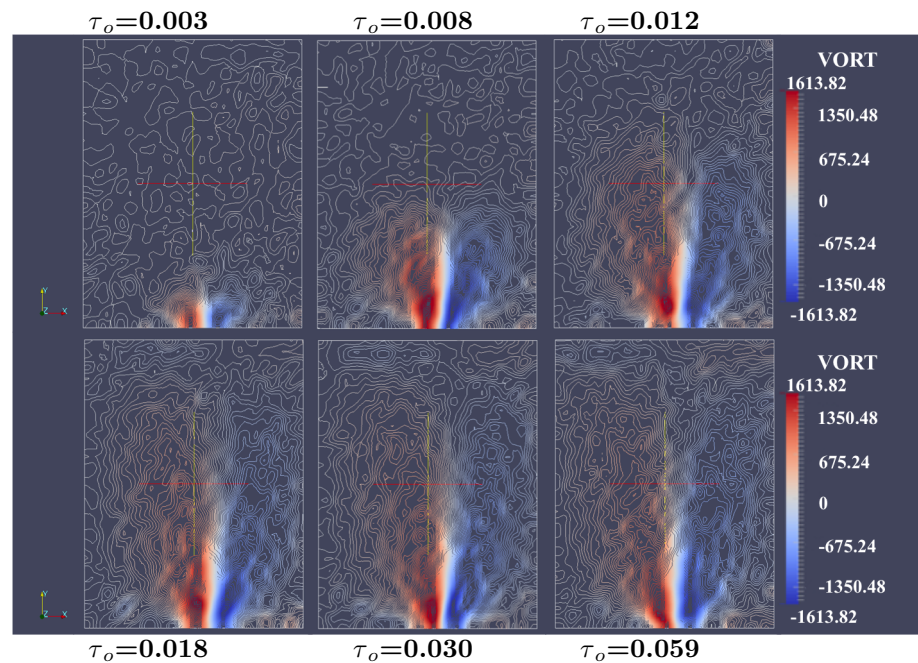
Figure 6.45: The non-dimensional vorticity contours (ω_o) for the ΔT=21°C plume. Images chosen at τ_o=0.003, 0.008, 0.012, 0.018, 0.030 and 0.059 after the beginning of the experiment.

6.3.2.5 ΔT=41.2°C SPIV experiment
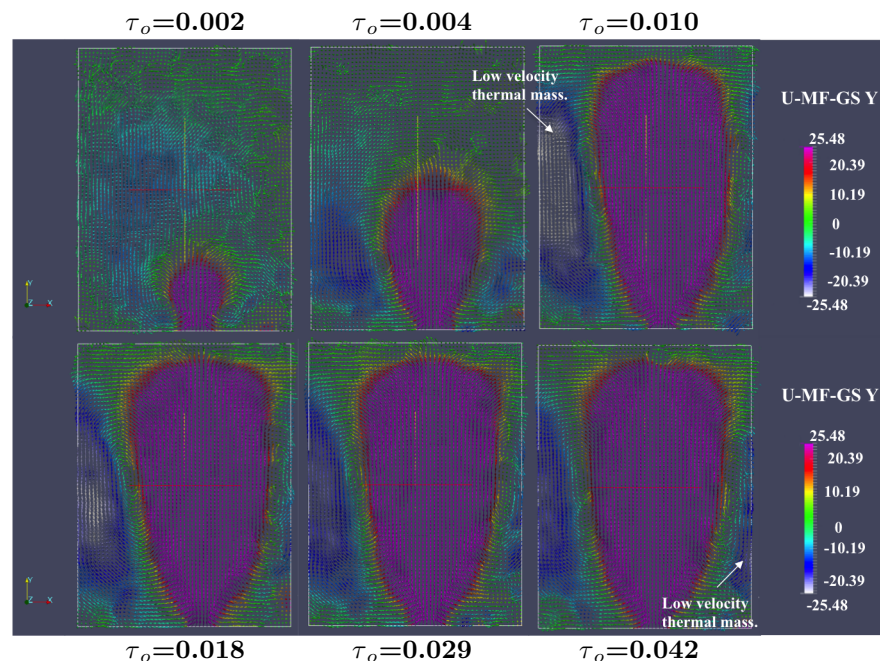
Figure 6.46: The non-dimensional velocity vectors (U_o) for the ΔT=41.2°C plume. Images are at τ_o=0.002, 0.004, 0.010, 0.018, 0.029 and 0.042 after the beginning of the experiment. The arrows in the images are the velocity vectors. The arrows point in the direction of flow. The plume appears axisymmetric and ascends to the surface of the tank.

In Figure 6.46 the plume ascended to the top of the tank and was axisymmetric. At the beginning (τ_o=0.002) a small low velocity down-welling was observed towards the LHS in the centre of the tank. The centre of the axisymmetric plume had a maximum velocity of U_o=25.48 and the RHS scroll was slightly smaller than the LHS in the plume head. As the experiment progressed, the plume ascended to the surface at τ_o=0.018, with the scrolls becoming more elongate and smaller in width. The low-velocity mass on the LHS increased in size between τ_o=0.010-0.018 with a velocity of U_o=-25.48. After τ_o=0.018, the low velocity thermal mass became smaller in size.

A new low velocity mass appeared on the RHS by τ_o=0.042. The velocity of the ΔT=41.2°C plume can be divided into two main regions as shown in Figure 6.47. The regions were divided the same way as for the ΔT=21°C plume; region 1 when the plume was ascending and region 2 when the plume was feeling and reaching the top of the tank. The plume reached the surface after τ_o=0.004 and the maximum velocity of U$_o$=375.00 remained fairly constant from this time. The first two images (τ_o=0.002-0.004) in Figure 6.46 show the plume ascending and the plume already in the upper half of the tank. By τ_o=0.010 (region 2) the plume was nearly at the surface and the maximum velocity was constant. The maximum velocity of the ΔT=41.2°C plume was U$_o$=244.00 faster than the ΔT=21°C.
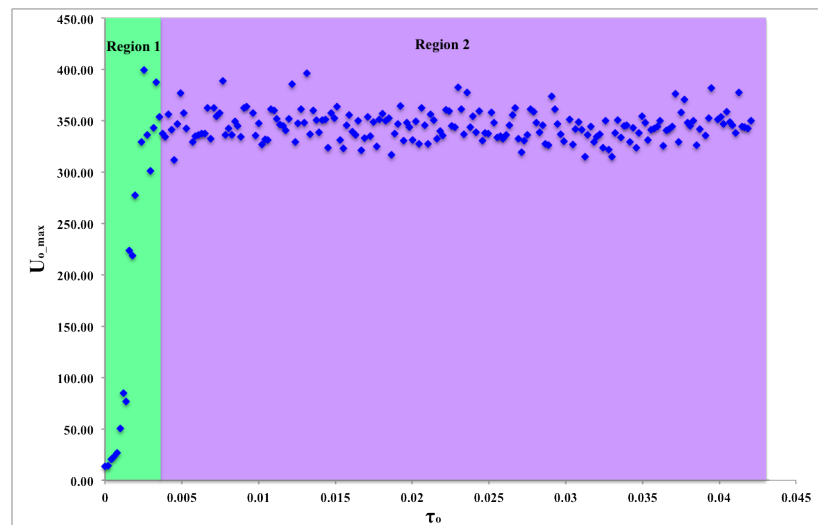
Figure 6.47: The maximum non-dimensional velocity of the ΔT=41.2°C plume as a function of non-dimensional time. The non-dimensional velocity is divided into two regions. Region 1 when the plume is ascending to the surface and region 2 when the plume is at the top of the tank.
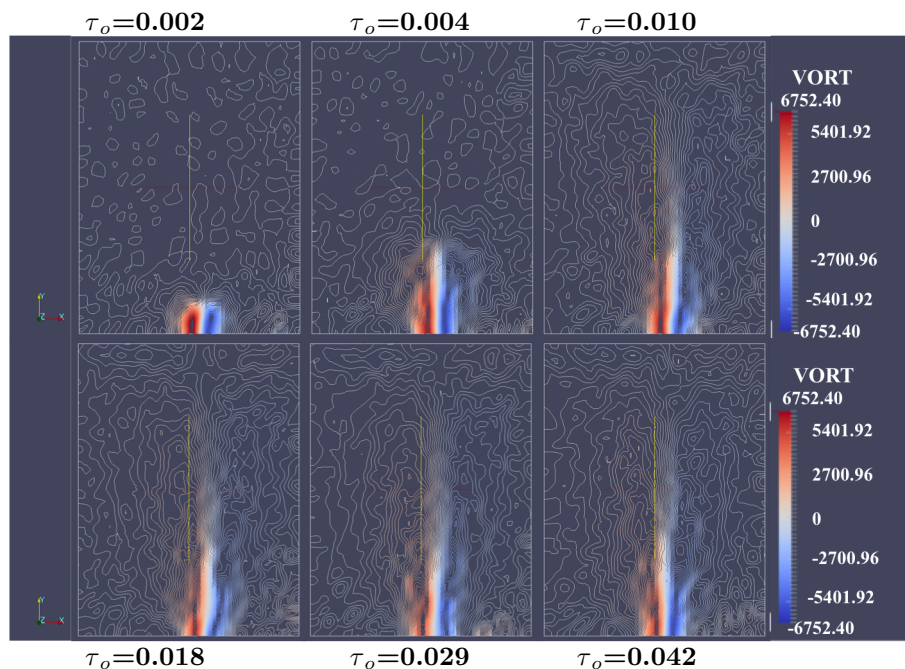
Figure 6.48: The non-dimensional vorticity contours (ω_o) for the ΔT=41.2°C plume with images selected at τ_o=0.002, 0.004, 0.010, 0.018, 0.029, 0.042 after the beginning of the experiment. The vorticity shows the plume was axisymmetric. The red colour is anticlockwise rotation and the blue colour was clockwise rotation of the fluid.

In Figure 6.48 the background rotation of the fluid was anticlockwise (between ω_o=0-1400.00).

At τ_o=0.002 the plume is observed as two extrema at the bottom of the tank of equal magnitude and size. As the plume evolved, the two lobes of material closest to the heater possessed the strongest vorticity in the tank. The centre of the conduit has a similar degree of vorticity to the ambient fluid in the tank. Observing the vorticity enables the determination of the axisymmetric nature of the plume.The vorticity in the ΔT=41.2°C plume was stronger than the ΔT=21.0°C plume by ω_o=5138.58.

6.3.3 Comparison of Shadowgraph and SPIV experiments

Similar phenomena were observed in both shadowgraph and SPIV visualisation techniques at the same ΔT despite some experiments having slightly differing η^*.

6.3.3.1 "Stalled" collapse comparison

Parameter	Shadowgraph experiment	SPIV experiment	Units
T_h	23.4	24.2	°C
T_∞	18.4	19.2	°C
ΔT	5.0	5.0	°C
η_h	51.80	48.15	Pa s
η^*	1.58	1.58	-
ρ_h	1438.08	1437.68	kg/m^3
Ra_h	8.64×10^4	9.29×10^4	-
Pr_h	3.47×10^5	3.23×10^5	-

Table 6.8: Comparison of measured and calculated parameters for "stalled" collapse experiments.

The two experiments compared had the same ΔT and viscosity contrast (Table 6.8) but different viscosity and density. The experimental results compare qualitatively well despite the experiments running for different lengths of time as both plumes stalled in the lower quarter of the tank and displayed asymmetric characteristics of scrolling in the plume head (Figure 6.49). In the shadowgraph experiment the scrolling in the plume head was larger on the LHS and this was opposite to the SPIV experiment. It appears that the plume was more developed in the SPIV experiment than the shadowgraph experiment as the same times. SPIV revealed that the stalling observed in the shadowgraph experiment was due to a thermal mass. Much of the behaviour observed in the SPIV plume, namely lateral spreading under the low-velocity thermal mass is visible in Figure 6.1 but not observed in Figure 6.49a. This difference in the behaviour could be due to the higher ambient temperature of the fluid in the SPIV experiment, which changed the viscosity of the fluid and made it easier for the plume to rise. Collapse was observed at the end of the shadowgraph experiment but not observed in the SPIV experiment. It is possible that if the SPIV experiment was run for longer this phenomenon would also have been identified.
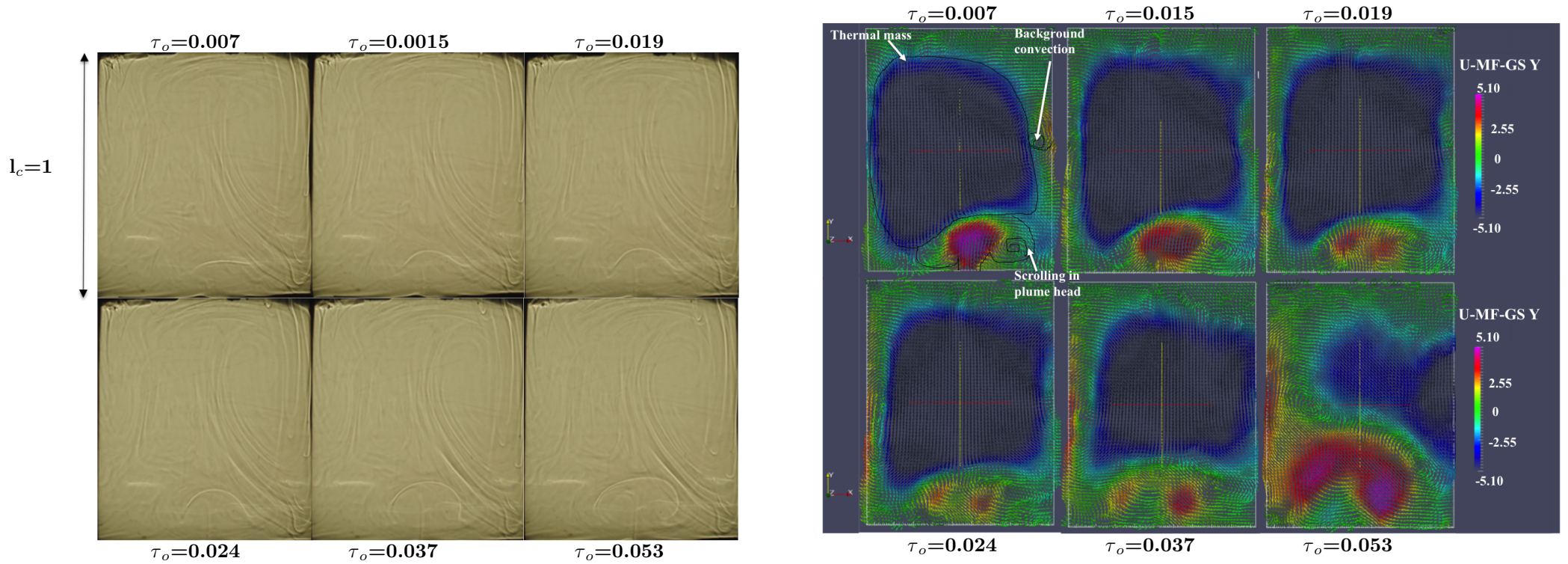
(a) The ΔT=5°C plume shadowgraph experiment with images at τ_o=0.007, 0.015, 0.019, 0.024, 0.037, 0.053 after the heater was activated.

(b) The ΔT=5°C SPIV experiment with non-dimensional velocity vectors. Images chosen at τ_o=0.007, 0.015, 0.019, 0.024, 0.037 and 0.053 after the beginning of the experiment.

Figure 6.49: A visual comparison of two different ΔT=5°C plumes. Both plumes were inhibited from rising to the surface of the tank. The SPIV experiment shows that the reason for this was the large thermal down-welling in the centre of the tank.

6.3.3.2   "Lenticular" collapse comparison

Parameter	Shadowgraph experiment	SPIV experiment	Units
T_h	30.1	31.3	°C
T_∞	16.8	18.0	°C
ΔT	13.3	13.3	°C
η_h	28.18	25.39	Pa s
η^*	3.36	3.36	-
ρ_h	1434.70	1434.09	kg/m^3
Ra_h	4.17×10^5	4.68×10^5	-
Pr_h	1.91×10^5	1.70×10^5	-

Table 6.9: Comparison of parameters for "lenticular" collapse experiments. The two experiments have the same temperature differences, despite the different heater and ambient temperatures.

Figure 6.50 demonstrates the similarities in the SPIV and shadowgraph plume experiments in terms of both plumes exhibiting the "lenticular" collapse phenomenon and both agree qualitatively well. The plumes both had the same temperature difference and viscosity contrast, despite the different heater and ambient temperatures (Table 6.9). The SPIV plume ascended to a greater height at an earlier stage than the shadowgraph plume because the lower viscosity in the SPIV experiment. However, the fully formed "lens shape" was observed at τ_o=0.033 for the SPIV and τ_o=0.034 in the shadowgraph experiment. During the "lenticular" collapse the vortex in the SPIV plume head was rotating clockwise, whilst the material in the plume head was attempting to ascend. A white line was observed at τ_o=0.017, which was the beginning of the formation of the "lens shape" in the shadowgraph experiment and the beginning formation of the vortex was observed at the same time in the SPIV experiment using Paraview. In both experiments the plume does not reach the top of the tank and any material that does ascend to the surface does so in-spite of material observed during the shadowgraph experiment descending. It is however, worth noting this downward motion was not corroborated by the SPIV experiment.
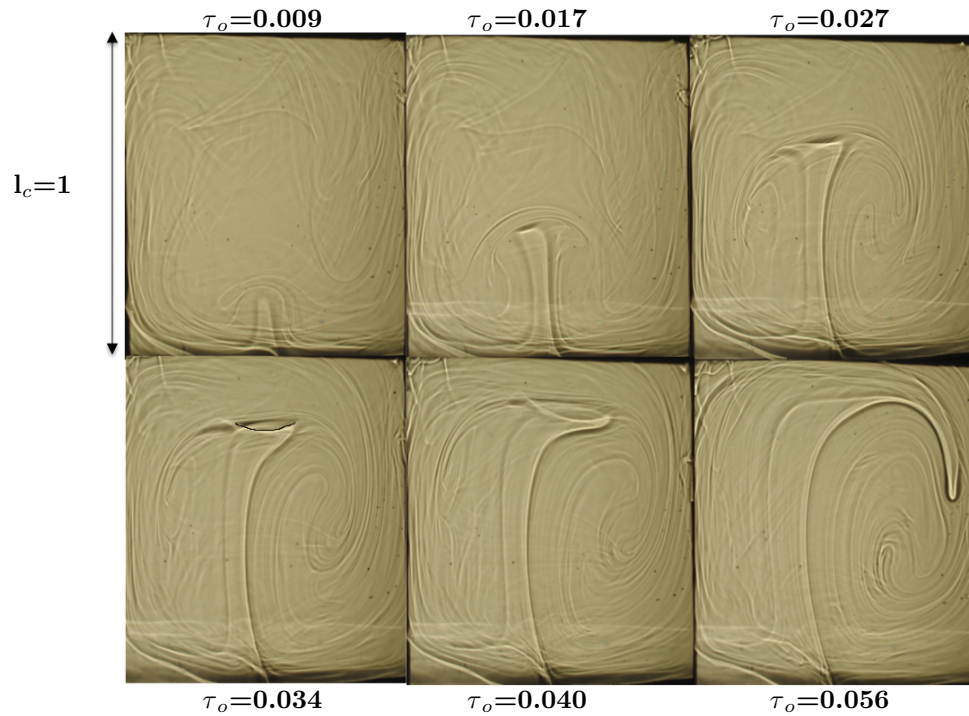
(a) ΔT=13.3°C shadowgraph experiment with images at τ_o=0.009, 0.017, 0.027, 0.034, 0.040 and 0.056 after heater activation.
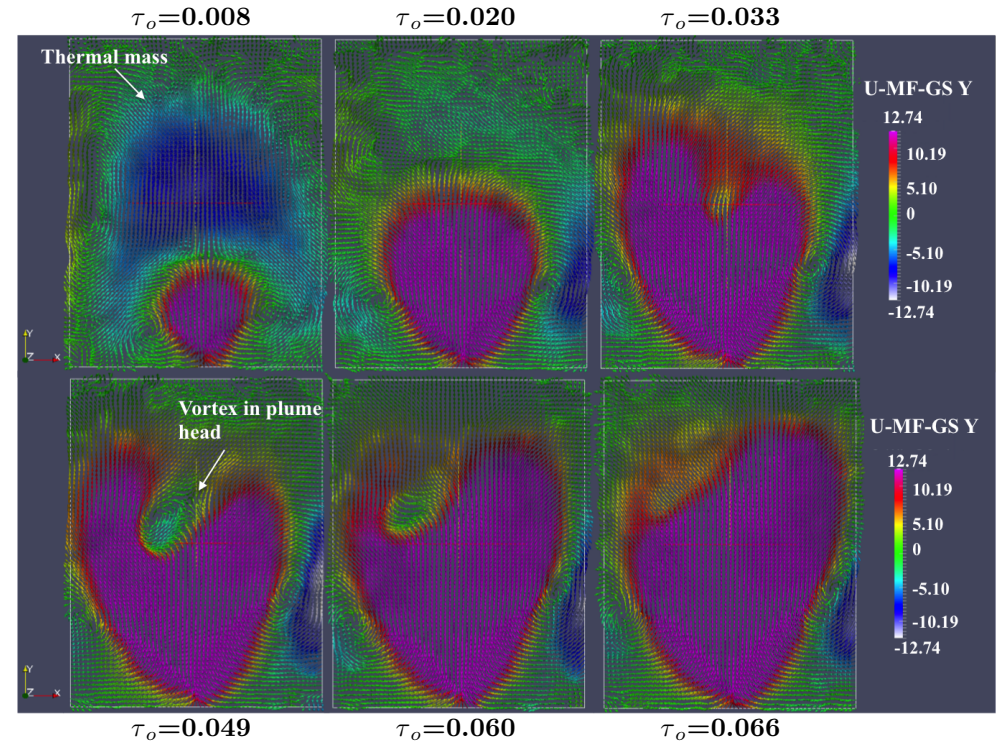
(b) ΔT=13.3°C SPIV experiment with non-dimensional velocity vectors. Images were chosen at 0.008, 0.020, 0.033, 0,049, 0.060 and 0.066 after the beginning of the experiment.

Figure 6.50: A visual comparison of two different ΔT=13.3°C plumes. The shadowgraph plume forms a "lens shape" between τ_o=0.027 and 0.034. A vortex appears to form from τ_o=0.033 in the SPIV experiment and shows the reason for the lens shape in the shadowgraph experiment.

6.3.3.3   Surviving plume comparison

Parameter	Shadowgraph experiment	SPIV experiment	Units
T_h	60.0	59.4	°C
T_∞	18.8	18.2	°C
ΔT	41.2	41.2	°C
η_h	2.31	2.41	Pa s
η^*	34.11	34.54	-
ρ_h	1419.61	1419.91	kg/m^3
Ra_h	1.56×10^7	1.49×10^7	-
Pr_h	1.55×10^4	1.62×10^4	-

Table 6.10: Comparison of measured and calculated parameters for surviving plume experiments.

The experiments conducted had similar ambient temperatures of the fluid and thus similar $\eta^*$and ΔT (Table 6.10). Figure 6.51 show that in both experiments the plume ascended to the top of the tank and therefore both experiments agree qualitatively. At τ_o=0.002 the shadowgraph plume was not observed but a black mound, likely representative of the growth of the TBL, was seen. At the same time, in the SPIV experiment the plume had grown and had the largest velocity (U_o=17.84) of all the material in the tank. There remained a difference between the two plumes height at about τ_o=0.003. However, by τ_o=0.009 the plumes in both visualisation techniques appeared to be at the same height and later ascended to the surface. The plumes are both axisymmetric but the SPIV experiment is pushed slightly off centre due to the low velocity thermal mass (U_o=-12.74) on the LHS of the tank.
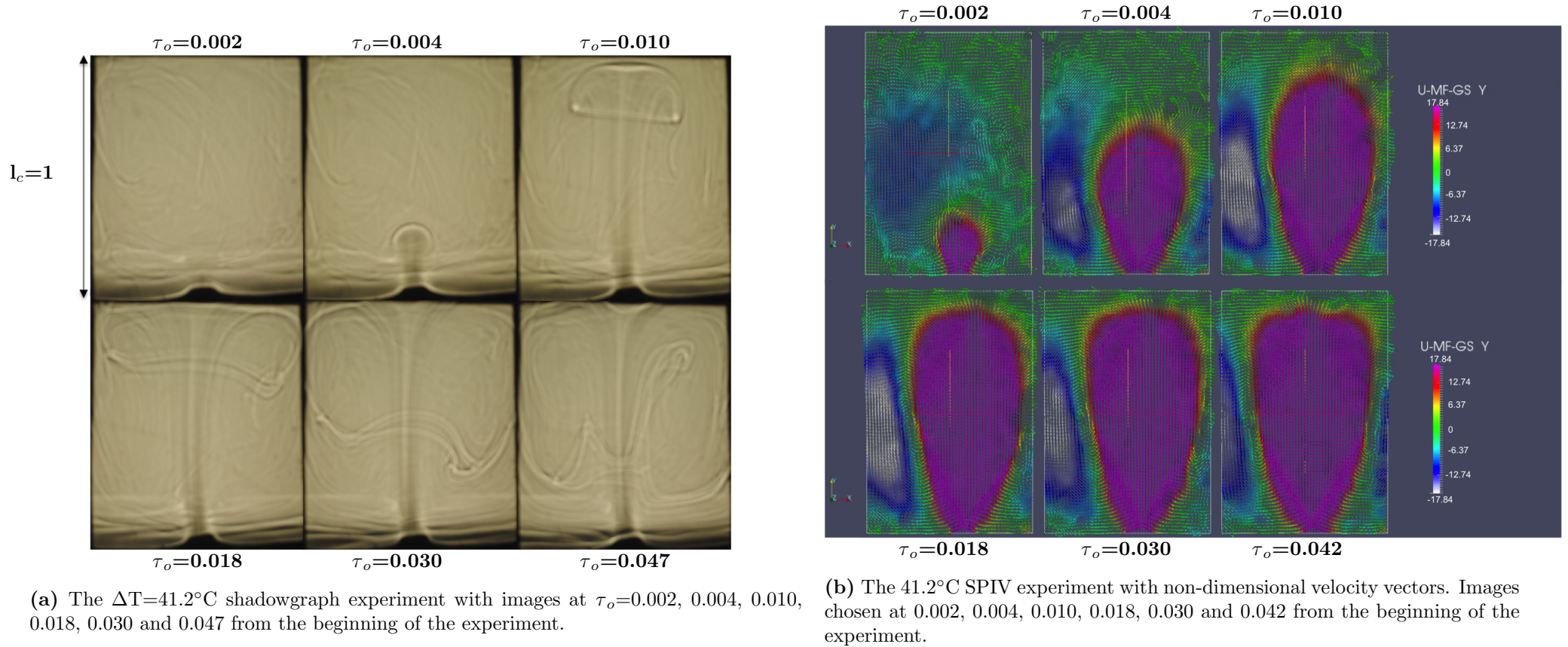
(a) The ΔT=41.2°C shadowgraph experiment with images at τ_o=0.002, 0.004, 0.010, 0.018, 0.030 and 0.047 from the beginning of the experiment.

(b) The 41.2°C SPIV experiment with non-dimensional velocity vectors. Images chosen at 0.002, 0.004, 0.010, 0.018, 0.030 and 0.042 from the beginning of the experiment.

Figure 6.51: A visual comparison of two different ΔT=41.2°C plumes. Both plumes ascend to the top of the tank and appear axisymmetric.

6.3.4   Comparison to a previous SPIV experiment

The result from the SPIV "lenticular" collapse was compared to the SPIV result of Newsome (2011), which was conducted in the same size tank and using the same experimental fluid. A comparison of parameters between the two experiments are displayed in Table 6.11.

Parameter	"lenticular" collapse	Newsome (2011) plume	Units
T_h	31.3	38.0	°C
T_∞	18.0	25.2	°C
ΔT	13.3	12.8	°C
η_h	25.29	7.10	Pas
η^*	3.36	4.44	-
ρ_h	1434.09	1433.01	kg/m^3
Ra_h	4.68x10^5	6.20x10^4	-
Pr_h	1.70x10^5	4.76x10^4	-

Table 6.11: Comparison of measured and calculated parameters between the two experiments with a similar temperature difference.

Figure 6.52 compares the maximum velocity of the Newsome (2011) plume at ΔT=12.8°C and the ΔT=13.3°C plume for this thesis. The experiments were run for different lengths of time but the change of velocity agrees closely in both plumes to ascertain a similar boundary for region 1. A dotted line has been shown for the commencement of velocity beginning to decrease in Newsome (2011), which was τ_o=2x10^{-3} earlier than for the ΔT=13.3°C plume. In region 2, the two plumes showed different velocities. The ΔT=12.8°C plume velocity was decreasing from U_o=26.21 to U_o=19.33, whereas, the velocity of the ΔT=13.3°C plume remained constant, at U_o=64.0. The velocity of the ΔT=13.3°C was on average approximately U_o=40.0 larger than for the ΔT=12.8°C plume.
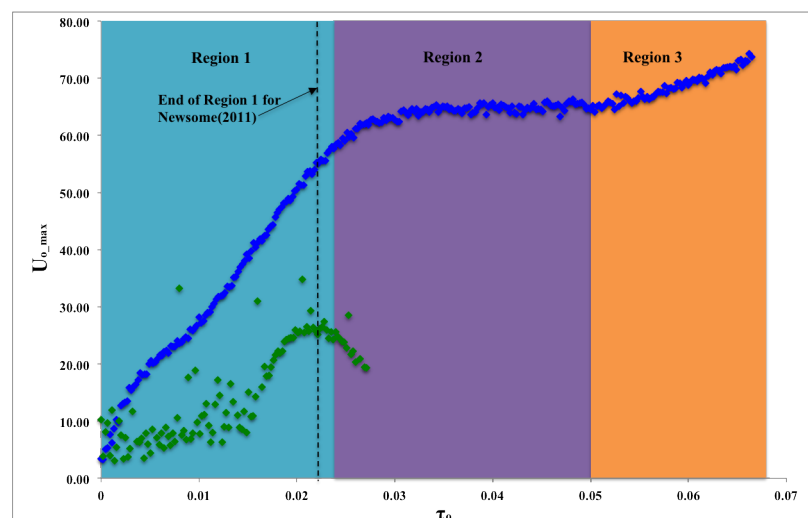
Figure 6.52: A comparison of the maximum U_o of the ΔT=13.3°C SPIV (blue diamonds) and ΔT=12.8°C plume (Newsome (2011), green diamonds) as a function of τ_o. The non-dimensional velocity of the ΔT=12.8°C plume began to decrease τ_o=2x10^{-3} earlier than the Liquidose 436 syrup plume.
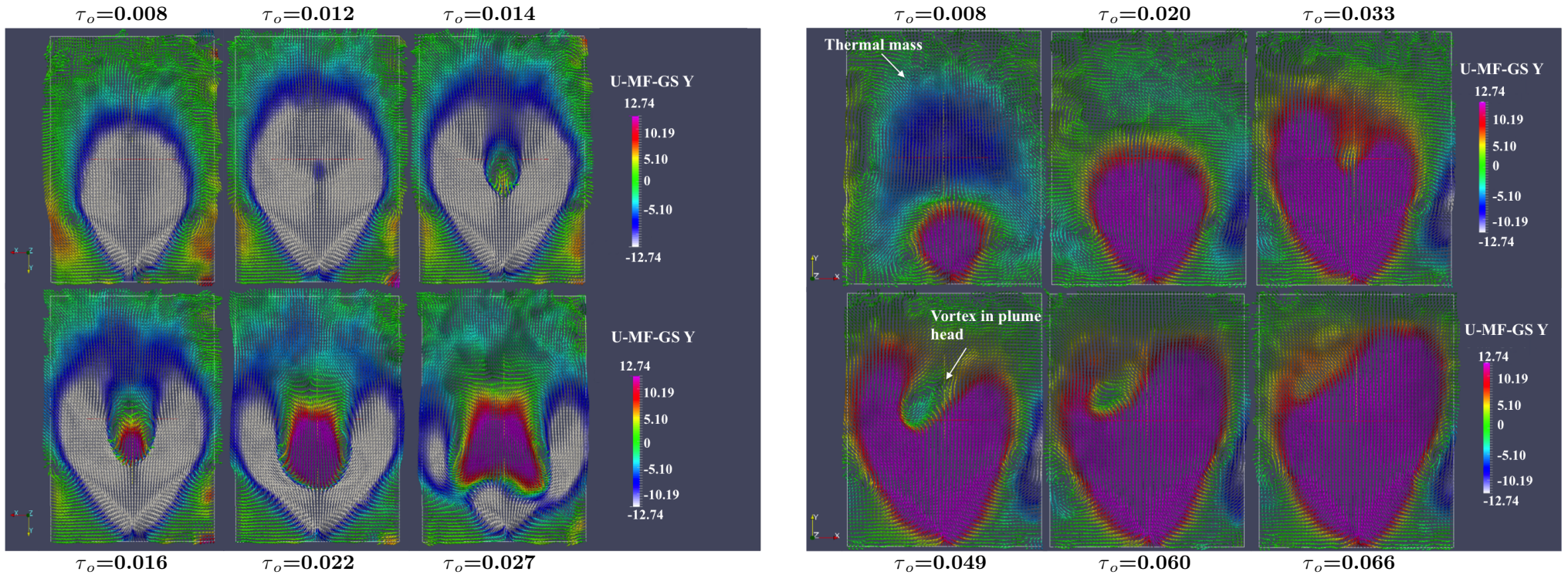
(a) ΔT=12.8°C SPIV experiment (Newsome, 2011), with images chosen at τ_o=0.008, 0.012, 0.014, 0.016, 0.022 and 0.027 after the beginning of the experiment.

(b) ΔT=13.3°C SPIV experiment, with images chosen at τ_o= 0.008, 0.020, 0.033, 0.049, 0.060 and 0.066 after the beginning of the experiment.

Figure 6.53: A visual comparison of the velocity vectors (U_o) for the ΔT=12.8°C plume (Newsome, 2011) and ΔT=13.3°C plume showing "lenticular" collapse. The non-dimensional velocity range ±12.74 was chosen to enable direct comparison in the data. Note that the general behaviour observed is the same in both experiments. However, the ΔT=12.8°C plume developed a central vortex earlier than the ΔT=13.3°C plume.

In Figure 6.53 both sets of images of the plumes demonstrate that the same central vortex appeared in the plume and the images compare qualitatively and quantitatively well. However, these vortices appear at different times (τ_o=0.012 in Newsome (2011) and τ_o=0.033 in the ΔT=13.3°C) but with similar maximum velocities (U_o=5.10). There is a significant difference in the velocity of the two plumes. The velocity of the Newsome (2011) plume is U_o=-12.74 and remained very low for the whole experiment. The ΔT=13.3°C plume had a maximum velocity of U_o=12.74. The Newsome (2011) plume began to collapse around τ_o=0.023 which was when the maximum velocity of the plume in Figure 6.52 was decreasing (region 2), this collapse however, was not observed in the ΔT=13.3°C plume. This higher temperature difference plume stalled for a period when the central vortex was observed, but then the plume began to ascend again in the tank. The velocities of the two plume vortices differed, with the Newsome (2011) plume's central vortex having a maximum velocity of U_o=12.74. In contrast, the ΔT=13.3°C plume had a velocity between U_o=±5.10. In addition, there was a large downward low velocity zone at the beginning of the ΔT=13.3°C plume experiment which was not observed in the ΔT=12.8°C plume, suggesting that there were differing starting conditions in the tanks. These conditions differ because the ΔT=12.8°C plume (Newsome, 2011) was in an isothermal system due to the presence of an outer tank in the laboratory used to regulate the temperature, which led to axisymmetric plume formation. Conversely, the ΔT=13.3°C plume was asymmetric because the plume was likely to have been affected by background flow. Despite this the general behaviour of these two plumes was the same.
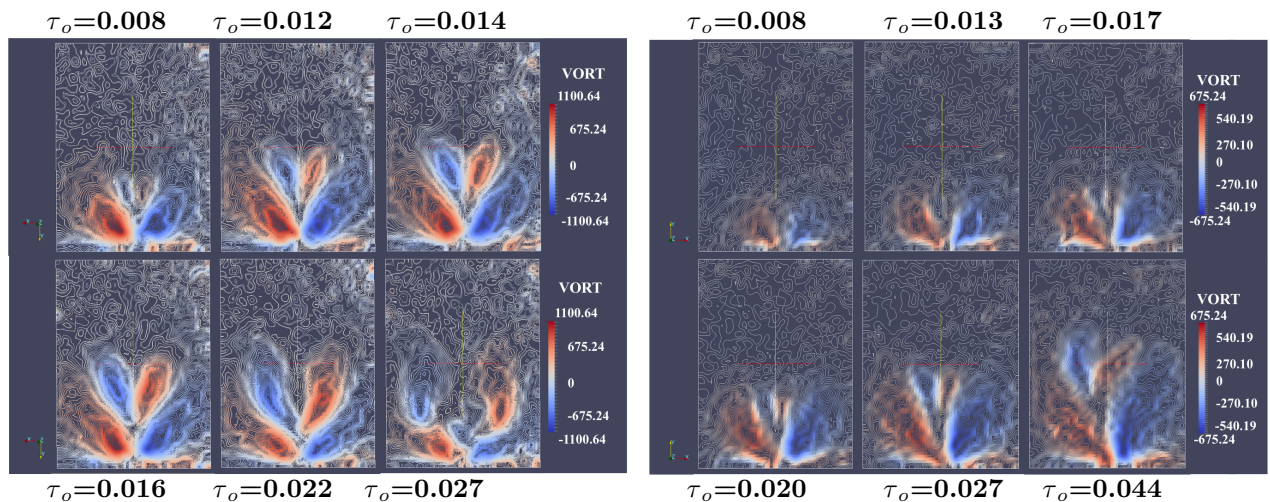
(a) Images at τ_o=0.008, 0.012, 0.014, 0.016, 0.022 and 0.027 after the beginning of the experiment.

(b) Images at τ_o=0.008, 0.013, 0.017, 0.020, 0.027 and 0.044 after the beginning of the experiment.

Figure 6.54: Comparison of the vorticity (ω_o) of the ΔT=12.8°C (Newsome, 2011) and ΔT=13.3°C plumes. Both show the plume split and two new lobes with opposite spin direction to the material spinning in the plume on that respective side.

In Figure 6.54a, the vorticity of the ΔT=12.8°C plume (Newsome, 2011) in the experiment showed similar rotation to the ΔT=13.3°C plume (Figure 6.54b) and thus are qualitatively

similar. At τ_o=0.008 the ΔT=12.8°C plume appeared to already be separating in the centre, with two new lobes forming. These extra lobes were not developed in the ΔT=13.3°C plume until τ_o=0.13. The vortices which developed in both plumes during the "lenticular" collapse showed that the material was spinning in two counter-rotating directions when compared to the lobes of the plume. Additionally, in both plumes the highs of the vorticity closest to the heater. While the vorticity in the ΔT=12.8°C plume was higher by 425.4, the behaviour observed was the same.

6.4   Sources of Experimental Error

In general, there are two types of error; instrumental error and experimental error in the analysis or interpretation of the results. Standard best practices were implemented to minimise measurements error during the experiments. Physical measurement of the fluid prior to experiments were averaged. The measurements undertaken for density and viscosity were repeated for multiple samples to evaluate the syrup variability between batches.

Experimental error is potentially a greater source of error and can occur throughout all measurements. Error estimation is difficult as the measurements of the shadowgraph plumes rely on the interpretation of the shadowgraphs; because there is no direct 1:1 correspondence between the object and its shadow, they are not to scale in general. Errors in the experimental data from the shadowgraphs can be associated with misalignment of the apparatus with respect to the light beam, noise generated at different stages of the experiment and intrinsic unsteadiness of the convection process itself. To help minimise error, the equipment was configured by the same investigator and markers put in place if equipment was moved between experiments. Measurement error was also minimised by undertaking measurements of the the whole plume's geometry in its entirety prior to moving on to another plume.

In practice it is typically difficult to quantify the error associated with PIV experiments. Although various researchers have estimated the uncertainty associated with numerous factors (such as Δt, particle size and seeding density to name a few) for ideal conditions (e.g ideal potential flow and noise free images - see discussions in Raffel et al. (2007) for further information) the empirical relations have limited use in practice, due to the fact that the errors are dependent on a number of factors including:

- Local shear in the flow - observed to be small in the experiments here.

- 3D flow - observed to be very small in the experiments.

- How the particles interact - we observe from image to image that the particles did not interact and therefore, there was no deformation between particles.

- Distribution of light from the lightline - It would be expected that it would have top hat distribution, but this is rarely the case. The distribution from the lightline had little effect but is related to the PIV system getting confused by changes in the brightness of the particles due to the normal distribution of light from the lightline.

- Noise from the cameras - all electrical components have noise but the effect will be insignificant in the experimental data.

The errors associated with the local shear and 3D flow (causing the patterns on neighbouring particles to deform or particles to 'drop out' of the lightsheet, respectively) can be largely eradicated by selecting an appropriately small Δt (discussed in Section 5.5). Although 'drop out' cannot be eradicated entirely, the rate of such occurrences will be approximately 1% if a small Δt is used. The three other errors mentioned are generally associated with the interpolation of the cross-correlation matrix (Raffel et al., 2007) and have an effect of ± 0.5 pixels. This value is represented as the extreme upper bound of uncertainty of the vector estimates. Using this extreme upper bound the percentage error for each experiment was calculated and is shown in Table 6.12. When configuring a PIV experiment it is important to select an appropriate Δt to ensure that the local shear and particle 'drop out' are not too large, but not too small a Δt that total particle displacements are too small and therefore the relative errors in the particle displacement become too large. By selecting appropriate Δts, these errors are effectively minimised.

$\mathbf{T}_h$ /$^\circ$C	$\mathbf{T}_\infty$ /$^\circ$C	$\Delta\mathbf{T}$ /$^\circ$C	Max Pixels	% error
24.2	19.2	5.0	5.88	8.50
31.3	18.0	13.3	10.5	4.76
39.4	18.4	21.0	25.9	1.93
59.4	18.2	41.2	22.4	2.23

Table 6.12: The percentage error of the selection of SPIV experiments displayed in this chapter.

6.5   Summary

This chapter presented a selection of the experiments conducted in the Fluid Dynamics laboratory at UCL to investigate the possibility that collapse can occur in a single viscous fluid with a constant heat source. In both methods of visualisation similar collapse phenomena were observed. These collapse phenomena were also observed in two differing fluids and the "lenticular"

collapse observed in two different laboratories. This suggests that these differing collapse phenomena can occur in multiple syrups. The interpretation of these observations will be discussed in Chapter 8.

Chapter 7

Simulating stall and collapse in mantle plumes

The use of numerical models to investigate the dynamics of Earth over geological timescales is firmly established as practice in the geodynamics community (May et al., 2013). Fluidity, a computational modelling finite element package (AMCG, 2014; Piggott et al., 2008) utilises a multi-phase Computational Fluid Dynamics code capable of solving numerically geodynamic problems using the Navier Stokes equation. The finite element simulations of Fluidity centre upon a discretisation of unstructured simplex meshes, by representing complex geometries in an uncomplicated way through increasing and decreasing mesh resolution and transferring continuous models and equations into discrete counterparts (Davies et al., 2011). Discretisation is usually one of the first steps in a numerical model to produce equations suitable for numerical evaluation and implementation. The main aim of this numerical investigation is to utilise Fluidity to investigate the possible stall and collapse of thermal plumes.

7.1   The Finite Element Method - Fluidity

The finite element method has the ability to be used in almost any mathematical or mathematically modelled physics problem and has been widely used in the studies of mantle dynamics (Christensen, 1984; Baumgardner, 1985; King et al., 1990; van den Berg et al., 1993; Moresi et al., 1996; Bunge et al., 1997; Zhong et al., 2000, 2007)). This technique has emerged as one of the most powerful numerical methods so far devised (Donea and Huerta, 2003). The finite element method is advantageous over other numerical methods such as finite difference models for a number of reasons. Finite difference is restricted to handle rectangular spaces. Whereas,

the finite element method handles geometries in a more straightforward manner and they do not overlap in space. Additionally, it solves differential equations, material properties and associated boundary conditions in complex geometry with ease, by breaking the continuum into discrete elements, which can be programmed in a flexible and general format (Zienkiewicz and Taylor, 2000; Donea and Huerta, 2003). Whereas, the finite difference procedure can be interpreted as an approximation based on local, discontinuous, shape functions. Early finite difference methods were based on a regular arrangement of nodes which (Zienkiewicz and Taylor, 2000) and is commonly restricted to applications with uniform grids which limits accuracy and application in solving general problems with irregular or curved boundaries (Zienkiewicz and Taylor, 2000). These reasons are why the finite element method was chosen to model mantle plumes.

Fluidity was selected for its ability to simulate mantle convection accurately and efficiently in both 2D and 3D (Davies et al., 2011). The adaptive nature reduces the computational requirements compared to a fixed mesh solution and improves the quality of solutions in convection-dominated geodynamic problems (Davies et al., 2007). The numerical simulations were undertaken because mathematical models to study geodynamic processes are complementary to analogue laboratory models (May et al., 2013) and have been used successfully to simulate mantle plumes by Davies et al. (2011) and Newsome (2011).

Davies et al. (2011) validated Fluidity for mantle plumes by simulating the combined experimental and numerical mantle plume investigations of Vatteville et al. (2009) using fixed and adaptive meshes in 3D. The experimental thermal plumes produced by Vatteville et al. (2009) were generated in a square tank of silicone oil at different heater powers and the numerical simulation reproduced these results in 2D using Sepran, a finite element method. The boundary conditions chosen for the Fluidity simulations mimicked the laboratory tank. Fluidity compared quantitatively well with the velocity field from the PIV experiments and corroborated the consistently predicted higher conduit-velocity observed by Vatteville et al. (2009) in their numerical code compared to experimental measurements. Therefore, Fluidity was chosen to simulate the experimental plumes from the Geophysical Fluid Dynamics laboratory at UCL. Furthermore, Fluidity was used by Newsome (2011) and showed good agreement with the experimental results.

In numerical simulations, mantle convection can be approximated as a fluid dynamical process, involving a number of complicated physical effects (Davies et al., 2011; Turcotte and Oxburgh, 1967; McKenzie et al., 1974). The equations governing mantle convection (Chapter 4) are derived from the conservation laws of mass, momentum and energy. The simplest mathematical formulation assumes incompressibility and the Boussinesq approximation (McKenzie et al., 1974; Davies et al., 2011). If a material is perfectly incompressible then its density cannot change.

The density of the material is therefore independent of pressure and temperature, giving $\rho=\rho_o$, with ρ_o the reference density. All real materials are compressible to some extent, which means that the changes in pressure and temperature cause changes in density. However, in many physical circumstances the change is sufficiently small for the assumption of incompressible flow to hold. In other words the Boussinesq approximation is used for buoyancy-driven flows, where density differences are sufficiently small to be neglected but means that the fluid can move in the simulations. Therefore, the fluid represented in the Fluidity simulations is incompressible.

7.1.1   Boundary conditions

To form a well-posed system upon which to attempt a numerical discretisation, the describing behaviour of the system must be supplemented with appropriate boundary conditions based on physics. These boundary conditions are as important as the underlying equations in the simulations and are strongly dependent upon the geometry and equations to be solved. Many problems are strongly influenced by the behaviour at boundaries; errors here are likely to pollute the solution everywhere. The boundary conditions that can be applied to simulations are strongly dependent on the discretisation that is used. With finite element methods there are many options available for the boundary conditions. Two different types of boundary conditions can be implemented in Fluidity: Dirichlet or Neumann. A Dirichlet boundary condition is implemented as a fixed boundary condition and prescribed for the momentum equation. A special case in fluid dynamics is the no-slip condition for viscous fluids that enforces all three components of velocity to be zero relative to the boundary. The point source heater in the simulations was also configured with a Dirichlet boundary condition. The Neumann boundary condition is imposed on an ordinary or a partial differential equation that specifies the value the derivative of a solution is to take on the boundary of the domain. The base of the tank in the simulations was configured to be a Neumann boundary condition.

7.2   Physical set-up of mantle plume simulations

The 3D numerical Stokes model for this study was configured with Dr. R. Davies, with the aim of investigating whether plumes simulated using Fluidity could demonstrate the observed experimental stall and collapse phenomena. The configuration involved only half of the tank to be simulated, for two main reasons. Firstly, the computational cost was reduced and, secondly, axial symmetry was assumed because there were no outside influences affecting the simulations. The geometry of the tank was easily defined in Cartesian space by points and straight lines. The

surface domain was represented and interior mesh configured in Gmsh (Geuzaine and Remacle, 209), with a length of 0.0075m for the side of the triangle mesh. Every 5 timesteps the mesh was optimised, with adaptive timestepping targeting a maximum Courant number of 2.5 (which is a necessary condition for stability when solving partial differential equations).

In each run the initial fixed input mesh was provided to define the initial conditions of the fields, with maximum and minimum edge lengths of the mesh set at 0.02 and 0.002m respectively. The experimentally measured heater evolution and the cold ambient fluid temperature were set as initial conditions and flow was driven by localised heater temperature at the bottom left corner of the simulated tank. The ambient temperature was applied to all tank sides bar the point source heater to impose isothermal conditions. This was a major difference to the physical set up of the experimental tank. The velocity field was configured to adapt to the temperature field because Stokes' flow couples these two fields. Additionally, no-slip boundaries were applied to the top, right hand sides and base of the tank as per the experiments and thus a Dirichlet boundary condition was used. A symmetry boundary was applied to the left hand side of the tank which would be the middle of the experimental tank. Simplified thermal boundary conditions were implemented to approximate the tank geometry of the laboratory. Additionally, a discretisation of 1 was used and the simulations were run for 128,000 seconds unless explicitly stated otherwise.

It is possible to vary parameters and extend the parameter range more easily in numerical simulations than in experiments. Therefore, to test whether the aspect ratio of the tank played a role in the stall and collapse of plumes, the height and width of the tank were varied systematically. Additionally, two different thermal expansions and thermal diffusivities were investigated, as was the difference between the fixed heater temperature and heater function generation of the plumes. Higher temperature difference simulations were conducted to compare with experimental results (Liquidose 436 syrup $\Delta T=25°C$ and Golden syrup $\Delta T=18°C$). There are two geometries fixed in the comparison to experimental results - the ratio of width to height of the tank fixed at 2 (due to half the tank width simulated) and the ratio of the size of the local heat source to bottom width of the tank set at 6.625. The viscosity and ambient density for the simulations were based on the experimental fluid properties for the relevant syrup observed previously (Table 5.3) and are presented along with the thermal expansion and thermal diffusivities for the Liquidose 436 syrup and Golden syrup in Table 7.1.

Parameter	Liquidose 436 syrup	Golden syrup
g (ms^{-2})	9.81	9.81
Ra_c	1700.33	1700.33
κ $(\mathrm{m}^2/\mathrm{s})$	$1.04\mathrm{x}10^{-7}$	$1.22\mathrm{x}10^{-7}$
α $(^\circ\mathrm{C}^{-1})$	$3.54\mathrm{x}10^{-4}$	$6.30\mathrm{x}10^{-4}$
ρ $(\mathrm{kg/m}^3)$	1449.89-0.505T	1460.91-0.895T
η (Pas)	$443.37\mathrm{e}^{(-T/10.84392)}+0.559$	$1846.59\mathrm{e}^{(-T/6.51504)}+2.345$

Table 7.1: Physical parameters for Liquidose 436 syrup and Golden syrup simulations

7.3   Numerical results

The results of the simulations undertaken were presented for the Liquidose 436 syrup and Golden syrup and visualised through the software package Paraview.

7.3.1   Liquidose 436 Syrup Experimental Results Comparison

The following temperature differences for experimental and numerical runs were compared (Table 7.2).

$\mathbf{T}_h/\ ^\circ\mathbf{C}$	$\mathbf{T}_\infty/\ ^\circ\mathbf{C}$	$\mathbf{\Delta T}$ $/^\circ\mathbf{C}$	**Thermal Expansion/** $^\circ\mathbf{C}^{-1}$	$\eta_h/$ **Pas**	$\rho_h/$ $\mathbf{kg/m}^3$	$\mathbf{Ra}_h$
23.4	18.4	5.0	$3.54\mathrm{x}10^{-4}$	51.80	1438.08	$8.64\mathrm{x}10^4$
30.1	16.8	13.3	$3.54\mathrm{x}10^{-4}$	28.18	1434.70	$4.14\mathrm{x}10^5$
42.4	17.4	25.0	$3.54\mathrm{x}10^{-4}$	9.44	1428.49	$2.34\mathrm{x}10^6$

Table 7.2: The parameter values of the experiments used for numerical simulations. Where the Rayleigh number is for the plume at the heater temperature.

Prior to undertaking any simulations, a convergence analysis was undertaken for the ΔT=13.3°C run because the mesh constructed was required to have the ability to solve the given problem and ensure numerical accuracy (Frey and George, 2008). The element size was reduced, without changing the element order, by increasingly refining the model for each run by changing the metric to estimate the convergence error. Without several runs, the error in the initial mesh would have been unknown (Table 7.3). The 0.0025 metric value displayed the most accurate result because of the maximum coordinate nodes (36,220) used in the mesh (Figure 7.1). However, due to the computational cost and the temperature differences to be investigated it was decided that the 0.005 metric would be used, because the percentage difference from the 0.0025 metric of 0.1% would lead to an insignificant increase in error and therefore would still lead to accurate results.

Metric	Coordinate mesh nodes	Coordinate Mesh Surface elements	Coordinate mesh elements	Height in m at 3hrs 15 minutes	Percentage difference from convergence
0.03	5275	2904	25822	0.14	2.1
0.02	6981	3418	34846	0.145	1.6
0.01	11529	4582	59385	0.15	1.1
0.0075	14430	5340	75247	0.157	0.4
0.005	20074	6524	106212	0.16	0.1
0.0025	36220	9536	195285	0.161	0.00

Table 7.3: Examining the convergence error through different metric simulations at ΔT=13.3°C for Liquidose 436.
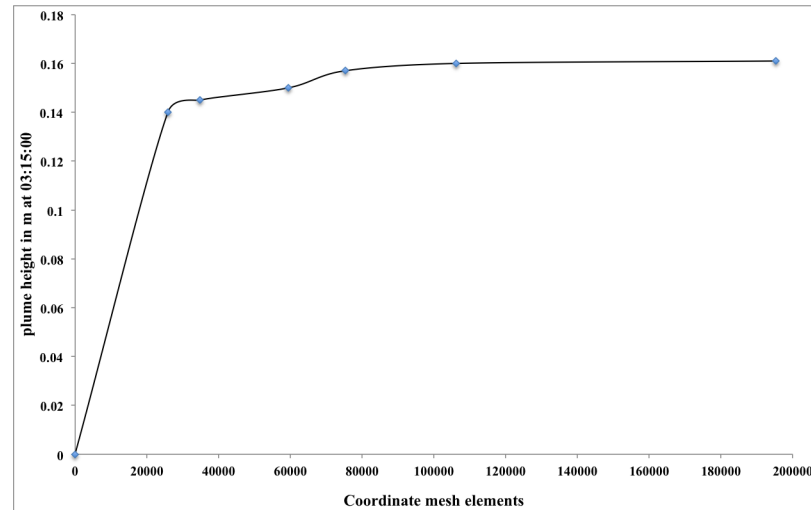
Figure 7.1: The convergence error analysis of the coordinate mesh elements for different metrics for the ΔT=13.3°C run.

7.3.1.1 ΔT=5°C plume comparison

Figure 7.2 is a visual comparison of the experimental and simulated plumes (visualised with the highest contour 0.0586°C above the ambient temperature of 18.4°C).
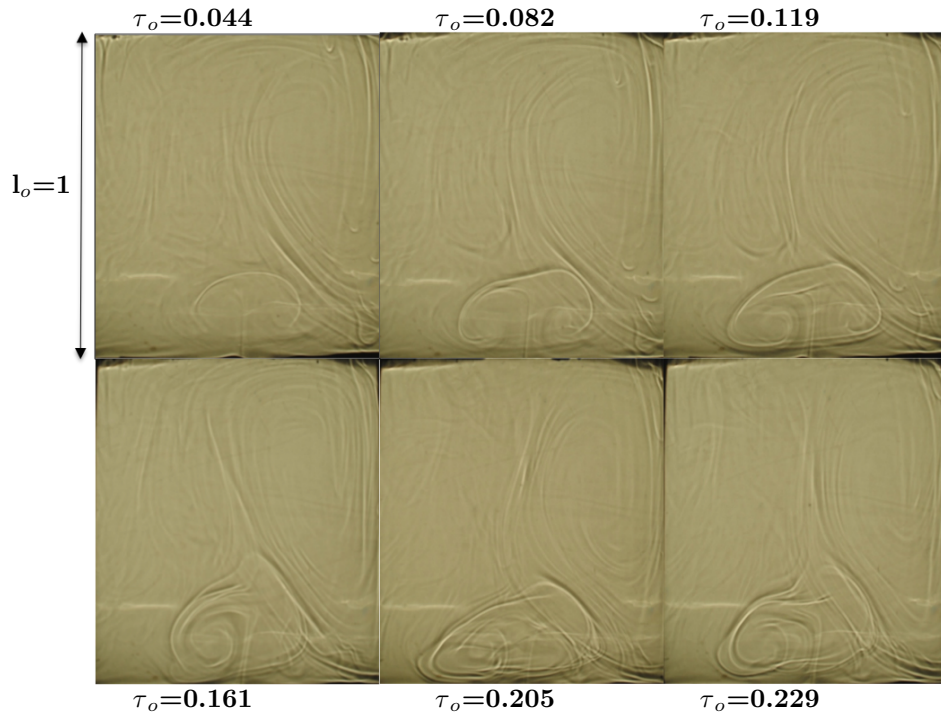
τ_o=0.044 τ_o=0.082 τ_o=0.119

l$_o$=1

τ_o=0.161 τ_o=0.205 τ_o=0.229

(a) Shadowgraph experiment images at τ_o=0.044, 0.082, 0.119, 0.161, 0.205 and 0.229 from the beginning of the experiment.

τ_o=0.044 τ_o=0.082 τ_o=0.119

τ_o=0.161 τ_o=0.173 τ_o=0.190
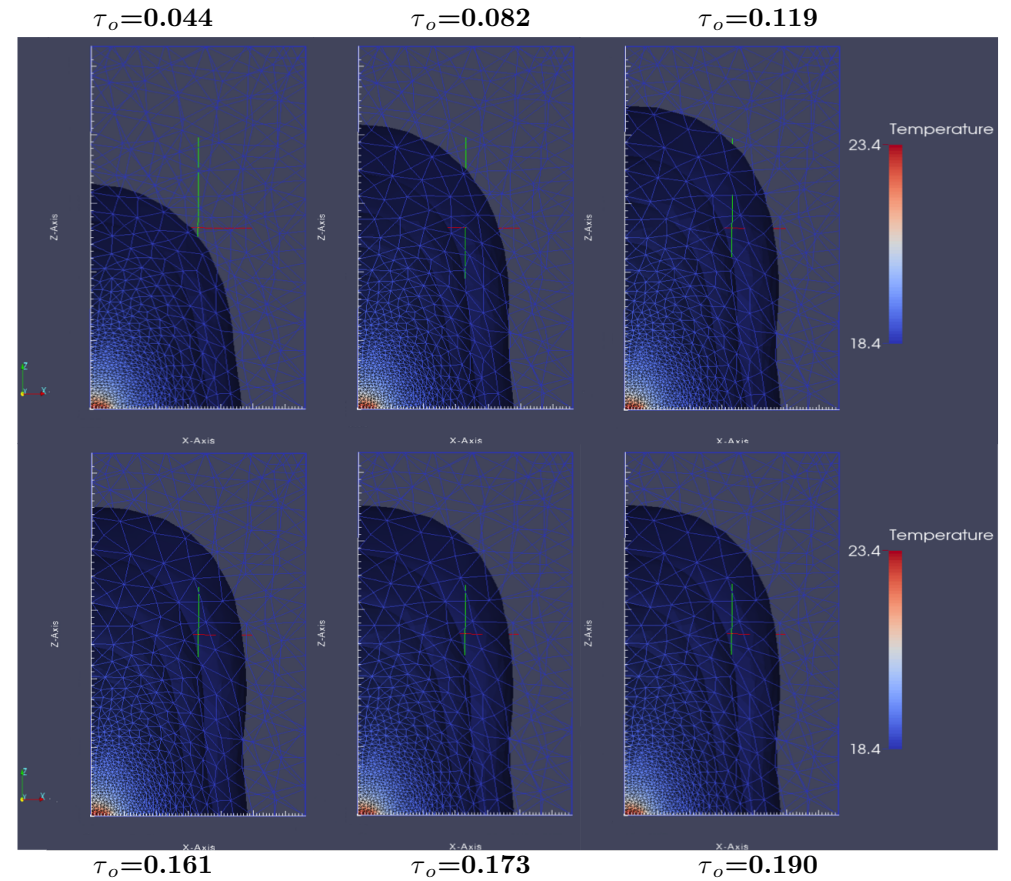
(b) Numerical simulations visualised with Paraview, with images at τ_o=0.044, 0.082, 0.119, 0.161, 0.173 and 0.190 after the beginning of the simulation.

Figure 7.2: A visual comparison of ΔT=5°C Liquidose 436 plumes. The experimental plume stalled and then collapsed, whereas the simulated plume ascended in the tank to near the surface and then stalled. Neither plume ascended to the top of the tank.

The simulated plume ascended l_o=0.468 further in the tank and stalled at l_o=0.851 (Figure 7.3), compared to the experimental plume, which ascended for τ_o=0.030 to a height of l_o=0.245 before, stalling for τ_o=0.089. The experimental plume then began to collapse but then grew in height to the maximum (l_o=0.380) before the collapsing once again at τ_o=0.157. In contrast, the simulated plume reached a maximum height (l_o=0.851) 123.9% greater than the maximum experimental plume height (l_o=0.380) as shown in Figure 7.3. The experimental plume formed after τ_o=0.004 due to the building of the thermal boundary layer. However, at the initiation of the numerical simulations there was already a perturbation of l_o=0.009. The plume shape also differed. The experimental plume displayed the typical mushroom head and thin conduit, while the simulated plume ascended more finger-like, as seen in the isothermal experiments of Whitehead and Luther (1975). Although the simulated plume did not display signs of collapse the plume did stall at τ_o=0.15.
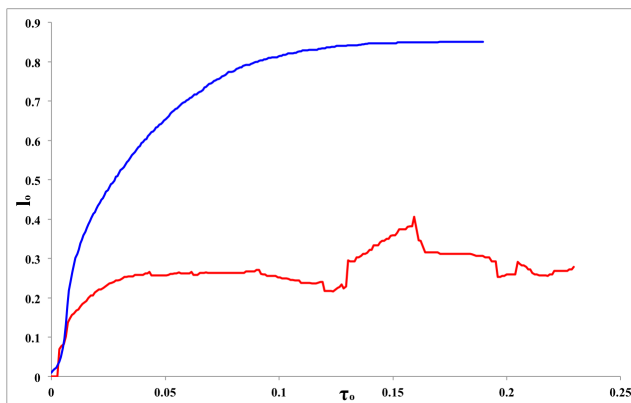
Figure 7.3: The comparison non-dimensional height (l_o) between the experimental results (red) and simulated results (blue) as a function of non-dimensional time (τ_o) for the ΔT= 5°C plume. Neither methods of plume generation led to the plume ascending to the top of the tank.
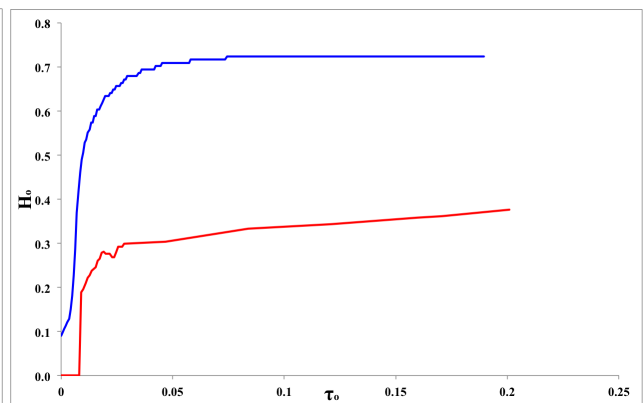
Figure 7.4: The comparison of the non-dimensional head width (H_o) between the experimental results (red) and simulated results (blue) as a function of non-dimensional time (τ_o) for the ΔT= 5°C plume.

Measurements were taken of the head width because the conduit was not discernible in the ΔT=5°C experimental plume. As the simulated plume rose in the shape of a finger, the conduit width and head width were the same. Figure 7.4 displays the difference between the experimental and simulated plume head width. The simulated plume began at a width of H_o=0.091 and increased to a maximum of H_o=0.725 after τ_o=0.074. This was 36% wider than the experimental plume; its maximum width H_o=0.38 at τ_o=0.532. By the end of the experiment the head width was decreasing because the plume was collapsing. The absolute velocity of the simulated plume was U_o=1.78 greater than the experimental plume at the beginning of the investigations (Figure 7.5). The experimental and simulated plume absolute velocities both decreased with a power-law; the experimental plume function was U_o=0.3745$\tau_o^{-0.857}$ and the simulated plume function was U_o=1.6468$\tau_o^{-0.671}$. The maximum absolute velocity reached by the simulated plume was U_o=28.93 whereas, the maximum absolute velocity of the experimental plume was

U_o=19.54. The main difference in the absolute velocity was due to the experimental plume collapsing, which led to a difference of U_o =3.28 at the termination of the investigations.
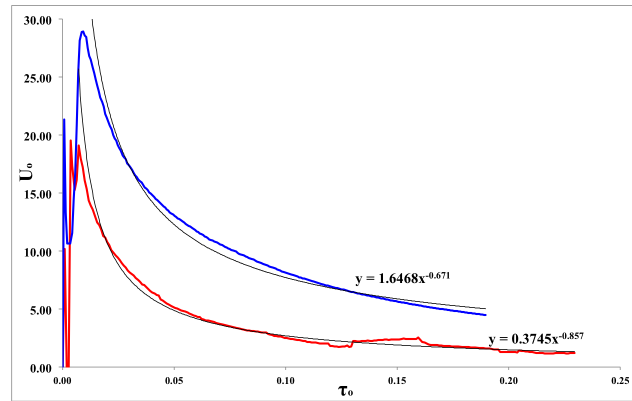
Figure 7.5: The comparison of non-dimensional absolute velocity (U_o) between the experimental results (red) and simulated results (blue) as a function of non-dimensional time (τ_o) for the ΔT=5°C plume. The absolute velocities decreased with power-law functions displayed on the graph.

7.3.1.2 ΔT= 13.3°C plume comparison

Figure 7.6 displays that the experimental and simulated plumes produced different phenomenon. The simulated plume was visualised with the highest contour 0.0585°C above the ambient temperature of 16.8°C. The experimental plume ascended to a height of l_o=0.592, prior to a "lens shape" forming and the plume collapsing. However, there was no sign of this collapse phenomenon in the simulated plume, but the plume did stall at l_o=0.970 (Figure 7.7); 39% higher in the the tank than the experimental plume. As the simulation progressed the shape of the simulated plume became more typical of the plume hypothesis than the ΔT=5°C simulated plume. However, it still remained more finger-like as seen in the results of Whitehead and Luther (1975) than expected. The experiment and simulation ran for different lengths of time, with the numerical simulation running for τ_o=0.19. Although the experiment ran for τ_o=0.107 the plume was only measured up to the point the "lens shape" was observed and material began to flow down the conduit. Comparatively, the simulated plume stalled after approximately τ_o=0.030, a time when the experimental plume was collapsing. This stalling behaviour was more pronounced than in the ΔT=5°C simulated plume with a l_o=0.094 difference in the height reached τ_o=0.096 earlier in the ΔT=13.3°C simulated plume. The conduit width of the experimental and simulated plumes showed significant difference similar to the height of the plumes (Figure 7.8). The plot shows that the simulated conduit width was at least D_o=0.415 (36%) greater than the experimental plume at approximately τ_o=0.024. Unlike the experimental conduit width, which decreased by D_o=0.038 as the plume collapsed, the simulated plume conduit width increased by 7% once the plume had stalled. The stalling of the simulated plume did not appear to inhibit growth of the conduit width.
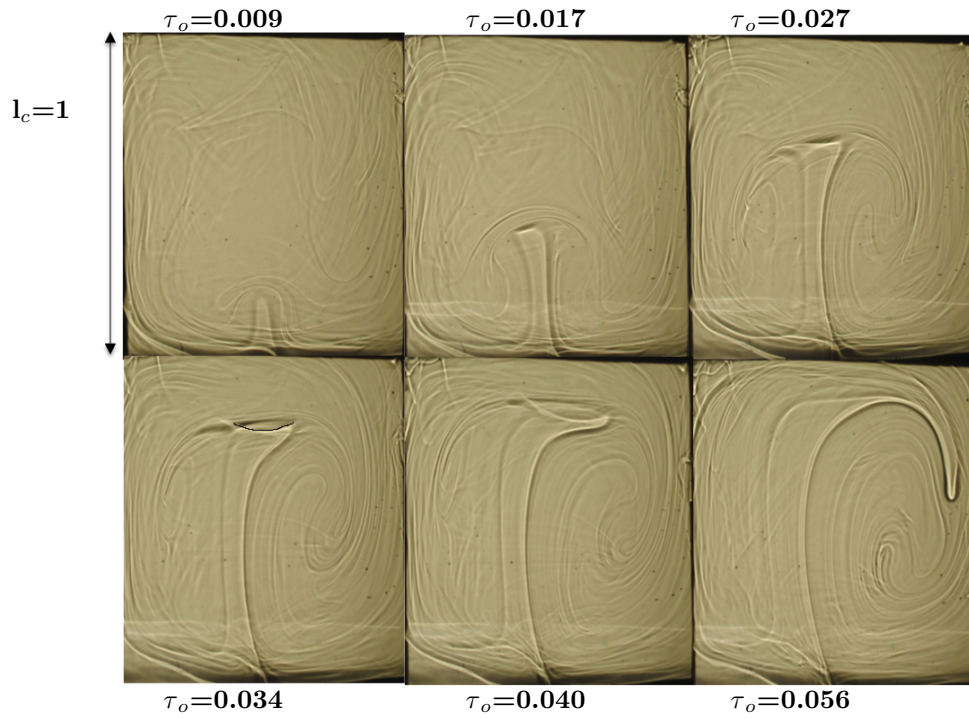
(a) Shadowgraph experiment images of the $\Delta T=13.3°C$ plume. Images are at $\tau_o=0.009$, 0.017, 0.027, 0.034, 0.040 and 0.056 after the beginning of the experiment.
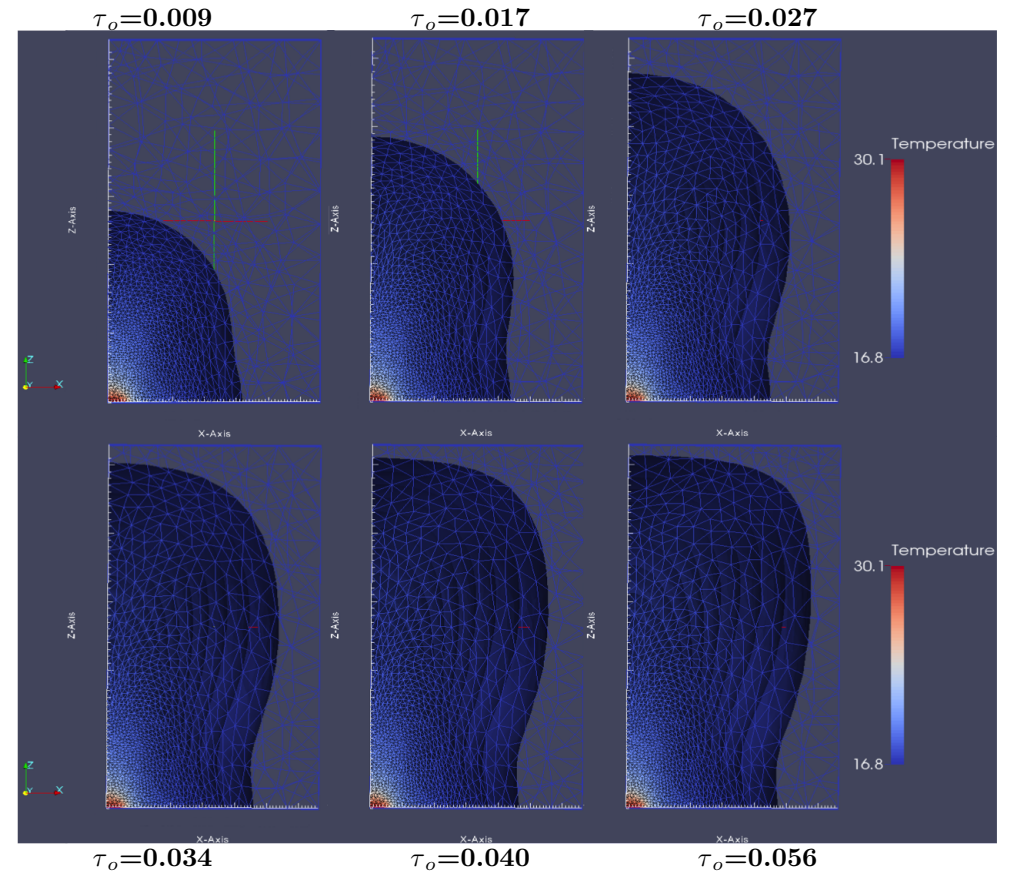
(b) Numerical simulations visualised with Paraview, with images at $\tau_o=0.009$, 0.017, 0.027, 0.034, 0.040 and 0.056 after the beginning of the simulation.

Figure 7.6: A visual comparison of $\Delta T=13.3°C$ Liquidose 436 plumes. The experimental plume showed "lenticular" collapse and the simulated plume stalled near the surface of the tank.
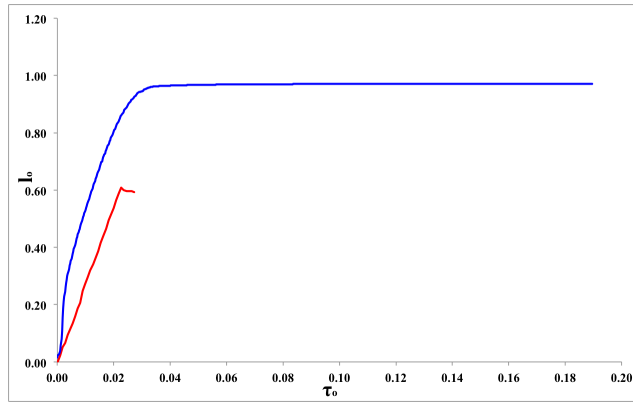
Figure 7.7: The comparison of l_o between the experimental results (red) and simulated results (blue) as a function of τ_o for the $\Delta T{=}13.3°C$ plumes.
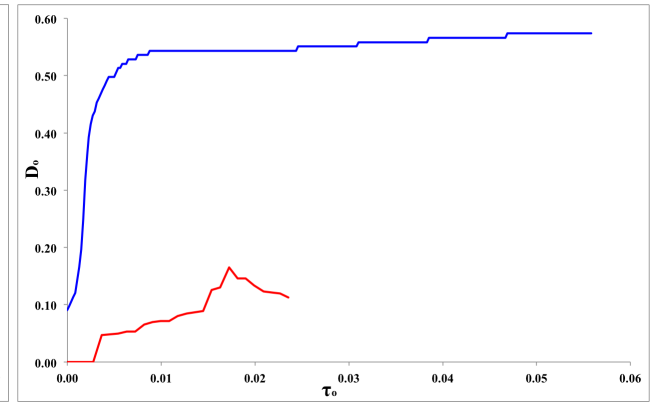
Figure 7.8: A comparison plot of non-dimensional conduit width (D_o) between the experimental results (red) and simulated results (blue) as a function of τ_o for the $\Delta T{=}13.3°C$ plumes.

The absolute velocities of the plumes were 73% different at $\tau_o{=}0.001$ (Figure 7.9). The simulated plume absolute velocity decreased with a power-law $U_o{=}1.4843\tau_o^{-0.813}$, which is not observed in the experimental plume. The absolute velocity of the experimental plume changed by $U_o{=}4.59$ from the beginning of the experiment to the point of "lenticular" collapse. However, the simulated plume absolute velocity changed markedly, by $U_o{=}103.3$ over the simulation, and after $\tau_o{=}0.126$ the simulated plume absolute velocity remained almost constant at $U_o{=}6.30$.
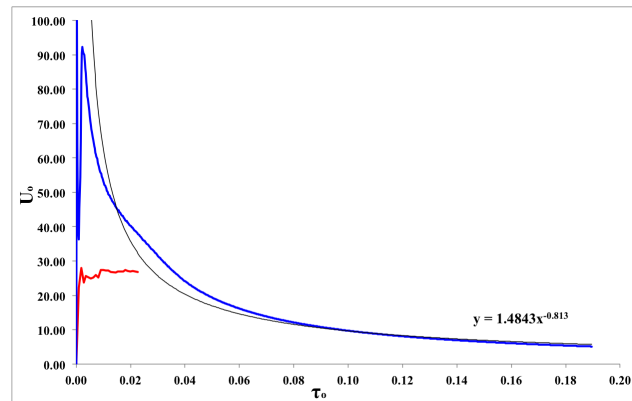
Figure 7.9: The comparison of U_o between the experimental results (red) and simulated results (blue) as a function of τ_o for the $\Delta T{=}13.3°C$ plumes.

7.3.1.3 $\Delta T{=}25°C$ plume comparison

At $\Delta T{=}25°C$, there was excellent agreement quantitatively and visually between the experimental and simulated plumes (Figure 7.10 and Figure 7.11), which both reached the top of the tank. The simulated plume was visualised with the highest contour $0.0583°C$ above the $17.2°C$ ambient temperature. Both methods of generating plumes displayed the expected mushroom shape and both plumes reach the surface at $\tau_o{=}0.022$. Once the plumes reached the top of the tank the plumes flattened and the head spread laterally.
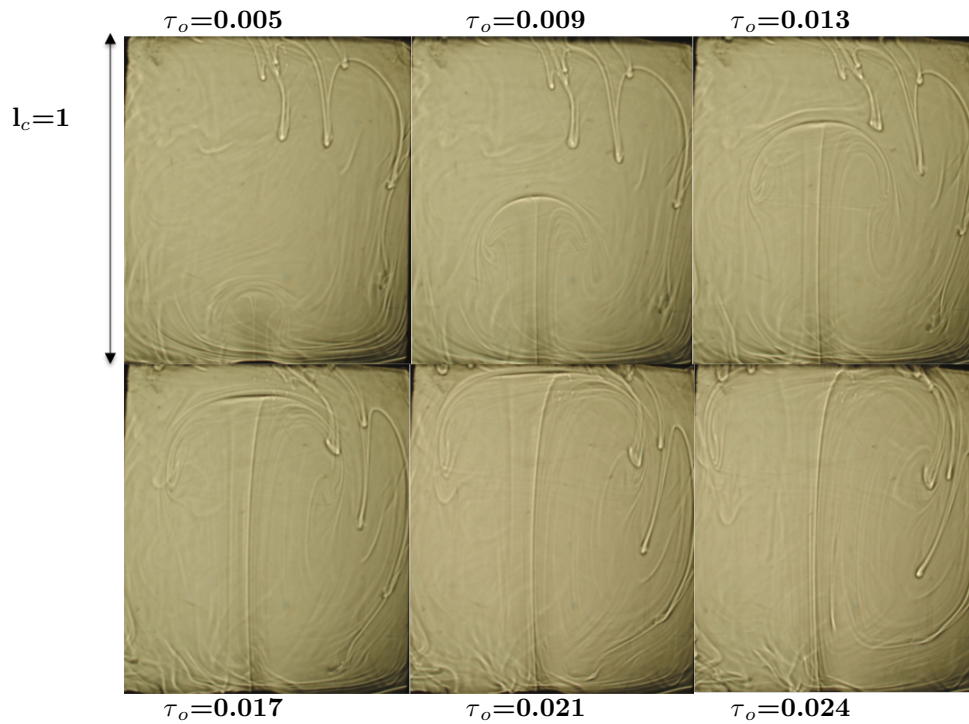
(a) Shadowgraph experiment images of the ΔT=25°C plume. Images are at τ_o=0.005, 0.009, 0.013, 0.017, 0.021 and 0.024 after the beginning of the experiment.
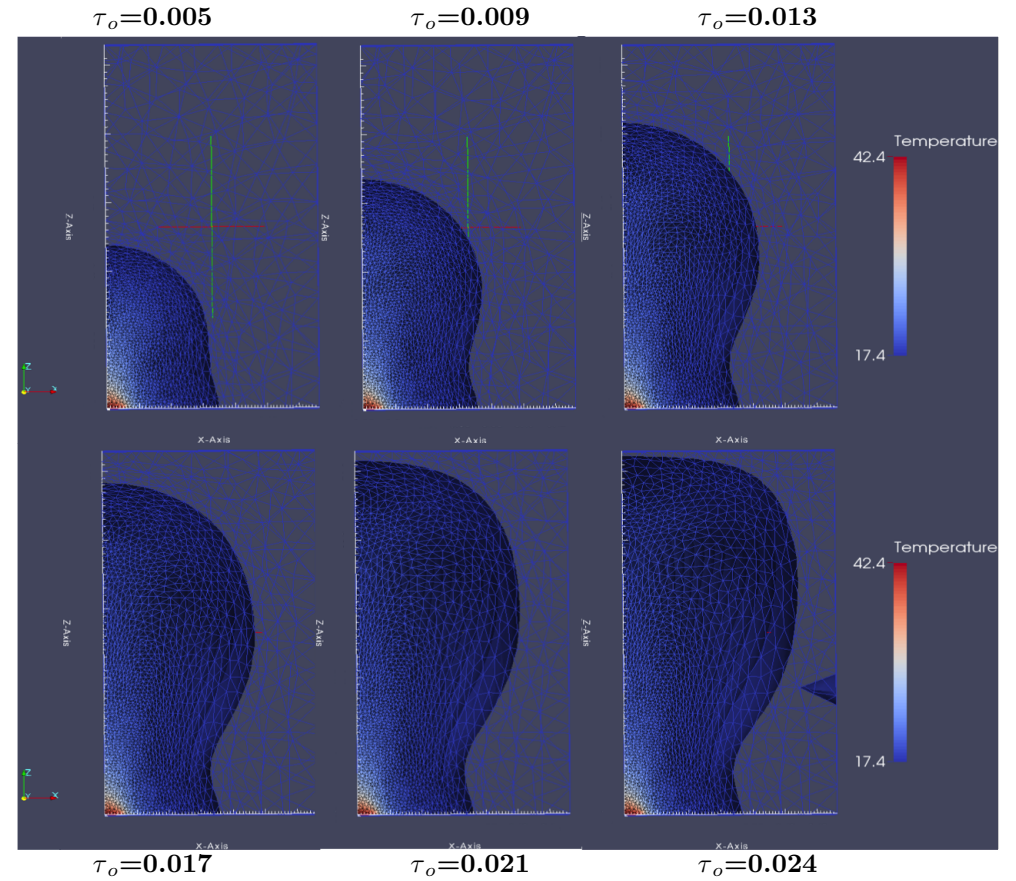
(b) Numerical simulations visualised with Paraview for the ΔT=25°C plume. Images are at τ_o=0.005, 0.009, 0.013, 0.017, 0.021 and 0.024 after the beginning of the simulation.

Figure 7.10: A visual comparison of ΔT=25°C Liquidose 436 plumes. Both plumes ascended to the top of the tank. The simulated plume has the classical plume shape that was not observed in the ΔT=5°C or ΔT=13.3°C simulated plumes.

Figure 7.12 displays the difference in the conduit widths for the experimental and simulated plumes. The simulated conduit width continued to grow throughout the simulation, although at a more steady pace and remained at an almost constant width once the plume has reached the top of the tank. The conduit width at the end of the simulations was $D_o = 0.664$, which was $D_o = 0.351$ greater than the experimental conduit width. Over the experiment the plume conduit width grew to a peak of $D_o = 0.355$, then decreased to $D_o = 0.312$ from $\tau_o = 0.031$ and remained constant for the rest of the experiment. The experimental and simulated conduit width was larger than for the small ΔT plumes.
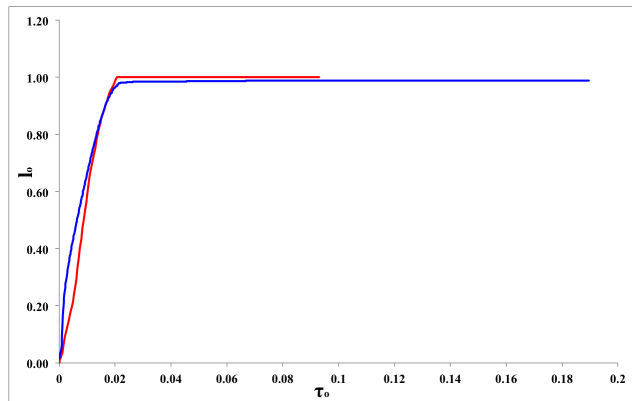
Figure 7.11: The comparison of l_o between the experimental (red) and simulated (blue) results as a function of τ_o for the $\Delta T = 25°C$ plumes
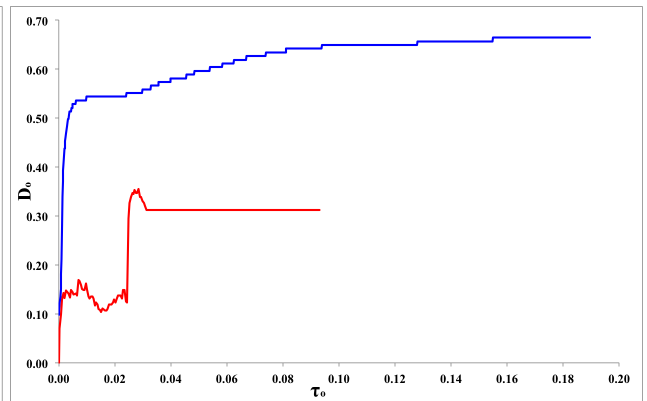
Figure 7.12: The comparison of D_o between the experimental (red) and simulated (blue) results as a function of τ_o for the $\Delta T = 25°C$ plumes.
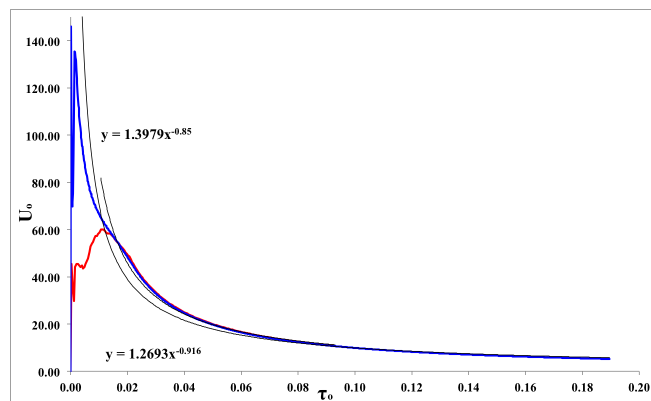
Figure 7.13: The comparison of U_o between the experimental (red) and simulated (blue) results as a function of τ_o for the $\Delta T = 25°C$ plumes. The power-law function of the velocities are displayed on the graph.

The absolute velocity of the simulated plume was $U_o = 101.92$ greater than the experimental plume at the beginning of the investigations (Figure 7.13). This was unexpected when the plume followed a similar height evolution. The experimental plume reached a maximum absolute velocity of $U_o = 60.05$ at $\tau_o = 0.010$ later after the simulated plume. While the experimental plume was at a maximum the simulated plume absolute velocity was decreasing with a power-law $U_o = 1.3979\tau_o^{-0.85}$. However, after approximately $\tau_o = 0.015$ the simulated plume absolute velocity was 0.5% greater than the experimental plume. The experimental plume absolute velocity also decreased by $\tau_o = 0.02$ with a power-law function $U_o = 1.2693\tau_o^{-0.916}$. At the termination

of the experiment the velocities of the two plumes were similar at U_o=10.75, although the absolute velocity of the simulated plume continued to decrease to a minimum absolute velocity of U_o=5.22. The absolute velocity field of the simulated plume was, as expected, relatively smoother than the measured experimental absolute velocity.

7.3.1.4 ΔT=41.2°C plume comparison for all three plume generation methods

The ΔT=41.2°C simulated plume was compared with the shadowgraph and SPIV plume (Figure 7.14 and Figure 7.15). The plumes from all three methods reached the top of the tank. The shadowgraph and simulated plume both finished with the typical mushroom shaped plume head (Figure 7.14), although the conduit remained fairly wide in the simulated plume for the whole simulation. However, the simulated plume conduit grows throughout the experiment based on the selection of the contours. However, whatever contour was chosen the conduit would increase during the simulation. The shadowgraph plume had a narrow conduit which thinned as the experiment progressed. Additionally, the shadowgraph plume ascended to the surface earlier than the simulated plume. At τ_o=0.002 the simulated plume was more developed in the tank than the shadowgraph plume because the shadowgraph plume was still forming from the TBL. The simulated plume remained more developed and higher in the tank than the shadowgraph plume at τ_o=0.004 and simulated plume does not display the typical expected shape of a plume. However, by τ_o=0.010 the shadowgraph plume had almost ascended to the surface but the simulated plume was only two-thirds of the way up the tank. The shadowgraph and SPIV plumes are more similar than the simulated plume from the beginning of the experiment until τ_o=0.018 after this time all three plumes have ascended to the surface of the tank and the shadowgraph and simulated plume can be seen to spread laterally along the surface.

Figure 7.15 displays that the SPIV plume had a higher velocity (by U_o=225.50) than the simulated plume and ascended to the surface earlier. Qualitatively the SPIV plume and simulated plume show similar velocity evolution in the plume. The centre of the plume remains the location where the fluid is moving the fastest. However, the SPIV plume has the highest velocity in a thin pipe to the location where the heater is present, which is not the case in the simulated plume. The scrolling in the plume head of the simulated plume was not evident from just visualising the temperature. This scrolling was also observed in the SPIV and shadowgraph experiments. This shows that the three techniques for visualising the plumes show qualitatively similar results. The background velocity of the SPIV experiment was between U_o=-30.58-0, whereas the background flow in the simulated plume was never below U_o=0.
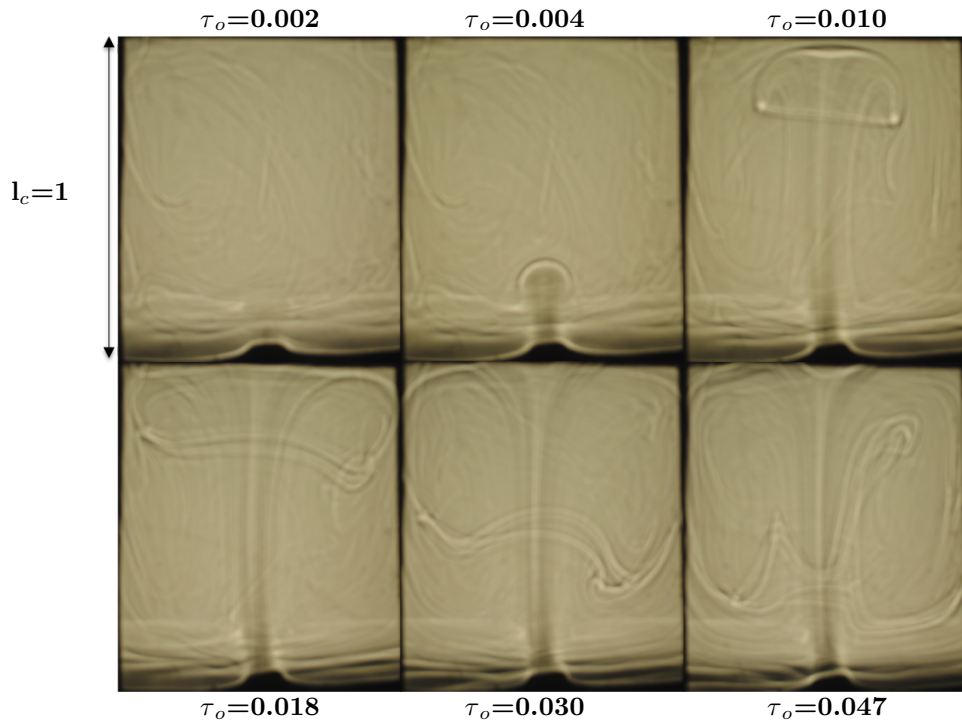
(a) The ΔT=41.2°C shadowgraph experiment with images at τ_o=0.002, 0.004, 0.010, 0.018, 0.030 and 0.047 from the beginning of the experiment.
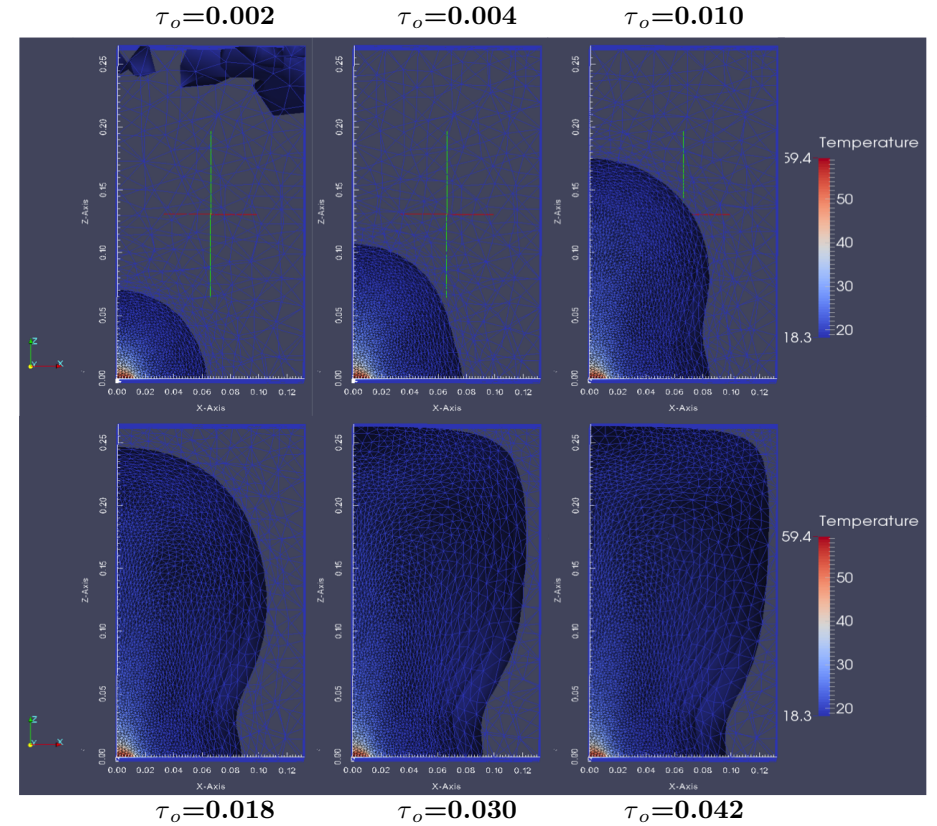
(b) The 41.2°C simulated plume. Images chosen at 0.002, 0.004, 0.010, 0.018, 0.030 and 0.042 from the beginning of the simulation.

Figure 7.14: A visual comparison of ΔT=41.2°C plumes. Both plumes ascend to the top of the tank and appear axisymmetric.
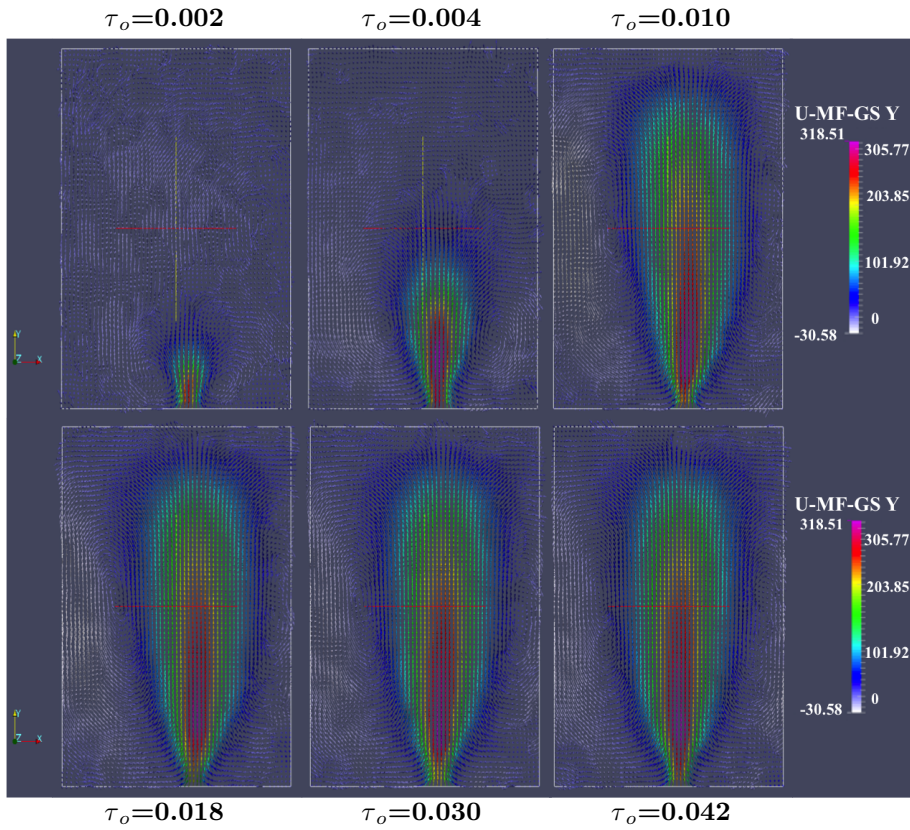
(a) The 41.2°C SPIV experiment with non-dimensional velocity vectors. Images chosen at 0.002, 0.004, 0.010, 0.018, 0.030 and 0.042 from the beginning of the experiment.
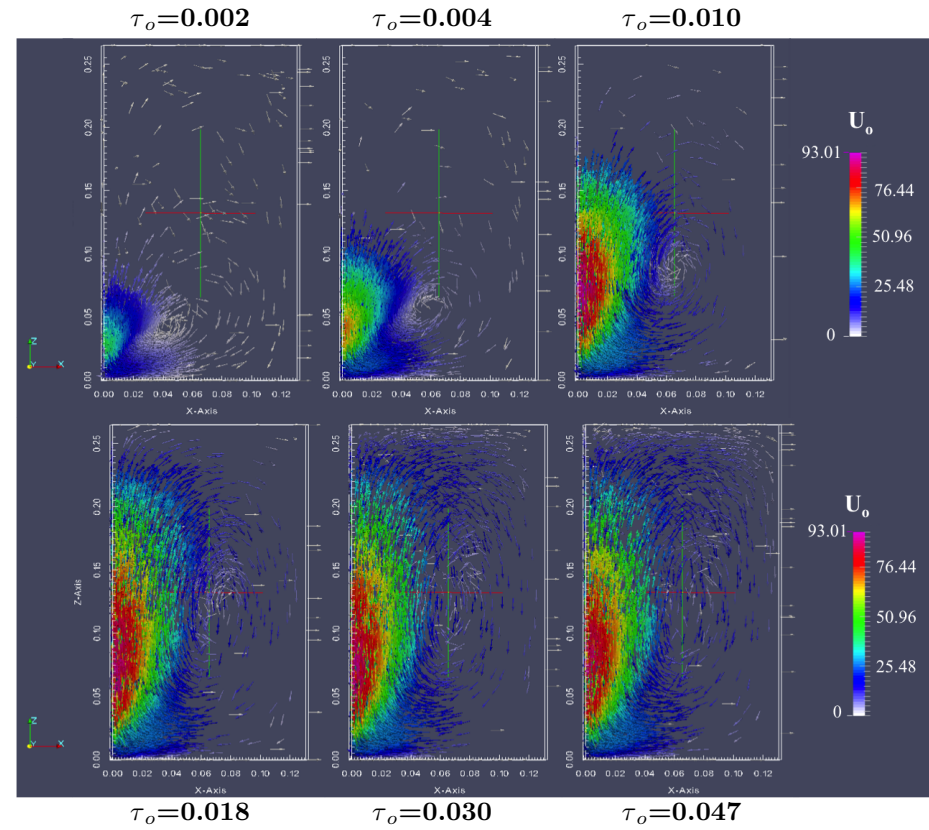
(b) The ΔT=41.2°C simulated plume with the arrows depicting the non-dimensional velocity vectors. The images are at τ_o=0.002, 0.004, 0.010, 0.018, 0.030 and 0.047 from the beginning of the simulation.

Figure 7.15: A visual comparison of ΔT=41.2°C plumes velocity vectors.

7.3.2   Golden Syrup Experimental Results Comparison

The physical configuration of the Golden syrup simulations and the governing equations were
the same as used in the Liquidose 436 simulations.

Metric	Coordinate mesh nodes	Coordinate Mesh Surface elements	Coordinate mesh elements	Height in metres at 3hrs 15 minutes	Percentage difference from convergence
0.03	2396	1734	11020	0.075	4.75
0.02	2784	1990	12890	0.085	3.75
0.01	4006	2430	19250	0.1075	1.5
0.0075	4840	2737	23514	0.114	0.85
0.005	6406	3198	31869	0.117	0.55
0.0025	10941	4444	56089	0.1225	0.00

Table 7.4: Examining the convergence error through different metric simulations at the same temperature.

For the Golden syrup convergence analysis different metrics were investigated for the $\Delta T=3°C$
plume and the results displayed in Table 7.4. The metric of 0.0025 produced the most accurate
results with the highest (10,941) coordinate mesh nodes (Figure 7.16). Despite the computa-
tional cost involved in such a fine mesh, it was decided all simulations for comparison with the
Golden syrup experiments would use this metric because it was closer to the percentage differ-
ence of 0.1% from convergence in the Liquidose 436 syrup.
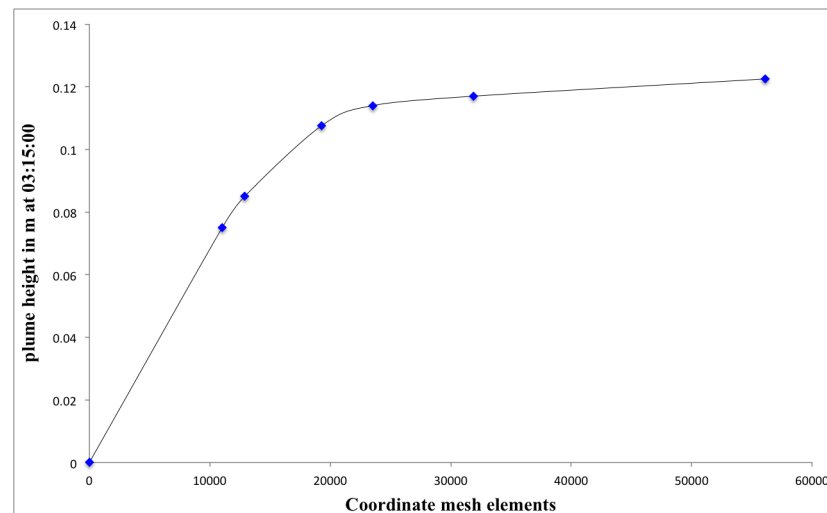
Figure 7.16: Convergence error analysis for the Golden syrup $\Delta T=3°C$ plume.

The results from the Lyle Golden syrup experiments (Pears, 2010) were compared with the
3D numerical simulations using the same temperature difference, viscosity contrast and heater
information as displayed in Table 7.5.

$\mathbf{T}_h/\ ^\circ\mathbf{C}$	$\mathbf{T}_\infty/\ ^\circ\mathbf{C}$	$\Delta\mathbf{T}/$ $^\circ\mathbf{C}$	$\rho_h/$ $\mathbf{kg/m^2}$	$\eta_h\ /\mathbf{Pa\ s}$	$\mathbf{Ra}_h$
25	22	3	1441.23	34.46	9.25×10^4
30	23	7	1440.33	21.75	4.35×10^5
40	22	18	1441.23	8.67	3.65×10^6

Table 7.5: Parameters similar in both experimental and numerical runs.

7.3.2.1 ΔT=3°C plume comparison

In both the numerical simulation and the experimental run the plume did not form the typically expected plume shape (Figure 7.19). The simulated plume was visualised with the highest contour at 0.0585°C above the ambient temperature of 22°C. Unlike in the experimental data the simulated plume began to grow immediately with a small perturbation of l_o=0.008 at τ_o=0 (Figure 7.17). The experimental plume, however, was not observed before τ_o=0.007 due to a period of TBL building. The experimental plume then ascended to a maximum height of l_o=0.196 at τ_o=0.017 before stalling for a period of τ_o=0.006, then collapsed towards the base of the tank. The simulated plume reached a maximum height of l_o=0.821, where it stalled and failed to reach the top of the tank, but did not show the collapse phenomenon. Due to the different viscosity, density, thermal expansion and thermal diffusivity, the maximum height the plume in the Liquidose 436 ΔT=5°C simulation was l_o=0.032 greater than the ΔT=3°C. However, both the Liquidose 436 syrup and Golden syrup simulations the plume ascended with a finger shape without a definitive distinction between the plume head and conduit.
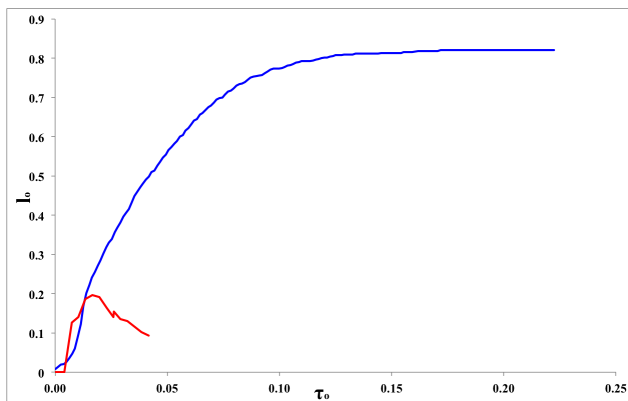
Figure 7.17: The comparison of l_o between the experimental (red) and simulated (blue) results as a function of τ_o for the ΔT=3°C plumes.
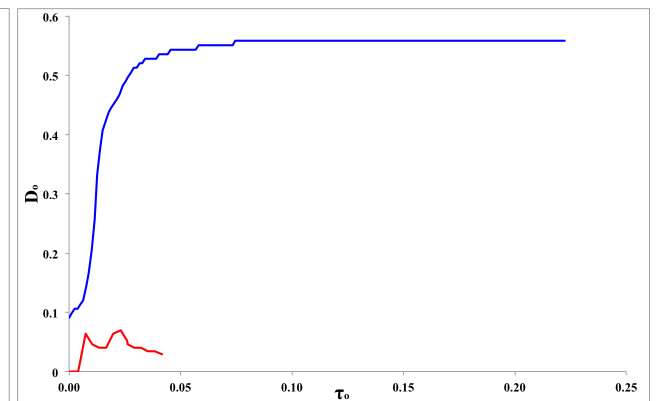
Figure 7.18: The comparison of D_o between the experimental (red) and simulated (blue) results as a function of τ_o for the ΔT=3°C plumes.

There was a D_o=0.528 difference between the conduit width of the experimental and simulated plumes at the end of the investigations (Figure 7.18). At τ_o=0 the simulated plume conduit was already D_o=0.091 and increased to D_o=0.558 at the termination of the simulation. While the experimental plume was ascending the conduit width increased to a maximum of D_o=0.069 at τ_o=0.023.

$l_c=1$

$\tau_o=0.007$ $\quad$ $\tau_o=0.014$ $\quad$ $\tau_o=0.023$

$\tau_o=0.026$ $\quad$ $\tau_o=0.029$ $\quad$ $\tau_o=0.038$
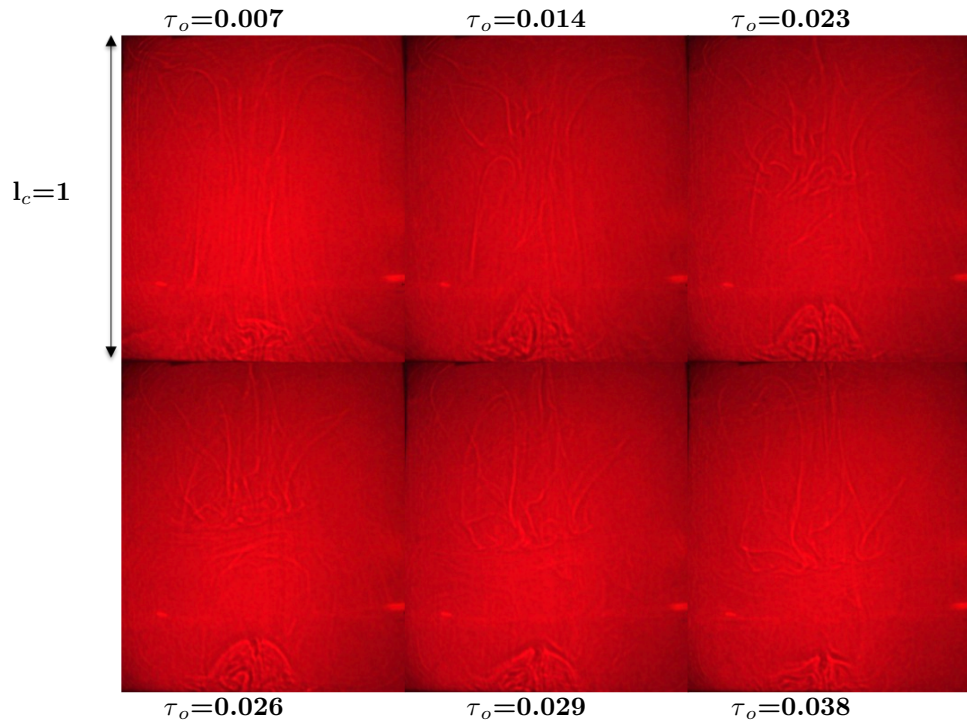
(a) Shadowgraph experiment for the ΔT=3°C plume. Images are at τ_o=0.007, 0.014, 0.023, 0.026, 0.029 and 0.038 after the beginning of the experiment.

$\tau_o=0.006$ $\quad$ $\tau_o=0.014$ $\quad$ $\tau_o=0.023$

$\tau_o=0.025$ $\quad$ $\tau_o=0.029$ $\quad$ $\tau_o=0.038$
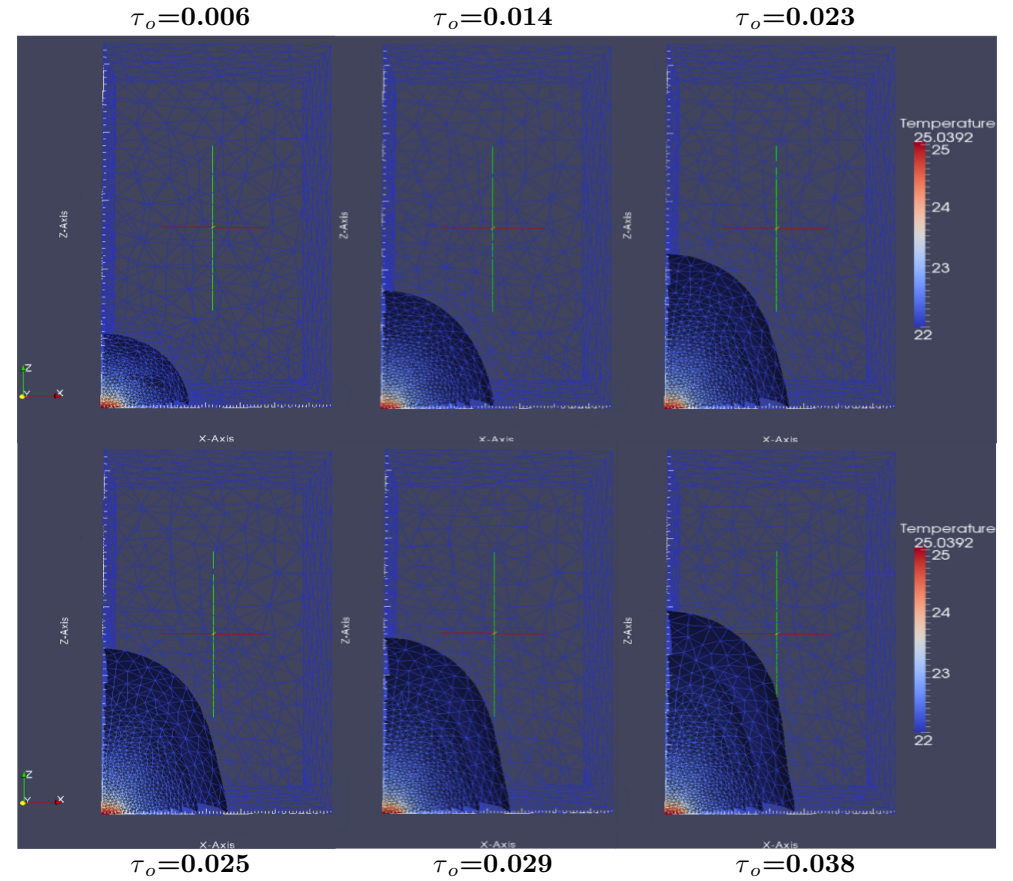
(b) The ΔT=3°C simulated plume visualised with Paraview. Images are at τ_o=0.006, 0.014, 0.023, 0.025, 0.029 and 0.038 after the beginning of the simulation.

Figure 7.19: A visual comparison of ΔT=3°C Golden syrup plumes. The experimental plume collapsed back to the base and the simulated plume stalled near the top of the tank.

Once experimental collapse began, the conduit width then decreased to D_o=0.030 (by 58.3%). Conversely, the simulated conduit grew continually, even when the plume height had stalled.

The simulated plume had a lower absolute velocity at the beginning of the simulation than the experimental plume (Figure 7.20), differing from the numerically simulated Liquidose 436 syrup plumes, which always had a higher absolute velocity than the similar experimental plumes. The absolute velocity of the experimental plume, although higher by U_o=2.17 at τ_o=0.002, then decreased more rapidly than the simulated plume to a minimum absolute velocity of U_o=2.24 at the termination of the experiment. At the termination of the experimental investigation the absolute velocity of the simulated plume was U_o=9.71 higher. The absolute velocities of both plumes decreased exponentially with the experimental plume function U_o=28.966e$^{-61.32\tau_o}$ and the numerical function U_o=15.634e$^{-6.822\tau_o}$.
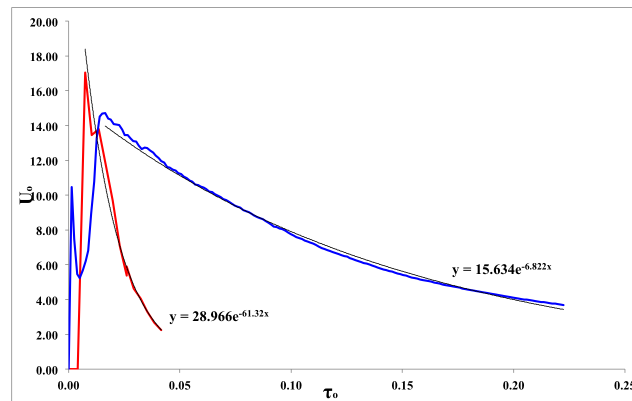
Figure 7.20: The comparison of U_o between the experimental (red) and simulated (blue) results as a function of τ_o for the ΔT=3°C plumes.

7.3.2.2 ΔT=7°C plume comparison
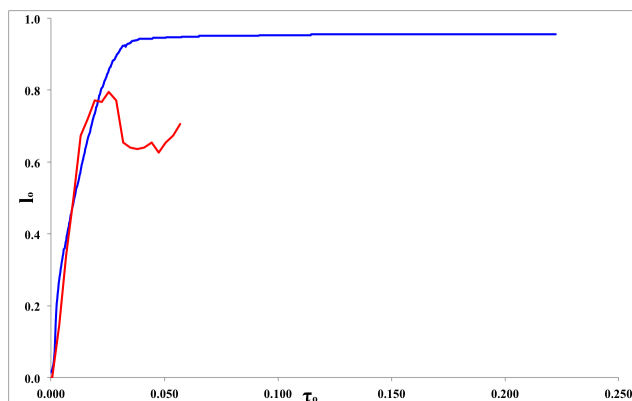
Figure 7.21: The comparison of l_o between the experimental (red) and simulated (blue) results as a function of τ_o for the ΔT=7°C plumes.
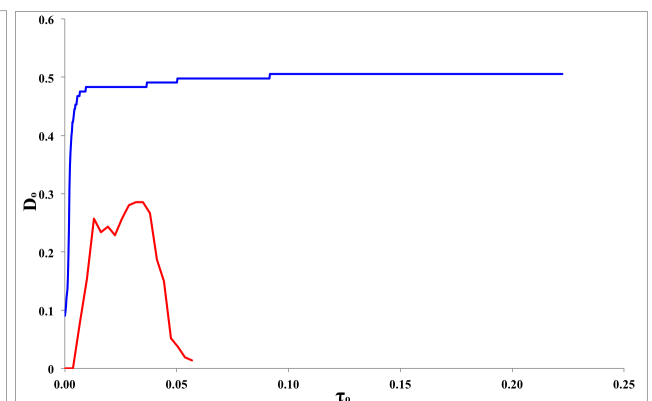
Figure 7.22: The comparison D_o between the experimental (red) and simulated (blue) results as a function of τ_o for the ΔT=7°C plumes.

Figure 7.24 shows the evolution of the simulated and experimental plumes. The simulated plume was visualised with the highest contour 0.0585°C above the ambient temperature of 23°C. It ascended to l_o=0.940 at τ_o=0.038 and increased to a maximum of l_o=0.955, then the plume

stalled (Figure 7.21). The experimental plume reached a lower maximum height of l_o=0.794 after τ_o=0.026 before the plume began to collapse. The collapse phenomenon was not observed in the simulated plume. In the tank, the experimental plume head was faint throughout the investigation (Figure 7.24), whereas, the simulated plume head was well defined and displayed the expected mushroom shaped head. Figure 7.22 demonstrates that there was a significant difference between the conduit widths of the two plumes. As with the other numerical simulations the conduit continued to grow throughout the plume ascent. The simulated conduit width began at D_o=0.091 at τ_o=0 and increased by D_o=0.415 by the end of the simulation. The experimental plume conduit width grew to a smaller maximum of D_o=0.285 by τ_o=0.035 and then decreased to D_o=0.014 at the end of the experiment as the plume was collapsing. The simulated plume conduit width after τ_o=0.007 increased by 6.3% over the rest of the simulation.
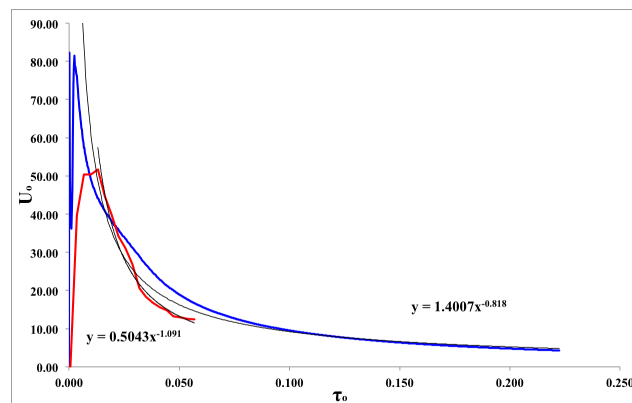
Figure 7.23: The comparison of U_o between the experimental (red) and simulated (blue) results as a function of τ_o for ΔT=7°C plumes. The velocities decrease with power-law functions displayed on the graph.

The absolute velocity of both plumes decreased with a power-law after reaching a maximum (Figure 7.23). The simulated plume power-law function was U_o=1.4007$\tau_o^{-0.318}$ and the experimental plume function was U_o=0.5043$\tau_o^{-1.091}$. The simulated plume reached a maximum within the beginning τ_o=0.002. The experimental plume maximum U_o=51.64 was τ_o=0.013 after the original peak of the simulated plume. The simulated plume absolute velocity began decreasing at τ_o=0.002, which was τ_o=0.017 earlier than the experimental plume.
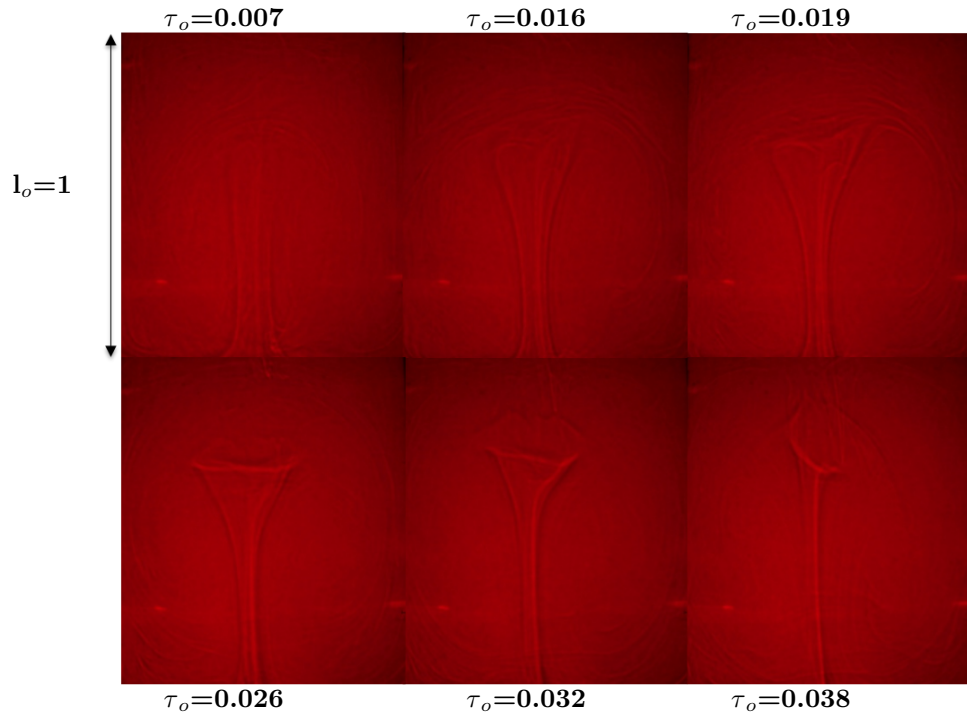
(a) Shadowgraph images for the ΔT=7°C plume. Images are at τ_o=0.007, 0.016, 0.019, 0.026, 0.032 and 0.038 after the beginning of the experiment.
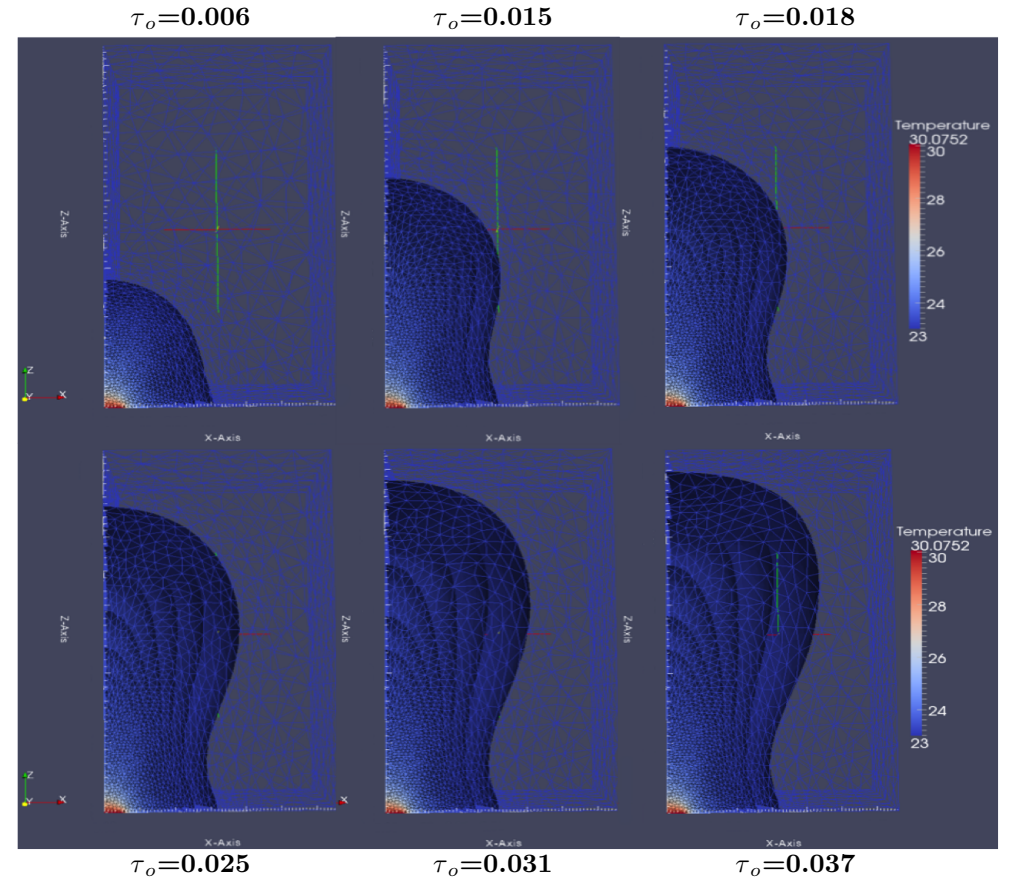
(b) The ΔT=7°C simulated plume visualised with Paraview. Images are at τ_o=0.006, 0.015, 0.018, 0.025, 0.031 and 0.037 after the beginning of the simulation.

Figure 7.24: A visual comparison of ΔT=7°C Golden syrup plumes. The experimental plume showed "lenticular" collapse, whereas the simulated plume stalled before reaching the surface.

7.3.2.3 ΔT=18°C plume comparison
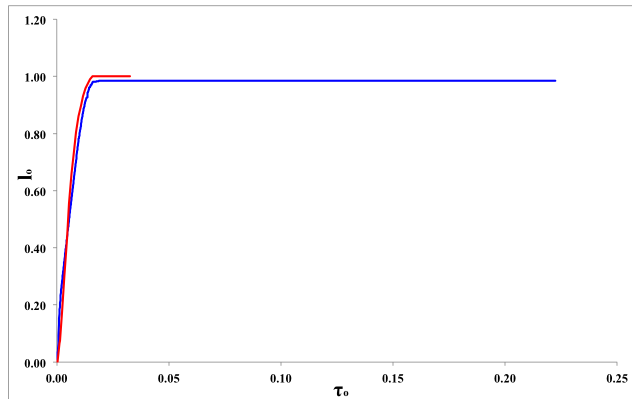
Figure 7.25: The comparison of l_o between the experimental (red) and simulated (blue) results as a function of τ_o for the ΔT=18°C plumes.
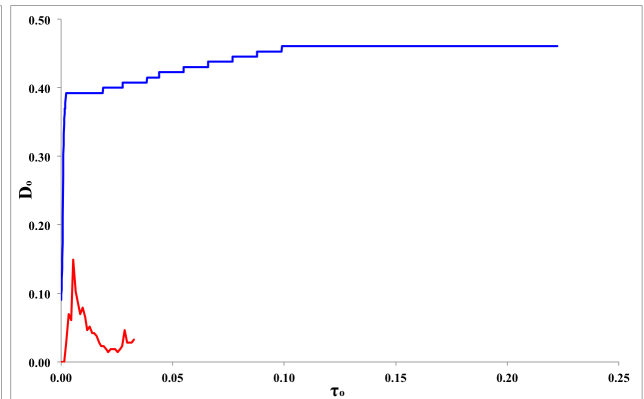
Figure 7.26: The comparison of D_o between the experimental (red) and simulated (blue) results as a function of τ_o for the ΔT=18°C plumes.

Both the experimental and simulated plumes reached the top of the tank (Figure 7.27). The simulated plume was visualised with the highest contour 0.0584°C above the ambient temperature 22°C. Both plumes displayed the typical mushroom shape, also observed in the Liquidose 436 ΔT=25°C experimental and simulated plumes. The plumes grew steadily up to τ=0.014, but once they had ascended towards the top of the tank they flattened and the head width increased (Figure 7.25). The experimental plume conduit grew to a maximum width of D_o=0.150 at τ_o=0.006 before thinning as the plume ascended to the top of the tank (Figure 7.26). However, the conduit width of the simulated plume conduit width increased to a larger maximum width of D_o=0.460 at τ_o=0.099 and remained constant for the remainder of the simulation. The simulated conduit width finished D_o=0.426 greater than the experimental plume conduit width. There appeared to be a small pulsing in the conduit of the experimental plume at τ_o=0.026. This could be related to the heating of the fluid above the heater and it beginning to move away from the source. The simulated plume conduit width increased linearly at the beginning of the simulation but after τ_o=0.002 the increase was D_o=0.094 in τ_o=0.097.

The absolute velocity of the experimental and simulated plumes differed by U_o=60.82 at τ_o=0.002 (Figure 7.28). At this time the simulated plume absolute velocity had already commenced a steep decrease by a power-law function U_o=1.2761$\tau_o^{-0.882}$. By τ_o=0.026 its absolute velocity had decreased by U_o=112.08. After τ_o=0.014 the decrease in absolute velocity of both plumes exhibited a similar gradient and the experimental plume terminated with a similar absolute velocity to the simulated plume. The experimental plume absolute velocity decreased by a power-law function U_o=2.4905$\tau_o^{-0.758}$. The maximum experimental absolute velocity of the plume was U_o=71.68 smaller and occurred τ_o=0.005 later than the maximum observed in the simulated plume.
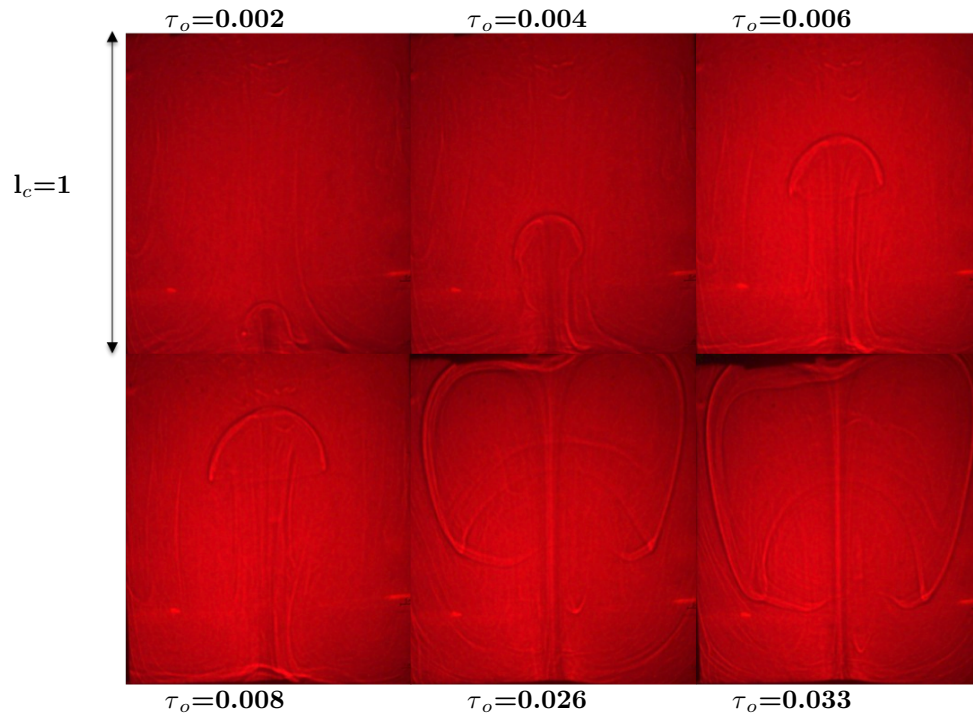
(a) Six shadowgraph images of the ΔT=18°C plume. Images are at τ_o=0.002, 0.004, 0.006, 0.008, 0.026 and 0.033 after the beginning of the experiment.
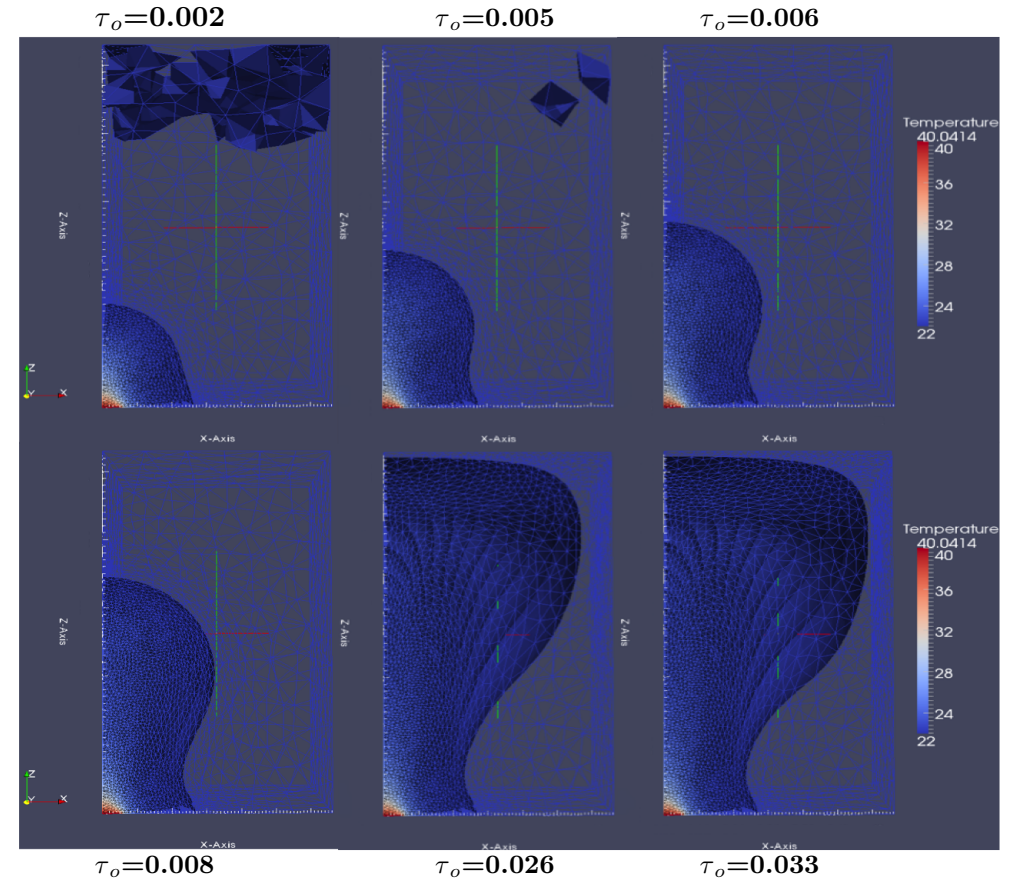
**(b)** The ΔT=18°C simulated plume visualised with Paraview. Images are at τ_o=0.002, 0.005, 0.006, 0.008, 0.026 and 0.033 after the beginning of the simulation.

Figure 7.27: A visual comparison of the ΔT=18°C Golden syrup plumes. Both plumes ascended to the top of the tank.
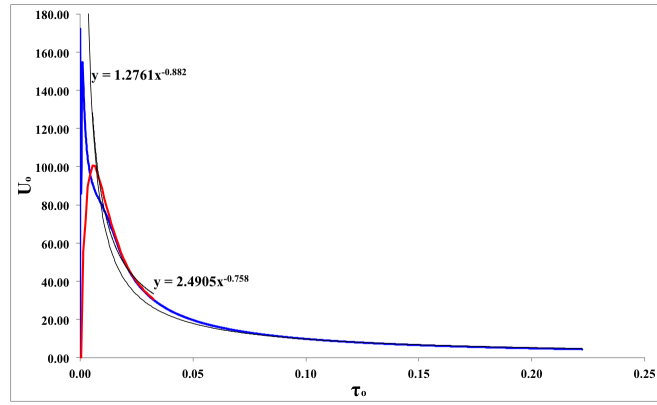
Figure 7.28: The comparison of U_o between the experimental (red) and simulated (blue) results as a function of τ_o for the $\Delta T = 18°C$ plumes. The velocities decrease by a power-law as shown on the graph.

7.4 Investigating the stalling phenomena

The temperature difference at which the stalling phenomena ceased to occur was investigated. Simulations were undertaken for a range of temperature differences with an ambient temperature of 19°C. The temperature was non-dimensionalised by $T_o = \frac{\Delta T}{T_\infty}$ where $T_\infty = 19°C$.

$T_h/$ °C	$T_\infty/$ °C	$\Delta T/$ °C	$\eta_h/$ Pas	Ra_h
24.0	19.0	5.0	49.13	9.08×10^4
25.0	19.0	6.0	44.65	1.21×10^5
26.1	19.0	7.1	40.60	1.56×10^5
27.0	19.0	8.0	37.19	1.93×10^5
28.0	19.0	9.0	34.07	2.36×10^5
29.1	19.0	10.0	30.99	2.89×10^5
30.0	19.0	11.0	28.40	3.46×10^5
31.0	19.0	12.0	25.89	4.14×10^5
32.0	19.0	13.0	23.66	4.91×10^5
33.0	19.0	14.0	21.62	5.78×10^5
34.0	19.0	15.0	19.76	6.77×10^5

Table 7.6: Different Rayleigh numbers for tanks of increased size.

Figure 7.29 shows that plume stalling ceased to exist at around $\Delta T = 14°C$ which was $T_o = 0.74$. For temperatures greater than this T_o the plume ascended to the top of the tank. Thus the stalling at $T_o = 0.74$ was probably related to an effect that the top of the tank was having on the plume. At small T_o the difference between the height at which the plume began to stall and the height at which the plume finished was approximately $l_o = 0.04$. This difference became smaller as the T_o increased. From Figure 7.29 it was possible to establish that for low T_o, these thermal plumes did not reach the top of the tank but that there was a boundary at approximately $T_o = 0.74$ where the plume ascended to almost the top of the tank ($l_o = 1$). This boundary was $T_o = 0.5$ greater than that at which the experimental plumes stalled (the experimental boundary is plotted on the graph).
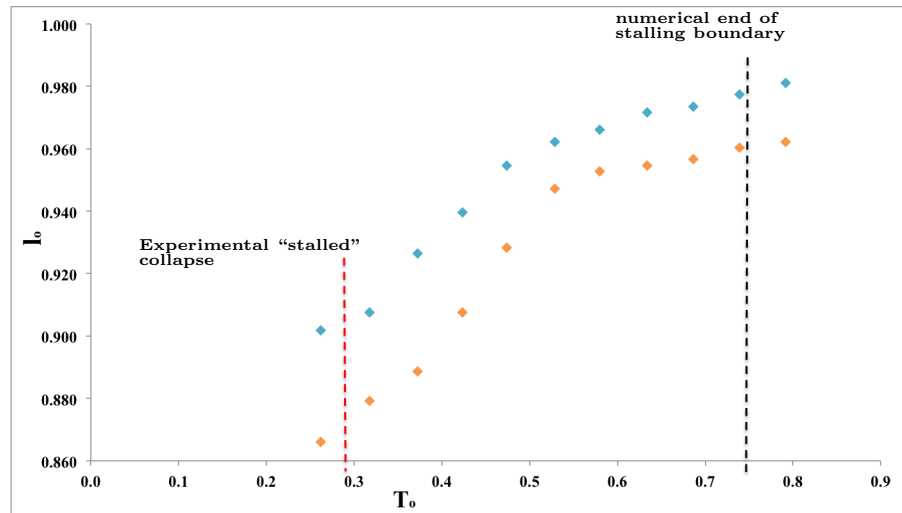
Figure 7.29: Plot showing the stalling phenomenon - the non-dimensional height reached in the tank (l_o) for a range of $T_o = \frac{\Delta T}{T_\infty}$ where $T_\infty = 19°C$. The orange is the height at which the plume began to stall and blue represents the maximum height reached when visualised with contours that gave $0.0585°C$ above the ambient temperature. The ΔT experimental "stalled" collapse boundary is implied.

7.4.1 Different sized tanks

In order to establish if the aspect ratio of the experimental tank played a role in the stalling of the plumes, the simulated tank dimensions were changed. Firstly, the stalling behaviour was investigated by altering the height of the tank. Three different heights were employed:

- The height of the tank was doubled, to 0.53m (l_o=2).

- The height of the tank was increased by 50% from the original height, to 0.3975m (l_o=1.5).

- Finally, the height of the tank was increased by 33% from the original height, to 0.3533m (l_o=1.33).

These heights were used to examine temperature differences of $\Delta T=5°C$ and $\Delta T=13.3°C$ for Liquidose 436 syrup and $\Delta T=3°C$ and $\Delta T=7°C$ for Golden syrup, as this was where the stalling phenomena was observed. A second investigation involved keeping the original height of the tank of 0.265m and instead increasing the width of the tank. Three different widths were used for the same temperature difference simulations:

- The width of the tank was doubled, to 0.265m (as only half the tank was simulated) (D_o=2).

- The width of the tank was increased by 50% from the original width, to 0.19875m (D_o=1.5).

- Finally, the width of the tank was increased by 33% from the original width, to 0.1767m (D_o=1.33).

7.4.1.1   Increased tank height

The tank height was increased from the original height of 0.265m to 0.530m (double height), 0.3975m (50% increase) and 0.3533m (33% increase). With the increased tank height the Rayleigh number changed (Table 7.7).

$T_h/$ °C	$T_\infty/$ °C	$\Delta T/$ °C	Tank height/ m	Ra
23.4	18.4	5.0	0.53	6.91×10^5
30.1	16.8	13.3	0.53	3.36×10^6
23.4	18.4	5.0	0.3975	2.92×10^5
30.1	16.8	13.3	0.3975	1.42×10^6
23.4	18.4	5.0	0.3533	2.05×10^5
30.1	16.8	13.3	0.3533	9.97×10^5

(a) Liquidose 436 plumes

$T_h/$ °C	$T_\infty/$ °C	$\Delta T/$ °C	Tank height/ m	Ra
25.0	22.0	3.0	0.53	7.40×10^5
30.0	23.0	7.0	0.53	3.48×10^6
25.0	22.0	3.0	0.3975	3.12×10^5
30.0	23.0	7.0	0.3975	1.47×10^6
25.0	22.0	3.0	0.3533	2.19×10^5
30.0	23.0	7.0	0.3533	1.03×10^6

(b) Golden syrup plumes

Table 7.7: Different Rayleigh numbers for simulations for the increased tank height.
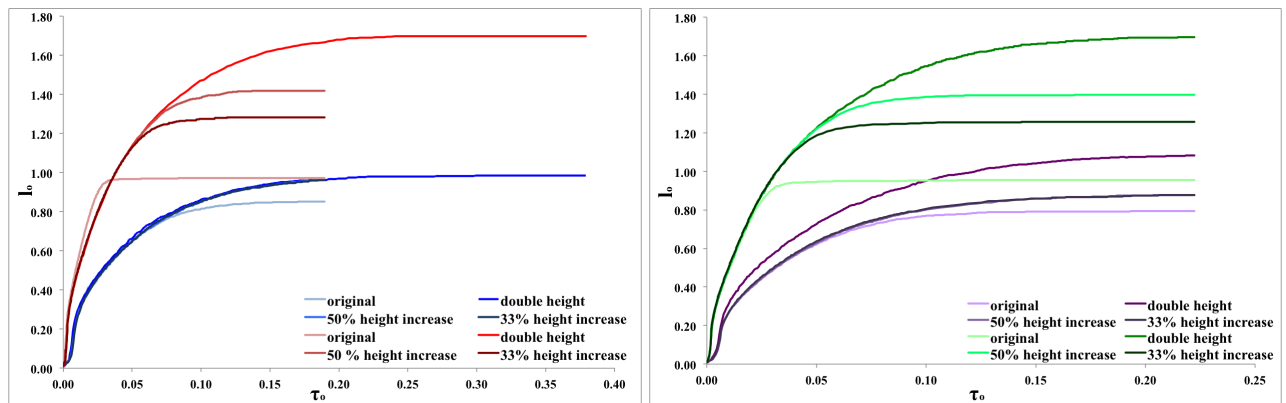
(a) Liquidose 436 syrup simulations, where blues represent the $\Delta T=5$°C plumes and reds represent the $\Delta T=13.3$°C plumes.

(b) Golden syrup simulations, where the purples represent the $\Delta T=3$°C plume and greens represent the $\Delta T=7$°C plume.

Figure 7.30: A comparison between the l_o for different tank heights as a function of τ_o of the plumes at different temperature differences.

When the height of the tank was increased the different ΔT plumes ascended higher in the tank compared to the original plumes (Figure 7.30). For all three increased tank heights at $\Delta T=5$°C (Figure 7.30a) the plumes reached approximately the same height in the tank ($l_o=0.096$). The percentage increase in plume height was 15.74%, 13.3% and 13.08% for the double, 50% and 33% height tank simulations respectively. Therefore, as it appeared that the $\Delta T=5$°C plume had not stalled in $\tau_o=0.222$ timestep, the double height tank simulation was re-run for double the timestep (to 256,000 seconds). The double timestep $\Delta T=5$°C plume, for the double height tank, was unable to ascend to the top of the tank and only reached $l_o=0.985$ because the plume stalled, which is 50.8% of the height of the tank. The $\Delta T=3$°C Golden syrup plume for $\tau_o=0.222$ only reached 45.8% of the height of the doubled height tank due to stalling. All other simulated ΔT

plumes simulated ascended further in the tank when the height parameter was increased. The $\Delta T = 13.3°C$ plume height increased by 74.8%, 45.8% and 32.0% from $l_o = 0.97$ for the double, 50% and 33% increased tank height respectively. In contrast, the $\Delta T = 7°C$ Golden syrup plume height increased by 77.7%, 46.4% and 31.6% from the original height of $l_o = 0.96$ for the double, 50% and 33% increased tank height respectively. The intermediate ΔT plume heights were close to the surface of the tank (within an average height of 9% from the surface for Liquidose 436 syrup and 7.6% for the Golden syrup).
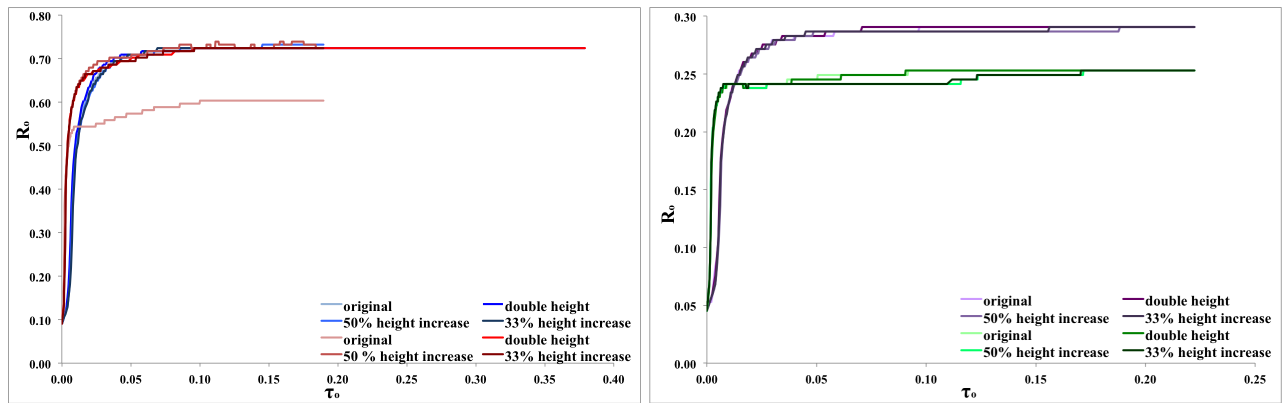
(a) Liquidose 436 simulations where the blues represent the $\Delta T = 5°C$ plumes and red represent the $\Delta T = 13.3°C$ plumes.

(b) Golden syrup simulations where the purples represent the $\Delta T = 3°C$ plumes and greens represent the $\Delta T = 7°C$ plumes.

Figure 7.31: A comparison between the non-dimensional radii (R_o) as a function of τ_o of the plumes at different temperatures.

Figure 7.31 shows no significant change in the conduit radii for all plumes in both syrups with increased tank height, with the exception of the $\Delta T = 13.3°C$ plume, where the conduit radii increased by 20% for the three increased tank heights. The conduit radii of the Liquidose 436 syrup $\Delta T = 5°C$ and the $\Delta T = 13.3°C$ were similar for all tank heights except the radius of the $\Delta T = 13.3°C$ plume at the original tank height, which was $R_o = 0.1$ smaller. This differed from the Golden syrup ΔT plumes where the $\Delta T = 7°C$ plume had a conduit radius 15% smaller than the $\Delta T = 3°C$ for all the tank height simulations.

Figure 7.32 demonstrates that the absolute velocities decreased with time during the course of the simulations. For the $\Delta T = 5°C$ plume, the increase in the absolute velocity at the termination of the simulations was 13% (from $U_o = 4.49$-5.09) for both the 50% and 33% tank height increase, but decreased by 42% for the double tank height. The $\Delta T = 13.3°C$ plume had an original plume velocity $U_o = 40.77$ greater than the other plumes at increased tank height. The original $\Delta T = 7°C$ plume showed a steeper absolute velocity decrease ($U_o = 13.03$ difference) between $\tau_o = 0.035$-0.070 compared to the three other plume simulations at the same ΔT.
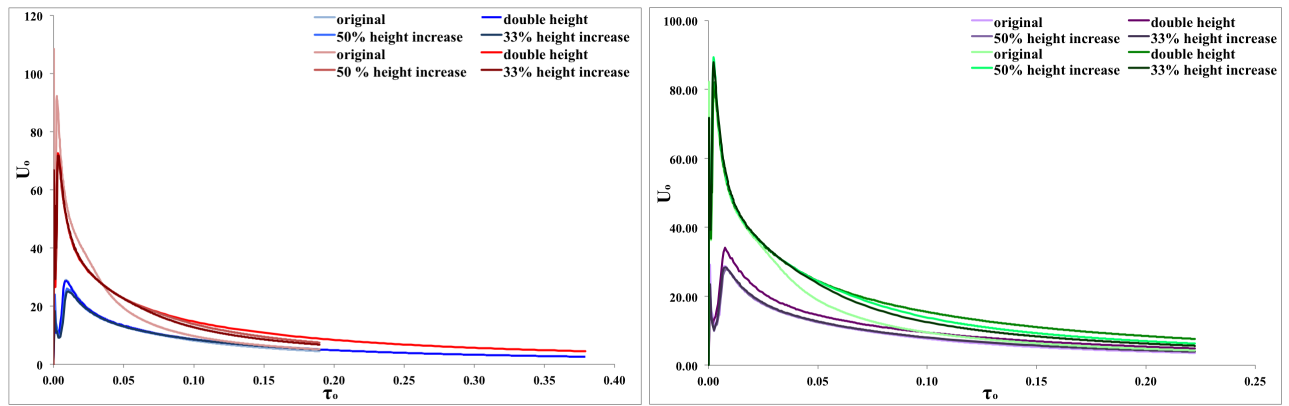
(a) Liquidose 436 simulations where the blues represent the $\Delta T=5°C$ plumes and red represent the $\Delta T=13.3°C$ plumes.

(b) Golden syrup simulations where the purples represent the $\Delta T=3°C$ plume and greens represent the $\Delta T=7°C$ plume.

Figure 7.32: A comparison of U_o as a function of τ_o for increased tank heights of the plumes at different temperatures.

7.4.1.2   Increased tank width

The half tank width was increased from 0.1325m to 0.265m (double width), 0.19875m (50% increase) and 0.1767m (33% increase) for simulations.
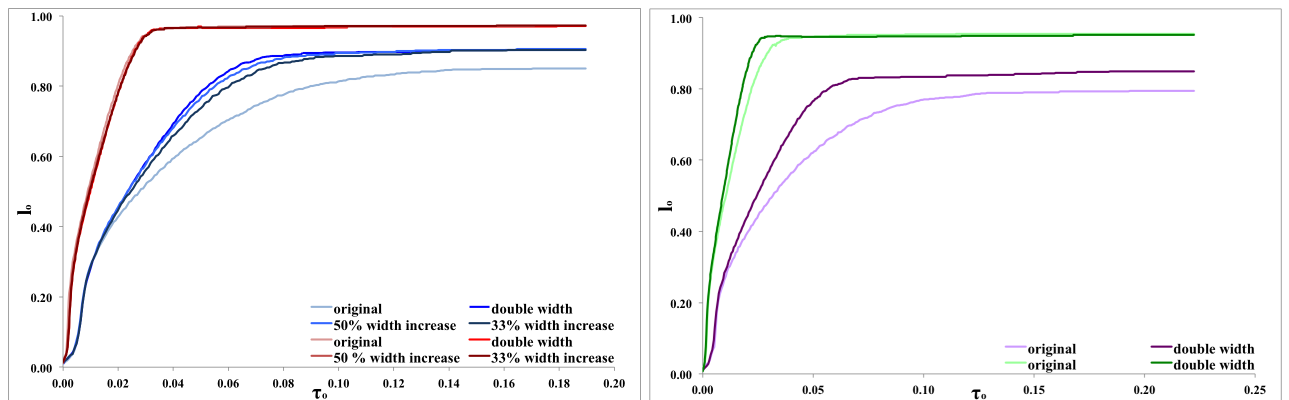
(a) Liquidose 436 simulations where the blues represent the $\Delta T=5°C$ plumes and red represent the $\Delta T=13.3°C$ plumes.

(b) Golden syrup simulations where the purples are $\Delta T=3°C$ plume and greens are $\Delta T=7°C$ plume.

Figure 7.33: Comparison plots of l_o as a function of τ_o for increased tank widths for different ΔTs.

Figure 7.33 displays plots of the height of the plume when the width of the tank was increased for different ΔT. At intermediate temperature differences ($\Delta T=13.3°C$ and $\Delta T=7°C$) there was insignificant change in the height of the plume for all the tank widths. The $\Delta T=13.3°C$ Liquidose 436 syrup plume height increase was 0%, -0.1% and 0.19% for double, 50% and 33% increased tank widths. The $\Delta T=7°C$ Golden syrup plume had height increase of -0.4% when the tank width was doubled. However, at low temperature differences ($\Delta T=5°C$ and $\Delta T=3°C$) the plumes ascended further in the tank when the width was increased. The $\Delta T=5°C$ Liquidose 436 plume height increase was 6.21%, 6.43% and 6.21% for double, 50% and 33% increased in

the tank width respectively. This shows that increasing the tank width had little effect on the $\Delta T=5°C$ plume. The $\Delta T=3°C$ Golden syrup plume also had a 6.44% increase in height from the original for the double width tank. The plumes appeared to stall $\tau_o=0.035$ earlier when the tank width had increased for all simulations except for the $\Delta T=13.3°C$ plume.
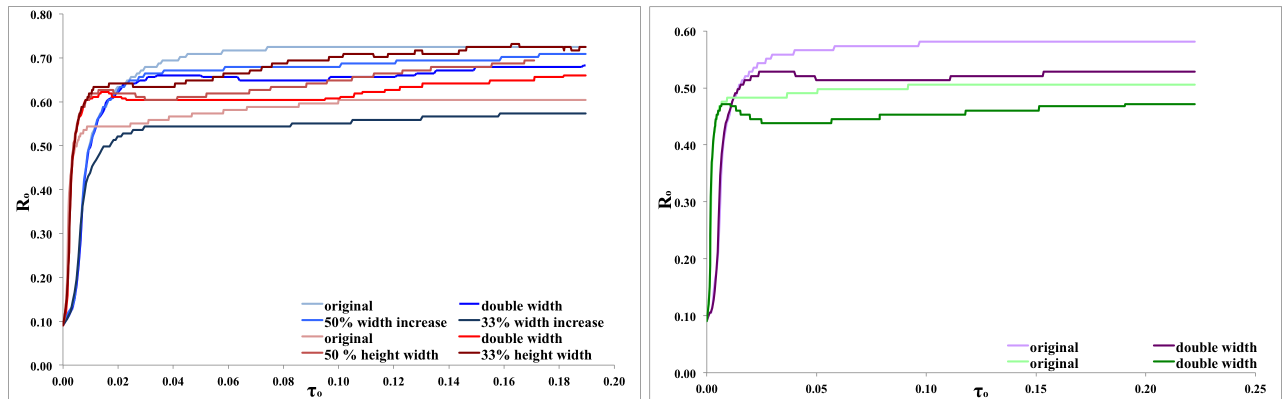
(a) Liquidose 436 simulations where the blues represent the $\Delta T=5°C$ plumes and red represent the $\Delta T=13.3°C$ plumes.

(b) Golden syrup simulations where the purples represent the $\Delta T=3°C$ plume and greens represent the $\Delta T=7°C$ plume.

Figure 7.34: Comparison plots of the R_o as a function of τ_o for increased tank widths at different ΔTs.

Figure 7.34 shows plots of the conduit radii change for different tank widths. The low temperature difference plumes ($\Delta T=5°C$ and $\Delta T=3°C$) conduit radii decreased as the tank width increased. The conduit radii measurements fell by 5.73%, 2.08% and 20.83% in the $\Delta T=5°C$ Liquidose 436 syrup plume from $D_o=0.72$ for double, 50% and 33% increased tank width respectively. There was a 10% decrease for $\Delta T=3°C$ Golden syrup plume from $D_o=0.58$ for double tank width. However, for intermediate temperature difference plumes, the conduit radius did not display similar results in both syrups. When the tank width was doubled the $\Delta T=7°C$ plume conduit radius decreased by 6.71% from $D_o=0.51$. However, the $\Delta T=13.3°C$ Liquidose 436 syrup plume's conduit radius increased by 9.38%, 15% and 20% from $D_o=0.60$ for double, 50% and 33% increased tank width respectively.

The absolute velocity of the plumes decreased during the investigations (Figure 7.35). At the end of the simulations the $\Delta T=13.3°C$ and $\Delta T=7°C$ plumes finished at the same absolute velocity of approximately $U_o=4.35$, which was an order of magnitude smaller than the beginning of the simulations. The $\Delta T=5°C$ Liquidose 436 plume had a absolute velocity increase of 6% for all the increased tank widths. However, the $\Delta T=13.3°C$ Liquidose 436 syrup plume had a 0.19% absolute velocity increase for the 50% and 33% increased tank width and no difference for the double tank width. The Golden syrup simulations at double tank width showed the absolute velocity increased by 6% for the $\Delta T=3°C$ plume and 0.4% for the $\Delta T=7°C$ plume at the end of the simulations.
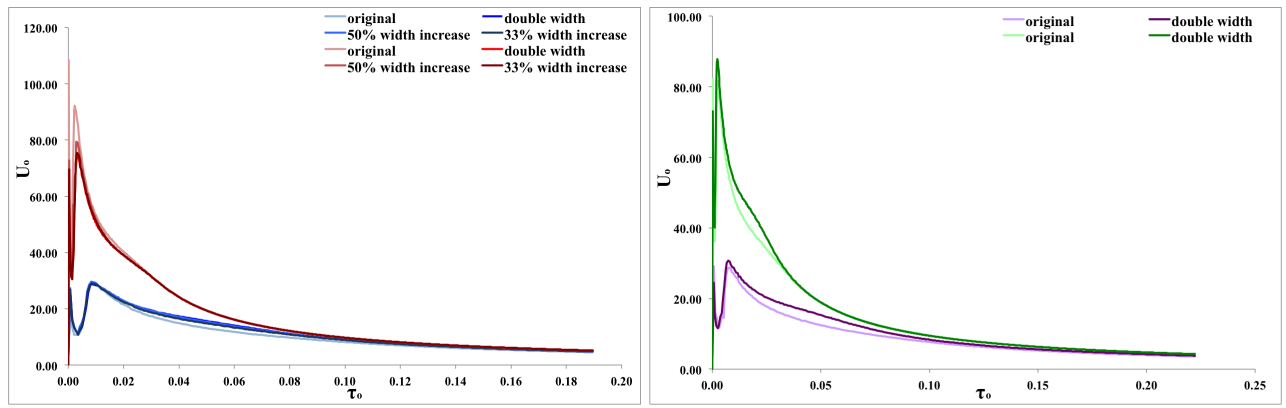
(a) Liquidose 436 simulations where the blues represent $\Delta T=5°C$ plumes and reds represent the $\Delta T=13.3°C$ plumes.

(b) Golden syrup simulations where the purples represent $\Delta T=3°C$ plumes and greens represent the $\Delta T=7°C$ plumes.

Figure 7.35: Comparison plots of the U_o as a function of τ_o for increased tank widths for different ΔTs.

7.4.2 Different fluid parameters and constant heater temperature

To further the understanding of the observed stalling behaviour in the plumes, the thermal diffusivity and thermal expansions were changed to understand how the plumes were affected. Additionally, the method of generating the plume was changed from a heater function to a constant heat source from the beginning of the simulation.

7.4.2.1 Increased Thermal Diffusivity

The thermal diffusivity used in the simulations was increased from $1.04\text{x}10^{-7}\text{m}^2/\text{s}$ to $2.08^{-7}\text{m}^2/\text{s}$ to understand if this value changes the height at which the plumes stalled. With the increased thermal diffusivity the Rayleigh number of the plume became smaller (Table 7.9).

ΔT /$°C$	Ra number at κ =1.04x10^{-7} m^2/s	Ra number at κ =2.08x10^{-7} m^2/s
5.0	8.64x10^4	4.32x10^4
13.3	4.21x10^5	2.10x10^5

Table 7.8: A table showing how the Rayleigh number changed for the same ΔT at different thermal diffusivities.

In Figure 7.36, increasing the diffusivity decreased the final height of the plume by 2.0% (l_o=0.019) in the $\Delta T=13.3°C$ and 13.5% (l_o=0.115) in the $\Delta T=5°C$ plume. As the achieved height decreased, the conduit radii increased for the double thermal diffusivity simulations (Figure 7.37). The largest increase related to the $\Delta T=13.3°C$ plume, where the conduit radius finished R_o=0.128 greater (42.5%) than the original conduit radius. The $\Delta T=13.3°C$ plume conduit radius also became constant τ_o=0.075 earlier than the plume with the original thermal

diffusivity.
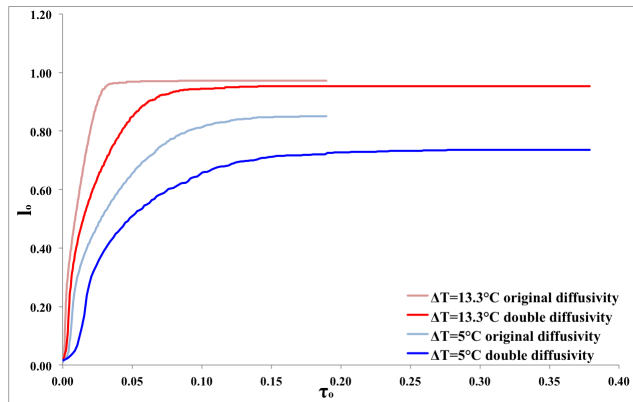
Figure 7.36: l_o as a function of τ_o for the Liquidose 436 plumes for two different thermal diffusivities.
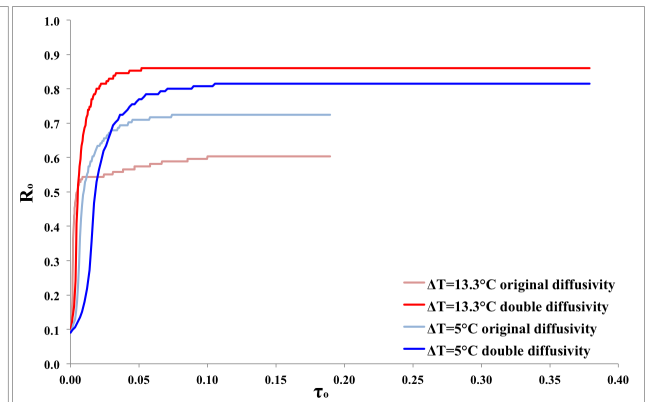
Figure 7.37: R_o as a function of τ_o for the Liquidose 436 plumes for two different diffusivity.
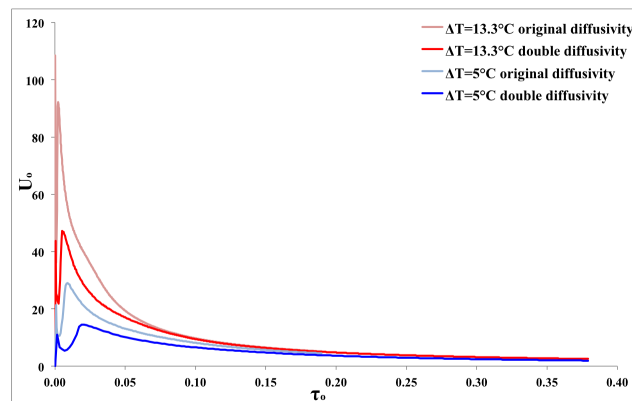
Figure 7.38: U_o as a function of τ_o for the Liquidose 436 plumes for two different diffusivity.

The absolute velocities of the plumes decreased after an initial peak (Figure 7.38). The $\Delta T=13.3°C$ plume was $U_o \approx 90.0$ greater than the $\Delta T=5°C$ plume absolute velocity in the beginning $\tau_o=0.002$. The $\Delta T=13.3°C$ plume at double diffusivity had a beginning absolute velocity 19% lower than the original diffusivity plume of the same temperature difference. However, the original diffusivity and double diffusivity plumes for the $\Delta T=13.3°C$ plume finish with a absolute velocity approximately $U_o=2.51$. In contrast, the $\Delta T=5°C$ double diffusivity plume began with an absolute velocity 2.3% greater than the original diffusivity but decreased to 13% lower than the original plume by the end of the simulations. The absolute velocity had a larger decline in the $\Delta T=13.3°C$ plume because the plume height had stalled after $\tau_o=0.030$.

7.4.2.2 Decreased Thermal Expansion

Simulations were undertaken to explore the effect of two different thermal expansions for each syrup (Table 7.9) on plume height, conduit radius and plume absolute velocity. The experimentally measured thermal expansion for the Liquidose 436 syrup and Golden syrup (Pears, 2010) were determined from the natural logarithm of the density and used for the simulations along with two published values as shown in Table 7.9.

ΔT /$^{\circ}$C	Syrup Type	Thermal Expansion/ $^{\circ}$C^{-1}	$\mathbf{Ra}_h$
5	Liquidose 436	3.54×10^{-4} (Measured)	8.64×10^4
5	Liquidose 436	3.10×10^{-4} (Newsome, 2011)	7.57×10^4
13.3	Liquidose 436	3.54×10^{-4} (Measured)	4.21×10^5
13.3	Liquidose 436	3.10×10^{-4} (Newsome, 2011)	3.63×10^5
3	Golden syrup	6.30×10^{-4} (Pears, 2010)	1.18×10^5
3	Golden syrup	4.33×10^{-4} (Wray, 1978; White, 1988)	8.11×10^4
7	Golden syrup	6.30×10^{-4} (Pears, 2010)	4.35×10^5
7	Golden syrup	4.33×10^{-4} (Wray, 1978; White, 1988)	2.99×10^5

Table 7.9: A table showing how the Rayleigh number changed for the same ΔTs at different thermal expansions.
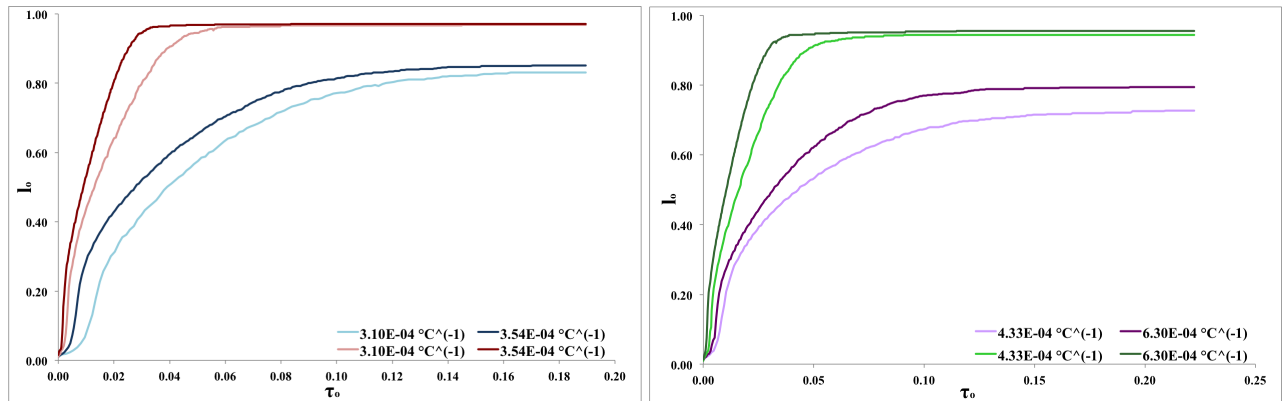
(a) Liquidose 436 syrup where the blues represent the ΔT=5°C plumes and reds represent the ΔT=13.3°C plumes.

(b) Golden syrup where purples represent the ΔT=3°C plumes and Green represent the ΔT=7°C plumes.

Figure 7.39: A comparison in l_o as a function of τ_o for plumes with different thermal expansions for each syrup.

Figure 7.39a and 7.39b show the comparison between the plume height for two different thermal expansions with time for the respective syrups. A lower thermal expansion leads to the plume ascending to a smaller height in the tank, with the largest effect on the height of the low ΔT plumes. Despite the similarity in the thermal expansions used for the Liquidose 436 syrup simulations, a height difference was generated. The ΔT=5°C plume height decreased by 2.44% from l_o=0.85. In contrast, in the Golden syrup simulations the thermal expansion was approximately 2×10^{-4} $^{\circ}$C^{-1} smaller from the original simulation. The ΔT=3°C Golden syrup plume height decreased by 8.55% from l_o=0.79.

Figure 7.40a and 7.40b show that lower thermal expansions led to larger conduit radii for both syrups. The Liquidose 436 syrup plumes finished with a conduit radii increase of 4.17% for the $\Delta T=5°C$ plume and a 27.5% increase for the $\Delta T=13.3°C$ plume for the lower thermal expansion value. In contrast, the Golden syrup plumes conduit radii also increased for the lower thermal expansion value, with a 13.0% increase for the $\Delta T=3°C$ plume and a 23.8% increase for the $\Delta T=7°C$ plume. The lower ΔT plumes in both syrups have wider conduit radii than the higher ΔT plumes. In the Golden syrup $\Delta T=3°C$ simulation the conduit radius became constant at $R_o= 0.650$ after $\tau_o=0.10$. However, for the $\Delta T=5°C$ plume the conduit radius became constant at $R_o= 0.755$ at $\tau_o=0.95$. Therefore, the $\Delta T=5°C$ plume conduit radius became constant $\tau_o=0.05$ earlier than the $\Delta T=3°C$ plume.
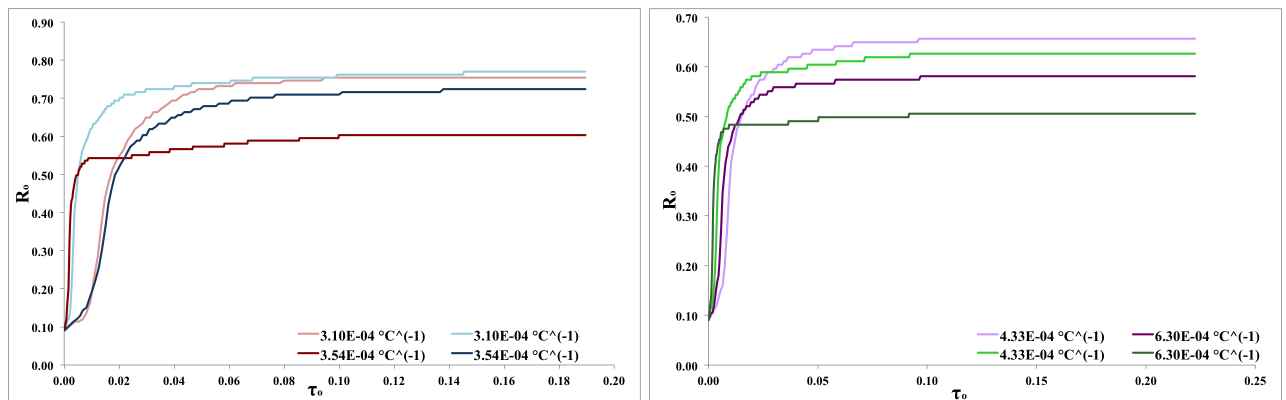
(a) Liquidose 436 syrup where blue represent the $\Delta T=5°C$ plumes and red represent the $\Delta T=13.3°C$ plumes.

(b) Golden syrup where Purple represent the $\Delta T=3°C$ plumes and green represent the $\Delta T=7°C$ plumes.

Figure 7.40: A comparison in the R_o as a function of τ_o for plumes with different thermal expansions for each syrup.

Figure 7.41a and 7.41b shows that the lower thermal expansion led to a decrease in the absolute velocity of the plumes. The absolute velocity at the end of the simulations in the Golden syrup was 8.6% lower in the $\Delta T=3°C$ plume and 1.2% lower in the $\Delta T=7°C$ plume for the lower thermal expansion value. The absolute velocity at the end of the simulations decreased by 2.4% for the $\Delta T=5°C$ plume and 0.4% $\Delta T=13.3°C$ plume for Liquidose 436 syrup lower thermal expansion value. The lower thermal expansion value for the Liquidose 436 syrup was 12.4% smaller than the original thermal expansion, but caused major changes in the plumes height, absolute velocity and conduit radius. In contrast the lower thermal expansion value was 31.3% smaller for the Golden syrup simulations and the change in the plume dimensions were similar as for the Liquidose 436 syrup plume. This is surprising given the percentage change in the thermal expansion for the Golden syrup being much larger.
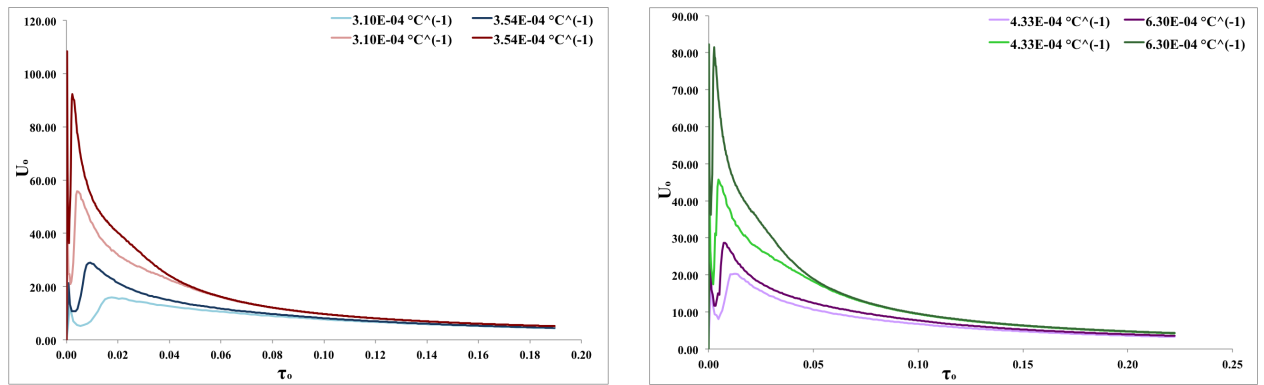
(a) Liquidose 436 syrup plume simulations where the blues represent the $\Delta T=5°C$ plumes and reds represent the $\Delta T=13.3°C$ plumes.

(b) Golden syrup plume simulations where the purples represent the $\Delta T=3°C$ and greens represent the $\Delta T=7°C$ plumes.

Figure 7.41: A comparison of U_o as a function of τ_o for plumes with different thermal expansions for each syrup.

7.4.2.3   Comparison of fixed heater temperature with heater function

The difference between the fixed heater temperature ($25°C$) and the heater function ($0.0524*t+22.0$, where t is time up to 58s and after that time the temperature is held constant at $25.0°C$) for the Golden syrup fluid (ambient temperature $22°C$) was investigated. Figure 7.42 shows that there was no significant difference (0.24% increase) in the height reached by the plume for the heater function versus the fixed heater. Additionally, there was no difference in the conduit radii (Figure 7.43). This is unexpected as it was assumed that the heater function would alter the height, conduit radius and absolute velocity of the plume compared to the fixed heater temperature. The maximum conduit radii for the two different simulations were $R_o=0.581$, which remained constant after $\tau_o=0.105$.
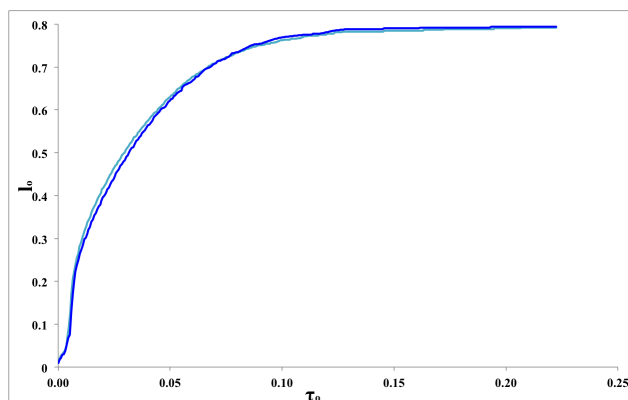
Figure 7.42: The comparison of l_o as a function of τ_o of the heater function (Dark blue) and the fixed heater(Light blue) for the $\Delta T=3°C$ plumes.
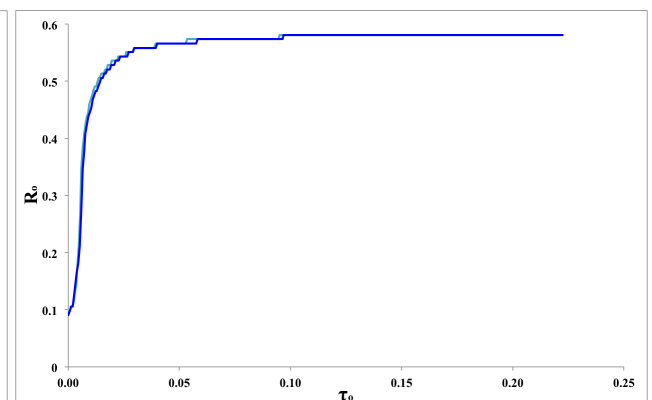
Figure 7.43: The comparison of R_o as a function of τ_o of the heater function (Dark blue) and the fixed heater (Light blue) for the $\Delta T=3°C$ plumes.

There was also a small discrepancy of 0.24% at the end of the simulations for the absolute velocity between the fixed and heater temperature plumes (Figure 7.44). Both plumes abso-

lute velocities decreased by a power-law, with the fixed plume simulation having the function $U_o = 1.3703\tau_o^{-0.713}$ and the heater function a power-law of $U_o = 1.4303\tau_o^{-0.693}$.
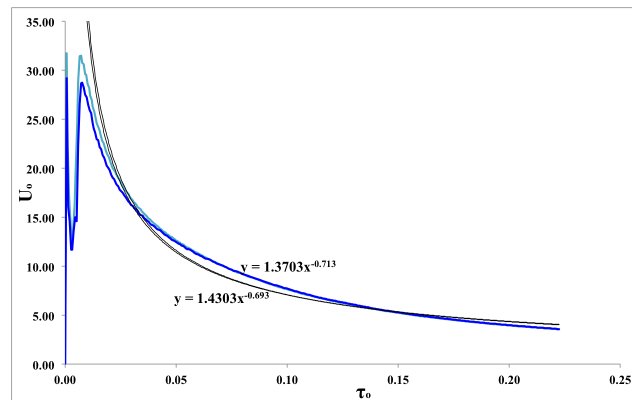
Figure 7.44: The comparison of U_o as a function of τ_o of the heater function (Dark blue) and the fixed heater (Light blue) for the $\Delta T=3^\circ C$ plume. The velocities of both plumes decrease with power-law functions as shown on the graph.

7.5 Summary

This chapter investigated stall and collapse in numerically simulated mantle plumes, using two different types of viscous fluids, through Fluidity; an adaptive mesh finite element code. The simulations undertaken were compared with the experimental results from Liquidose 436 syrup and also the Lyle's Golden syrup from Pears (2010). The simulated plumes did not collapse but stalled at the low and intermediate temperature differences up to $\Delta T=14^\circ C$. This shows that the collapse phenomena observed in the experimental investigations were not possible in an isothermal environment, according to the parameters of the simulations.

Chapter 8

Discussion

At the end of any study it is important to review the work undertaken and draw conclusions; such a review is presented here. The research presented in this study represents the first experimental and numerical investigation of thermal plume collapse applicable to planetary interiors. The experiments, using a cubic tank (26.5cm per inner side) and Liquidose 436 syrup, spanned a large range of conditions. Hypotheses and parameter ranges were further tested with the adaptive finite element code Fluidity, which has been benchmarked against laboratory experiments (Davies et al., 2011; Newsome, 2011).

This chapter will discuss the experimental results of Chapter 6, where two types of collapse were presented, and the numerical findings of stalled behaviour from Chapter 7. These results will be discussed in view of the phenomena observed and with reference to previous studies of mantle plumes. The plumes will be scaled using the Péclet number to enable the implications of this research to Earth and, in particular, Iceland where the plume waxes and wanes (Jones et al., 2002; Poore et al., 2009). Implications for Mars are also briefly considered.

8.1 Experimental Discussion

The aim of this study was to address the lack of experimental data on stall and collapse in thermal plumes through experiments with a point source heater. In laboratory experiments the plumes were driven by buoyancy resulting from thermal expansion and the conduction of heat, leading to dramatic effects (Griffiths and Campbell, 1990; Griffiths, 1986b,a). There are four main reasons that analogue experiments were extensively used for discovering new phenomena (Davaille and Limare, 2007):

- Experiments can explore new physical phenomena for which such equations do not yet exist.

- They can also explore ranges of parameters, or geometries where the equations are too non-linear to be solved analytically or numerically.

- They are inherently three-dimensional.

- They do not suffer from the limitations of numerical resolution.

The results of the laboratory experiments are applicable to other natural systems such as the mantle if the dynamics are similar between the scaled-down system and the natural system is respected (Davaille and Limare, 2007). Dynamical similarity can be viewed as a generalisation of the concept of geometrical similarity and requires the following:

- Similar boundary conditions (mechanical, thermal, geometry).

- Similar rheological laws. In other words, the mechanical equation of state that relates differential flow stress to strain rate should differ only in the proportionality constant.

- Similar balances between the different forces or operative physical effects. Ra and Pr reflect such balances.

Although experimental methods do not necessarily display the full complexity of Earth's mantle, in experiments the laboratory flow is real and precisely captures all the relevant physics that govern it's behaviours. This is why experiments are important for ascertaining new fluid phenomena.

The shadowgraph technique was used because it was suitable for strong gradients in plumes creating sharp contrasts in screen illumination. It was a simple method to implement and in this study allowed a large volume of experiments to be conducted. As mantle dynamics on geological time scales is dominated by "fluid" behaviour, liquids in experiments were able to be used at room temperature with fluid mechanics techniques. The experiments were designed to study a fluid dynamical regime (high Ra and Pr) that is relevant to the generation of mantle plume collapse in Earth. This was investigated through the formation of thermal plumes, from a traditional point source heater in the bottom boundary layer, and examined the behaviour of the plume through various Rayleigh numbers over many experimental runs. Shadowgraphs provided information on the instantaneous movement of the rising plume and the results observed that plumes collapse in two different ways, termed "stalled" and "lenticular" collapse. This was

then further investigated through SPIV experiments. It can be concluded that the collapse phenomena observed was contrary to the perceived wisdom that thermal plumes would not collapse.

8.1.1   Experimental Phenomena

The shadowgraph and SPIV results of plumes at the same temperature differences were qualitatively similar and show the same phenomena. Three regimes were determined from the experimental results, which will be discussed further below.

8.1.1.1   "Stalled" collapse regime

"Stalled" collapse was observed in unmixed syrup plumes between ΔT=3-6°C. The cause of the collapse and stalling was difficult to understand from the shadowgraph experiments alone; with the addition of the SPIV experiments it was possible to observe the presence of a large down-welling low velocity thermal mass, which was inhibiting the plume from ascending in the tank (Figure 6.49). It is possible that the plume stalled because the buoyancy force from the heater was not large enough to move the plume through the thermal mass or force the low velocity mass to move aside in the tank. In the SPIV experiment at ΔT=5°C, the flow in the tank was unsteady, because the background convection in the tank was observed to be scrolling on both sides of the tank and changed in size during the experiment. The scrolling in the plume head of the "stalled" collapse Liquidose 436 syrup plumes was visually similar to the scrolling in the injection experiments (e.g. Griffiths and Campbell, 1990). The collapse observed demonstrates that the assumption that thermal plumes should always survive because of their high Rayleigh number does not hold true here.

The velocity of the plume changed over the experiments as the down-welling thermal mass moved and the convection in the tank changed. The maximum velocity of the plume in Figure 6.25 increased in region 1 when the plume was forming in the tank and beginning its ascent. However, in region 2 when the plume was stalled the velocity of the plume decreased to U_o=3.10 from U_o=6.26. It was unexpected that in region 3 plume velocity would begin to increase once again, but this occurred because the migrations of the down-welling low velocity thermal mass to the RHS of the tank allowed the plume to begin to ascend more easily. Unlike the ΔT=5°C Liquidose 436 syrup and ΔT=3°C Golden syrup shadowgraph experiments where the plume collapsed, the ΔT=5°C SPIV experiment did not show signs of collapse. It is hypothesised that this may be because the experiment was not run for long enough. The "stalled" collapse occurred τ_o=0.243

earlier in the Golden syrup than in the Liquidose 436 syrup (Figure 6.11), which was expected because of the higher Ra number in the Golden syrup, due to the lower viscosity.

The vorticity images (e.g. Figure 6.28) from the SPIV facilitate further understanding of the "stalled" collapse. The thermal mass observed in Figure 6.24 was shown to have anticlockwise spin which was as strong as the the lobe of anticlockwise spin in the plume. The vorticity became stronger in the plume head and two extremes were observed by τ_o=0.007, which showed that the plume velocity was increasing in the tank. However, during the stalling phenomenon the vorticity decreased with the extremes becoming less pronounced. This implied that the fluid was spinning less because the plume had stalled and therefore velocity had reduced or remained more constant as shown in Figure 6.34. In region 3 the velocity in the centre of the plume appeared stronger and the anticlockwise spinning material in the plume increased in strength and was observed above the heater where a new scroll was observed at the base of the tank. This scroll could be background flow of material or some material trapped near the heater between the plume, which was attempting to ascend. The vorticity in the ΔT=5°C plume had the lowest value compared to the other SPIV plumes investigated which meant that there was less efficient stirring of material in the plume compared to higher ΔT plumes.

8.1.1.2 "Lenticular" collapse regime
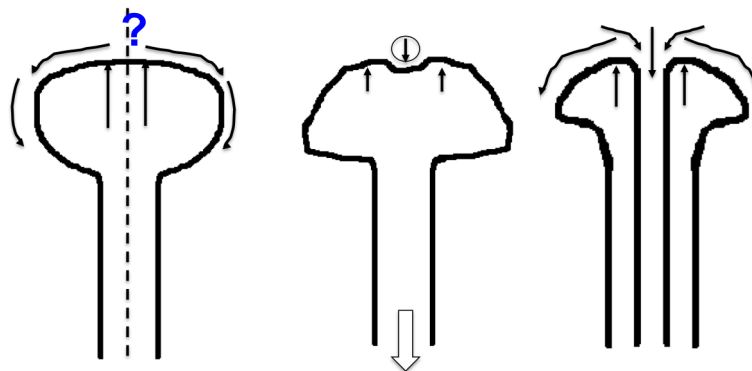
Figure 8.1: A diagram of the singularity at the top of the plume

"Lenticular" collapse was observed in the experiments between ΔT=7-23°C. Understanding what caused the "lenticular" collapse was complex. A possible explanation relates to the plume conduit, which was rising as a hot pipe of material as the experiment progressed. The material above the plume was flowing around the head (Figure 8.1) as observed in Figure 6.33. This material at the top of the plume was at ambient temperature and it began to inhibit the fluid in the centre of the plumes ascending in the tank. The material flowing around the plume head

could be gaining some heat from the head of the plume, which cools the point at the centre of the plume head. This would cause the material in the centre to become denser and material flowing up the plume conduit to flow around this denser material. The "lens shape" would then be observed in the shadowgraph experiment and the vortex observed in the SPIV experiment. With the heater still active, material would continue to ascend up the conduit to feed the plume head. However, the material that was originally flowing around the plume head which had cooled the centre would then begin to descend and the plume head to separate. This would form a singularity in the plume. The material which is still being fed to the plume by the heater would rise up the sides of this singularity, which is why in the experiment images the plume appeared to be still ascending and growing whilst the vortex/"lens shape" remained.

In the experiments both the Liquidose 436 and Golden syrup plumes demonstrated "lenticular" collapse, which was unexpected when the heater was active throughout the experiments. The SPIV experiment (Figure 6.33) was observed to have a down-welling low velocity mass which was inhibiting the plume from rising in the tank at the beginning (τ_o=0.020) of the experiment. However, this low velocity mass dissipated to the RHS of the tank, which meant that the plume possibly had a higher buoyancy causing the down-welling to disperse. After this occurred, a central vortex began forming in the plume head similar to that observed in Newsome (2011). The derived vorticity of the plume and the z-component of the plume velocity enabled further understanding of the behaviour of this central vortex. The central vortex was shown to be counter rotating versus the outer margins of the plume head within a central axis. However, the z-component of velocity showed that the material was also flowing inwards in the central vortex along the z-axis. This vortex and its behaviour supports the idea of a singularity in the plume head. The similarity in the vorticity in Figure 6.54 for the ΔT=13.3°C plume and the ΔT=12.8°C plume experiment from Newsome (2011), conducted in the laboratory in Michigan, show that the "lenticular" collapse can be reproduced in the same fluid in different locations. Additionally, the vorticity displayed the collapse in the ΔT=12.8°C plume from Newsome (2011), but that the central lobes of the vortex in the ΔT=13.3°C plume head elongated and there was no sign of collapse.

The maximum velocity of the SPIV ΔT=13.3°C experiment changed, from increasing in region 1 to almost constant in region 2, which was when the low velocity mass was dissipating (Figure 6.34). In region 2, the plume remained stalled in the tank because the central vortex in the plume head appeared at τ_o=0.039. Unexpectedly the velocity of the plume began to increase again in region 3, when the central vortex was still present, but there were signs that material was beginning to rise again in the tank around the central vortex.
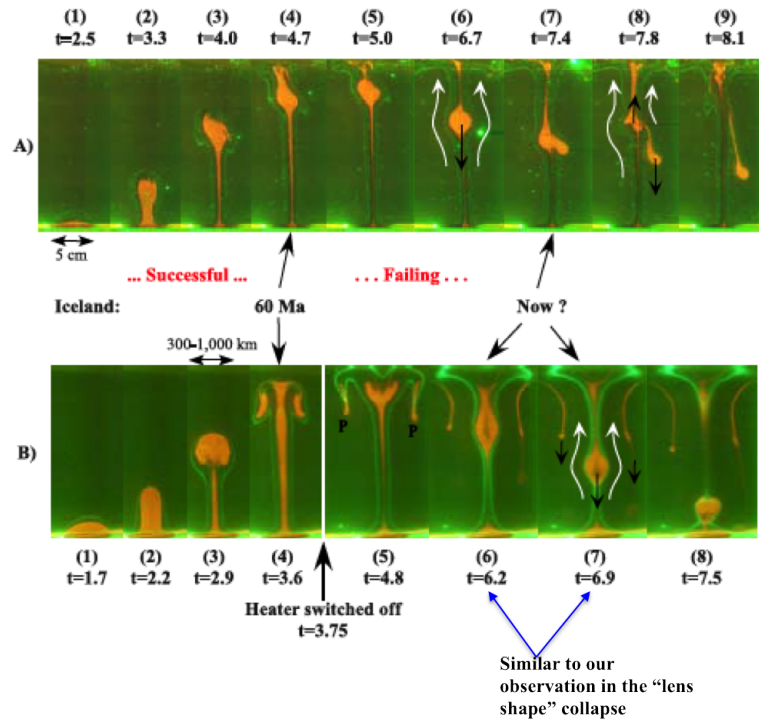
Figure 8.2: The evolution of the thermochemical plume with buoyancy flux 0.47. Time is normalised by the onset time of doming of 160 seconds. The isolated hot thermo-chemical blob is failing in the later stage of the experiment after the heater has been extinguished. From Kumagai et al. (2008).

The collapse observed whilst present in the laboratory during the experiments appeared to be similar to an observation by Kumagai et al. (2008) in Figure 8.2. In Figure 8.2, B6 and B7, the central part of the plume was bulbous in form. This was similar to what was observed in the "lenticular" collapse with, material flowing back to the base. Additionally, it fits with the observations of Newsome (2011). However, one major difference between the observations of the plumes in this study and Newsome (2011), and the plumes "failing" in Kumagai et al. (2008), is that the heater was extinguished in Kumagai et al. (2008). Another caveat, is that the plumes in Kumagai et al. (2008) were thermochemical in nature because two fluids were used in the experiments with densities 100kg/m^3 smaller than the density of the fluid used in the experiments in this thesis. This suggests that the reason for collapse, or "failing" as Kumagai et al. (2008) termed it, is due to the initially hotter but chemically heavier material in the plume head cooling enough to become denser than the ambient fluid before reaching the surface, the heterogeneous material therefore ceases to rise and sinks back to the base. This is likely to be what is happening in the "lenticular" collapse plumes because material continues to rise but some material was sinking down the conduit. Since the experiments in this thesis use only one fluid, it follows that the density difference is much smaller than for the experiments of Kumagai et al. (2008).

8.1.1.3 Surviving plumes regime

The plumes which were observed to survive had a $\Delta T > 23°C$. These plumes followed the expectation of plumes produced from a point source heater, having a mushroom shaped head and thin conduit (Figure 6.18) as observed in many other studies (e.g. Griffiths and Campbell, 1990). These surviving plumes that ascended to the surface agreed with the assumption that plumes with high Rayleigh numbers and ever present heat sources continue to rise for the duration of the experiment (Figure 6.7 and Figure 6.47). The rise of the plumes was characterised into two regions based on the maximum velocity from the SPIV experiments (Figure 6.47). The almost linear increase in height (Figure 6.17) and velocity (Figure 6.47) was termed region 1, while the steady-state and almost constant velocity when the plume had reached the surface was region 2. The conduit radii for the surviving plumes (Figure 6.7) were thinner than for the intermediate ΔT plumes. This followed the wisdom that the conduit decreases in size with time and increasing Rayleigh number (Parmentier et al., 1975; Lithgow-Bertelloni et al., 2001).

Figure 6.18 shows that the Golden syrup plumes appeared to rise faster in the tank than the Liquidose 436 syrup plumes. This was expected, because the Golden syrup plume had a lower viscosity at a lower temperature difference and the Rayleigh number would be higher than the Liquidose 436 syrup at the same temperature difference. Therefore in the ratio of time scales, the buoyant mass of the Golden syrup plumes was able to ascend easier because of the lower resisting effects of thermal diffusion. The Golden syrup plumes had higher Ra numbers because of the higher values in the thermal expansion ($2.76 \times 10^{-4}°C^{-1}$ greater), thermal diffusivity ($1.9 \times 10^{-8} m^2/s$ greater), and density ($3.22 kg/m^3$ greater at $20°C$) as well as a lower value of viscosity ($4.26 Pas$ less at $20°C$) in comparison to Liquidose 436 syrup. These different parameter values affected the formation of the plume and its growth.

The vorticity determined from the SPIV experiments pointed to two extrema in the plume ("vorticity centres") and the spinning observed in the plume head was well predicted by the vorticity (Davaille et al., 2011). Tanny and Shlien (1985) stated that in a thermal plume the vorticity distribution is spread over a wide area, which explains why the background vorticity was low. The vorticity was zero on the axis of the plume and the main plume had two distinctive lobes counter-rotating relative to each other. Rotation in the lobes of the plume was in the same direction as the scrolling in the plume head. The peak of vorticity was in the central region of the plume, closest to the heater, where conduit material was constantly heated throughout the experiment.

8.1.2   Determining whether the collapse is thermal or thermochemical

The principal question from the experiments undertaken is why was the collapse occurring? There are two possible scenarios:

- thermochemical contributions.

- the collapse was purely thermal and thus related to a thermal mass.

As two different types of collapse were observed it is possible that each of the scenarios relate to a different form of collapse. These scenarios were investigated through time series analysis of the refractive index of the Liquidose 436 syrup, to understand if the unexpected collapse phenomena were purely thermal or thermochemical. The overall aim was to determine whether the syrup was stratifying into layers in the tank, meaning that the supposed thermal plumes that collapsed underwent some small changes in buoyancy due to chemistry and thus could be thermochemical plumes.

The time series was configured in the bottle of similar height to the tank, to enable direct comparison and conclusions to be drawn between the two similar height systems of the settling of the syrup over time. The refractive index of the Liquidose 436 syrup was measured for approximately one year over a series of time intervals to ascertain how the refractive index changed and if the system was chemically well mixed (Figure 5.23). The syrup maintained its homogeneous nature within two standard errors, with an annual trend observed. After the first month the refractive index of the syrup was basically constant and there was no statistically significant difference. The Golden syrup time series (Appendix B, Figure B.1) cannot be said to have an annual trend because it was measured over a period of approximately one third of a year, but was nonetheless homogeneous in nature within two standard errors. As there was no change over one year in the Liquidose 436 syrup, the system was likely to be chemically well mixed and thus there was no stratification in the bottle. It should be noted that the bottle had a much smaller width than the tank and the same type of convection may not be occurring. However, in terms of the collapse observed in the experiments this refractive index would imply that there was unlikely to be stratification in the tank. If there was any stratification it could be a cause of the "lenticular" collapse, because the plumes rise far away from the thermal boundary layer into the main body of the tank.

The likely maximum density difference was determined from Figure 5.23 where the maximum variation in the refractive index was 0.005 and using data supplied by ADM (Table B.1 in Appendix B) it was calculated that 0.005 change in refractive index is a 0.2% change in sugar

content. This leads to a density difference of 0.13%. It should be noted that this is a small chemical difference and it is unlikely that this would have such an effect on density as to cause the plumes to collapse. Furthermore, Lin and van Keken (2006b) determined that the compositionally distinct region in D'' can survive throughout Earth's history if the density contrast is >2%. This could imply that the small density difference observed from the refractive index measurements may be unable to survive in the mantle for long periods and therefore, could lead to thermal conditions. However, if the tank remained well mixed within error then it is surprising that the mixing of the tank produced plumes that always rose to the surface yet when the syrup was unmixed the plumes were distinct and two collapse phenomena were observed. This implies there must be some form of compositional changes in the syrup, even on a minor scale. Further work could be conducted to gain further knowledge of the compositional change through heating and chemical investigations.
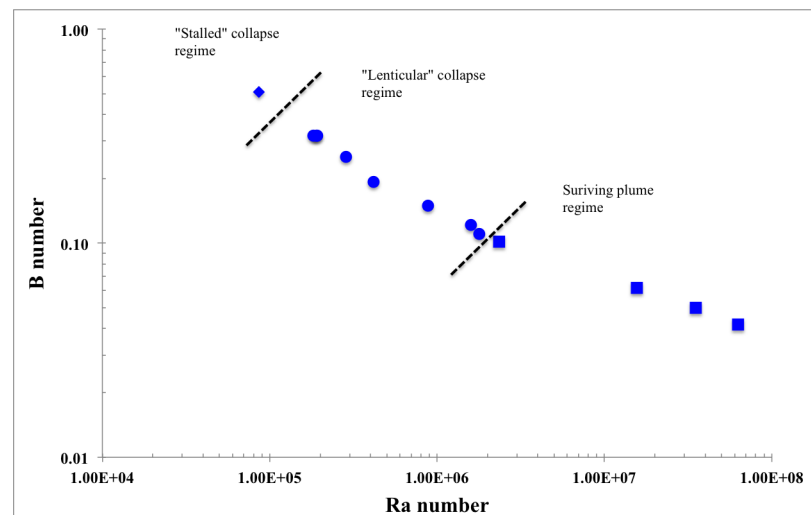
Figure 8.3: The Buoyancy of the time series analysis from the tank

From this density difference the buoyancy ratio (calculated with Equation 2.1) was calculated for all the unmixed experiments (Figure 8.3). Kumagai et al. (2008) stated that when the buoyancy number tended towards zero purely thermal plumes were produced. However, if the buoyancy number was greater than 1 then the thermal effects would not counterbalance the chemically denser anomaly. The surviving plumes in this thesis had a B number between 0-0.1 which fits that they are purely thermal plumes. However, the collapsing plumes occurred at B numbers below 1. "lenticular" collapse was determined to occur between B=0.11-0.32 and "stalled" collapse for B>0.5. Therefore, the "lenticular" collapse which is most similar to the results of Kumagai et al. (2008) do not fit his findings. Kumagai et al. (2008) presented the idea that separation between the active rising and sinking regions of the plume occurred for B=1.0. Active rising and sinking was observed in the "lenticular" collapse plumes however, the values of B calculated were between 0.11-0.32. This value could be so low due to the lack of a second

fluid with a greater density difference that 1.3kg/m^3. In contrast, Le Bars and Davaille (2002) determined that density contrasts smaller than 1% could change the dynamics of convection if coupled with viscosity contrast. Therefore, it is possible that the 0.13% density difference observed in the refractive index could invoke some change in the plume formation and provoke collapse. However, a chemical perturbation alone may not be sufficient to produce significant mantle plumes and is likely to be coupled with thermal perturbations (Lui and Chase, 1991).
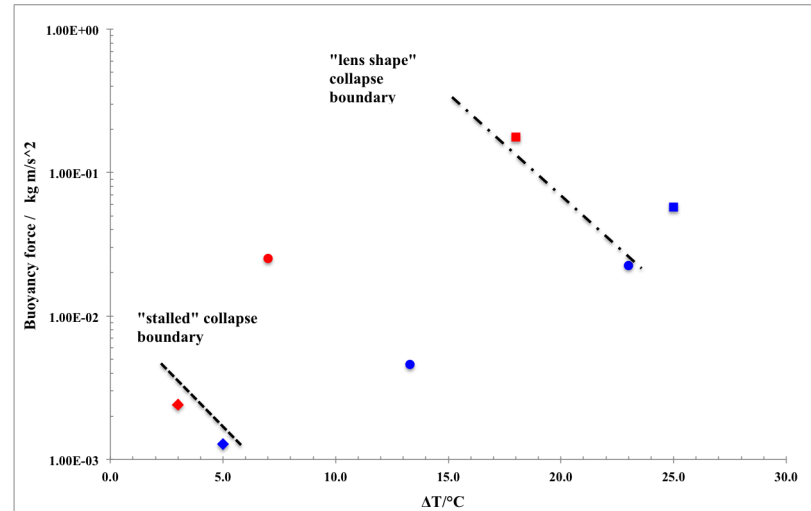
Figure 8.4: The buoyancy force for the shadowgraph plumes. Where red represents the Golden syrup, Blue represents the Liquidose 436 syrup. Diamonds represent "stalled" collapse, circles "lenticular" collapse and squares surviving plumes.

However, calculating the buoyancy force using $B_f = g\alpha\rho_h\Delta T V$, where V is the volume of the head of the plume with the radius measured at 6120 seconds, enabled implied boundaries to be obtained for the different regime plumes (Figure 8.4). The buoyancy of the higher ΔT plumes was at least an order or magnitude greater than the buoyancy of the "stalled" collapse plumes. The buoyancy forces were greater in the Golden syrup plumes and the difference between the buoyancy forces was most pronounced in the surviving plumes, where the $\Delta T=25°C$ plume buoyancy force was 0.12kgm/s^2 smaller than the Golden syrup $\Delta T=18°C$ plume.

When examining the dates of shadowgraph experiments and whether the plumes collapsed, it appeared that there needed to be a period of at least 10 days between experiments for collapse to occur in the plume experiments (Figure 8.5). If an experiment was conducted that had a large enough temperature difference ($\Delta T>23°C$) to rise to the surface, then the syrup would be mixed and the collapse would not be present in the next experiment conducted if the gap was smaller than 10 days and the $\Delta T<23°C$. The large gap in experiments on the graph was when the tank was undergoing some maintenance, followed by the preparation of the syrup for experiments. In terms of the difference in the $\Delta T=21°C$ plume behaviour in the shadowgraph and SPIV experiments, it could be related to time period between experiments. The SPIV experiment was conducted less than a week after another experiment and thus "lenticular" collapse was not

observed. Additionally, this ΔT is towards the upper end of the "lenticular" collapse regime and close to the beginning of the surviving plumes, thus making it possible the plume could survive.
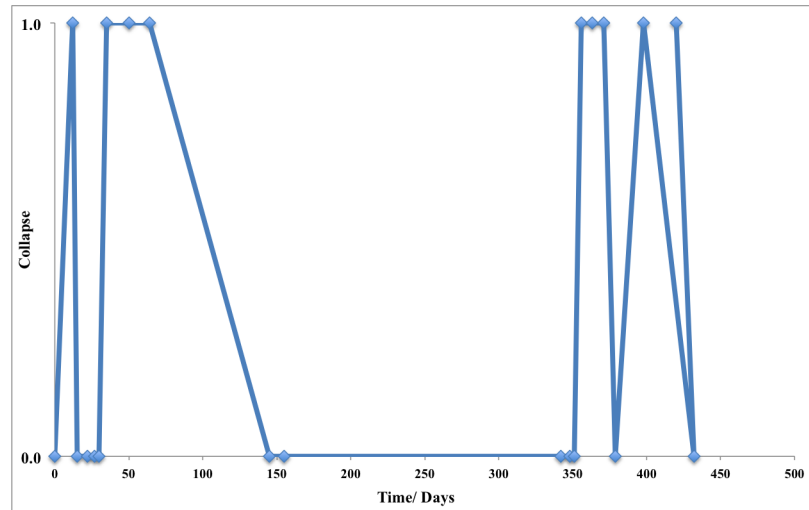
Figure 8.5: A plot showing whether a shadowgraph experiment collapsed or not. 1 is collapse, 0 is no collapse

The second scenario is that a thermal mass existed in the tank. This was observed in many of the SPIV experiments and appeared to be the reason why low ΔT experiments were unable to ascend further than the lower third of the tank. It is likely, therefore, that the "lenticular" collapse was primarily due to some thermochemical change in the syrup and the "stalled" collapse arose due to the down-welling low velocity thermal mass.

8.1.3 Analysis

It would be expected that all systems with the same dimensionless parameters (e.g. Ra) would behave in the same way, irrespective of their size (Davaille and Limare, 2007). The results would differ if the size of the system influenced the time scales and/or distance over which the phenomenon is observed. The convection in the laboratory on a scale of hours can be analogous to convection in the mantle over geological times and geological systems through the use of dimensionless numbers (Section 4.0.3).

From the shadowgraph images, measurements and SPIV data, further analysis was conducted with dimensionless numbers. As only a selection of experiments were presented some of the analysis contains the experiments portrayed in Chapter 6 and some will involve all the experiments undertaken.

8.1.4   Viscosity Contrast

Experimental studies in the viscous fluids with large Prandtl numbers illustrate that a laminar thermal plume rises with different regimes depending on the viscosity contrast (Kaminski and Jaupart, 2003).

The viscosity contrast (η^*) of the experimental plume was measured to ascertain whether it played a role in the three different regimes observed in the experiments (data for the viscosity contrast is in Appendix B). η^* is defined as:

$$\eta^* = \frac{\eta_\infty}{\eta_h} \tag{8.1}$$

where η_∞ is the viscosity of the ambient fluid at T_∞ and η_h the viscosity of the plume rising from the heat source at T_h. As stated earlier, the fluid is highly temperature-dependent and in terms of plume generation, collapse and survival there is some competition between the viscous stress (the resisting force) and the buoyancy (the driving force).
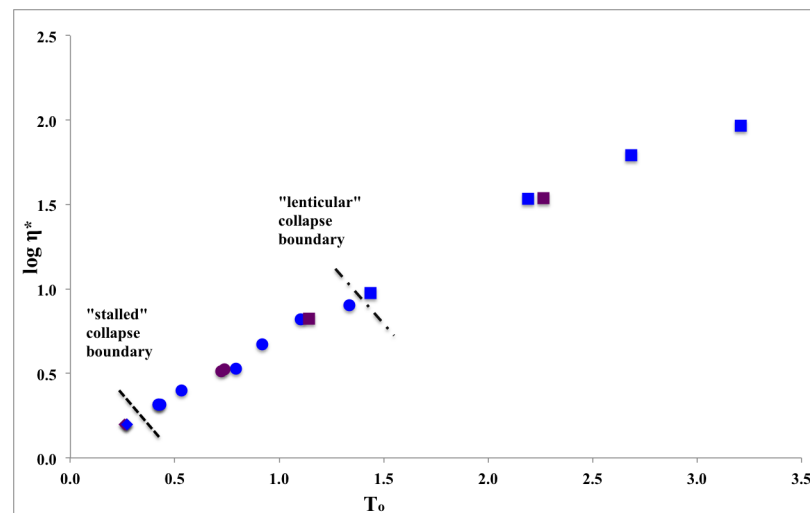
Figure 8.6: The regime diagram for unmixed Liquidose 436 syrup experiments where $T_o = \frac{\Delta T}{T_\infty}$. The diamond represent "stalled" collapse, circle "lenticular" collapse and squares surviving plumes. Blue is for the shadowgraph experiments and purple for SPIV experiments.

Figure 8.6 displays all the unmixed syrup experiments undertaken with Liquidose 436 syrup. The parameters were chosen for the Newtonian fluid to display the thermal relationship of the non-dimensionalised temperature to η^* for the experiments undertaken. It is possible to group the experiments into three regimes and thus boundaries are implied on the graph, chosen because viscosity of the fluid is temperature dependent and as the temperature of the fluid increases there is a direct implication on the viscosity. However, these boundaries are not truly known and could have a different gradient. The surviving plumes reached the top of the tank and occurred after $1.5T_o$. Below this boundary, to 0.35-$0.4T_o$, "lenticular" collapse was observed. Under the 0.35-

$0.4T_o$ boundary the "stalled" collapse phenomena occurred. The $\Delta T=21°C$ SPIV experiment that did not collapse (instead survived) and is positioned in the region of "lenticular" collapse due to the time period between experiments leading to plume survival.
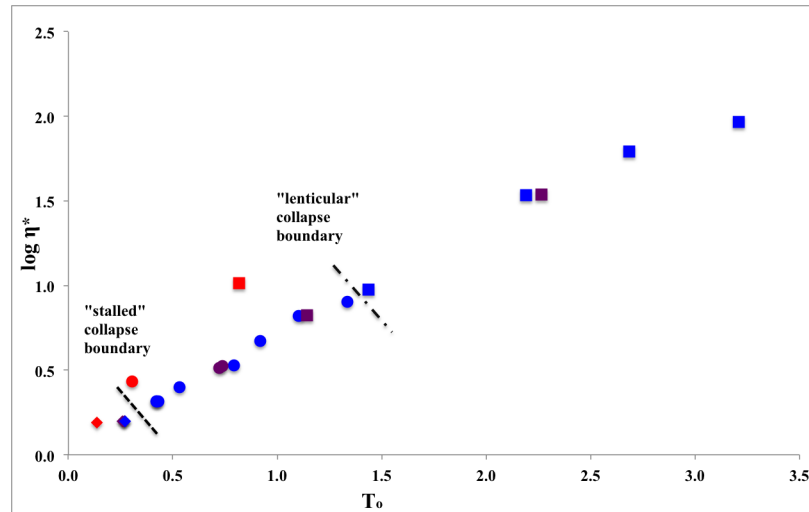
Figure 8.7: The regime diagram for all unmixed experiments. Blue represents Liquidose 436 syrup shadowgraph experiments, Purple Liquidose 436 syrup SPIV experiments, Red Golden syrup experiments. Diamond represent "stalled" collapse, circle "lenticular" collapse and squares surviving plumes.

Figure 8.7 is a regime diagram which includes the Golden syrup experiments from Pears (2010). The "stalled" collapse of both syrups, fall into the same lower boundary region. It was expected that the experiments would be located higher on the viscosity axis because the viscosity of the two syrups differ. The $\Delta T=7°C$ Golden syrup plume is plotted very close to the $\Delta T=5°C$ Liquidose 436 syrup. It does, however, remain within the boundary region of the "lenticular" collapse. There is a significant difference, however, in the placement of the surviving Golden syrup plume, as this does not fit into the boundary area of the other surviving plume experiments undertaken with Liquidose 436 syrup. It would have been useful to have further filled out the regime diagram (Figure 8.7) with more Golden syrup experiments to enable the exact boundaries for the two collapse phenomena to be known. However, this was not possible because the light source used for the Liquidose 436 syrup experiments was unsuitable for visualisation of the Golden syrup shadowgraph experiments, as discussed in Table 5.5. Additionally, as the mixing and settling of the syrup took one month (Subsection 5.2.2) it was not practical to change syrups regularly. Further work could be undertaken to add more Golden syrup experiments once different light sources have been tested.

In Figure 8.8, the regime diagram displays both the well mixed and unmixed experiments in Liquidose 436 syrup. The well mixed experiments undertaken were at low and intermediate ΔT and thus fall in the boundary where "stalled" collapse and "lenticular" collapse would be expected. However, all these experiments ascended to the top of the tank and thus this gives further support to the idea that when the syrup is mixed there is no stratification in the syrup
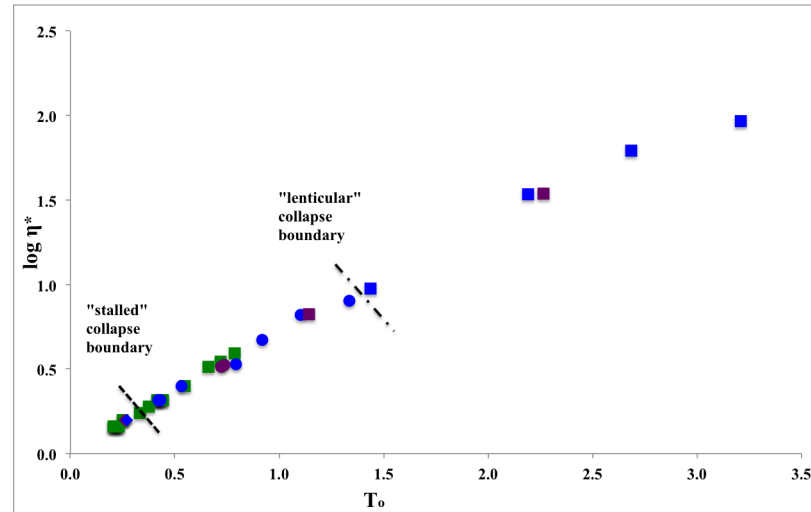
Figure 8.8: The regime diagram for all corn syrup experiments. Blue represents the unmixed shadowgraph experiments, Purple represents unmixed SPIV experiments and Green well mixed shadowgraph experiments. Diamonds represent "stalled" collapse, circle "lenticular" collapse and squares surviving plumes.

and the plumes are purely thermal in nature. However, the unmixed syrup may have some stratification, which changes the nature of the syrup and thus inhibits the plume's ascension to the top of the tank. The distinctive difference between the two well mixed and unmixed syrup was presented in Figures 6.23 and 6.20. It was unexpected that the mixed plume was so faint in the tank for the first 0.15m (l_o=0.615) of ascent as shown in Figure 6.21, because the shadowgraphs should only observe temperature differences of the index of refraction. Therefore, when the syrup was unmixed the structure that was observed in the shadowgraph images was more a visual representation of the changes in refractive index with chemistry than temperature.

8.1.5 Time Scales

The diffusion time for the plume can be obtained using the diffusive time scale (Equation 6.2). The l used for this investigation of time scales is the diameter of the heater (2cm) and thus the diffusion time is the same for all the plumes of the same syrup. This time was compared to the time taken for the plume to rise 3cm in the tank (Table 8.1). The ratio of the rise time compared to the diffusion time could be a controlling factor in the three regimes observed experimentally.

Table 8.1 and Figure 8.9 show that the ratio of rise time to diffusion time was largest for the "stalled" collapse plumes and smallest for the surviving plumes. The surviving plumes were able to ascend in the tank unimpeded because the rise time was very small compared to the diffusion time. Therefore, the plume was able to traverse the tank before too much heat diffused out to the ambient fluid. However, the rise time and the diffusion time for the "lenticular" collapse plume were fairly comparable and thus the plume was losing heat at the same rate that it was rising.

(a) Liquidose 436 plumes

Description	ΔT /°C	τ_c/ s	t_{rise} /s	t_{rise}/τ_c
Experiment	5.0	3857	3000	0.78
Experiment	13.3	3857	2800	0.73
Experiment	25.0	3857	1680	0.44
Numerical	5.0	3857	3821	0.99
Numerical	13.3	3857	1125	0.29
Numerical	25.0	3857	768	0.20

(b) Golden syrup plumes

Description	ΔT /°C	τ_c/ s	t_{rise} /s	t_{rise}/τ_c
Experiment	3.0	3265	4260	1.30
Experiment	7.0	3255	2100	0.65
Experiment	18.0	3235	900	0.2
Numerical	3.0	3265	6400	1.96
Numerical	7.0	3255	1056	0.32
Numerical	18.0	3235	474	0.15

Table 8.1: The ratio of rise times to diffusion times of the experimental and numerical plumes

The Golden syrup experimental plumes had a smaller diffusion time, by ~600 seconds because the thermal diffusivity was $1.9 \times 10^{-8} m^2/s$ larger. For the "lenticular" collapse experiments the Liquidose 436 plume showed diffusion time comparable to rise time. However, this rise time was 1154 seconds smaller than the diffusion time in the Golden syrup plume, signifying that the plume could ascend in the tank quicker than the plume was diffusing out heat. It is likely that the diffusion time comparable to the rise time is another reason affecting the "stalled" collapse plumes, which failed to ascend further than the lower quarter to one third of the tank. However, it is unlikely that this ratio of rise time to diffusion time was the sole reason for the "lenticular" collapse, because the plumes were able to rise at least half way up the tank before collapse was observed. Therefore, it could be that the chemistry in the tank could also be contributing to the collapse.
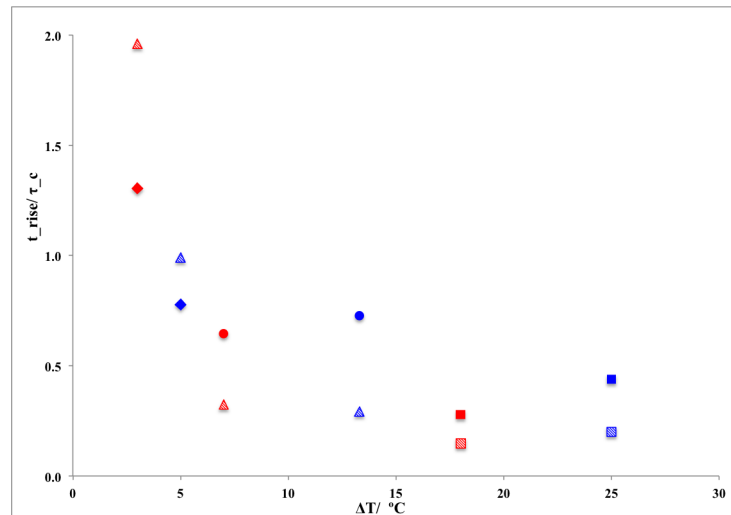
Figure 8.9: The temperature difference against the ratio of rise time to diffusion time for the experimental and numerical plumes. Red represents Golden syrup, blue represents Liquidose 436 syrup, stripes represent numerical simulations, Diamonds represent "stalled" collapse, circles "lenticular" collapse and squares surviving plumes, triangles represent stalled simulated plumes.

In the numerical simulations the plumes divided into more distinct boundaries. The simulated plumes that stalled had a ratio of rise time to diffusion time of 0.29 or greater. The ratios smaller than 0.29 ascended to the surface of the tank. Additionally, the low ΔT simulated plume in the Liquidose 436 syrup had a rise time comparable to diffusion time, whereas, the $\Delta T = 3$°C

simulated plume rise time was almost double the diffusion time. This is surprising because the plume was still able to ascend 0.2175m (l_o=0.82) in the tank.

8.1.6   Rayleigh number

The Rayleigh number gives a concise summary of the convective system and thus can aid with further understanding of the regimes observed. As the temperature difference of the plume experiments increased, the Rayleigh number also increased (Figure 8.10). The Liquidose 436 plumes had lower Rayleigh numbers than the Golden syrup plumes at the same temperature differences, due to the different viscosities and densities of the syrups as shown in Figure 6.54.
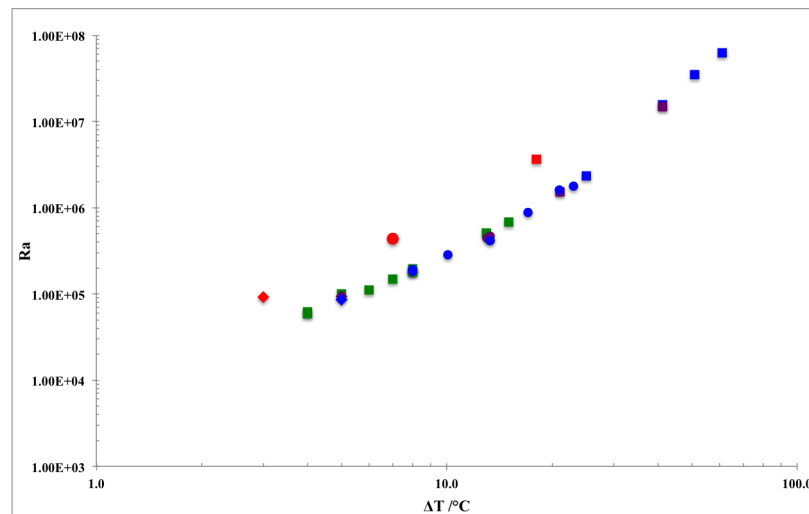
Figure 8.10: The Rayleigh number of the plumes as a function of the temperature difference. Purple represents the SPIV Liquidose 436 syrup experiments, blue represents the shadowgraph Liquidose 436 syrup experiments and red represents the Golden syrup shadowgraph experiments. The diamonds, circles and squares represent the "stalled" collapse, "lenticular" collapse and the plumes that survived, respectively.

The thermal boundary layer grows by conduction above the heater following activation, until the buoyancy generated is sufficient for the layer to become unstable and the plume to develop (Newsome, 2011). In the purely conductive heat transfer phase, the depth of the fluid had little impact and the thickness of the boundary layer was the important length scale. Therefore, the original Rayleigh number (Equation 4.4) was modified to Equation 8.2:

$$Ra_\delta = \frac{\rho g \alpha \Delta T \delta^3}{\kappa \eta} \tag{8.2}$$

Where δ is the thermal boundary layer. The longest stage of plume formation in the low temperature difference plumes is the conductive thermal boundary building (Davaille and Vatteville, 2005). Once the thermal boundary layer has been exhausted, it is rebuilt by heat conduction and the cycle begins again. The TBL becomes unstable once the local Rayleigh number (Equa-

tion 8.2) exceeds the critical value and forms a plume (Howard, 1964) and is investigated to understand whether the TBL plays a role in the collapse regimes. The TBL thickness increases by thermal diffusion and grows by Equation 8.3:

$$\delta = 2.32(\kappa t_b)^{0.5} \tag{8.3}$$

where t_b is onset time.

ΔT /$^{\circ}C$	t_b/ s	δ/ cm
5.0	1800	3.17
8.0	1500	3.01
10.0	1560	2.95
13.3	600	1.83
25.0	300	1.30

(a) Liquidose 436 plumes

ΔT /$^{\circ}C$	t_b/ s	δ/ cm
3.0	2340	3.39
7.0	2040	3.17
18.0	720	1.89

(b) Golden syrup plumes

Table 8.2: The thermal boundary layer thickness of the experimental shadowgraph plumes.

Table 8.2a and Table 8.2b compare the results from the calculated TBL for the two different syrups. The Golden syrup experiments had thicker TBLs than the Liquidose 436 syrup experiments, meaning the plume appeared later in those experiments. This was unexpected because the viscosity of the Golden syrup was less than for Liquidose 436 syrup. The thermal boundary layers of the "stalled" collapse plumes were only a few centimetres smaller than the maximum height reached by the plume before collapse began. This implied that the majority of the plume head and conduit actually remained part of the TBL for the experiment. Therefore it is likely that the size of the thermal boundary layer does play a role in the "stalled" collapse phenomenon. However, the TBL and rise and diffusion times are likely to play a less important role in the "lenticular" collapse phenomenon because the TBL is much smaller than the maximum height reached by the plume before the "lens shape" was observed. Therefore, it is likely that "lenticular" collapse occurs due to small-scale density heterogeneities in the syrup.

Figure 8.11 displays the qualitative nature of the Ra_δ dependence on the natural logarithm of η^* as stated in the work of Stengel et al. (1982) and White (1988). Both authors observed Rayleigh-Bénard convection in fluids with exponential or super-exponential temperature-dependent viscosity. The Ra_δ increased with viscosity contrast $\ln\eta^*$ but began plateauing in their experiments at $\ln\eta^*$=8.0 and then decreased. The viscosity contrasts investigated in this thesis are in the lower region of the work from Stengel et al. (1982) and White (1988).

In Figure 8.12 the location of the unexpected collapse plume from Newsome (2011) fits in the location of the other "lenticular" collapse data. It is therefore possible to imply boundaries for
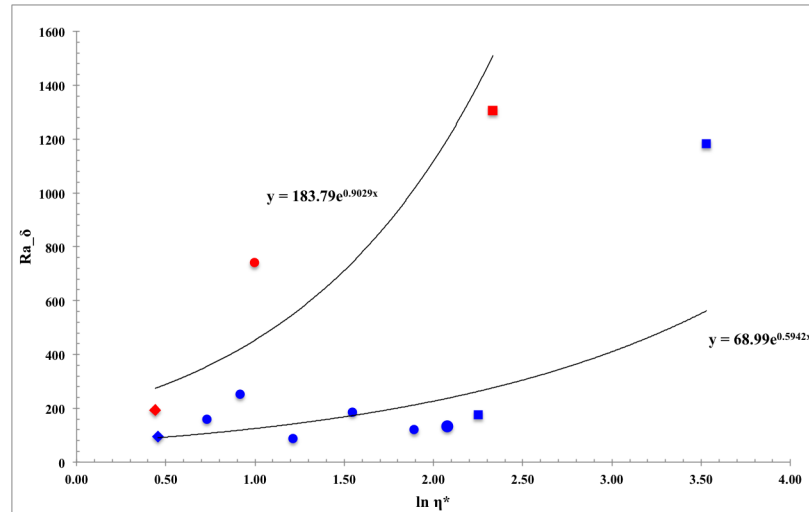
Figure 8.11: A plot of Ra_δ versus $\ln\eta^*$, where blue represents the Liquidose 436 shadowgraph experiments and red represents the Golden syrup shadowgraph experiments. The diamonds represent the "stalled" collapse, circles represent the "lenticular" collapse and the squares, surviving plumes.
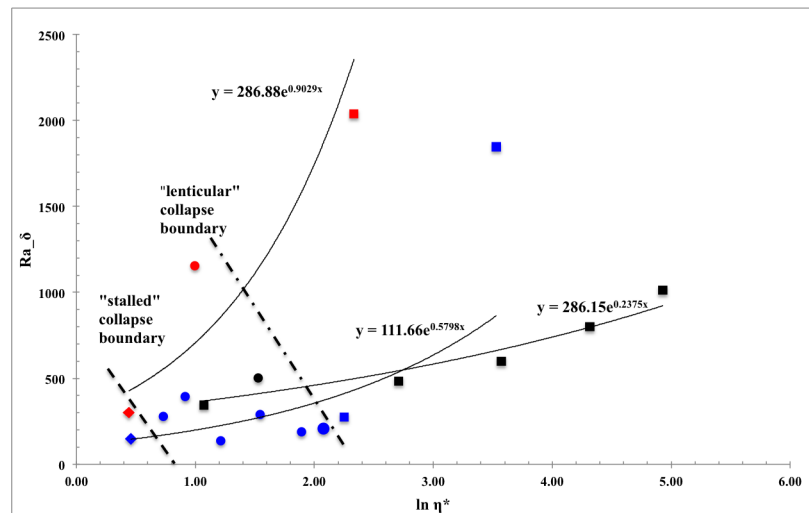
Figure 8.12: A plot of Ra_δ versus $\ln\eta^*$ including Newsome (2011) data. Where blue is the Liquidose 436 shadowgraph experiments, black the SPIV experiments of Newsome (2011) and red, the Golden syrup shadowgraph experiments. The diamonds represent "stalled" collapse, circles "lenticular" collapse and squares the surviving plumes.

the collapse. Although one other of Newsome's (2011) plumes plots in the "lenticular" collapse boundary but was a surviving plume, because Newsome (2011) only observed collapse in one experiment. The plot shows that the different regimes fall into different regions for the onset of Rayleigh-Bénard convection.

A further way of understanding the plume regimes is to investigate the onset time (t_b) of the plume (i.e first appearance in the tank) which was inputted into Equation 8.3. This time was determined from visualising the plumes using ImageJ and was plotted (Figure 8.13) for the shadowgraph plumes in the Golden and Liquidose 436 syrups. As the Rayleigh numbers of the plumes increased, the onset time of the plumes decreased. Following the fit used by Davaille (1999b) a power-law fit of $t_b = aRa^c$ was applied to the plot, where for Liquidose 436 syrup plumes a=156767 and c=-0.396 and for Golden syrup plumes a = 118032 and c= -0.331, although

the fit of Davaille (1999b) was $Ra^{-2/3}$ for two-layered thermal convection. The surviving plumes from this study form a short period after heater activation and thus have thin thermal boundary layers. The stalled plumes take at least 30 minutes to form and the thermal boundary layer, by implication, is thicker as seen in Table 8.3. It is important to note that the onset time for the shadowgraph experiments cannot be truly representative of when the plumes first appear because the images were only captured in 5-minute intervals.
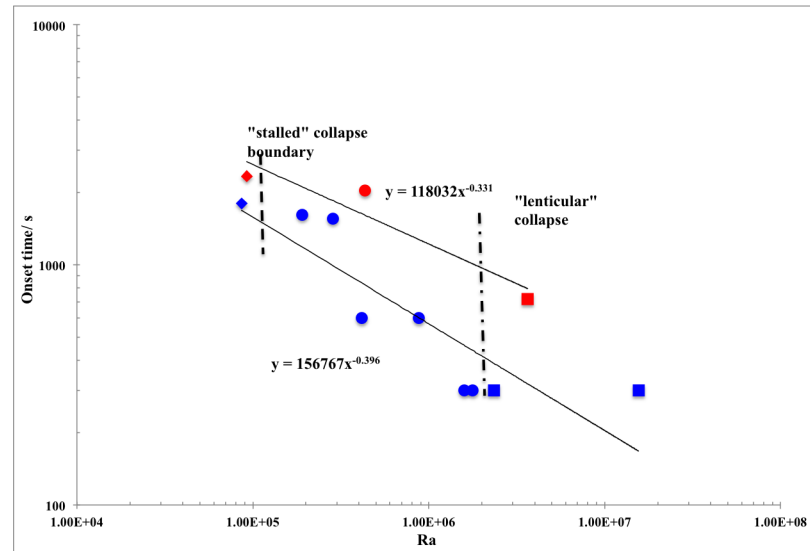
Figure 8.13: A plot of the onset time of the plume against Rayleigh number. Blue represents the Liquidose 436 syrup, red the Golden syrup. Diamonds represent "stalled" collapse, circles "lenticular" collapse and squares surviving plumes.

8.1.6.1 Ra-Pr relationship

The relationship between the Rayleigh number and the Prandtl numbers gives additional understanding into the three regimes. The ratio of the buoyancy forces to momentum, illustrates the sensitivity of the plume to small changes in temperature because the temperature-dependent fluid alters the amount of thermal diffusion from the plume (Figure 8.14). There are distinctive boundaries implied on the graph for the different plume phenomena. The Prandtl number decreases with increasing Ra number because of the temperature dependence of the fluid. For the surviving plumes, the Rayleigh number is high when the buoyancy forces are greater than the viscous forces and thus the Prandtl number is low because the viscous diffusion is less. This allows the plume to ascend with ease in the tank and reach the surface within a few hours. However, when the Pr number is high, the plumes stall in the tank before collapsing, because the dominant force is the viscous force occurring and thermal diffusion plays a smaller role.

Plotting the data from the experiments on to the graph from Manga and Weeraratne (1999) shows that the surviving plumes fit into their region of plume dominated flow. The $\Delta T=21°C$ SPIV plume that was expected to collapse but actually survived is situated on the graph in the
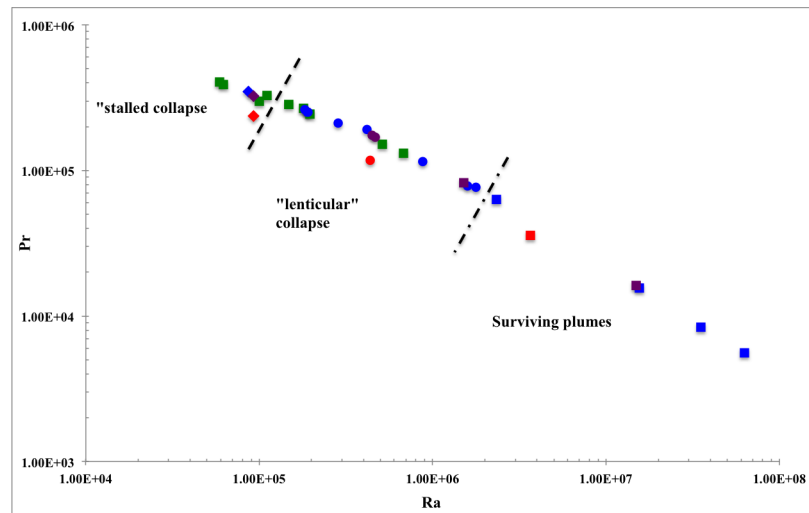
Figure 8.14: A plot showing the Pr and Ra for the different temperature difference experiments. Where blue represents the Liquidose 436 syrup shadowgraph experiments, purple the SPIV Liquidose 436 syrup experiments, green the mixed Liquidose 436 shadowgraph experiments and red the Golden syrup shadowgraph experiments. Diamonds represent the "stalled" collapse, circles the "lenticular" collapse and squares the surviving plumes.

transitional region of the results of Manga and Weeraratne (1999). This is interesting because the $\Delta T = 21°C$ plume is towards the upper boundary of the "lenticular" collapse that was previously observed. The lower boundary of the temperature difference for "lenticular" collapse plumes fits in the unsteady location on Figure 8.15 and the "stalled" collapse appears in the region where the plumes are both steady and unsteady. From observation in the $\Delta T = 5°C$ SPIV plume the flow appeared qualitatively to be unsteady. It should be noted that the experiments conducted by Manga and Weeraratne (1999) involved basal heating of the tank, which would generate multiple plumes. However, it is interesting that the results from the experimental work in this thesis fit into the locations of the experiments of Manga and Weeraratne (1999), thus helping to explain the three different regimes observed in this study.
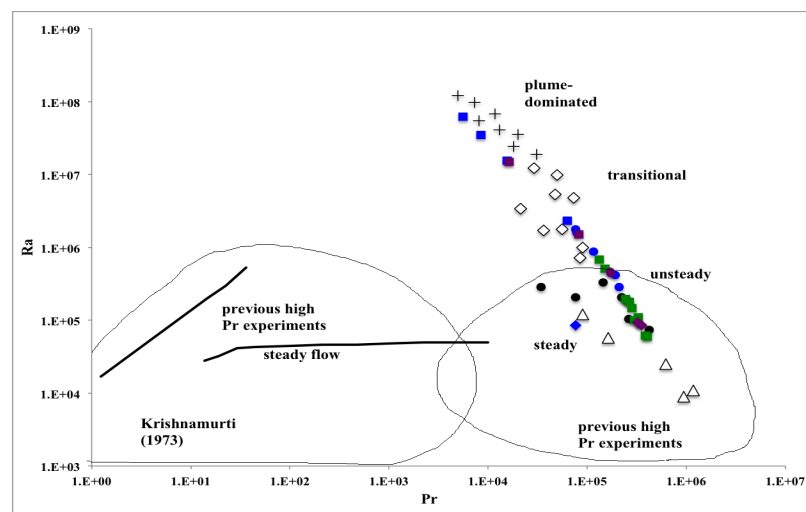
Figure 8.15: Regime diagram showing the Liquidose 436 shadowgraph experiments and the ranges of parameter space covered by other studies and fluids. Adapted graph from Manga and Weeraratne (1999). Experimental data from this thesis is plotted, where blue represents shadowgraphs, purple represents SPIV and green represents well mixed shadowgraph experiments. Diamonds represent "stalled" collapse, circles the "lenticular" collapse and squares the surviving plumes.

8.1.7   Pr-Gr relationship

Further insight of the three regimes can be gained by examining the relationship between Prandtl number and Grashof numbers, (the ratios of the buoyancy and viscous forces to kinematic viscosity and thermal diffusivity). This illustrates how sensitive the plumes are to small differences in viscosity. The product of the Grashof and Prandtl numbers gives the Rayleigh number.
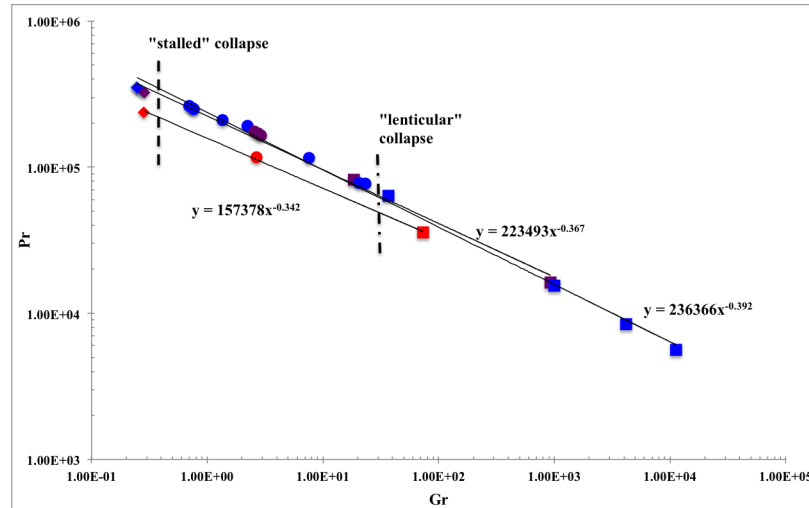
Figure 8.16: A plot showing the Gr and Pr for the different temperature difference experiments. Where red represents Golden syrup, blue the shadowgraph Liquidose 436 syrup, purple the SPIV experiments. The diamonds represent "stalled" collapse, circles the "lenticular" collapse and squares the surviving plumes.

Figure 8.16 shows that the three different regimes fall into boundaries which are implied by lines on the graph. A power-law was fitted to the graph $Pr = aGr^{-x}$, where for the shadowgraph Liquidose 436 syrup a=236366 and x=0.392, for Golden syrup, a=157378 and x=0.342 and SPIV Liquidose 436 syrup experiments a= 223493 and x=0.367. The power-law was chosen because the Prandtl number from experiments scales with the Ra$^{\sim\frac{-1}{3}}$ and the Pr also scales with Gr$^{\sim\frac{-1}{3}}$. The Prandtl number is only dependent on the fluid state, whereas the Grashof number is also dependent on the length scale; in this case the tank height. When the Pr is high the Gr number is low. The "stalled" collapse plumes had large viscous forces compared to the buoyancy and thus they could not rise in the tank and stalled before collapsing. However, when Gr for the surviving plumes is high, the viscous forces are small and the high buoyancy enables the plume to rise to surface of the tank. This implies that the strength of the flow in the surviving plumes is the greatest and the strength of the flow in the "stalled" collapse plumes is weak. The heat transfer is less conductive in the "stalled" collapse compared to the surviving plumes. When the Pr is high the heat diffuses quickly compared to the momentum of the plume rising. Therefore, the "stalled" plumes were diffusively losing heat quicker than the plume was ascending and the viscous forces in the tank were also inhibiting the plume from growing. The values of the Gr for the experiments were between 0.14-1.12x10^4 which is well within the laminar regime because

the transition to the turbulent regime occurs at 10^9 (Kays et al., 2004). Therefore the motion of flow in the plumes was laminar and stable. When the Pr number is low there is less heat transfer to the surroundings and the plume has a long lifetime in the tank.

8.2 Discussion of Numerical Simulations

The use of Fluidity to simulate experimental results enabled an extension of the parameter ranges used in the experiments and the ability to eliminate the possibility of chemical contributions to the buoyancy of the plume. This study demonstrated that at low ΔTs for the Liquidose 436 and Golden syrup simulations the plumes could not collapse but instead stalled. The collapse phenomena was not observed in the numerical simulations for three reasons. Firstly, the simulations were isothermal, enabling a purely thermal system with no outside influences such as air-conditioning generating a temperature gradient horizontally and vertically in the tank or natural temperature variations with seasons. The plumes simulated are the dominant and only flow occurring in the tank, whereas the experimental plumes are ascending in a fluid where there is a weaker large-scale convection induced by the low Rayleigh critical number and material cooling at the imperfect insulating top and side walls. In the simulations the walls were modelled as with constant temperature. Secondly, it was not possible to simulate a small thermochemical aspect or potential sugar layering in the syrup. It is likely that the experimentally convecting system is more closely relevant to conditions seen in the mantle than a purely isothermal system with no convection as in the numerical simulations. Finally, the viscosity of the syrup varies by $\sim$10% between batches and during experiments. This is something that has not been simulated in the numerical tank. The fact that no collapse was observed numerically implies that collapse cannot occur in an isothermal system which is well mixed. This also leads to the implication that the tank of Newsome (2011) was not truly isothermal, with the likelihood of some stratification in the syrup as determined from the refractive index measurements made in this study, or water from the external tank having an impact.

The plumes simulated using Fluidity had a more typical and expected plume shape as the ΔTs became larger. Prior to this at low ΔTs the plumes appeared to rise with more of a fingerlike shape such as the isothermal compositional injection experiments of Whitehead and Luther (1975) (Figure 2.1). The authors described plumes rising as a finger when the viscosity of the plume was greater than the ambient fluid, but in these simulations the plume is less viscous than the surrounding fluid. The experimental plumes ascended in the tank slower than the numerically simulated plumes and this was due to the fact that the simulations were isothermal

and the plumes did not have to overcome the convection and large thermal down-welling observed in the SPIV experiments.

Two regimes were observed in the numerically simulated plumes. The plumes under $\Delta T=14°C$ stalled in the tank, whereas those above this temperature difference ascended to the surface. In relation to the experimental results the high ΔT plumes were qualitatively similar, as the plumes rise to the surface of the tank as expected. However the intermediate and low ΔT simulated and experimental plumes were qualitatively similar in the stalling behaviour only. At the ΔT boundary where stalling ceased in the simulations, the experimental plumes continued. In the experiments, below $\Delta T=6°C$ the "stalled" collapse phenomenon was observed and between $\Delta T=6\text{-}23°C$ "lenticular" collapse occurred. The numerical stalling phenomenon is expected in the low and intermediate temperature difference plumes because the diffusion time and rise times are comparable, especially in the low ΔTs. It is expected that with an ever-present heat source the plumes would continue to ascend until they reach the surface due to the continued supply of less dense material rising up the conduit.

At $\Delta T=41.2°C$ all three methods for visualising plumes were qualitatively similar and can be used to corroborate aspects of the plumes evolution. The conduits of the simulated plume do not show the same behaviour as the experimental plumes. The experimental plume grew rapidly after the TBL formation whereas the simulated plume was observed to grow at a more steady pace.

All the conduits in the numerical simulations with the original tank width continued to grow throughout the simulations. This was an unexpected finding because it differed to the experimental results (e.g. Figure 7.4) and the theory that the plume conduit in thermal plumes should decrease in size as the plume ascends (Figure 7.12). Additionally, for increasing Rayleigh numbers the simulated plume did not follow the perceived understanding that the conduit radii should reduce in size (Parmentier et al., 1975; Lithgow-Bertelloni et al., 2001). Figure 7.31a displayed the increasing conduit width at $\Delta T=13.3°C$ with an increased Rayleigh number compared to the $\Delta T=5°C$ simulated plume. However, when the thermal diffusivity increased the conduit radii (Figure 7.37) followed this idea of Parmentier et al. (1975) and Lithgow-Bertelloni et al. (2001).

When the thermal expansion of the plumes was decreased correspondingly the height the plumes reached in the tank decreased (Figure 7.39a and 7.39b). This was expected because in the Rayleigh number a lower thermal expansion leads to a decreased amount of buoyant mass, but the amount of thermal diffusion that can occur remains unchanged. Furthermore, when the

thermal diffusion was increased, the height reached by the plumes decreased (Figure 7.36). The higher velocities of the simulated plumes for higher ΔTs follows the assumption that the higher Rayleigh number will lead to a larger buoyant mass. This enables the plume to rise faster in the tank as the resisting forces are lower compared to the small thermal expansion (Figure 7.41a and 7.41b).

The simulations undertaken at different aspect ratios proved that changing the aspect ratio of the tank would not affect the plume evolution and inhibit the stalling phenomenon and thus could not be the reason for the "stalled" and "lenticular" collapse observed experimentally. The increased height of the tank influenced the ascension of the plume. In Figure 7.30, the plume continued to stall at the three new tank heights and, in particular, when the tank height was doubled the ΔT=5°C plume was only able to traverse 50.8% of the tank. Therefore, the tank height was not the reason for the stalling behaviour observed. It is likely that the plume was diffusing out heat faster than heat was transported up the conduit from the base. Increased height leads to increased time for diffusion. Alternatively, the increased tank width simulations led to the plumes ascending further at low ΔTs, which is unexpected because the Rayleigh number for the plumes remained constant. Therefore, at low temperature differences the original width of the tank appeared to inhibit the growth of the plume. However, it did not stop the stalling phenomenon from occurring; it just occurred at a higher height but at an earlier time.

8.3   Dynamical similarity and scaling

The goal with any study in fluid mechanics modelling is to determine 'scaling laws' which enable predictions of the behaviour of similar systems. No reliable scaling laws have been determined thus far to describe the evolution of size and speed of all plume heads, and presently there are conflicting results from different studies (Davaille and Limare, 2007).

The seminal scaling paper of Batchelor (1954) has been the basis for numerous scaling studies since the 1950s, such as Moses et al. (1991) and Moses et al. (1993). Howard (1964) developed a phenomenological model for plume formation, scalings for the onset time of thermal instabilities and the boundary heat flux. This model agrees with experimental data from Sparrow et al. (1970), Manga and Weeraratne (1999), Parmentier and Sotin (2000) and Davaille and Vatteville (2005). However, plumes are complex as they combine the effects of buoyancy, diffusion and advection (Moses et al., 1993). Despite vast research into plumes there remains diversity and some confusion based on the fact that plumes may originate from a point, a line source or basal source, can have sustained or 'one-shot' heat input (thermals), can be steady (the stem) or

starting (the cap), can be turbulent or laminar and thus a unified view is hard to achieve (Moses et al., 1993). Limare et al. (2008) believed that the source of scaling discrepancies lies not only in the different experimental configurations but originates from the fact that plume definition often depends upon the visualisation technique employed. Therefore, different scaling laws are proposed for different studies and there is no unified view. It has been difficult to find scaling laws for the collapse regimes because not all of the plumes ascended to the surface. Despite this difficulty, an attempt is made here to scale the plumes using the Péclet number.

The Péclet number (Pe, a dimensionless number) is used for scaling experimental plumes to Earth's mantle (Equation 8.4) because of its representation of the imposed large-scale velocity of the plume in non-dimensional form (Gonnermann et al., 2004). It investigates the transport phenomena in fluid flows, as the ratio of advection of a physical quantity by the flow to the rate of diffusion, or also known as the product of the Reynolds (Equation 4.3) and Prandtl number (Equation 4.2):

$$Pe = \frac{l_c U}{\kappa} \tag{8.4}$$

where l_c is the height of the tank, U the velocity of the plume and κ is the thermal diffusivity.

8.3.1 Scaling Length and velocity

Scaling of the fluid properties is possible due to the fact that all fluid of the same type behave in the same fundamental way.

The scaling of the tank length to the mantle was undertaken. The Pe number (Equation 8.4) calculated for the experiments was used to scale the tank length to the mantle, with the thermal diffusivity (κ) of the mantle as the oceanic lithospheric value of $1\times10^{-6} \mathrm{m^2/s}$ and the velocity (U) of the Icelandic spreading ridge $5.80\times10^{-10}\mathrm{m/s}$. The characteristic length for the mantle was determined and presented in Table 8.4. However, if the length of the mantle was inputted as 2891km the U_{scaled} could be determined instead (Table 8.4).

Investigation type	$\Delta T/$ °C	$l_{tank}/$ m	$\kappa/$ m^2/s	$U_{max}/$ m/s	Pe	$l_{scaledmantle}/$ km	$U_{scaledmantle}$ / m/s
Shadowgraph Liquidose 436 syrup	5.0	0.265	1.04x10^{-7}	7.67x10^{-6}	19.60	33.80	6.78x10^{-12}
Shadowgraph Liquidose 436 syrup	13.3	0.265	1.04x10^{-7}	1.10x10^{-5}	27.98	48.24	9.68x10^{-12}
Shadowgraph Liquidose 436 syrup	25.0	0.265	1.04x10^{-7}	2.36x10^{-5}	59.83	103.18	2.07x10^{-11}
Shadowgraph Golden syrup	3.0	0.265	1.23x10^{-7}	7.85x10^{-6}	16.98	29.28	5.78X10^{-12}
Shadowgraph Golden syrup	7.0	0.265	1.23x10^{-7}	2.38x10^{-5}	51.27	88.41	1.77x10^{-11}
Shadowgraph Golden syrup	18.0	0.265	1.23x10^{-7}	4.63x10^{-5}	100.24	172.85	3.47x10^{-11}
SPIV Liquidose 436 syrup	5.0	0.265	1.04x10^{-7}	2.50x10^{-6}	6.38	11.01	2.21x10^{-12}
SPIV Liquidose 436 syrup	13.3	0.265	1.04x10^{-7}	2.56x10^{-5}	65.40	112.77	2.26x10^{-11}
SPIV Liquidose 436 syrup	21.0	0.265	1.04x10^{-7}	6.04x10^{-5}	153.40	264.53	5.31x10^{-11}
SPIV Liquidose 436 syrup	41.2	0.265	1.04x10^{-7}	1.57x10^{-4}	397.74	685.87	1.38x10^{-10}
Numerical Liquidose 436 syrup	5.0	0.265	1.04x10^{-7}	1.20x10^{-5}	30.66	52.88	1.06x10^{-11}
Numerical Liquidose 436 syrup	13.3	0.265	1.04x10^{-7}	4.26x10^{-5}	108.50	187.09	3.75x10^{-11}
Numerical Liquidose 436 syrup	23.0	0.265	1.04x10^{-7}	4.36x10^{-5}	110.84	191.14	3.83x10^{-11}
Numerical Liquidose 436 syrup	25.0	0.265	1.04x10^{-7}	5.73x10^{-5}	145.44	3250.79	5.03x10^{-11}
Numerical Golden syrup	3.0	0.265	1.23x10^{-7}	1.20x10^{-5}	12.75	21.99	4.41x10^{-12}
Numerical Golden syrup	7.0	0.265	1.23x10^{-7}	4.26x10^{-5}	164.07	282.93	5.68x10^{-11}
Numerical Golden syrup	18.0	0.265	1.23x10^{-7}	4.36x10^{-5}	168.99	291.41	5.85x10^{-11}

Table 8.3: Scaling of the experiments and numerical simulations to the length of the mantle and mantle velocity using the Pe number.

There are difficulties with scaling the plumes to Earth as shown in Table 8.4. As three different regimes were observed it would be expected that the two sets of plumes which collapsed would not reach the surface. However, it would be expected that the $\Delta T=25°C$ plume and $\Delta T=18°C$ experimental plumes would scale to the mantle adequately because they reached the surface of the tank. Consequently these plumes had a scaled length of 103.18 km and 172.85 km respectively which implies that the plumes would only traverse one tenth of the lower mantle. The scaling of length appears to be somewhat more successful for the simulated plumes with the length scale calculated leading to the plumes travelling further in the mantle. However, the $\Delta T=25°C$ simulated plume scaled to have a length greater than the height of the mantle. Nonetheless the Pe numbers calculated from the experiments and numerical simulations fit mostly within the ranges of values determined by Richter and Parsons (1975), where the author's experimental Peclet numbers were between 30-1700 for Rayleigh numbers between 10^3 and $7x10^5$ and their plumes had rise times of between 51-8000Myr. Although it should be noted that the experiments conducted by Richter and Parsons (1975) had an analogue plate at the surface of the tank.

Scaling using the Peclet number to discover the velocity led to very low values of velocity for plumes in the mantle. The majority of the values calculated in both the numerical and experimental plumes have velocities which move less than 1mm/a, an order of magnitude greater in time than the 100Myr predicted by Campbell (2005) for a plume to ascend to the surface. Only a few plumes from those in the table were actually simulated to reach the surface, but even those would be expected to travel to the surface before 1000Myr. The plume that rises with a scaled velocity of 4.35mm/a is the $\Delta T=41.2°C$. Apart from the collapse, the reason that these plumes are not scaling as predicted could be due to the very low temperature differences. In the mantle, plumes are often 200-300°C hotter than the surrounding mantle (Herzberg et al., 2007).

The relationship between Pe and Ra can be expressed as Equation 8.5:

$$Pe = aRa + b \tag{8.5}$$

as shown in Figure 8.17. Where a $= 2x10^{-5}$ for all the experiments and b $= 19.302$, 28.118 and 57.047 for the Liquidose 436 shadowgraph, Golden syrup shadowgraph and Liquidose 436 SPIV experiments respectively. The linear fit was chosen because of the nearly linear relationship of the rise velocity in the numerical and experimental plumes up to their maximum velocity. Using the relationships from Figure 8.17 it is possible to calculate the rise time of plumes in the mantle with a 1000km diameter (Campbell, 2005), using the Rayleigh number 10^7 (the average value for the mantle) and the thermal diffusivity as stated earlier. This predicts the plume head rise
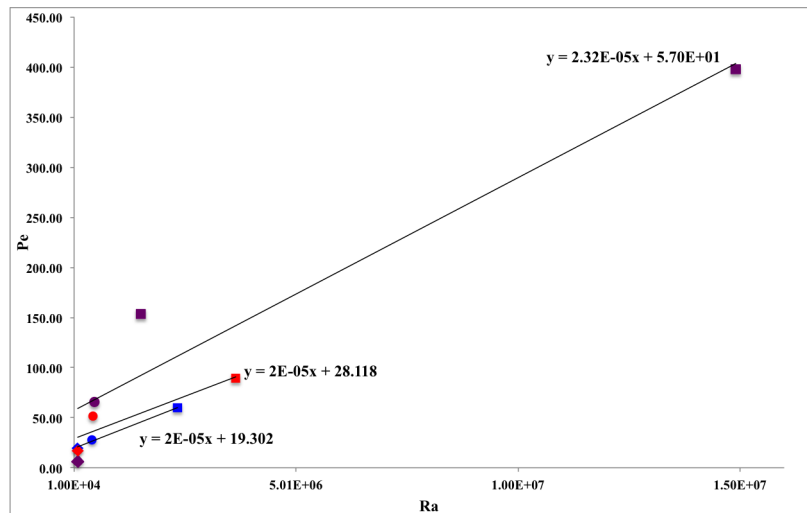
Figure 8.17: The Pe number against the Ra number for the experimental plumes for Earth. Where the squares represent the surviving plumes, circles represent the "lenticular" collapse and diamond represent the "stalled" collapse. Blue represent the Liquidose 436 syrup and red represent the Golden syrup and purple represent the SPIV experiments.

velocity of 9.12mm/a for the SPIV plumes, 6.92mm/a for Liquidose 436 plumes and 7.2 mm/a for Golden syrup plumes. The plumes would therefore take 311Myr, 410Myr and 394Myr to ascend to the surface. These numbers are more suitable for the mantle, but are only possible because of the higher Rayleigh number.

Mars is another planet where mantle plumes are thought to exist and have been attributed to the formation of Tharsis. Scaling has been implemented for Mars because it is the planet in the solar system that is most like Earth, but is a single plate planet with a radius half that of Earth. The values used for scaling were $\kappa = 9.6 \times 10^{-7} \text{m}^2/\text{s}$ (Reese et al., 2002), which is smaller than the value for Earth, and $\text{U}_{max} = 2.76 \times 10^{-10} \text{m/s}$ (Schubert et al., 1990). Firstly, the length of the tank was scaled to Mars, then the length of Mars' mantle ($1.80 \times 10^6 \text{m}$) was held constant and the velocity scaled to Mars.

Scaling using the Pe number for Mars was equally difficult. The plumes that rose to the surface of the tank were not scaled adequately for Mars' mantle and only the SPIV $\Delta \text{T}=41.2°\text{C}$ plume managed to almost reach the surface. This high temperature difference SPIV experiment had a velocity which is consistent with Mars. All the other velocities scaled are an order of magnitude or two too small compared to the velocity of plumes in Mars' mantle. The Péclet numbers are so low for all bar the $\Delta \text{T}=41.2°\text{C}$ plume which is why the velocities and lengths do not scale adequately. However, as before, the collapse plumes show that they would not reach the surface and the scaling is showing that the intermediate ΔT plumes would traverse half to two-thirds of the way through the mantle.

Investigation type	$\Delta T/$ °C	$l_{tank}/$ m	$\kappa/$ m^2/s	$U_{max}/$ m/s	Pe	$l_{scaledMars}/$ km	$U_{scaledMars}$
Shadowgraph Liquidose 436 syrup	5.0	0.265	1.04×10^{-7}	7.67×10^{-6}	19.60	68.25	1.05×10^{-11}
Shadowgraph Liquidose 436 syrup	13.3	0.265	1.04×10^{-7}	1.10×10^{-5}	27.98	97.42	1.49×10^{-11}
Shadowgraph Liquidose 436 syrup	25.0	0.265	1.04×10^{-7}	2.36×10^{-5}	59.83	208.35	3.19×10^{-11}
Shadowgraph Golden syrup	3.0	0.265	1.23×10^{-7}	7.85×10^{-6}	16.98	59.13	9.06×10^{-12}
Shadowgraph Golden syrup	7.0	0.265	1.23×10^{-7}	2.38×10^{-5}	51.27	178.52	2.73×10^{-11}
Shadowgraph Golden syrup	18.0	0.265	1.23×10^{-7}	4.63×10^{-5}	100.24	349.04	5.35×10^{-11}
SPIV Liquidose 436 syrup	5.0	0.265	1.04×10^{-7}	2.50×10^{-6}	6.38	22.23	3.41×10^{-12}
SPIV Liquidose 436 syrup	13.3	0.265	1.04×10^{-7}	2.56×10^{-5}	65.40	227.72	3.49×10^{-11}
SPIV Liquidose 436 syrup	21.0	0.265	1.04×10^{-7}	6.04×10^{-5}	153.40	534.17	8.18×10^{-11}
SPIV Liquidose 436 syrup	41.2	0.265	1.04×10^{-7}	1.57×10^{-4}	397.74	1384.98	2.10×10^{-10}
Numerical Liquidose 436 syrup	5.0	0.265	1.04×10^{-7}	1.20×10^{-5}	30.66	106.77	1.64×10^{-11}
Numerical Liquidose 436 syrup	13.3	0.265	1.04×10^{-7}	4.26×10^{-5}	108.50	377.80	5.79×10^{-11}
Numerical Liquidose 436 syrup	23.0	0.265	1.04×10^{-7}	4.36×10^{-5}	110.84	385.97	5.91×10^{-11}
Numerical Liquidose 436 syrup	25.0	0.265	1.04×10^{-7}	5.73×10^{-5}	145.44	506.43	7.76×10^{-11}
Numerical Golden syrup	3.0	0.265	1.23×10^{-7}	1.20×10^{-5}	12.75	44.41	3.41×10^{-12}
Numerical Golden syrup	7.0	0.265	1.23×10^{-7}	4.26×10^{-5}	164.07	571.31	3.49×10^{-11}
Numerical Golden syrup	18.0	0.265	1.23×10^{-7}	4.36×10^{-5}	168.99	588.45	8.18×10^{-11}

Table 8.4: Scaling of the experiments and numerical simulations to the length of Mars' mantle and Mars' mantle velocity using the Pe number.

8.3.2 Scaling the temperature

The temperature of the experimental and numerical plumes can be scaled to the mantle using the Rayleigh number (Equation 4.4). The values used for Earth were the viscosity of mantle material 1×10^{21}Pas, the thermal expansion of 4.00×10^{-5}°C^{-1}, the density of 4000kg/m^3, thermal diffusivity as stated above of 1×10^{-6}m^2/s and the depth of the mantle.

Experimental $\Delta\mathbf{T}$/°C	Ra	$\Delta\mathbf{T}_{scaled}$/°C
5	8.64×10^4	2.28
13.3	4.17×10^5	10.99
21	1.51×10^6	39.94
25	2.34×10^6	61.68
41.2	1.56×10^7	410.22

(a) Liquidose 436 plumes

Experimental $\Delta\mathbf{T}$/°C	Ra	$\Delta\mathbf{T}_{scaled}$/°C
3.0	9.25×10^4	2.44
7.0	4.35×10^5	11.48
18.0	3.65×10^6	96.25

(b) Golden syrup plumes

Table 8.5: Scaled temperature difference to Earth for the experimental and numerical investigations.

The scaling of the temperature in Table 8.5 shows that all bar the ΔT=41.2°C plume would have very low ΔTs in the mantle. The ΔT=41.2°C plume temperature difference may actually be too high, when the material expelled at hotspots is usually 200-300°C hotter than the normal mantle. The low ΔTs derived from the scaling imply that most of the plumes generated experimentally would be unable to be observed by seismic tomography.

8.4 Application to Earth

While plumes from point heat sources are conceptually useful, they are unlikely to represent fully the behaviour of mantle plumes, which arise from instabilities of hot TBLs (Ribe et al., 2007). However, a thermal perturbation is undoubtedly the dominant driving mechanism for the development of deep mantle plumes (Parmentier et al., 1975; Loper and Stacey, 1983) and thus a point source heater is valid for investigation of plumes. Many important features in Earth are not simulated (no plate tectonics, no radioactive heating, no temperature- or pressure- dependence of κ and α, depth-dependent viscosity variations associated with pressure rather than temperature), which are thought to play a key role in governing the pattern and character of the convection in Earth (Davaille, 1999a; Manga and Weeraratne, 1999). Yet the experiments conducted at high Rayleigh and Prandtl numbers garnered important clues to behaviour in different regions in the mantle. The simulated and experimental plumes, which have a temperature-dependent viscosity, are important because it has long been recognised that mantle rheology is temperature- and pressure- dependent, and studies have shown that

temperature-dependent viscosity is important for mantle plume generation (Yuen and Peltier, 1980). The thermal expansivity may also vary significantly across the mantle (Chopelas and Boehler 1989). However, in the numerical simulations this was held constant. Although the model used for generating plumes here may not incorporate all the important aspects of mantle plumes in the mantle such as the varying thermal expansivity, it can be helpful for the basic physics for understanding mantle plumes.

The plumes that fail to reach the surface that have been termed "stalled" collapse are unlikely to traverse more than approximately 50-60km in the mantle according to the Pe number scaling of length. Therefore, the plume will only interact with a small portion of the mantle just above the CMB, with many likely to struggle to leave the TBL. This implies that the "stalled" collapse plumes are unlikely to have any significant effect on the redistribution of chemistry in the mantle. However, they may become part of the thermochemical piles which have been observed deep in the mantle below Africa and the central Pacific (Lassak et al., 2007). These "stalled" collapse plumes have incredibly low ΔTs and thus may even not form in the mantle. If they are possible, they would not be able to be imaged/detected by seismic tomography, as confirmed by Montelli et al. (2004) who noted that is more difficult to image plumes in the lower mantle compared to the upper mantle.

The "lenticular" collapse plumes may be responsible for periods during which hotspots are less effusive, or have a temperature reduction. These plumes would ascend in the mantle away from the CMB but not all of the material would be transported to the surface. The material from the plume that was able to reach the surface would be the small portion that travelled around the sides of the "lens shape" as observed in the ΔT=13.3°C SPIV experiment. The majority of the material would potentially be flowing back towards the CMB as was observed in the laboratory during a shadowgraph experiment and from the SPIV experiment of Newsome (2011). This would mean that a rising plume would be potentially entraining material during its ascent until collapse was initiated. At this point, the heterogeneous material would be redistributed in the mantle. Material would continue to rise up the conduit even as the collapse was initiated leading to deep-rooted sources from where the plume originated in the lower mantle becoming depleted. The material in the collapsing "lens shape" may not descend fully to the base but instead redistribute the material in the location where the central vortex in the head/"lens shape" is observed. This region may be a location such as the D'', where other plumes may be generated from, or a region entirely unrelated to plume formation. In the case of the latter, it is likely that this material will take many millions of years before becoming entrained into a plume and ascending to the surface. This idea is corroborated by Farnetani and Richards

(1995) who showed that hotspot lavas do not sample and entrain a large volume of the mantle into the plumes during its ascent. The material which continues to rise up the sides of the "lens shape" (as seen in SPIV $\Delta T=13.3°C$ experiment) could make it to surface forming a less effusive volcanism and certainly generate a thinner oceanic crust.

The Icelandic plume has had temperature variations on geological time scales (from a few million years to tens of millions of years). The temperature has decreased by over $\sim50°C$ over the first 5Myr following continental breakup and then oscillated by $\sim25°C$ over a ~3Myr period (O'Connor et al., 2000). The spreading centre has generated temporal variations in oceanic crustal thickness, which could be controlled by passive decompression of mantle rising beneath the spreading centre (Parkin et al., 2007) from material that has not formed the "lens shape" in the plume collapse. A pulse of Iceland plume material interacting with the local spreading axis has also been proposed to explain cyclicity in the Pb composition on Iceland during the past ~15Myr (O'Connor et al., 2000). Plume productivity in the North Atlantic volcanic province is related to pulsing of large volumes of hot Iceland plume material, since at least the Late Cretaceous, on time scales of 5-10 Myr. Additionally, there is evidence in the Irminger and Icelandic basins that this plume has waxed and waned with different periodicities (Jones et al., 2002; Poore et al., 2009; White et al., 2013). It is possible that this waxing and waning could be periods of collapse and survival in the plume. In the thermochemical plume research of Kumagai et al. (2008) it was postulated that the Iceland plume could presently be in a failing stage.

The features of temperature variation are likely to occur in all mantle plumes (Parkin et al., 2007). Episodic volcanism on time scales of $\sim$1-2Myr for the Hawaiian plume trail has been identified and $\sim$1Myr timescales for the Foundation plume trail both indicate variable and faster plume ascent speeds due to greater viscosity differences in an upper mantle operating at a reasonable Rayleigh number of 10^6 (O'Connor et al., 2000). Other plumes that may be in a 'failing' or collapsing stage are Ontong-Java/Louisville and Parana-Etendeka/Tristan which have been estimated by Courtillot et al. (2003) to be failing because they are between 100-140Myr old. Alternatively, the numerical simulations of Farnetani and Samuel (2005) have suggested that in thermochemical plumes the head of a weak plume can contain a high proportion of dense mantle component (such as a subducted former basaltic crust), this head could stall at the 660km discontinuity and separate into low- and high-density components, which was also mentioned by Kumagai et al. (2008). This could be what is happening in the "lenticular" collapse. However, in relation to the fact that there could be as little as 0.13% density difference in the experiments in this thesis, in Earth this would seem difficult. Although the idea of Le Bars and Davaille (2002) that just 1% density difference could have a profound effect on the regimes could hold true here.

At this small density difference the plume would be undetectable by seismic tomography, because the method cannot ascertain the small-scale structure and heterogeneity within a mantle plume (Kumagai, 2002). Furthermore, the tomography is only a snapshot of the mantle as it presently is and therefore it cannot be known how the mantle plumes evolved in different geological time periods. From this study it is possible to conclude that Earth like conditions will produce plumes that are more complex than previously hypothesised within the plume theory of axisymmetric laminar plumes.

8.5   Limitations with the research

There were some limitations with the existing experimental arrangement. Despite the air-conditioning set at 19°C there appeared to be a variation in the ambient temperature of the syrup, dependent on the weather. The air-conditioning, however, produced the small (0.5°C) temperature gradient vertically and horizontally in the tank which led to asymmetric plumes. Therefore, because the temperature conditions of the tank were not isothermal and the ambient temperature of the syrup was not continuously the same, it cannot be assumed the conditions in the tank were identical for each experiment. However, in the mantle there is constant evolution and change and thus it is possible that the conditions for plume generation could vary. As the SPIV and shadowgraph experiments were not conducted simultaneously, just having the same ΔT is not enough to determine if the experiments are truly similar, as a different η of ambient fluid will lead to differing formation time of the plume, and thus may also change the phenomena observed.

Another caveat in the experimental arrangement is that the operating parameters for each experiment must be well-controlled and measurable in order for the results to be comparable. The heater temperature control should be further refined for future experiments as much as possible to decrease the ± 0.4°C variation. It is possible that a small amount of heat from the copper heater could have been lost to the Plexiglas (an insulating material) base of the tank despite the use of an o-ring surrounding it to inhibit large amounts of heat loss. It is certainly plausible that not all the heat was transferred to the syrup and, therefore, to quantify this amount with the use of a thermal imaging camera would be a worthwhile addition to the experiments.

A leading limitation with shadowgraph visualisation is the integration of the 3D flow from the tank on to one plane. This leads to difficulty in knowing where exactly the different fluid dynamic features are occurring in the tank. Due to this, the experiments were furthered using

the SPIV technique to gain quantitative results of the plumes. The shadowgraph measurements were somewhat subjective and the shadows can underestimate the size of the plumes (Limare et al., 2008). The edge of the temperature profile can also become obscured by shadowgraphs, where the gradients are small and the temperature slowly falls off (Moses et al., 1993). However, the error was estimated and added to all graphs.

In relation to Earth an important caveat is that the experiments were conducted with no-slip boundaries on all sides. Earth's mantle has a free-slip bottom boundary as the liquid iron core ($3x10^{-3}$Pas) (Poirier, 1988) has a viscosity near that of water ($8.9x10^{-4}$Pas), therefore the plumes may be smaller than in the mantle (Lithgow-Bertelloni et al., 2001).

8.6   Summary

All three techniques (shadowgraph, SPIV and numerical) used in this thesis give qualitatively similar results. The higher temperature plumes survived and thus this was easily observed in all three different methods. However, at low and intermediate ΔT the plumes showed differing behaviours. Stalling has been observed in simulated plumes up to $\Delta T=14°C$ and, after this, the plumes ascended to the surface. The two experimental methods work well together to form an understanding of how the fluid was behaving. The shadowgraphs enabled quick visual results, which were further investigated with SPIV. The experiments undertaken were important because they show two regimes that have not been previously observed in thermal plumes and that were not able to be observed numerically in the parameters investigated via simulations. The "stalled" collapse was caused by the low velocity down-welling thermal mass in the centre of the tank which inhibited plume growth. Additionally, the collapse in this regime was also caused by the comparable ratio of rise time and diffusion time and the fact that the plume did not traverse far out of the boundary layer. These plumes would be very small in the mantle and consequently unable to ascend out of the TBL layer according to the Pe number scaling and, therefore, would also be unable to be detected by seismic tomography. The "lenticular" collapse is likely to be caused by a range of factors. Firstly a low velocity down-welling thermal mass was present at the beginning of the experiment. Once the plume rose to a half to two-thirds of the tank it was likely that the 0.13% density difference present in the tank could have caused the "lens shape"/vortex to appear the centre of the plume head. This was likely to be a singularity which caused material to separate and material to descend towards the base whilst additional material rose up the sides of the "lens shape". Additionally, the ratio of the diffusion time to rise time was only different by a few 100th of a second in the Liquidose 436 plume. Therefore,

diffusion was likely to also play a role. In the mantle these "lenticular" collapse plumes could cause the redistribution of material and deplete the deep-rooted source. The material that was able to ascend to the surface could cause the temperature variations on geological time scales of locations such as Iceland and less effusive volcanism.

Chapter 9

Reflections and Further work

The experiments conducted in this study play a fundamental role in identifying new fluid phenomena and the three techniques gave qualitatively similar results.

This study has investigated thermal plume collapse from a point heat source. This involved;

- Configuring the novel motion-controlled system for the SPIV experiments.

- Laboratory experiments of thermal plumes using Liquidose 436 syrup visualised through white light shadowgraphs and SPIV.

- Numerical simulations using Fluidity to investigate if collapse could occur in a purely thermal system

Two unexpected collapse regimes were observed in the experimental results. The "stalled" collapse occurred in plumes between $\Delta T = 3\text{-}6°C$ and is likely to have been caused by a low velocity thermal down-welling mass in the tank inhibiting the plumes growth. These "stalled" collapse plumes also have a large TBL compared to the height of the plume and comparable rise time to diffusion times. These plumes are unlikely to cause any major impact on the mantle and will be impossible to be imaged through seismic tomography. There will be little redistribution of the material they are carrying as they are unable to traverse far out of the thermal boundary layer in the mantle.

The "lenticular" collapse is more difficult and complex to understand. The collapse regime has a fairly wide temperature variation between $\Delta T = 7\text{-}23°C$. The likely cause of this collapse is a mixture of the thermal mass which was observed in the SPIV experiments and some form of compositional layering in the tank, as discovered from the refractive index measurements. The

small change in buoyancy calculated could be enough to inhibit the plumes growth and cause the lens shape in the plume head.

Additional evidence, which corroborates the likelihood of some form of compositional layering is that when the tank was well mixed the plumes produced could not collapse. Additionally, if experiments were conducted more frequently than with a 10 day gap then collapse also was not possible for low and intermediate ΔTs. This implies that there is some thermochemical aspect to the experiments yet because just one syrup type is used the plumes are still deemed thermal plumes.

The numerical findings additionally corroborated the idea that thermal plumes could not collapse in a truly thermal system. However, the stalling phenomena validates the stalling observed in the experimental plume but was unexpected in the isothermal tank and was not eradicated by the change of tank dimensions, thermal expansion, change from heater evolution to constant heating or change of thermal diffusivity.

The laminar plumes in this study are complex. This highlights the on-going difficulties in understanding fully what is occurring in the centre of Earth and the need for continued refinement in experiments and numerics to gain further knowledge. The experiments conducted have shown that collapse phenomenon can occur in a thermal laboratory system where some small density difference is present, which previously would have been unexpected and deemed unlikely. However, the numerics provided validation of the stalling phenomenon observed in the low temperature difference plumes.

9.1 Further Work

The observations above highlighted several ideas for further investigation.

9.1.1 Different Size Experimental Tank

Testing the collapse experiments in a different size experimental tank could reveal whether the side walls affect the plume collapse. As the collapse phenomena was not found in the numerical investigations it would be interesting to see what effect a wider tank would have on the collapse. A new rectangular tank has been constructed with the distance between the heater and the side wall approximately 10 times the diameter of the (2cm) heater and the sides of the tank 0.265m (current size). This would increase the aspect ratio, which is desirable because the largest aspect

ratio possible would mean the effects of horizontal boundaries are small (Manga and Weeraratne, 1999).

9.1.2   SPIV of the Whole Tank

For this study only the middle plane (centre of the heater) of the tank was imaged, which led to further understanding of the plume behaviour directly above the heat source. Imaging the whole tank using multiple planes during an experiment would enable a 3D reconstruction of the plume behaviour during collapse and give increased knowledge of the evolution and velocity. The same methods can be applied to imagine further the behaviour of dying and surviving plumes.

9.1.3   Free-slip Experiments

Free-slip conditions at boundaries confine and influence fluid flow (van Keken et al., 2013). Transforming the top surface of the tank from a no-slip to a free-slip surface could be investigated to ascertain if the plume evolution and velocity alters from the no-slip experiments. Van Keken et al. (2013) observed the free-slip top boundary had a strong influence on the velocity structure. The bottom boundary could also be modified to a free-slip surface with a very thin layer of oil or another high density and low viscosity fluid relative to the Liquidose 436 syrup. This would enable a truer representation of the thermal boundary layer at the CMB with the liquid outer core. Using a free-slip base may also lead to smaller plumes in the tank and thus the mantle (Lithgow-Bertelloni et al., 2001).

9.1.4   Dying Plume

Dying plumes were observed during one experiment with Lyle's Golden syrup in the laboratory (Pears, 2010). The temperature of the heater was activated at 50°C for one hour before removal and re-introduced four hours later at 25°C. The evolution of the plume death and how the plume dissipated in the colder syrup was observed (Figure 9.1).

Dying plumes could be further investigated for a range of temperatures to investigate whether plumes at low temperature differences exhibit identical death evolution. Investigations could begin with analysis of the dying plume experiment from Pears (2010) and conducting similar experiments with the same time periods for activation, deactivation of the heater and the same temperature difference for both shadowgraph and SPIV visualisation techniques. The shadowgraphs will give quick visual results of the death of the plumes, which could then be furthered
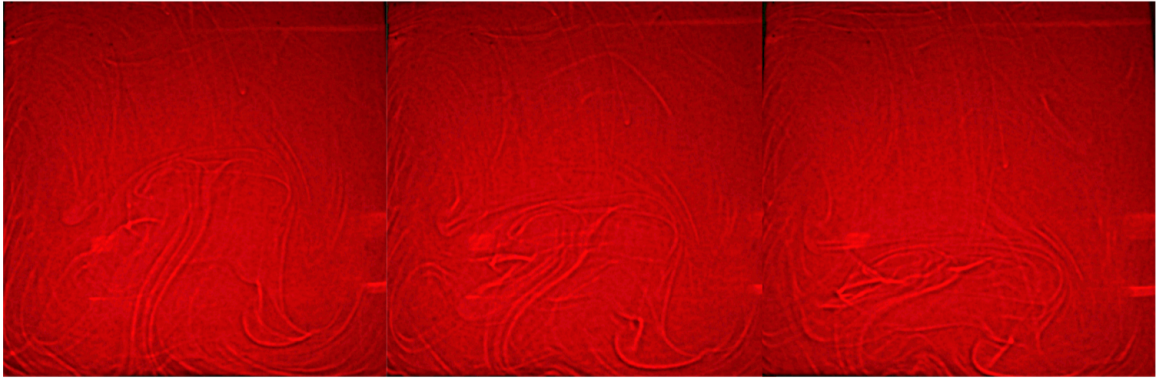
Figure 9.1: Dying plume experiment in Lyle's Golden syrup

with SPIV experiments to gain quantitative knowledge of the plume velocity during death. These plumes are not only interesting fluid dynamically but they could cause redistribution of material in the mantle and also explain what happens to a plume after the 100-140Myr (suggested by Courtillot et al., 2003) time period for the failing stage of a plume. Additionally the Azores hot-spot plume is believed to exemplify a present-day dying plume (Silveira et al., 2006) and thus the experiment may help understand the fluid processes occurring there.

9.1.5 Waves in Plumes

Figure 9.2: A wave seen developed in the conduit of the $\Delta T = 18°C$ Golden syrup experiment.

Waves in plumes were observed in some experiments conducted in this thesis but no further investigation into this was undertaken. The reason for wave formation in plumes was that conduits are likely to be time variable with disturbances travelling along them; these could be wave like or may take the shape of secondary plume heads. Waves are associated with increased conduit flux which may explain flux variations in mantle plumes (Suetsugu et al., 2004). Wave-

like stabilities have been observed by Bercovici (1992) in a horizontally flowing, disk-shaped head of a plume. Additionally, Scott et al. (1986) observed waves in buoyant fluid flowing up a pipe. The beginning of a possible wave has been observed in Pears (2010) as shown in Figure 9.2. Plume generation is a cyclical process in which the TBL grows by thermal diffusion, becomes unstable, forms a plume and then the cycle begins again. It could be investigated through shadowgraph and SPIV experiment to understand at what time the waves occur in relation to the temperature difference of the plume.

9.1.6   Further Numerical Modelling of Plumes

Fluidity is a very powerful finite element package. It should be possible to investigate mantle plumes in a number of ways.

One such area of interest is dying plumes. Generating a dying plume could be initiated by turning off the point source heater during the simulations, varying the time at which the point-source heater is extinguished, eradicating the basal and point heat sources simultaneously or in isolation to examine the plume behaviour once the heat sources are removed.

A second area of interest is simulating mantle plume collapse through purely basal heating instead of point-source heating, or using the two methods of heating simultaneously. A third investigation could centre on multiple plumes generated from basal heating. Additionally, the boundary conditions used in the simulations could be varied. This could be implemented in the form of free-slip sides, free-slip top surface with no-slip other boundaries or with free-slip top and bottom and no-slip sides.

Finally, thermochemical plumes could be investigated. Although at present Fluidity is not validated/benchmarked for thermochemical simulations. However, it would be useful when it is possible to input a very small density difference (e.g. 0.13%) between two fluids and observing how the plumes that develop are different from the simulated plumes in the thesis and whether they are similar to the experimental plumes.

9.1.7   Use of a Laser

The SPIV system could be modified to use a green laser and a mirror, like the experiments of Davaille and Limare (2007), instead of the white light optic fibre lightline (Figure 9.3). As viscous fluid motions are slow, it is possible to scan the experimental cell with a laser sheet using an oscillating mirror, driven by a galvanometer, to obtain the temperature field (Davaille and
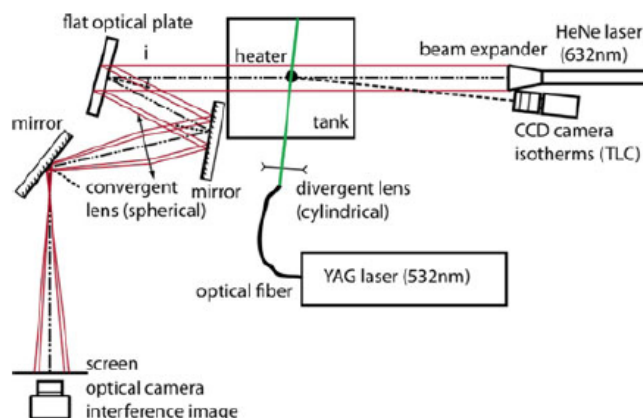
Figure 9.3: Top down view of the experimental set up of Davaille et al. (2011) experiments

Limare, 2007). The collapse researched in this thesis could be investigated with thermochromic crystals to understand the plume temperature change by generating isotherms. At a single wavelength of light the thermochromic crystals give detailed results through isobars which is not possible with white light due to the colour play[1] of 1.8°C. The laser can be easily obtained and different densities of thermochromic crystals can be seeded into the tank brightening at different temperatures producing isotherms. This laser could also be used to investigate how multiple plumes heat interacts with the collapsing plume through basal heating.

9.1.8   An Analogue Tectonic Plate

Further experiments could be conducted by adding a Plexiglas block to the top of the tank (to simulate a lithospheric plate on top of the mantle) to investigate how a plate affects the plume collapse observed in this study. The tank would not be filled to the top to accommodate the Plexiglas top and thus would be a free-slip boundary. The plate would be able to freely move during the experiment and the lid would be fixed on the top of the tank to avoid the drying effect on the syrup. The plate motion may end up advecting some of the plume material in the direction of plate motion (e.g. Ribe and Christensen, 1994). A lithospheric plate on top will potentially generate mantle convection inside the tank, allowing observation of how plumes collapse, survive and interact in a convecting mantle.

A different way of producing an analogue plate would be by inducing a form of convection at the top of the tank such as the experiments of Gonnermann et al. (2004) and determining how this interacts with the surviving and collapsing plumes. This rotating top would potentially lead to a subdivision of the convective flow (Gonnermann et al., 2004) and produce plumes of different regimes. This should enable knowledge on the time-scale that collapsing plumes can survive in

---

[1]Thermochromic liquid crystal materials change through a spectrum of colours known as colour lay, commonly from red, very quickly through yellow, moving through green and blue on temperature change

the convecting mantle and information of other new regimes possible in the mantle.

9.1.9   Heating the Whole Base of the Tank

Multiple plumes can be generated from basal heating of the tank. Shadowgraph and SPIV experiments would be conducted with basal heating or basal heating and point source heating simultaneously. The aim of the experiment would be to investigate if either types of heating would replicate the two types of collapse behaviour observed or if multiple plumes would coalesce and inhibit collapse from occurring.

Appendix A

A.1 Motion-Controlled System Apparatus configuration

The configuration of the motion-controlled system required several stages: the placement of the equipment, the set up of the lightline and the cameras and measurements for SPIVET-Control for automating the system and repeatability testing. Prior to any experiments being conducted, the precision of the configuration and placement of the apparatus is crucial.

The important aspect of placement was determining the exact location of the linear slides on the optical table. Once the position was ascertained, the slides were bolted to the table top (a steel plate with drilled holes fixed to air mounts) to ensure stability when the system was automated. This configuration enabled the cameras to capture the plane illuminated across the tank by the lightline.

After positioning the linear slides, a location for the stage on the optical table was determined. The stage, an anodised black mini-table, elevated the tank to enable a clear uninterrupted visualisation by the cameras. The position was determined by the cameras (with 15mm focal length) requiring an equal field of view and the necessity of the lightline to be able to illuminate the whole tank whilst it traversed the slide. The length of the slides had an impact on the location of the stage (Figure 5.4). As the system was constructed to compare datasets from
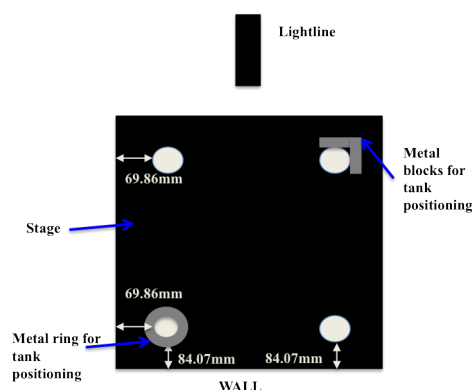
Figure A.1: Top down view showing where to place the tank on the stage, drawn in Google layout

Camera number	Angle rotated /°	Angle from 180° /°	Tuning dial /mm
Camera 0	173.5	6.5	12.21
Camera 1	186.0	-6.0	1.10

Table A.1: The exact position information for the camera configuration on the cross bar, drawn in Google SketchUp

different experimental runs, it was imperative to have the tank located in a repeatable fixed position. This permitted the datasets to have the same laboratory coordinate system. The permanent, accurate and consistent position of the tank was implemented by using calipers to fix two metal blocks to the stage (Figure A.1).

The crossmember (which can be adjusted to raise and lower the cameras) was fixed at 32cm, the optimal height for the cameras to visualise the entire tank. The CCD cameras were attached to the crossmember and separated by a distance of 19cm (Figure A.3). After this placement the cameras were rotated 90° from the horizontal, levelled, angled inwards with an each camera having an angle of 6.5° and -6.0 respectively and focused. Once fixed in place, the position of the cameras was further refined using the tuning dial (Table A.1). All these features in the configuration of the cameras enabled the largest field-of-view to be achieved for stereoscopy (Figure 3.5).

A.1.1   Lightline and Camera configuration

The second major aspect of the motion-controlled system configuration was the implementation of the lightline and the two 3-CCD cameras for visualisation of the experiments.
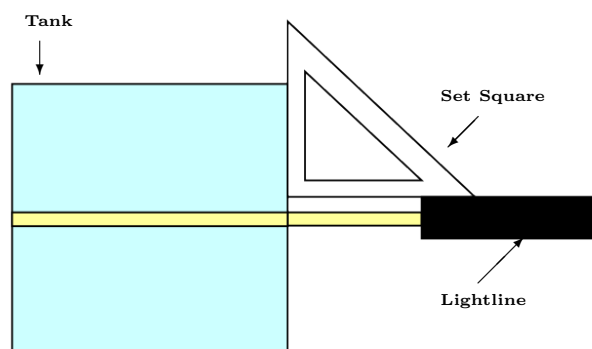
Figure A.2: The configuration of how to make the lightline parallel and perpendicular with the tank

The configuration of the lightline was undertaken by employing a set square to adjust the lightline to be parallel and perpendicular with the respective edges of the tank (Figure 5.5 and Figure A.2). The light sheet was shone on to squared paper placed on the closest tank face.
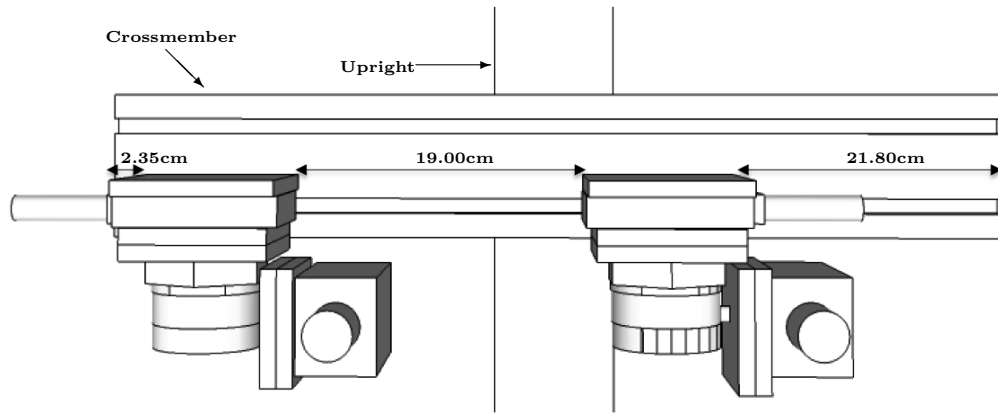
Figure A.3: The exact position of the two cameras on the crossmember of the linear slide, drawn in Google SketchUp

Metal strips (in front of the lens inside the casing) were adjusted and secured to produce a thin beam of constant thickness 2.12mm.

A.1.2 Configuring the carriage position for experiments

Item	Average distance when viewing the back of the tank /mm	Distance from stepper motor to carriage when in home position /mm	PHO /mm
Lightline	84.3050	61.6000	23.7050
Camera	406.0000	85.0305	321.9695

Table A.2: Measurements for finding the PHO

Prior to any experiments the position of the camera and lightline carriages for the beginning of an experiment were chosen, configured and set. This location enabled repeatability and reduced error in the extracted velocity field. The lightline was set grazing the back of the tank and the cameras were placed in position, focused on the lightline. The distance from the front of the stepper to the carriage, known as the post home offset (PHO), was measured. Additionally, measurements were taken with the carriage in the home position (when the carriage was depressing the plunger attached to the stepper motor, Table A.2). The PHO was calculated by Equation A.1 and the values inputted into SPIVET-Control for automating the slides for experiments. During an experiment, when the carriage touched the home switch, it would move the PHO distance away, ready to capture the next set of frames.

$$PHO = \text{back of tank average distance} - \text{home position distance} \qquad \text{(A.1)}$$

The SPIVET-Control interface (Figure A.4) allows for the input of all the information needed for executing an experiment, along with the starting PHO for the experiments and the step

intervals of the lightline and cameras if required. The black box in the Right hand corner is a view of what is happening in the tank. The image is black in Figure A.4 is due to the presence of the lens cap when the image was captured. During an experiment the information from the SPIVET-Control interface automates the carriages with the lightline and cameras to traverse the linear slides, through commands sent to the STAC6-Si stepper drives.
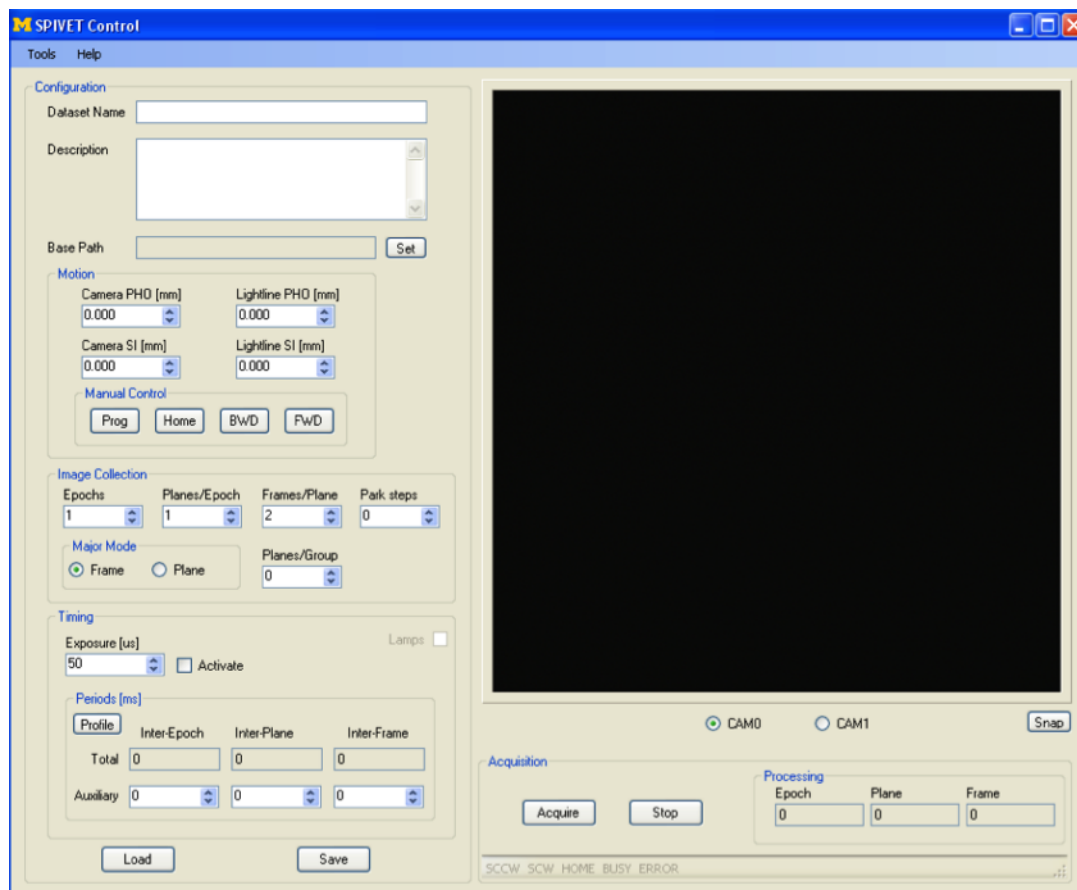
Figure A.4: The SPIVET-Control interface on the computer. Where all information for executing an experiment is input. This interface also shows the user the number of Epochs, planes and frames captured during the experiment, which is cumulative throughout the experiment.

A.2 Repeatability Tests

The repeatability of the movement of the slides returning to the same position was ascertained through the following tests:

- **Home** - This test was undertaken to ascertain if the carriages returned to the home position, depressing the plunger attached to the stepper motor with precision.

  This test was undertaken to discover the accuracy of the Home command when executed. The error was expected to have a virtually imperceptible variation ($\ll 10\mu$m) each time it was executed.

- **Accuracy** - This test was conducted to ascertain whether the forward command (the carriage moving forward a determined distance) automated from SPIVET-Control was accurate. It was expected that every time the forward step was executed there would be a 5mm displacement, as per the configured step interval. An error of less than 12μm was anticipated for each reading.

- **Backlash** - This test was undertaken to ascertain if the forward and backward steps of the carriages were both accurate.

  The backlash test involved the difference between the two forward steps (r_1 and r_2) of the carriage and a backward step (r_3). The backlash (b) was then calculated using $b = r_3 - r_2 + r_1$. It was anticipated that at each step the reading on the dial would be 5μm.

- **Long PHO** - This test was undertaken to check that after the carriage reached the home position it would rebound to the correct distance away from home.
  For this test the PHO was set to 200mm. The test was executed by commanding the carriage to seek the home switch. The error was expected to be zero and definitely less than $\ll 10$ μm, with virtually no variation.

- **Step repeatability** - This test was conducted to confirm the reliability of the step interval. The carriage was commanded to seek home, the forward command was executed ten times and the dial indicator fixed to the table with the plunger touching the carriage. This test was then repeated and the error discovered (expected to be zero).

A.3   CCD cameras

CCD cameras have an imaging system with three separate charge coupled devices (CCD). Each of the charged coupled devices takes separate measurements of the primary colours: red, green and blue light. The cameras have superior image quality with enhanced resolution and precision and lower noise than cameras with just one-CCD. The light entering the lens is split by a trichroic prism assembly. The appropriate wavelength ranges of light are directed into their respective CCDs.

A.4   Tsai method

Camera calibration is a major issue in computer vision because it is related to many vision problems such as stereovision, structure from motion and change detection (Heikkila and Silven,

1997). The camera calibration involves estimating a model for an un-calibrated camera. The aim then is to discover the external parameters (the position and orientation relatively to a world co-ordinate system) and the internal parameters of the camera (image centre, focal length and distortion coefficients). The method used most often for this is the one proposed by Tsai (1987). The implementation involves using the 2D pixels from the image to ascertain the corresponding 3D point co-ordinates.

The Tsai (1987) model was based on a pinhole perspective projection model and the following eleven parameters are used to estimate this model:

- f - Focal length of camera

- k - Radial lens distortion coefficient

- C_x, C_y - Coordinates of the centre of radial lens distortion

- S_x - Scale factor to account for any uncertainty due to imperfections in hardware timing for scanning and digitisation

- R_x, R_y, R_z - Rotation angles for the transformation between the world and camera coordinates.

- T_x, T_y, T_z - Translation components for the transformation between the world and camera coordinates.

The extrinsic parameters of the camera are considered within the transformation from world (X_w, Y_w, Z_w) to image (X_i, Y_i, Z_i) coordinates in Equation A.2:

$$\begin{bmatrix} X_i \\ Y_i \\ Z_i \end{bmatrix} = R \begin{bmatrix} X_w \\ Y_w \\ Z_w \end{bmatrix} + T \tag{A.2}$$

where R and T characterise the 3D transformation from the world to camera coordinate system and are defined as follows in Equation A.3:

$$R = \begin{bmatrix} r_1 & r_2 & r_3 \\ r_4 & r_5 & r_6 \\ r_7 & r_8 & r_9 \end{bmatrix} T = \begin{bmatrix} T_x \\ T_y \\ T_z \end{bmatrix} \tag{A.3}$$

with:

$r_1 = \cos(R_y)\cos(R_z)$
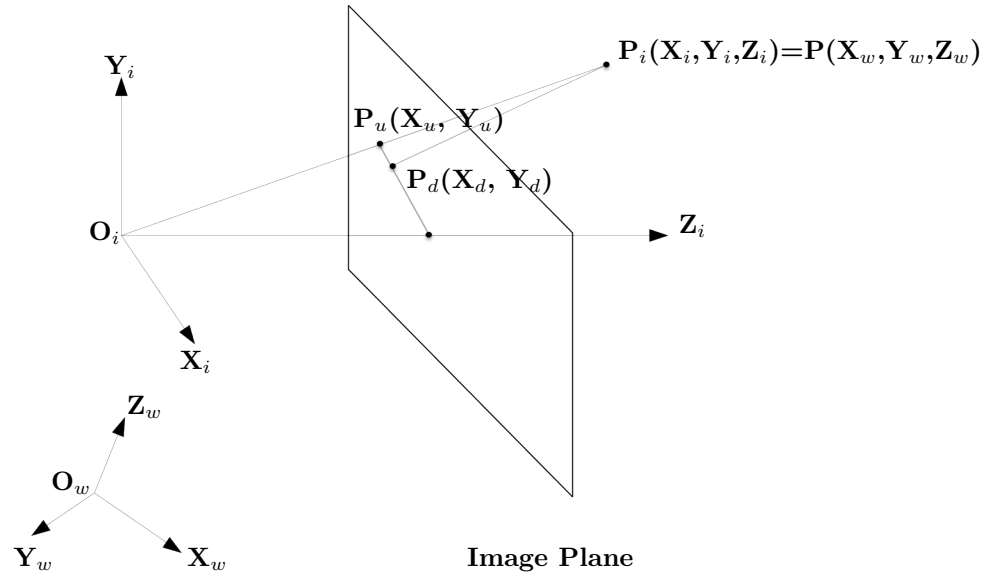
Figure A.5: Tsai Camera re-projection model with perspective projection and radial distortion

$r_2 = \cos(R_z)\sin(R_x)\sin(R_y)\text{-}\cos(R_x)\sin(R_z)$

$r_3 = \sin(R_x)\sin(R_z)\text{+}\cos(R_x)\cos(R_z)\sin(R_y)$

$r_4 = \cos(R_y)\cos(R_z)$

$r_5 = \sin(R_x)\sin(R_y)\sin(R_z)\text{+}\cos(R_x)\cos(R_z)$

$r_6 = \cos(R_x)\sin(R_y)\sin(R_z)\text{-}\cos(R_z)\sin(R_x)$

$r_7 = \text{-}\sin(R_y)$

$r_8 = \cos(R_y)\sin(R_x)$

$r_9 = \cos(R_x)\cos(R_y)$

where: (R_x, R_y, R_z) are the Euler angles of rotation around three axes

(T_x, T_y, T_z) are the 3D translation parameters from world to image coordinates.

The transformation from 3D position (in the image coordinate frame) to the image plane is then computed through the following steps (Figure A.5):

- Transformation from 3D world coordinates (X_i, Y_i) to undistorted image plane (X_u, Y_u) coordinates

$$X_u = f\frac{X_i}{Zi} \tag{A.4}$$

$$Y_u = f \frac{Y_i}{Z_i} \tag{A.5}$$

- Transformation from undistorted (X_u, Y_u) to distorted (X_d, Y_d) image coordinates.

$$X_u = X_d(1 + kr^2) \tag{A.6}$$

$$Y_u = Y_d(1 + kr^2) \tag{A.7}$$

where:

$$r = \sqrt{X_d^2 + Y_d^2} \tag{A.8}$$

and k is the lens distortion coefficient.

- Transformation from distorted coordinates in image plane (X_d, Y_d) to the final image coordinates $(X_f$ - Equation A.9), Y_f - Equation A.10):

$$X_f = \frac{S_x X_x}{d_x} + C_x \tag{A.9}$$

$$Y_f = \frac{Y_d}{d_y} + C_y \tag{A.10}$$

with (d_x, d_y): distance between adjacent sensor elements in X and Y direction. d_x and d_y are fixed parameters of the camera. They only depend on the CCD size and the image resolution, (X_f, Y_f) are the final pixel position in the image.

A.5   Alternative method for finding intersections

An alternative method for finding intersections for when the target was not completely parallel to the cameras was devised. Firstly, GIMP was used to find the (x,y) coordinates of the pixels at the four corners of the image (highlighted with red dots, Figure A.6).

The coordinates were:

- Point$_1$: 138, 37

- Point$_2$: 969, 45
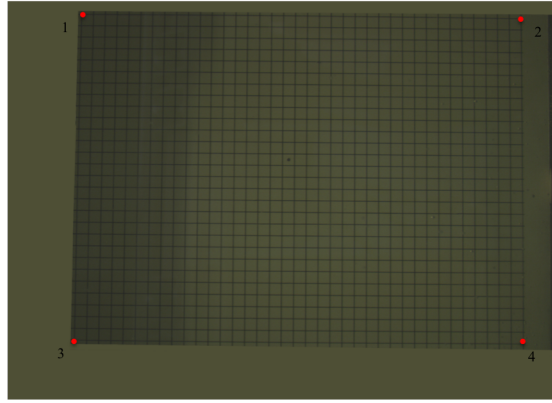
Figure A.6: The image used for finding the pixel location of all the intersections. The image contains 37 vertical lines and 28 horizontal lines.

- Point$_3$: 125, 669

- Point$_4$: 973, 677

The difference between the x-value of Point$_3$ and Point$_1$ and Point$_4$ and Point$_2$ was calculated to be 632. This value was then used to ascertain the change per line horizontally:

$$\frac{632}{28} = 22.57 \tag{A.11}$$

The value from Equation A.11 was then used to calculate the pixel number of all the lines (numbered 0-28) between pixels 37 and 669 between Point$_1$ and Point$_3$ using Equation A.12 and from Point$_2$ and Point$_4$. These values are displayed in Table A.3a.

Starting pixel number + (line number x change horizontally per line) =

pixel number of the line   (A.12)

The same method was used for locating the y values at all intersections in the image. The difference between Point$_1$ and Point$_2$ was calculated to be 8 and the pixel change per line vertically was calculated to be 0.22. The pixel change value was then used to calculate all the points along the horizontal lines where the vertical lines (numbered 0-37) intersect, using Equation A.12. The same method was used to find the horizontal lines for Point$_3$ and Point$_4$ and are displayed in Table A.4. The same steps were undertaken for locating the pixel x values (Table A.3b) of the lines and then, for the intersections (Table A.5). The last step was that the x and y values for the same intersections for photographs CAL0-C1 were concatenated, to make the pixel coordinates for each intersection. This was repeated for all 9 remaining photographs captured during the photogrammetric calibration.

Line number	x	y	x_1	y_1
0	138.00	37.00	969.00	45.00
1		59.57		67.57
2		82.14		90.14
3		104.71		112.71
4		127.29		135.29
5		149.86		157.86
6		172.43		180.43
7		195.00		203.00
8		217.57		225.57
9		240.14		248.14
10		262.71		270.71
11		285.29		293.29
12		307.86		315.86
13		330.43		338.43
14		353.00		361.00
15		375.57		383.57
16		398.14		406.14
17		420.71		428.71
18		443.29		451.29
19		465.86		473.86
20		488.43		496.43
21		511.00		519.00
22		533.57		541.57
23		556.14		564.14
24		578.71		586.71
25		601.29		609.29
26		623.86		631.86
27		646.43		654.43
28	125.00	669.00	973.00	677.00

(a) y pixel values for one photograph.

Line number	x	y	x_1	y_1
0	138.00	37.00	969	45
1	137.54		969.14	
2	137.07		969.29	
3	136.61		969.43	
4	136.14		969.57	
5	135.68		969.71	
6	135.21		969.86	
7	134.75		970.00	
8	134.29		970.14	
9	133.82		970.29	
10	133.36		970.43	
11	132.89		970.57	
12	132.43		970.71	
13	131.96		970.86	
14	131.50		971.00	
15	131.04		971.14	
16	130.57		971.29	
17	130.11		971.43	
18	129.64		971.57	
19	129.18		971.71	
20	128.71		971.86	
21	128.25		972.00	
22	127.79		972.14	
23	127.32		972.29	
24	126.86		972.43	
25	126.39		972.57	
26	125.93		972.71	
27	125.46		972.86	
28	125.00	669.00	973.00	677.00

(b) x pixel values for one photograph.

Table A.3: Tables for the calculated pixel values for $\text{Points}_{1,2,3and4}$.

0.00	1.00	2.00	3.00	4.00	5.00	6.00	7.00	8.00	9.00	10.00	11.00	12.00	13.00
37.00	37.22	37.43	37.65	37.86	38.08	38.30	38.51	38.73	38.95	39.16	39.38	39.59	39.81
59.57	59.79	60.00	60.22	60.44	60.65	60.87	61.08	61.30	61.52	61.73	61.95	62.17	62.38
82.14	82.36	82.58	82.79	83.01	83.22	83.44	83.66	83.87	84.09	84.31	84.52	84.74	84.95
104.71	104.93	105.15	105.36	105.58	105.80	106.01	106.23	106.44	106.66	106.88	107.09	107.31	107.53
127.29	127.50	127.72	127.93	128.15	128.37	128.58	128.80	129.02	129.23	129.45	129.66	129.88	130.10
149.86	150.07	150.29	150.51	150.72	150.94	151.15	151.37	151.59	151.80	152.02	152.24	152.45	152.67
172.43	172.64	172.86	173.08	173.29	173.51	173.73	173.94	174.16	174.37	174.59	174.81	175.02	175.24
195.00	195.22	195.43	195.65	195.86	196.08	196.30	196.51	196.73	196.95	197.16	197.38	197.59	197.81
217.57	217.79	218.00	218.22	218.44	218.65	218.87	219.08	219.30	219.52	219.73	219.95	220.17	220.38
240.14	240.36	240.58	240.79	241.01	241.22	241.44	241.66	241.87	242.09	242.31	242.52	242.74	242.95
262.71	262.93	263.15	263.36	263.58	263.80	264.01	264.23	264.44	264.66	264.88	265.09	265.31	265.53
285.29	285.50	285.72	285.93	286.15	286.37	286.58	286.80	287.02	287.23	287.45	287.66	287.88	288.10
307.86	308.07	308.29	308.51	308.72	308.94	309.15	309.37	309.59	309.80	310.02	310.24	310.45	310.67
330.43	330.64	330.86	331.08	331.29	331.51	331.73	331.94	332.16	332.37	332.59	332.81	333.02	333.24
353.00	353.22	353.43	353.65	353.86	354.08	354.30	354.51	354.73	354.95	355.16	355.38	355.59	355.81
375.57	375.79	376.00	376.22	376.44	376.65	376.87	377.08	377.30	377.52	377.73	377.95	378.17	378.38
398.14	398.36	398.58	398.79	399.01	399.22	399.44	399.66	399.87	400.09	400.31	400.52	400.74	400.95
420.71	420.93	421.15	421.36	421.58	421.80	422.01	422.23	422.44	422.66	422.88	423.09	423.31	423.53
443.29	443.50	443.72	443.93	444.15	444.37	444.58	444.80	445.02	445.23	445.45	445.66	445.88	446.10
465.86	466.07	466.29	466.51	466.72	466.94	467.15	467.37	467.59	467.80	468.02	468.24	468.45	468.67
488.43	488.64	488.86	489.08	489.29	489.51	489.73	489.94	490.16	490.37	490.59	490.81	491.02	491.24
511.00	511.22	511.43	511.65	511.86	512.08	512.30	512.51	512.73	512.95	513.16	513.38	513.59	513.81
533.57	533.79	534.00	534.22	534.44	534.65	534.87	535.08	535.30	535.52	535.73	535.95	536.17	536.38
556.14	556.36	556.58	556.79	557.01	557.22	557.44	557.66	557.87	558.09	558.31	558.52	558.74	558.95
578.71	578.93	579.15	579.36	579.58	579.80	580.01	580.23	580.44	580.66	580.88	581.09	581.31	581.53
601.29	601.50	601.72	601.93	602.15	602.37	602.58	602.80	603.02	603.23	603.45	603.66	603.88	604.10
623.86	624.07	624.29	624.51	624.72	624.94	625.15	625.37	625.59	625.80	626.02	626.24	626.45	626.67
646.43	646.64	646.86	647.08	647.29	647.51	647.73	647.94	648.16	648.37	648.59	648.81	649.02	649.24
669.00	669.22	669.43	669.65	669.86	670.08	670.30	670.51	670.73	670.95	671.16	671.38	671.59	671.81

Table A.4: Table of calculated y pixel values for Points$_{1,2,3 and 4}$ for one photograph.

0.00	1.00	2.00	3.00	4.00	5.00	6.00	7.00	8.00	9.00	10.00	11.00	12.00	13.00
138.00	160.46	182.92	205.38	227.84	250.30	272.76	295.22	317.68	340.14	362.59	385.05	407.51	429.97
137.54	160.01	182.49	204.96	227.44	249.92	272.39	294.87	317.34	339.82	362.29	384.77	407.25	429.72
137.07	159.56	182.06	204.55	227.04	249.53	272.03	294.52	317.01	339.50	361.99	384.49	406.98	429.47
136.61	159.12	181.62	204.13	226.64	249.15	271.66	294.17	316.68	339.19	361.69	384.20	406.71	429.22
136.14	158.67	181.19	203.72	226.24	248.77	271.29	293.82	316.34	338.87	361.39	383.92	406.44	428.97
135.68	158.22	180.76	203.30	225.84	248.39	270.93	293.47	316.01	338.55	361.09	383.64	406.18	428.72
135.21	157.77	180.33	202.89	225.45	248.00	270.56	293.12	315.68	338.24	360.79	383.35	405.91	428.47
134.75	157.32	179.90	202.47	225.05	247.62	270.20	292.77	315.34	337.92	360.49	383.07	405.64	428.22
134.29	156.88	179.47	202.06	224.65	247.24	269.83	292.42	315.01	337.60	360.19	382.78	405.37	427.97
133.82	156.43	179.04	201.64	224.25	246.86	269.46	292.07	314.68	337.29	359.89	382.50	405.11	427.71
133.36	155.98	178.60	201.23	223.85	246.47	269.10	291.72	314.35	336.97	359.59	382.22	404.84	427.46
132.89	155.53	178.17	200.81	223.45	246.09	268.73	291.37	314.01	336.65	359.29	381.93	404.57	427.21
132.43	155.08	177.74	200.40	223.05	245.71	268.37	291.02	313.68	336.34	358.99	381.65	404.31	426.96
131.96	154.64	177.31	199.98	222.66	245.33	268.00	290.67	313.35	336.02	358.69	381.36	404.04	426.71
131.50	154.19	176.88	199.57	222.26	244.95	267.64	290.32	313.01	335.70	358.39	381.08	403.77	426.46
131.04	153.74	176.45	199.15	221.86	244.56	267.27	289.97	312.68	335.39	358.09	380.80	403.50	426.21
130.57	153.29	176.02	198.74	221.46	244.18	266.90	289.63	312.35	335.07	357.79	380.51	403.24	425.96
130.11	152.85	175.58	198.32	221.06	243.80	266.54	289.28	312.01	334.75	357.49	380.23	402.97	425.71
129.64	152.40	175.15	197.91	220.66	243.42	266.17	288.93	311.68	334.44	357.19	379.95	402.70	425.46
129.18	151.95	174.72	197.49	220.26	243.03	265.81	288.58	311.35	334.12	356.89	379.66	402.43	425.20
128.71	151.50	174.29	197.08	219.86	242.65	265.44	288.23	311.02	333.80	356.59	379.38	402.17	424.95
128.25	151.05	173.86	196.66	219.47	242.27	265.07	287.88	310.68	333.49	356.29	379.09	401.90	424.70
127.79	150.61	173.43	196.25	219.07	241.89	264.71	287.53	310.35	333.17	355.99	378.81	401.63	424.45
127.32	150.16	173.00	195.83	218.67	241.51	264.34	287.18	310.02	332.85	355.69	378.53	401.36	424.20
126.86	149.71	172.56	195.42	218.27	241.12	263.98	286.83	309.68	332.54	355.39	378.24	401.10	423.95
126.39	149.26	172.13	195.00	217.87	240.74	263.61	286.48	309.35	332.22	355.09	377.96	400.83	423.70
125.93	148.81	171.70	194.59	217.47	240.36	263.25	286.13	309.02	331.90	354.79	377.68	400.56	423.45
125.46	148.37	171.27	194.17	217.07	239.98	262.88	285.78	308.68	331.59	354.49	377.39	400.29	423.20
125.00	147.92	170.84	193.76	216.68	239.59	262.51	285.43	308.35	331.27	354.19	377.11	400.03	422.95

Table A.5: Table of calculated x pixel values for $Points_{1,2,3 and 4}$ for one photograph.

Appendix B

B.1 Time series analysis

B.1.1 Golden syrup time series analysis

A time series analysis for measuring refractive index values was also implemented for the Golden syrup fluid. The Golden syrup was measured for less time than the Liquidose 436 syrup because it was first ascertained that the Liquidose 436 time series was showing adequate results. The time series was configured in a similar plastic bottle as the Liquidose 436 time series to ensure that the refractive index measurements from both syrups could be extrapolated to the tank and thus conclusions could be drawn.
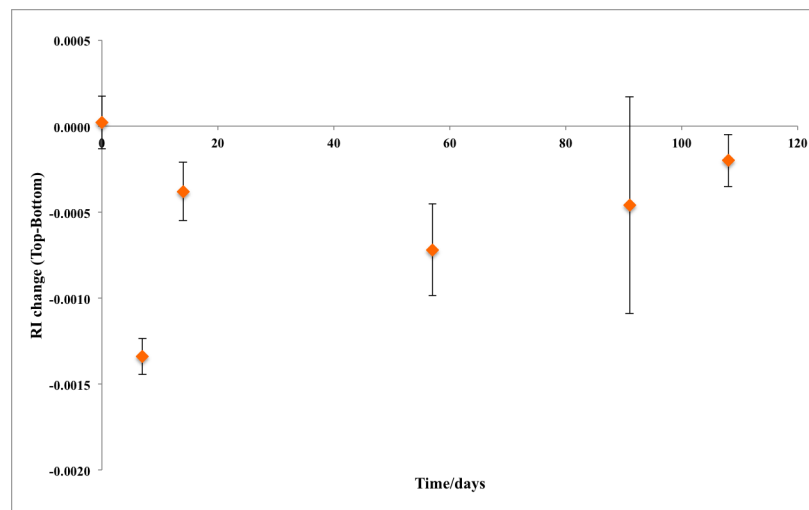
Figure B.1: Time series analysis of the refractive index of the Golden syrup. The error bars are two standard errors.

The results in Figure B.1 show that the results were all within two standard errors. This shows a similar trend as Figure 5.23 from 50 days. It cannot be said with certainty that the Golden syrup refractive index had an annual trend as it was not measured for long enough. However, the refractive index difference was tending towards zero and therefore was showing that the syrup was tending towards being well mixed.

B.1.2   Data from ADM

The data in Table B.1 was supplied by ADM with the syrup batches and was used to calculate the density difference in the tank.

%Dry solid	RI at 20°C	RI at °C	Specific Gravity at 60F
81.6	1.49715	1.49205	1.4237
81.7	1.49742	1.49232	1.4243
81.8	1.49769	1.49258	1.4259
81.9	1.49796	1.49285	1.4257
82.0	1.49823	1.49312	1.4264
82.1	1.4985	1.49339	1.4270
82.2	1.49877	1.49365	1.4277
82.3	1.49904	1.49392	1.4284
82.4	1.49931	1.49419	1.4291
82.5	1.49958	1.49446	1.4297

Table B.1: Physical Constants supplied by ADM for Liquidose 436 syrup batch

With a maximum variation in refractive index from Figure 5.23 of 0.005 the % Dry solid would be 0.2%. This 0.2% leads to a 0.0013 density difference which is 0.13%.

B.2   Shadowgraph Experiments undertaken

The Liquidose 436 syrup experiments (Table B.3) that were conducted were more numerous, with only two Golden syrup experiments (Table B.2). The tables have detailed observations of the experiments and whether collapse was observed.

Date	T_h/ °C	T_∞ /°C	ΔT/°C	Collapsed Yes/ No/ ?
7/9/11	27.6	19.6	8.0	It is difficult to observe the location of the plume. Additionally, something went wrong with the imaging. It appears that the plume was veering to the right.
19/9/11	77.0	19.7	57.3	It is hard to see what is happening once the plume has risen half the way up the tank. The resolution of the images is not good.

Table B.2: Golden syrup experiments conducted

Date	T_h/ °C	T_∞ /°C	ΔT/°C	Collapsed Yes/ No/ ?
25/1/11			2.0	The images are quite dark and not good enough quality for publishing. There is a lot of structure in the tank. There could be a lens shape although the location of the plume is not obvious in the tank.
26/1/11	23.3	19.3	4.0	The images are not very clear. It is hard to observe the location of the plume head. There appears to be a lot of structure in the tank but it is unclear where the plume is exactly.
7/2/11	27.0	19.0	8.0	Collapse is occurring. A dimple appears to form near the top of the plume and the plume does not reach the top of the tank.
10/2/11	70.0	19.0	51.0	Very nice clear images of the plume. The manifold of the plume is observable and distinct. There are possibly waves of plumes.
17/2/11	23.1	19.1	4.0	The experiment was not run for long enough. Insufficient data was recorded. The plume appeared to be growing as a thin bullet shape. There is no clear sign of the head.
22/2/11	22.0	18.0	4.0	The experiment was not run for long enough. Insufficient data was recorded. There may be collapse but the plume is faint.
25/2/11	26.0	18.0	8.0	There are only a few photographs. The plume appeared to veer off to the right side about $\frac{1}{3}$ of the way up the tank.
2/3/11	26.5	18.5	8.0	Collapse occurs. There appears to be a dimple forming in the photographs. The plumes seem axisymmetric. Some of the plume head reaches the top of the tank.
17/3/11	28.9	18.9	10.0	Collapse occurs. The beginning of the plume is very faint. It appears to be like the MSci $\Delta T=7$°C experiment and flattens out and looks like a lens at $\frac{2}{3}$ of the way up the tank.
24/3/11	80			Dying Plume is occurring in the experiment.
28/3/11	26.6	18.6	8.0	The experiment was not run for long enough. Insufficient data was recorded. Plume is rising and appears that it is about to collapse. It is very asymmetric in the tank. On the left hand side there appears to be a more obvious plug looking shape.
31/3/11	26.9	18.9	8.0	Collapse occurs. The images are good quality and the plume is asymmetric like the 28/3/11 plume. The plume seems to get a lens like the MSci $\Delta T=7$°C experiment.
20/6/11	33.0	19.2	13.8	Far too many bubbles on the glass, making the images poor quality. Additionally there is a mark on the side of the tank. The plume rose to the top of the tank.
29/6/11		19		There is a bulge in the middle of the plume, where material is observed to be rolling up on itself. There also appears to be material at the top of the tank in a thin strip.

Date	T_h/ °C	T_∞/ °C	ΔT/°C	Collapsed Yes/ No/ ?
30/6/11	80.0	19.0	61.0	There is a dimple at the top of the plume head. There is far too much structure in the tank to properly understand exactly what is happening in the plume head and tail. A wave is observed in the plumes and material from the head is spilling down from the top of the tank once the plume reached the top.
3/1/12	70.0	19.0	51.0	The images are slightly blurry. The plume rose to the top of the tank and a dimple was observed in the last few cm before reaching the surface. This then seemed like material was collapsing down from the dimple.
9/1/12	23.4	19.4	4.0	The images are really blurry. It is difficult to observe the plume location in the tank, which is possibly due to the low ΔT.
12/1/12	60.0	18.8	41.2	A dimple appears in plume in the last few cm before the plume reaches the surface. There appears to be a large scrolling in the plume. Possibly a wave in the plume.
13/1/12				This a downward looking plume. There is scrolling in the head. This is after 60°C plume had been turned off from 12/1/12 and it looks like a plume is descending instead of ascending
17/1/12	40.0	19.0	21.0	The plume appears to collapse like the MSci $\Delta T=7$°C experiment. It travelled about $\frac{2}{3}$ of the tank before collapsing.
24/1/12	30.0	16.8	13.3	The plume appeared to collapse and was asymmetric. It appears to collapse like the MSci $\Delta T=7$°C experiment. The plume reached near the surface but lots of material was flowing down to the base.
1/2/12	35.6	18.6	17.0	Yes, a wave in the plume is observed. The second plume is obvious and attains the lens shape like the MSci $\Delta T=7$°C experiment. There is also other scrolling up of a head of the other plume obvious in the tank.
9/2/12	42.4	17.4	25.0	No, Could be wave in plume. The head of the plume appears to reach the bottom of the tank and big scrolls of material are observed and continually rolling round.
28/2/12	23.4	18.4	5.0	Yes it is collapsing. It appears to be neutrally buoyant, the plume only travelled a $\frac{1}{3}$ of the tank, even after 36 hrs.
21/3/12	40.2	17.2	23.0	Yes I think it is collapsing, approximately $\frac{1}{2}$ of the way up the tank the lens appears like the MSci $\Delta T=7$°C experiment.
2/4/12	21.2	17.2	4.0	The plume appears to start growing but it is not the typical shape. Its gets deflected to the left hand side and disappears. The images do not show collapse.
10/8/12	27.3	19.3	8.0	No, it does not collapse.
24/9/12	32.6	19.6	13.0	The experiment appears to not collapse and syrup spills out of the tank at the top during the experiment.

Date	T_h/ °C	T_∞ /°C	ΔT/°C	Collapsed Yes/ No/ ?
8/10/12	34.1	19.1	15.0	The experiment appears to not collapse. Maybe the new stirring of the syrup and heating has changed the syrup so that the collapse before was thermochemical.
22/10/12	21.7	17.7	4.0	The light died during the experiment.
29/10/12	26.3	18.3	8.0	The plume is faint and rose to the top of the tank. No collapse is observed. The right hand side head limb is bigger than the left hand side. Another plume is possibly coming up.
7/11/12	25.6	18.6	7.0	No collapse. The plume does not appear centrally positioned in the tank. It is off to the left. The plume is deflected right before reaching the top of the tank.
22/11/12	24.1	18.1	6.0	The plume is really faint. It is hard to see the location of the plume head or tail. The left hand side appears obvious in the middle of the tank and it deflects towards the right hand side after a period of time. No collapse is observed.
26/11/12	25.0	20.0	5.0	The plume is really faint. Shows similar characteristics to the experiments from the 22/11/12.

Table B.3: Liquidose 436 syrup shadowgraph experiments.

B.3 SPIV experiments

The SPIV experiments that were undertaken are presented in Table B.4.

Date	T_h/ °C	T_∞ /°C	ΔT/°C	Collapsed Yes/ No/ ?
8/1/14	24.2	19.2	5.0	The plume stalls like one of the ΔT=5°C. The plume is asymmetric. There is a low-velocity thermal mass in the centre of the tank.
14/1/14	31.3	18.0	13.3	The plume shows a central vortex in the plume head similar to Newsome (2011). The plume shows signs of collapse but then also material rises at the sides of the plume.
20/1/14	31.0	18.0	13.0	The plume appears to rise to the top of the tank but then seems like it becomes swept up in the flow and tilted and descends to towards the base of the tank.
30/1/14	23.8	18.8	5.0	Very complicated flow is occurring in this experiment. The plume appears to rise to approximately $\frac{1}{2}$ the way up the tank before strange flow patterns are observed at the bottom of the tank. It appears like the plume material is becoming pushed towards the base by the end of the experiment.
6/2/14	23.4	18.4	5.0	There appears to be a low velocity thermal mass at the beginning of the experiment. The plume grows and pushes the mass to the right and grows $\frac{2}{3}$ of the way up the tank. The low velocity thermal mass then starts to move back into the centre of the tank and pushes the plume back to the base.
13/2/14	31.6	18.3	13.3	The plume rose to the top of the tank.
20/2/14	39.4	18.4	21.0	The plume rose to the top of the tank and did not collapse as expected.
27/2/14	59.4	18.2	41.2	The plume rose to the top of the tank.
20/3/14	31.2	17.9	13.3	The plume rose to the top of the tank.

Table B.4: Liquidose 436 syrup SPIV experiments.

B.4 Viscosity data

Temperature/ °C	Viscosity/ Pas			
	this study	(Lithgow-Bertelloni et al., 2001)	(Newsome, 2011)	ADM
20	70.67	87.18	61.23	256.98
21	64.49	75.47	53.75	223.10
22	58.86	65.44	47.24	193.71
23	53.72	56.84	41.57	168.21
24	49.04	49.46	36.62	146.09
25	44.77	43.11	32.31	126.90
26	40.88	37.64	28.54	110.25
27	37.32	32.92	25.24	95.81
28	34.08	28.85	22.35	83.29
29	31.13	25.32	19.81	72.42
30	28.44	22.26	17.59	63.00
31	25.98	19.61	15.63	54.82
32	23.74	17.30	13.91	47.72
33	21.70	15.29	12.40	41.57
34	19.84	13.54	11.06	36.23
35	18.14	12.01	9.88	31.60
36	16.59	10.67	8.83	27.58
37	15.18	9.50	7.91	24.10
38	13.89	8.47	7.09	21.07
39	12.72	7.56	6.37	18.45
40	11.65	6.77	5.72	16.18
41	10.67	6.06	5.15	14.20
42	9.78	5.44	4.64	12.49
43	8.97	4.90	4.19	11.01
44	8.23	4.41	3.78	9.72
45	7.55	3.98	3.42	8.60
46	6.93	3.60	3.10	7.63
47	6.37	3.26	2.81	6.79
48	5.86	2.96	2.55	6.06
49	5.39	2.69	2.32	5.43
50	4.97	2.45	2.11	4.88
51	4.58	2.23	1.92	4.40
52	4.23	2.04	1.76	3.99
53	3.90	1.87	1.60	3.63
54	3.61	1.71	1.47	3.32
55	3.34	1.57	1.34	3.05
56	3.09	1.45	1.23	2.82
57	2.87	1.33	1.13	2.61
58	2.67	1.23	1.04	2.44
59	2.48	1.14	0.96	2.28
60	2.31	1.05	0.88	2.15
61	2.16	0.98	0.81	2.04
62	2.02	0.91	0.75	1.94
63	1.89	0.85	0.70	1.85
64	1.77	0.79	0.64	1.78
65	1.66	0.74	0.60	1.71
66	1.57	0.69	0.56	1.65
67	1.48	0.65	0.52	1.60
68	1.40	0.61	0.48	1.56
69	1.32	0.57	0.45	1.53
70	1.26	0.54	0.42	1.49

Table B.5: Comparison of different viscosity measurements of Liquidose 436 syrup

B.5   Viscosity contrast

The viscosity contrast of the two syrups was calculated based on the measured viscosities (Table B.6 and Table B.7). The viscosity for the Golden syrup was calculated for each experiment using $\eta = 343.76 * e^{(-0.092*T)}$ and the Liquidose 436 syrup as stated in Section 5.3.1.

T_h/ °C	T_∞ /°C	ΔT/°C	$\Delta T/T_\infty$	η /Pas	η_∞ /Pas	η^* / Pas	log η^*
25.0	21.0	4.0	0.2	34.46	49.80	1.44	0.160
30.0	23.0	7.0	0.3	21.76	41.43	1.90	0.280
40	22.0	18.0	0.8	8.67	45.42	5.24	0.719

Table B.6: The viscosity of Lyle's Golden syrup from Pears (2010).

T_h/ °C	T_∞ /°C	ΔT/°C	$\Delta T/T_\infty$	η /Pas	η_∞ /Pas	η^* / Pas	log η^*
80.0	19.0	61.0	3.2	0.84	77.43	92.73	1.967
70.0	19.0	51.0	2.7	1.26	77.43	61.70	1.790
60.0	18.8	41.2	2.2	2.31	78.86	34.12	1.533
42.4	17.4	25.0	1.4	9.44	89.66	9.49	0.977
27.0	19.0	8.0	0.4	37.32	77.43	2.07	0.317
26.5	18.5	8.0	0.4	39.06	81.06	2.08	0.317
28.9	18.9	10.1	0.5	31.41	78.50	2.50	0.398
26.9	18.9	8.0	0.4	37.66	78.15	2.07	0.317
40.0	19.0	21.0	1.1	11.65	77.22	6.63	0.822
30.0	16.8	13.2	0.8	28.44	94.72	3.33	0.523
35.6	18.6	17.0	0.9	17.19	80.62	4.69	0.671
23.4	18.4	5.0	0.3	51.80	81.81	1.58	0.198
40.2	17.2	23	1.3	11.44	91.31	7.98	0.902
34.1	19.1	15.0	0.8	19.66	76.73	3.90	0.591
32.6	19.6	13.0	0.66	22.49	73.10	3.25	0.512
27.3	19.3	8.0	0.41	36.32	75.34	2.07	0.317
21.7	17.7	4.0	0.23	60.49	87.22	1.44	0.159
26.3	18.3	8.0	0.44	39.77	82.56	2.08	0.317
25.6	18.6	7.0	0.38	42.39	80.32	1.89	0.278
24.1	18.1	6.0	0.33	48.59	84.09	1.73	0.238
25.0	20.0	5.0	0.25	44.77	70.66	1.58	0.198
22.2	18.2	4.0	0.22	57.79	83.32	1.44	0.159
28.5	18.4	10.1	0.55	32.57	81.81	2.51	0.400
23.3	19.3	4.0	0.21	52.27	75.34	1.44	0.159
23.1	19.1	4.0	0.21	53.23	76.73	1.44	0.159
22.0	18.0	4.0	0.22	58.86	84.86	1.44	0.159
26.0	18.0	8.0	0.44	40.87	84.86	2.08	0.317
26.6	18.6	8.0	0.43	38.70	80.32	2.08	0.317
33.0	19.2	13.8	0.72	21.70	76.03	3.50	0.545
23.4	19.4	4.0	0.21	51.80	74.65	1.44	0.159
21.2	17.2	4.0	0.23	63.32	91.31	1.44	0.159

Table B.7: The viscosity data of Liquidose 436 syrup.

Appendix C

C.1 Non-dimensional numbers

This is a glossary of non-dimensional numbers used in the thesis.

- **Rayleigh Number**

  The Rayleigh number (Ra) is the ratio of two time-scales that are necessary for a buoyant mass to create a displacement and that of the resisting effects of thermal diffusion (Davaille and Vatteville, 2005) and can be defined following White (1988), Davaille and Jaupart (1993) and Lithgow-Bertelloni et al. (2001) as Equation C.1:

  $$Ra = \frac{\rho \alpha g \Delta T l_c^3}{\eta \kappa} \tag{C.1}$$

  here ΔT is the temperature difference applied across the depth of the convecting domain, g the gravitational acceleration and α the thermal expansivity, l_c is the characteristic length scale (height of the tank), η is the dynamic viscosity, ρ is the density and κ is the thermal diffusivity.

- **Prandtl Number**

  The Prandtl number (Pr) is defined as the ratio of momentum diffusivity (kinematic viscosity) to thermal diffusivity (Equation C.2, Tritton (1988)):

  $$Pr = \frac{\eta}{\rho \kappa} \tag{C.2}$$

- **Nusselt Number**

  In heat transfer at a boundary within a fluid, the Nusselt number (Equation C.3, Turcotte and Schubert (2002)) is the ratio of convective to conductive heat transfer across the boundary and is defined as:

$$Nu = \frac{hl_c}{k} \tag{C.3}$$

where h is the convective heat transfer coefficient of the fluid and k is the thermal conductivity of the fluid. A Nusselt number close to 1, namely convection and conduction of similar magnitude is characteristic of laminar flow. A large Nu number corresponds to more active convection, with turbulent flow typically in the 100-1000 range.

- **Reynolds Number**

  The Reynolds number (Equation C.4, Tritton (1988)) is used to help predict similar flow patterns in different fluid flow situations and is defined as:

$$Re = \frac{vl_c\rho}{\eta} \tag{C.4}$$

  where v is plate velocity. The Reynolds number the ratio of inertial forces to viscous forces and quantifies the relative importance of the two types of forces for given flow conditions. Laminar flow occurs at low Reynolds numbers, where viscous forces are dominant and is characterised by smooth, constant fluid motion.

- **Grashof Number**

  The Grashof number (Gr (Tritton, 1988), Equation C.5) approximates the ratio of buoyancy to viscous stress force acting on the fluid and is defined as:

$$Gr = \frac{g\alpha(T_h - T_\infty)l_c^3}{\nu^2} \tag{C.5}$$

The T_h and T_∞ relate to the heater surface temperature and the bulk temperature respectively.

References

Abramoff, M. D., Magelhaes, P. J., and Ram, S. J. (2004). Image Processing with ImageJ. *Biophotonics International*, 11(7):36–42.

Adrian, R. J. (1991). Particle-Imaging Techniques for Experimental Fluid Mechanics. *Annual Review of Fluid Mechanics*, 23(1):261–304.

Allègre, C. J. (1987). Isotope geodynamics. *Earth and Planetary Science Letters*, 86(2-4):175–203.

Allègre, C. J., Moreira, M., and Staudacher, T. (1995). ^{4}He/^{3}He dispersion and mantle convection. *Geophysical Research Letters*, 22:2325–2328.

AMCG (2014). Fluidity manual v4.1.10. *Imperial College London*, (Earth Sciences and Engineering Department).

Anderson, D. L. and Natland, J. H. (2005). *A brief history of the plume hypothesis and its competitors: Concept and controversy*, volume Special Paper 388, pages 119–145. The Geological society of America, Colorado.

Antonelis, K., Johnson, D. J., Meghan Miller, M., and Palmer, R. (1999). GPS determination of current Pacific–North American plate motion. *Geology*, 27(4):299–302.

Ballmer, M. D., van Hunen, J., Ito, G., Bianco, T. A., and Tackley, P. J. (2009). Intraplate volcanism with complex age-distance patterns: A case for small-scale sublithospheric convection. *Geochemistry, Geophysics, Geosystems*, 10(6):Q06015.

Barfod, D. N., Ballentine, C. J., Halliday, A. N., and Fitton, J. G. (1999). Noble gases in the Cameroon line and the He, Ne, and Ar isotopic compositions of high μ(HIMU) mantle. *Journal of Geophysical Research*, 104(B12):29509–29527.

Bargar, K. E. and Jackson, E. D. (1974). Calculated volumes of individual shield volcanoes along the Hawaiian-Emperor Chain. *J. Res. U.S Geol. Surv*, 2:545–550.

Barnea, D. I. and Silverman, H. F. (1972). A Class of Algorithms for Fast Digital Image Registration. *Computers, IEEE Transactions on*, C-21(2):179–186.

Batchelor, G. K. (1954). Heat convection and buoyancy effects in fluids. *Quarterly Journal of the Royal Meteorological Society*, 80(345):339–358.

Baumgardner, J. (1985). Three-dimensional treatment of convective flow in the Earth's mantle. *Journal of Statistical Physics*, 39(5-6):501–511.

Bercovici, D. (1992). Wave dynamics in mantle plume heads and hotspot swells. *Geophysical Research Letters*, 19(17):1791–1794.

Bercovici, D. (2007). *Mantle Dynamics Past, Present, and Future: An Introduction and Overview*, chapter 7.01, pages 1–30. Elsevier, Amsterdam.

Bijwaard, H. and Spakman, W. (1999). Tomographic evidence for a narrow whole mantle plume below Iceland. *Earth and Planetary Science Letters*, 166(3–4):121–126.

Bina, C. R. (1998). Lower mantle mineralogy and the geophysical perspective. *Reviews in Mineralogy and Geochemistry*, 37(1):205–239.

Blankenbach, B., Busse, F., Christensen, U., Cserepes, L., Gunkel, D., Hansen, U., Harder, H., Jarvis, G., Koch, M., Marquart, G., Moore, D., Olson, P., Schmeling, H., and Schnaubelt, T. (1989). A benchmark comparison for mantle convection codes. *Geophysical Journal International*, 98(1):23–38.

Bourdon, B., Ribe, N. M., Stracke, A., Saal, A. E., and Turner, S. P. (2006). Insights into the dynamics of mantle plumes from Uranium-series geochemistry. *Nature*, 444(7120):713–717. 10.1038/nature05341.

Brossard, C., Monnier, J.-C., Barricau, P., Vandernoot, F.-X., Le Sant, Y., Champagnat, F., and Le Besnerais, G. (2009). Principles and Applications of Particle Image Velocimetry. *Journal Aerospace Lab*, December 2009(1):1–11.

Brown, L. G. (1992). A survey of image registration techniques. *ACM Comput. Surv.*, 24(4):325–376.

Bunge, H.-P., Richards, M. A., and Baumgardner, J. R. (1997). A sensitivity study of three-dimensional spherical mantle convection at 10^8 Rayleigh number: Effects of depth-dependent viscosity, heating mode, and an endothermic phase change. *Journal of Geophysical Research: Solid Earth*, 102(B6):11991–12007.

Burke, K. C. and Wilson, J. T. (1976). Hot Spots on the Earth's Surface. *Scientific American*, 235(2):46–59.

Burton, R. A., Bailey, D. Z., Barry, F. W., A, d. L., and Nuemann, E. P. (1953). *Optical measuring techniques*, chapter Chpt 9, pages 167–184. MIT Gas Turbine Lab, Cambidge.

Busse, F. H., Christensen, U., Clever, R., Cserepes, L., Gable, C., Giannandrea, E., Guillou, L., Houseman, G., Nataf, H. C., Ogawa, M., Parmentier, M., Sotin, C., and Travis, B. (1994). 3D convection at infinite Prandtl number in Cartesian geometry - a benchmark comparison. *Geophysical and Astrophysical Fluid Dynamics*, 75(1):39–59.

Campbell, I. H. (2005). Large Igneous Provinces and the Mantle Plume Hypothesis. *ELEMENTS*, 1(5):265–269.

Campbell, I. H. and Griffiths, R. W. (1990). Implications of mantle plume structure for the evolution of flood basalts. *Earth and Planetary Science Letters*, 99(1–2):79–93.

Chabaux, F. and Allègre, C. J. (1994). ^{238}U-^{230}Th-^{226}Ra disequilibria in volcanics: A new insight into melting conditions. *Earth and Planetary Science Letters*, 126(1–3):61–74.

Chopelas, A. (2000). Thermal expansivity of mantle relevant magnesium silicates derived from vibrational spectroscopy at high pressure. *American Mineralogist*, 85(2):270–278.

Chopelas, A. and Boehler, R. (1992). Thermal expansivity in the lower mantle. *Geophysical Research Letters*, 19(19):1983–1986.

Christensen, U. (1984). Convection with pressure- and temperature-dependent non-Newtonian rheology. *Geophysical Journal of the Royal Astronomical Society*, 77(2):343–384.

Conrad, C. P., Bianco, T. A., Smith, E. I., and Wessel, P. (2011). Patterns of intraplate volcanism controlled by asthenospheric shear. *Nature Geosci*, 4(5):317–321. 10.1038/ngeo1111.

Coulliette, D. L. and Loper, D. E. (1995). Experimental, numerical and analytical models of mantle starting plumes. *Physics of the Earth and Planetary Interiors*, 92(3-4):143–167.

Courtillot, V., Davaille, A., Besse, J., and Stock, J. (2003). Three distinct types of hotspots in the Earth's mantle. *Earth and Planetary Science Letters*, 205(3-4):295–308.

Crough, S. T. (1978). Thermal origin of mid-plate hot-spot swells. *Geophysical Journal of the Royal Astronomical Society*, 55(2):451–469.

Dabiri, D. (2009). Digital Particle Image Thermometry/Velocimetry: a review. *Experiments in Fluids*, 46(2):191–241.

Davaille, A. (1999a). Simultaneous generation of hotspots and superswells by convection in a heterogeneous planetary mantle. *Nature*, 402(6763):756–760.

Davaille, A. (1999b). Two-layer thermal convection in miscible viscous fluids. *Journal of Fluid Mechanics*, 379:223–253.

Davaille, A. and Jaupart, C. (1993). Transient high-Rayleigh-number thermal-convection with large viscosity variations. *Journal of Fluid Mechanics*, 253:141–166.

Davaille, A., Le Bars, M., and Carbonne, C. (2003). Thermal convection in a heterogeneous mantle. *Comptes Rendus Geoscience*, 335(1):141–156.

Davaille, A. and Limare, A. (2007). *Laboratory Studies of Mantle Convection*, chapter 7.03, pages 89–165. Elsevier, Amsterdam.

Davaille, A., Limare, A., Touitou, F., Kumagai, I., and Vatteville, J. (2011). Anatomy of a laminar starting thermal plume at high Prandtl number. *Experiments in Fluids*, 50(2):285–300.

Davaille, A. and Vatteville, J. (2005). On the transient nature of mantle plumes. *Geophysical Research Letters*, 32(14).

Davies, D. R., Davies, J. H., Hassan, O., Morgan, K., and Nithiarasu, P. (2007). Investigations into the applicability of adaptive finite element methods to two-dimensional infinite Prandtl number thermal and thermochemical convection. *Geochemistry, Geophysics, Geosystems*, 8(5):Q05010.

Davies, D. R., Wilson, C. R., and Kramer, S. C. (2011). Fluidity: A fully unstructured anisotropic adaptive mesh computational modeling framework for geodynamics. *Geochemistry, Geophysics, Geosystems*, 12(6):20.

Davies, G. F. (1988). Ocean bathymetry and mantle convection: 1. Large-scale flow and hotspots. *Journal of Geophysical Research: Solid Earth*, 93(B9):10467–10480.

Davies, G. F. and Richards, M. A. (1992). Mantle Convection. *The Journal of Geology*, 100(2):151–206.

Davies, J. H. (2005). Steady plumes produced by downwellings in earth-like vigor spherial whole mantle convection models. *Geochemistry Geophysics Geosystems*, 6(12):1–25.

Donea, J. and Huerta, A. (2003). *Finite Element Methods for Flow Problems*. John Wiley and Sons Ltd., Chichester.

Dvorák, V. (1880). Über eine neue einfache art der schlierenbeobachtung. *Ann. Phys. Chem.*, 9:502–512.

Dziewonski, A. M. and Anderson, D. L. (1981). Preliminary reference Earth model. *Physics of the Earth and Planetary Interiors*, 25(4):297–356.

Elkins-Tanton, L. T. (2007). Continental magmatism, volatile recycling, and a heterogeneous mantle caused by lithospheric gravitational instabilities. *Journal of Geophysical Research: Solid Earth*, 112(B3):B03405.

Engel, A. E. J., Engel, C. G., and Havens, R. G. (1965). Chemical Characteristics of Oceanic Basalts and the Upper Mantle. *Geological Society of America Bulletin*, 76(7):719–734.

Farnetani, C. G. (1997). Excess temperature of mantle plumes: The role of chemical stratification across D''. *Geophysical Research Letters*, 24(13):1583–1586.

Farnetani, C. G. and Hofmann, A. W. (2011). *Mantle Plumes*, pages 857–869. Encyclopedia of Earth Sciences Series. Springer Netherlands.

Farnetani, C. G. and Richards, M. A. (1995). Thermal entrainment and melting in mantle plumes. *Earth and Planetary Science Letters*, 136(3-4):251–267.

Farnetani, C. G. and Samuel, H. (2005). Beyond the thermal plume paradigm. *Geophysical Research Letters*, 32(7):L07311.

Farrell, P. E., Piggott, M. D., Gorman, G. J., Ham, D. A., Wilson, C. R., and Bond, T. M. (2011). Automated continuous verification for numerical simulation. *Geosci. Model Dev.*, 4(2):435–449. GMD.

Fincham, A. M. and Spedding, G. R. (1997). Low cost, high resolution DPIV for measurement of turbulent fluid flow. *Experiments in Fluids*, 23(6):449–462.

Forsyth, D. and Uyeda, S. (1975). On the Relative Importance of the Driving Forces of Plate Motion. *Geophysical Journal of the Royal Astronomical Society*, 43(1):163–200.

Forsyth, D. W., Harmon, N., Scheirer, D. S., and Duncan, R. A. (2006). Distribution of recent volcanism and the morphology of seamounts and ridges in the GLIMPSE study area: Implications for the lithospheric cracking hypothesis for the origin of intraplate, non–hot spot volcanic chains. *Journal of Geophysical Research: Solid Earth*, 111(B11):B11407.

Foulger, G. (2010). *Plate vs Plumes: A Geological Controversy*. Wiley-Blackwell.

French, S., Lekic, V., and Romanowicz, B. (2013). Waveform Tomography Reveals Channeled Flow at the Base of the Oceanic Asthenosphere. *Science*, 342(6155):227–230.

Frey, P. J. and George, P.-L. (2008). *Mesh Generation Application to Finite Elements.* ISTE Ltd John Wiley and Sons, Inc, London Hoboken, USA, second edition edition.

Gast, P. W., Tilton, G., and Hedge, C. (1964). Isotopic Composition of Lead and Strontium from Ascension and Gough Islands. *Science*, 145:1181–1185.

Geuzaine, C. and Remacle, J.-F. (209). Gmsh: A 3-D finite element mesh generator with built in pre- and post-processing facilities. *International Journal for Numerical Methods in Engineering*, 79(11):1309–1331.

Giannandrea, E. and Christensen, U. (1993). Variable viscosity convection experiments with a stress-free upper boundary and implications for the heat transport in the Earth's mantle. *Physics of the Earth and Planetary Interiors*, 78(1–2):139–152.

Goes, S., Cammarano, F., and Hansen, U. (2004). Synthetic seismic signature of thermal mantle plumes. *Earth and Planetary Science Letters*, 218(3–4):403–419.

Gonnermann, H. M., Jellinek, A. M., Richards, M. A., and Manga, M. (2004). Modulation of mantle plumes and heat flow at the core mantle boundary by plate-scale flow: results from laboratory experiments. *Earth and Planetary Science Letters*, 226(1-2):53–67.

Gonnermann, H. M., Manga, M., and Jellinek, A. M. (2002). Dynamics and longevity of an initially stratified mantle. *Geophysical Research Letters*, 29(10):1399.

Griffiths, R. W. (1986a). The differing effects of compositional and thermal buoyancies on the evolution of mantle diapirs. *Physics of the Earth and Planetary Interiors*, 43(4):261–273.

Griffiths, R. W. (1986b). Thermals in extremely viscous fluids, including the effects of temperature-dependent viscosity. *Journal of Fluid Mechanics*, 166:115–138.

Griffiths, R. W. (1991). Entrainment and Stirring in Viscous Plumes. *Physics of Fluids a-Fluid Dynamics*, 3(5):1233–1242.

Griffiths, R. W. and Campbell, I. H. (1990). Stirring and structure in mantle starting plumes. *Earth and Planetary Science Letters*, 99(1–2):66–78.

Hamblin, W. K. and Christiansen, E. H. (2003). Hotspots and Mantle Plumes. *Earth's Dynamic Systems*, 10th Edition:632–657.

Hanan, B. and Graham, D. (1996). Lead and Helium Isotope Evidence from Oceanic Basalts for a Common Deep Source of Mantle Plumes. *Science*, 272:991–995.

Hart, S. R., Hauri, E. H., Oschmann, L. A., and Whitehead, J. A. (1992). Mantle Plumes and Entrainment: Isotopic Evidence. *Science*, 256(5056):517–520.

Haskell, N. A. (1935). The Motion of a Viscous Fluid Under a Surface Load. *Physics*, 6(8):265–269.

Heikkila, J. and Silven, O. (1997). A four-step camera calibration procedure with implicit image correction. *Computer Vision and Pattern Recognition, 1997. Proceedings., 1997 IEEE Computer Society Conference on*, pages 1106–1112.

Henderson, A., Ahrens, J., and Law, C. (2004). *The Paraview Guide*. Kitware Inc., Clifton Park, NY.

Herrick, R. R. (1999). Small mantle upwellings are pervasive on Venus and Earth. *Geophysical Research Letters*, 26(6):803–806.

Herzberg, C., Asimow, P. D., Arndt, N., Niu, Y., Lesher, C. M., Fitton, J. G., Cheadle, M. J., and Saunders, A. D. (2007). Temperatures in ambient mantle and plumes: Constraints from basalts, picrites, and komatiites. *Geochemistry, Geophysics, Geosystems*, 8(2):2006.

Hill, R. I., Campbell, I. H., Davies, G. F., and Griffiths, R. W. (1992). Mantle plumes and continental tectonics. *Science*, 256(5054):186–193.

Hofmann, A. W. (1997). Mantle geochemistry: the message from oceanic volcanism. *Nature*, 385(6613):219–229. 10.1038/385219a0.

Hooke, R. (1665). *Micrographia*. J. Martyn and J.Allenstry, London.

Horn, B. K. P. (2000). Tsai's Camera Calibration Method revisited.

Howard, L. N. (1964). Convection at high Rayleigh number. *Proceedings of the 11th International Congress Applied Mechanics*, pages 1109–1115.

Hwang, Y. K., Ritsema, J., van Keken, P. E., Goes, S., and Styles, E. (2011). Wavefront healing renders deep plumes seismically invisible. *Geophysical Journal International*, 187(1):273–277.

Jellinek, A. M., Gonnermann, H. M., and Richards, M. A. (2003). Plume capture by divergent plate motions: implications for the distribution of hotspots, geochemistry of mid-ocean ridge basalts, and estimates of the heat flux at the core–mantle boundary. *Earth and Planetary Science Letters*, 205(3–4):361–378.

Jellinek, A. M., Lenardic, A., and Manga, M. (2002). The influence of interior mantle temperature on the structure of plumes: Heads for Venus, Tails for the Earth. *Geophysical Research Letters*, 29(11):27–1–27–4.

Jellinek, A. M. and Manga, M. (2004). Links between long-lived hot spots, mantle plumes, D″, and plate tectonics. *Reviews of Geophysics*, 42(3):RG3002.

Jones, S. M., White, N., and Maclennan, J. (2002). V-shaped ridges around Iceland: Implications for spatial and temporal patterns of mantle convection. *Geochemistry, Geophysics, Geosystems*, 3(10):1059.

Kaminski, E. and Jaupart, C. (2003). Laminar starting plumes in high-Prandtl-number fluids. *Journal of Fluid Mechanics*, 478:287–298.

Kays, W. M., Crawford, M. E., and Weigand, B. (2004). *Convective Heat and Mass Transfer*. Mcgraw-Hill Series in Mechanical Engineering. Mcgraw-Hill, 4th edition.

Kellogg, L. H. and Wasserburg, G. J. (1990). The role of plumes in mantle Helium fluxes. *Earth and Planetary Science Letters*, 99(3):276–289.

Kincaid, C. and Griffiths, R. W. (2004). Variability in flow and temperatures within mantle subduction zones. *Geochemistry Geophysics Geosystems*, 5(6):Q06002.

King, S. D., Raefsky, A., and Hager, B. H. (1990). Conman: vectorizing a finite element code for incompressible two-dimensional convection in the Earth's mantle. *Physics of the Earth and Planetary Interiors*, 59(3):195–207.

King, S. D. and Redmond, H. L. (2007). The Structure of Thermal Plumes and Geophysical Observations. *geological Society of America Special Papers*, 430:103–120.

King, S. D. and Ritsema, J. (2000). African Hot Spot Volcanism: Small-Scale Convection in the Upper Mantle Beneath Cratons. *Science*, 290(5494):1137–1140.

Krishnamurti, R. (1973). Some further studies on the transition to turbulent convection. *J. Fluid Mechanics*, 60(2):285–303.

Kumagai, I. (2002). On the anatomy of mantle plumes: effect of the viscosity ratio on entrainment and stirring. *Earth and Planetary Science Letters*, 198(1–2):211–224.

Kumagai, I., Davaille, A., and Kurita, K. (2007). On the fate of thermally buoyant mantle plumes at density interfaces. *Earth and Planetary Science Letters*, 254(1-2):180–193.

Kumagai, I., Davaille, A., Kurita, K., and Stutzmann, E. (2008). Mantle plumes: Thin, fat, successful, or failing? Constraints to explain hot spot volcanism through time and space. *Geophysical Research Letters*, 35(16).

Laske, G., Markee, A., Orcutt, J. A., Wolfe, C. J., Collins, J. A., Solomon, S. C., Detrick, R. S., Bercovici, D., and Hauri, E. H. (2011). Asymmetric shallow mantle structure beneath the Hawaiian Swell-evidence from Rayleigh waves recorded by the PLUME network. *Geophysical Journal International*, 187(3):1725–1742.

Lassak, T. M., McNamara, A. K., and Zhong, S. J. (2007). Influence of thermochemical piles on topography at Earth's core-mantle boundary. *Earth and Planetary Science Letters*, 261:443–455.

Laudenbach, N. and Christensen, U. R. (2001). An optical method for measuring temperature in laboratory models of mantle plumes. *Geophysical Journal International*, 145(2):528–534.

Le Bars, M. and Davaille, A. (2002). Stability of thermal convection in two superimposed miscible viscous fluids. *Journal of Fluid Mechanics*, 471:339–363.

Le Bars, M. and Davaille, A. (2004a). Large interface deformation in two-layer thermal convection of miscible viscous fluids. *Journal of Fluid Mechanics*, 499:75–110.

Le Bars, M. and Davaille, A. (2004b). Whole layer convection in a heterogeneous planetary mantle. *Journal of Geophysical Research: Solid Earth*, 109(B3):B03403.

Limare, A., Kumagai, I., Vatteville, J., and Davaille, A. (2008). Thermal plumes visualisation: Differential interferometry versus Thermochromic liquid crystals. *ISFV13-13th International Symposium on Flow Visualization FLUVISU12-12th French Congress on Visualization in Fluid Mechanics*.

Lin, S.-C. and van Keken, P. E. (2006a). Deformation, stirring and material transport in thermochemical plumes. *Geophysical Research Letters*, 33(20):L20306.

Lin, S.-C. and van Keken, P. E. (2006b). Dynamics of thermochemical plumes: 1. Plume formation and entrainment of a dense layer. *Geochemistry, Geophysics, Geosystems*, 7(2):Q02006.

Lithgow-Bertelloni, C., Richards, M. A., Conrad, C. P., and Griffiths, R. W. (2001). Plume generation in natural thermal convection at high Rayleigh and Prandtl numbers. *Journal of Fluid Mechanics*, 434:1–21.

Loper, D. E. (1984). *Structure of the Core and Lower Mantle*, volume Volume 26, pages 1–34. Elsevier.

Loper, D. E. and Stacey, F. D. (1983). The dynamical and thermal structure of deep mantle plumes. *Physics of the Earth and Planetary Interiors*, 33(4):304–317.

Lui, M. and Chase, C. G. (1991). Boundary-layer model of mantle plumes with thermal and chemical diffusion and buoyancy. *Geophysical Journal International*, 104:433–440.

Malamud, B. D. and Turcotte, D. L. (1999). How many plumes are there? *Earth and Planetary Science Letters*, 174(1-2):113–124.

Manga, M. and Weeraratne, D. (1999). Experimental study of non-Boussinesq Rayleigh–Bénard convection at high Rayleigh and Prandtl numbers. *Physics of Fluids*, 11(10):2969–2976.

Manthilake, G. M., de Koker, N., Frost, D. J., and McCammon, C. A. (2011). Lattice thermal conductivity of lower mantle minerals and heat flux from Earth's core. *Proceedings of the National Academy of Sciences*, 108(44):17901–17904.

Marat, J. (1780). *Recharches physiques sur le feu*. Cl. Ant Jombert. Paris.

May, D. A., Schellart, W. P., and Moresi, L. (2013). Overview of adaptive finite element analysis in computational geodynamics. *Journal of Geodynamics*, 70(0):1–20.

McKenzie, D. and Bickle, M. J. (1988). The Volume and Composition of Melt Generated by Extension of the Lithosphere. *Journal of Petrology*, 29(3):625–679.

McKenzie, D. P., Roberts, J. M., and Weiss, N. O. (1974). Towards a numerical simulation. *J. Fluid Mechanics*, 62(3):465–538.

Melling, A. (1997). Tracer particles and seeding for Particle Image Velocimetry. *Measurement Science and Technology*, 8(12):1406.

Melling, A. and Whitelaw, J. H. (1973). Seeding of gas flows for laser anemometry. *DISA Information*, 15:5–14.

Mitrovica, J. X. (1996). Haskell [1935] revisited. *Journal of Geophysical Research*, 101(B1):555–569.

Molnar, P. and Stock, J. (1987). Relative motions of hotspots in the Pacific, Atlantic and Indian Oceans since late Cretaceous time. *Nature*, 327(18th June):587–591.

Monnereau, M. and Cazenave, A. (1990). Depth and geoid anomalies over oceanic hotspot swells: A global survey. *Journal of Geophysical Research: Solid Earth*, 95(B10):15429–15438.

Montelli, R., Nolet, G., Dahlen, F. A., Masters, G., Engdahl, E. R., and Hung, S.-H. (2004). Finite-Frequency Tomography Reveals a Variety of Plumes in the Mantle. *Science*, 303(5656):338–343.

Moresi, L. N., Zhong, S. J., and Gurnis, M. (1996). The accuracy of finite element solutions of Stokes' flow with strongly varying viscosity. *Physics of the Earth and Planetary Interiors*, 97:83–94.

Morgan, W. J. (1971). Convection Plumes in the Lower Mantle. *Nature*, 230(5288):42–43.

Morgan, W. J. (1972). Deep Mantle Convection Plumes and Plate Motions. *AAPG Bulletin*, 56(2):203–213.

Morgan, W. J. (1978). Rodriguez, Darwin, Amsterdam, A second type of hotspot island. *Journal of Geophysical Research*, 83(B11):5355–5360.

Morgan, W. J. (1981). *Hotspot tracks and the opening of the Atlantic and Indian Oceans*. The oceanic lithosphere. John Wiley and Sons, New York.

Moses, E., Zocchi, G., and Libchaberii, A. (1993). An experimental study of laminar plumes. *Journal of Fluid Mechanics*, 251:581–601.

Moses, E., Zocchi, G., Procaccia, I., and Libchaber, A. (1991). The Dynamics and Interaction of laminar thermal plumes. *Europhysics Letters*, 14(1):55–60.

Nataf, H.-C. and VanDecar, J. (1993). Seismological detection of a mantle plume? *Nature*, 364(6433):115–120.

Newsome, W. H. (2011). Experimental Investigation of Mass Transport, Dynamics and Stirring in Isolated Thermal Plumes. *University of Michigan, Geological Sciences Department*, PhD Thesis.

O'Connor, J. M., Stoffers, P., Wijbrans, J. R., Shannon, P. M., and Morrissey, T. (2000). Evidence from episodic seamount volcanism for pulsing of the Iceland plume in the past 70Myr. *Nature*, 408(6815):954–958.

Oldham, D. and Davies, J. H. (2004). Numerical investigation of layered convection in a three-dimensional shell with application to planetary mantles. *Geochemistry, Geophysics, Geosystems*, 5(12):Q12C04.

Olson, P. (1990). *Hot spots, swells and mantle plumes*. John Wiley and Sons Ltd.

Olson, P. and Singer, H. (1985). Creeping plumes. *Journal of Fluid Mechanics*, 158:511–531.

Parkin, C. J., Lunnon, Z. C., White, R. S., and Christie, P. A. F. (2007). Imaging the pulsing Iceland mantle plume through the Eocene. *Geology*, 35(1):93–96.

Parmentier, E. M. and Sotin, C. (2000). Three-dimensional numerical experiments on thermal convection in a very viscous fluid: Implications for the dynamics of a thermal boundary layer at high Rayleigh number. *Physics of Fluids*, 12(3):609–617.

Parmentier, E. M., Turcotte, D. L., and Torrance, K. E. (1975). Numerical Experiments on the Structure of Mantle Plumes. *Journal of Geophysical Research*, 80(32):4417–4424.

Pears, M. (2010). Collapse in the thermal evolution in the mantle: An experimental fluid dynamical approach. *University College London, Earth Sciences Department*, MSci Thesis.

Phipps Morgan, J. (1997). The generation of a compositional lithosphere by mid-ocean ridge melting and its effect on subsequent off-axis hotspot upwelling and melting. *Earth and Planetary Science Letters*, 146(1–2):213–232.

Piggott, M. D., Gorman, G. J., Pain, C. C., Allison, P. A., Candy, A. S., Martin, B. T., and Wells, M. R. (2008). A new computational framework for multi-scale ocean modelling based on adapting unstructured meshes. *International Journal for Numerical Methods in Fluids*, 56(8):1003–1015.

Poirier, J. P. (1988). Transport properties of liquid metals and viscosity of the Earth's core. *Geophysical Journal*, 92(1):99–105.

Poore, H. R., White, N., and Jones, S. (2009). A Neogene chronology of Iceland plume activity from V-shaped ridges. *Earth and Planetary Science Letters*, 283(1-4):1–13.

Prasad, A. K. (2000). Stereoscopic Particle Image Velocimetry. *Experiments in Fluids*, 29(2):103–116.

Raffel, M., Willert, C., and Kompenhans, J. (1998). *Particle Image Velocimetry - A practical guide*. Springer-Verlag Berlin Heidelberg.

Raffel, M., Willert, C., Wereley, S., and Kompenhans, J. (2007). *Particle Image Velocimetry: A Practical Guide*. Springer, 2nd edition edition.

Reese, C., Solomatov, V., and Baumgardner, J. R. (2002). Survival of impact-induced thermal anomalies in the Martian mantle. *Journal of Geophysical Research*, 107:12–24.

Ribe, N. M. (2007). *Analytical Approaches to Mantle Dynamics*, volume 7.04 of *Treatise on Geophysics*. Elsevier, Amsterdam.

Ribe, N. M. and Christensen, U. R. (1994). Three-dimensional modeling of plume-lithosphere interaction. *Journal of Geophysical Research: Solid Earth*, 99(B1):669–682.

Ribe, N. M., Davaille, A., and Christensen, U. (2007). *Fluid Dynamics of Mantle Plumes*, pages 1–48. Springer Berlin Heidelberg.

Richards, M. A., Duncan, R. A., and Courtillot, V. E. (1989). Flood Basalts and Hot-Spot Tracks: Plume Heads and Tails. *Science*, 246(4926):103–107.

Richards, M. A. and Griffiths, R. W. (1989). Thermal entrainment by deflected mantle plumes. *Nature*, 342(6252):900–902.

Richards, M. A., Hager, B. H., and Sleep, N. H. (1988). Dynamically Supported Geoid Highs Over Hotspots: Observation and Theory. *Journal of Geophysical Research*, 93(B7):7690–7708.

Richter, F. M. and Parsons, B. (1975). On the Interaction of Two Scales of Convection in the Mantle. *Journal of Geophysical Research*, 80(17):2529–2541.

Ritsema, J. and Allen, R. M. (2003). The elusive mantle plume. *Earth and Planetary Science Letters*, 207(1–4):1–12.

Schaeffer, N. and Manga, M. (2001). Interaction of rising and sinking mantle plumes. *Geophysical Research Letters*, 28(3):455–458.

Schubert, G., Bercovici, D., and Glatzmaier, G. (1990). Mantle Dynamics in Mars and Venus: Influence of an Immobile Lithosphere on Three-Dimensional Mantle Convection. *Journal of Geophysical Research*, 95(B9):105–129.

Schubert, G., Turcotte, D. L., and Olson, P. (2001). *Mantle Convection in the Earth and Planets*. Cambridge University Press.

Scott, D. R., Stevenson, D. J., and Whitehead, J. A. (1986). Observations of solitary waves in a viscously deformable pipe. *Nature*, 319(6056):759–761. 10.1038/319759a0.

Settles, G. S. (2001). *Schlieren and Shadowgraph Techniques*. Springer.

Shlien, D. J. (1976). Some laminar thermal and plume experiments. *Physics of Fluids*, 19(8):1089–1098.

Shlien, D. J. and Thompson, D. W. (1975). Some experiments on the motion of an isolated laminar thermal. *Journal of Fluid Mechanics*, 72(01):35–47.

Silveira, G., Stutzmann, E., Davaille, A., Montagner, J.-P., Mendes-Victor, L., and Sebai, A. (2006). Azores hotspot signature in the upper mantle. *Journal of Volcanology and Geothermal Research*, 156(1-2):23–34.

Sleep, N. H. (1990). Hotspots and Mantle Plumes: Some Phenomenology. *Journal of Geophysical Research*, 95(B5):6715–6736.

Sparrow, E. M., Husar, R. B., and Goldstein, R. J. (1970). Observations and other characteristics of thermals. *Journal of Fluid Mechanics*, 41(04):793–800.

Stamhuis, E. (2006). Basics and principles of particle image velocimetry (PIV) for mapping biogenic and biologically relevant flows. *Aquatic Ecology*, 40(4):463–479.

Steinberger, B. (2000). Plumes in a convecting mantle: Models and observations for individual hotspots. *Journal of Geophysical Research: Solid Earth*, 105(B5):11127–11152.

Steinberger, B. and O'Connell, R. J. (1998). Advection of plumes in mantle flow: implications for hotspot motion, mantle viscosity and plume distribution. *Geophysical Journal International*, 132(2):412–434.

Steinberger, B. and O'Connell, R. J. (2000). *Effects of Mantle Flow on Hotspot Motion*, pages 377–398. American Geophysical Union.

Stengel, K. C., Oliver, D. S., and Brooker, J. R. (1982). Onset of convection in a variable-viscosity fluid. *J. Fluid Mechanics*, 120:411–431.

Suetsugu, D., Steinberger, B., and Kogiso, T. (2004). *Hotspots and Mantle Plumes*. Earth Processes. Elsevier Ltd.

Tackley, P. J. (2000). Mantle convection and plate tectonics: Toward an integrated physical and chemical theory. *Science*, 288(5473):2002–2007.

Tanny, J. and Shlien, D. J. (1985). Velocity field measurements of a laminar starting plume. *Physics of Fluids (1958-1988)*, 28(4):1027–1032. (Tanai).

Tatsumoto, M. (1966). Genetic relations of oceanic basalts as indicated by lead isotopes. *Science*, 153:1094–1101.

Tritton, D. (1988). *Physical Fluid Dynamics*. Oxford University Press, New York.

Tsai, R. (1987). A versatile Camera Calibration Technique for High-Accuracy 3D Machine Vision Metrology Using Off-the-Shelf TV Cameras and Lenses. *IEEE Journal of Robotics and Automation*, RA-3(4):323–344.

Turcotte, D. L. and Oxburgh, E. R. (1967). Finite amplitude convection cells and continental drift. *J. Fluid Mechanics*, 28:29–42.

Turcotte, D. L. and Oxburgh, E. R. (1978). Intra-Plate Volcanism [and Discussion]. *Philosophical Transactions of the Royal Society of London. Series A, Mathematical and Physical Sciences*, 288(1355):561–579.

Turcotte, D. L. and Schubert, G. (2002). *Geodynamics*. Cambridge University Press.

van den Berg, A. P., van Keken, P. E., and Yuen, D. A. (1993). The effects of a composite non-Newtonian and Newtonian rheology on mantle convection. *Geophysical Journal International*, 115(1):62–78.

van Keken, P. E. (1997). Evolution of starting mantle plumes: a comparison between numerical and laboratory models. *Earth and Planetary Science Letters*, 148(1–2):1–11.

van Keken, P. E., Davaille, A., and Vatteville, J. (2013). Dynamics of a laminar plume in a cavity: The influence of boundaries on the steady state stem structure. *Geochemistry Geophysics Geosystems*, 14(XX):1–21.

Vatteville, J., van Keken, P. E., Limare, A., and Davaille, A. (2009). Starting laminar plumes: Comparison of laboratory and numerical modeling. *Geochemistry, Geophysics, Geosystems*, 10(12):Q12013.

White, D. B. (1988). The planforms and onset of convection with a temperature-dependent viscosity. *Journal of Fluid Mechanics*, 191:247–286.

White, N. J., Mackay, L. M., Jones, S. M., Lovell, J. P. B., and Davis, M. W. (2013). Reply to comment by Hillis et al. 2013. *Geophysical Journal International*, 194:680–682.

White, W. M. (2010). Oceanic Island Basalts and Mantle Plumes: The Geochemical Perspective. *Annual Review of Earth and Planetary Sciences*, 38(1):133–160.

Whitehead, J. A. J. and Luther, D. S. (1975). Dynamics of Laboratory Diapir and Plume Models. *Journal of Geophysical Research*, 80(5):705–717.

Willert, C. E. and Gharib, M. (1991). Digital Particle Image Velocimetry. *Experiments in Fluids*, 10(4):181–193.

Wilson, J. T. (1963a). A Possible Origin of the Hawaiian Islands. *Canadian Journal of Physics*, 41(6):863–870.

Wilson, J. T. (1963b). Evidence from Islands on the Spreading of Ocean Floors. *Nature*, 197(4867):536–538.

Wilson, J. T. (1965). A New Class of Faults and their Bearing on Continental Drift. *Nature*, 207(4995):343–347.

Wolfe, C. J., Solomon, S. C., Laske, G., Collins, J. A., Detrick, R. S., Orcutt, J. A., Bercovici, D., and Hauri, E. H. (2011). Mantle P-wave velocity structure beneath the Hawaiian hotspot. *Earth and Planetary Science Letters*, 303(3-4):267–280.

Wolfe, C. J., Th. Bjarnason, I., VanDecar, J. C., and Solomon, S. C. (1997). Seismic structure of the Iceland mantle plume. *Nature*, 385(6613):245–247.

Wray, F. (1978). Some convective flows of geophysical interest. *PhD thesis*, University of Cambridge.

Yuen, D. A. and Peltier, W. R. (1980). Mantle plumes and thermal stability of the D'' layer. *Geophysical Research Letters*, 7(9):625–628.

Zhao, D. (2001). Seismic structure and origin of hotspots and mantle plumes. *Earth and Planetary Science Letters*, 192(3):251–265.

Zhong, S., Zuber, M. T., Moresi, L., and Gurnis, M. (2000). Role of temperature-dependent viscosity and surface plates in spherical shell models of mantle convection. *Journal of Geophysical Research: Solid Earth*, 105(B5):11063–11082.

Zhong, S. J., Yuen, D. A., and Moresi, L. N. (2007). *Numerical Methods for Mantle Convection*, chapter 7.05, pages 227–252. Elsevier, Amsterdam.

Zienkiewicz, O. C. and Taylor, R. L. (2000). Finite Element Method (5th Edition) Volume 1 - The Basis.

Zindler, A. and Hart, S. (1986). Chemical Geodynamics. *Annual Review of Earth and Planetary Sciences*, 14:493–571.